**DOT/FAA/AR-07/56,V3**

Air Traffic Organization
NextGen & Operations Planning
Office of Research and
Technology Development
Washington, DC 20591

# Assessment of Residual Stresses and Hole Quality on the Fatigue Behavior of Aircraft Structural Joints

## Volume 3: Finite Element Simulation of Riveting Process and Fatigue Lives

March 2009

Final Report

This document is available to the U.S. public through the National Technical Information Service (NTIS), Springfield, Virginia 22161.

U.S. Department of Transportation
**Federal Aviation Administration**

## NOTICE

This document is disseminated under the sponsorship of the U.S. Department of Transportation in the interest of information exchange. The United States Government assumes no liability for the contents or use thereof. The United States Government does not endorse products or manufacturers. Trade or manufacturer's names appear herein solely because they are considered essential to the objective of this report. This document does not constitute FAA certification policy. Consult your local FAA aircraft certification office as to its use.

This report is available at the Federal Aviation Administration William J. Hughes Technical Center's Full-Text Technical Reports page: actlibrary.tc.faa.gov in Adobe Acrobat portable document format (PDF).

**Technical Report Documentation Page**

| 1. Report No. | 2. Government Accession No. | 3. Recipient's Catalog No. |
|---|---|---|
| DOT/FAA/AR-07/56,V3 | | |

| 4. Title and Subtitle | 5. Report Date |
|---|---|
| ASSESSMENT OF RESIDUAL STRESSES AND HOLE QUALITY ON THE FATIGUE BEHAVIOR OF AIRCRAFT STRUCTURAL JOINTS<br><br>VOLUME 3: FINITE ELEMENT SIMULATION OF RIVETING PROCESS AND FATIGUE LIVES | March 2009 |
| | 6. Performing Organization Code |
| 7. Author(s) | 8. Performing Organization Report No. |
| A. Atre[1], W. Steven Johnson[1], and James C. Newman, Jr.[2] | |
| 9. Performing Organization Name and Address | 10. Work Unit No. (TRAIS) |
| [1] Georgia Institute of Technology<br>Atlanta, GA 30332<br><br>[2] Mississippi State University<br>Mississippi State, MS 39762 | 01-C-AW-MSU AMD 003, 012, 013 |
| | 11. Contract or Grant No. |
| 12. Sponsoring Agency Name and Address | 13. Type of Report and Period Covered |
| U.S. Department of Transportation<br>Federal Aviation Administration<br>Air Traffic Organization NextGen & Operations Planning<br>Office of Research and Technology Development<br>Washington, DC 20491 | Final Report |
| | 14. Sponsoring Agency Code<br>ANM-100 |

15. Supplementary Notes

The Federal Aviation Administration Airport and Aircraft Safety R&D Division Technical Monitor was Dr. Felix Abali.

16. Abstract

Aircraft fuselages are fatigue-critical structures, and operational damage in the lap joints have been widely recognized as a safety issue. The Federal Aviation Administration and Delta Air Lines teamed in an effort to conduct destructive evaluation, inspection, and extended fatigue testing of a retired Boeing 727 passenger aircraft near its design service goal. Inspections revealed a large number of cracks in the fuselage joints emanating from the rivet/skin interface. The presence of these cracks was attributed to the sharp stress gradients arising from contact between the installed rivet and the rivet holes. The residual-stress field generated during the rivet installation has a strong impact on the nucleation and propagation of fatigue cracks at and around the rivet/skin interface. The main objective of this research was to establish a link between critical riveting process parameters and the potential of fatigue damage in the joint. The significance of contact and plasticity in the riveting process made the problem well-suited to a finite element (FE) modeling solution. In addition, there was also a need to understand how manufacturing process variations affect the residual-stress state produced in the joint. Both of these objectives were addressed in this research. The study was conducted in four phases. First, a two-dimensional axisymmetric model of the riveting process was developed, which was deliberately designed to simulate previous experiments conducted by a team of Canadian researchers. The second phase used the FE approach and the lessons learned from the first phase to specifically focus on the development of a three-dimensional displacement controlled riveting process model for the lap joint configuration. In the third phase, the residual stress and strain generated from the riveting process models served as an input to a global three-rivet lap joint model designed to approximate the in-service loading experienced by the B727 fuselage splice. Finally, fatigue tests on riveted lap joint specimens were conducted to forge a link between rivet installation and hole-quality effects on fatigue performance of the joint. A comparison of the surface strains predicted by the FE models to the surface strains of the tested specimen captured through thermal imaging techniques offered an additional source of validation to the analysis. An observed correlation between the fatigue lifetimes of the tested specimens and controlled parameters showed underdriven rivets to be the most threatening in reducing the fatigue life of the joint.

| 17. Key Words | 18. Distribution Statement |
|---|---|
| Fatigue, Finite element analyses, Residual stress, Aircraft, Joints | This document is available to the U.S. public through the National Technical Information Service (NTIS), Springfield, Virginia 22161 |

| 19. Security Classif. (of this report) | 20. Security Classif. (of this page) | 21. No. of Pages | 22. Price |
|---|---|---|---|
| Unclassified | Unclassified | 166 | |

**Form DOT F 1700.7** (8-72) Reproduction of completed page authorized

TABLE OF CONTENTS


| | | Page |
|---|---|---|
| EXECUTIVE SUMMARY | | xiii |
| 1. | INTRODUCTION | 1-1 |
| 1.1 | Description of Findings | 1-1 |
| 1.2 | Approach | 1-7 |
| 1.2.1 | Development of a Two-Dimensional Axisymmetric Force-Controlled Rivet Installation Simulation Using ABAQUS/Standard™ | 1-8 |
| 1.2.2 | Three-Dimensional Quasi-Static Rivet Installation Simulation Using ABACUS/Explicit™ | 1-8 |
| 1.2.3 | Development of a Baseline 3D Model Based on the Data Available From DAL for the B727 Rivet Configuration | 1-8 |
| 1.2.4 | Experimental Fatigue Testing of Riveted Lap-Joint Specimens | 1-9 |
| 1.3 | Research Outcomes | 1-9 |
| 2. | BACKGROUND AND LITERATURE REVIEW | 2-1 |
| 2.1 | Analytical Study of Residual Stresses Around Fastener Holes | 2-2 |
| 2.2 | Experimental Measurements of Residual Stresses Around Fastener Holes | 2-3 |
| 2.3 | Finite Element Methods to Characterize Residual Stresses Around Fastener Holes | 2-4 |
| 2.4 | Other Methods to Characterize Residual Stresses Around Fastener Holes | 2-7 |
| 2.5 | Mechanical Properties of Rivet Materials | 2-7 |
| 2.6 | Study of Fretting Fatigue | 2-7 |
| 2.7 | Study of Fatigue Cracking in Lap Joints | 2-8 |
| 2.8 | Summary | 2-11 |
| 3. | INITIAL MODEL VALIDATION | 3-1 |
| 3.1 | ABAQUS/Standard Model Validation | 3-1 |
| 3.2 | ABACUS/Explicit Model Validation | 3-6 |
| 3.3 | Summary | 3-11 |

4. PARAMETRIC STUDIES 4-1

4.1 Baseline Model 4-1
4.2 Rivet Deformation 4-8
4.3 Effect of Variations on Baseline Model 4-10

4.3.1 Increased Rivet Displacement (Overdriven Rivet) 4-12
4.3.2 Increased Coefficient of Friction 4-12
4.3.3 Hole Misalignment 4-12
4.3.4 Decreased Lower Skin Hole Size 4-12
4.3.5 Decreased Upper Skin Hole Size 4-12
4.3.6 Presence of Debris 4-13
4.3.7 Decreased Hole Clearance 4-13
4.3.8 Decreased Rivet Displacement (Underdriven Rivet) 4-13

4.4 Effect of Hole-Quality Variations With Underdriven Rivets 4-14
4.5 Effect of Variations on Baseline Model With Sealant 4-15

4.5.1 Baseline Interference and Sealant 4-17
4.5.2 Baseline Interference and Sealant Coverage Variation 4-19
4.5.3 Baseline Interference, Sealant, and Drill Shavings 4-19
4.5.4 Low Interference and Sealant 4-20
4.5.5 Low Interference, Sealant, and Drill Shavings 4-21
4.5.6 Low Interference and Sealant Coverage Variation 4-21
4.5.7 Rivet Tilt and Sealant 4-21

4.6 Effect of Load Transfer on Countersunk Joints 4-22
4.7 Application of Models to Fretting Fatigue 4-23
4.8 Summary 4-29

5. GLOBAL FUSELAGE LAP JOINT ANALYSIS 5-1

5.1 Background 5-1
5.2 Analysis 5-1
5.3 Fatigue Crack Growth Analysis 5-7
5.4 Analysis of Critical Process Variations 5-9

5.4.1 Effect of Underdriven Rivets 5-10
5.4.2 Effect of Overdriven Rivets 5-10
5.4.3 Variation in Rivet Interference 5-10
5.4.4 Effect of Sealant 5-11
5.4.5 Effect of Sealant and Underdriven Rivets 5-11
5.4.6 Effect of Sealant, Drill Shavings, and Underdriven Rivets 5-11
5.4.7 Effect of Friction 5-11

5.5 Summary 5-11

6. EXPERIMENTAL FATIGUE TESTING 6-1

6.1 Fatigue Test Matrix 6-1
6.2 Specimen and Test Details 6-3
6.3 Test Setup 6-5
6.4 Fatigue Test Results 6-6
6.5 Summary of Fatigue Test Results 6-14

7. SUMMARY 7-1

8. CONCLUSIONS 8-1

9. RECOMMENDATIONS FOR RIVET INSTALLATION 9-1

10. FUTURE WORK 10-1

11. REFERENCES 11-1

APPENDICES

A—Thermoghaphic Stress Analysis
B—Some Modeling Considerations
C—ABAQUS Capabilities
D—Archive of Lap Joint Failures

LIST OF FIGURES


| Figure | | Page |
|---|---|---|
| 1-1 | Aircraft Selected for the FAA/DAL Teardown Program | 1-2 |
| 1-2 | Aircraft With Panels Removed for Damage Characterization | 1-2 |
| 1-3 | Schematic of the Removed Panels and the Fuselage Lap Joint | 1-3 |
| 1-4 | Example of Crack Indications at the Rivet Holes in the Right-Hand Side Panel | 1-4 |
| 1-5 | Example of the Rivet Hole Defects in the Right-Hand Side Panel | 1-5 |
| 1-6 | Microscopy of Riveted Sections Along the Right-Hand Side Panel | 1-6 |
| 1-7 | View of the Installed Rivets Along the Left-Hand Side Panel | 1-6 |
| 1-8 | Flowchart Outlining the Approach of This Research | 1-7 |
| 2-1 | Schematic of Rivet Installation | 2-1 |
| 2-2 | Locations of Crack Origins in the Experimental Tests Conducted by Piascik | 2-9 |
| 2-3 | Locations of Crack Origins Observed by Liao, et al. | 2-10 |
| 2-4 | An Example of Models Developed by Harris, et al. to Predict Fatigue Crack Growth in Riveted Lap Joints | 2-11 |
| 3-1 | Specimen Configuration Analyzed in ABAQUS/Standard View Above Joint Inner Sheet Surface, Side View of Specimen and Close-Up of Rivet | 3-2 |
| 3-2 | The 2D Axisymmetric FE Model With Three Deformable Bodies and One Rigid Pusher | 3-3 |
| 3-3 | Deformed Rivet Parameters | 3-4 |
| 3-4 | Deformed Configuration for a Range of Applied Squeeze Forces | 3-5 |
| 3-5 | Comparison of Force-Displacement Curves | 3-5 |
| 3-6 | Riveted Joint Parameters for Model Validation in ABAQUS/Explicit | 3-6 |
| 3-7 | Boundary Conditions for ABAQUS/Explicit Model Validation | 3-7 |

| | | |
|---|---|---|
| 3-8 | von Mises Stress Contour in MPa and Equivalent Plastic Strains at End of the Riveting | 3-8 |
| 3-9 | Comparison of Residual Strains | 3-8 |
| 3-10 | Comparison of Force-Displacement Diagram for the ABAQUS/Explicit Solution | 3-9 |
| 3-11 | Energy Response in the Model | 3-9 |
| 3-12 | Equivalent Plastic Strain Contours for the ABAQUS/Standard and ABAQUS/Explicit Analyses | 3-10 |
| 3-13 | Residual-Stress Contours in MPa for the ABAQUS/Standard and ABAQUS/Explicit Analyses | 3-10 |
| 3-14 | Comparison of Rivet Head Deformation From Experiment to the FE Analyses | 3-11 |
| 4-1 | Geometry Parameters for the Baseline Model | 4-2 |
| 4-2 | Boundary Conditions | 4-2 |
| 4-3 | Deformed Shape and Residual Hoop Stress Contours in the Skin After Unload in ABAQUS/Standard Analysis | 4-4 |
| 4-4 | An Example of the Through-the-Thickness and Unsymmetrical Variation of the Hoop Stress: Constrained Side and Unconstrained Side | 4-5 |
| 4-5 | An Example of the Unsymmetrical Variation of the Hoop Stress Along the Length of the Skin: Constrained Side and Unconstrained Side | 4-6 |
| 4-6 | Symmetric Stress State Resulting From Zero Clearance Between Rivet and Hole | 4-6 |
| 4-7 | Comparison of the Equivalent Plastic Strain Contours From the ABAQUS/Standard and ABACUS/Explicit Analyses | 4-7 |
| 4-8 | Kinetic Energy Plot for the Whole Model | 4-7 |
| 4-9 | Residual Hoop Stress Contours in Upper and Lower Skin as Predicted by ABAQUS/Explicit Analysis | 4-8 |
| 4-10 | Deformed Configuration for an Applied Displacement of 0.0027 m (0.11 in.), 0.0033 m (0.13 in.) (Standard), 0.0035 m (0.14 in.), 0.004 m (0.16 in.) Top to Bottom, Respectively | 4-9 |
| 4-11 | Rivet Head Deformation Compared With Applied Displacement | 4-9 |

4-12 A View of the Models Showing Reduced Hole Size, Increase Hole Size, Lower Skin Misalignment, Increased Upper Skin Hole Size, Hole Defects Such as Scars and Gouges, Increased Lower Skin Hole Size, and Presence of Debris 4-11

4-13 An Example of the Rivet Bulging Resulting From Effects Such as Skin Misalignment and Varying Hole Sizes 4-13

4-14 Underdriven Rivets and Effects Such as Skin Misalignment 4-14

4-15 Maximum Tensile Hoop Stress as a Function of Rivet Interference, Countersunk Skin, and Straight-Shank Skin 4-15

4-16 Stress-Strain Data for Hyperelastic Material Model 4-16

4-17 A View of the Model With the Sealant 4-17

4-18 Final Deformed Shape With Sealant: ABAQUS/Standard and ABAQUS/Explicit 4-18

4-19 Residual Hoop Stress Contour in ABAQUS/Standard for the Upper and Lower Skin 4-18

4-20 Residual Hoop Stress Contour in ABAQUS/Explicit for the Upper and Lower Skin 4-18

4-21 Model With Sealant Coverage Reduced Near Hole 4-19

4-22 Rivet Section Showing Drill Shaving and Deformed Plot of Representative FE Model in ABAQUS/Explicit 4-20

4-23 Final Deformed Shape With Sealant and Low Interference in ABAQUS/Standard 4-20

4-24 Rivet Section Showing Rivet Tilt and Deformed Plot of Representative FE Model in ABAQUS/Standard 4-21

4-25 Definition of LTR in Riveted Lap Joints 4-22

4-26 Effect of LTR on Maximum Principal Stress State in the Upper Skin for Underdriven Rivets 4-22

4-27 Effect of LTR on Maximum Principal Stress State in the Upper Skin for Overdriven Rivets 4-23

4-28 Possible Locations Susceptible to Fretting in Riveted Lap Joints 4-25

4-29 Angular Locations and Depth in the FE Model 4-25

4-30 Angular Variations of Contact Pressure at Faying Surface for Different Rivet Interferences 4-26

4-31 Angular Variations of Damage Parameter $F_1$ at Faying Surface (z=t) for Different Rivet Interferences 4-26

4-32 Example 1 of Fretting Damage Observed for Some Rivet Holes From the Teardown Inspection (Faying Surface, Right-Hand Side Panel Joint) 4-27

4-33 Example 2 of Fretting Damage Observed for Some Rivet Holes From the Teardown Inspection (Faying Surface, Right-Hand Side Panel Joint) 4-28

4-34 Angular Variations of Tangential Stress and Damage Parameter $F_2$ at the Faying Surface (z=t) for Different Rivet Interferences 4-29

5-1 Schematic of Lap Joint Typically Susceptible to Widespread Fatigue Damage 5-2

5-2 Typical Three-Rivet Fuselage Splice 5-2

5-3 Geometry of the Fuselage Lap Joint Model and FE Model Analyzed in This Study 5-3

5-4 Deformed Plot (Exaggerated 20 Times) of Fuselage Splice After Residual Stress Application and Cyclic Pressurization 5-4

5-5 Maximum Principal Stress State in Inner and Outer Skins 5-5

5-6 Comparison of Cracking Observed in Teardown Inspection and Stress State Predicted by the FE Analysis in the Lap Joint 5-5

5-7 Complexity of Stress Distribution at the Inner Skin Lower Row Rivet Hole 5-6

5-8 Fuselage Splice Model for the Left-Hand Side Panel Joint With Modified Rivet Spacing 5-6

5-9 Stress State at the Critical Hole for the Inner Skin (Left-Hand Side Panel Joint) 5-7

5-10 The SWT Parameter Plotted With the Number of Cycles to Crack Nucleation $N_n$ 5-8

5-11 Schematic of Model Used for Crack Growth Analysis 5-9

6-1 Specification of the Joint 6-3

6-2 Schematic of the Specimen Based on NASM 6-4

6-3 Schematic of the Assembled Joint 6-4

6-4 Final Assembled and Riveted Specimens 6-5

6-5 Comparison of Baseline and Underdriven Specimens 6-5

6-6 Fatigue Test Setup 6-6

6-7 Observed Failure Location for Specimens and Sealant Separation 6-7

6-8 Comparison of Fatigue Lifetimes for Rivet Installation 6-8

6-9 Comparison of Fatigue Lifetimes for Sealant Type 6-9

6-10 Comparison of Fatigue Lifetimes for Hole Quality 6-10

6-11 Optical Micrographs for Specimen S26s: View of the Faying Surface, View of the Crack Growth Away From the Hole, and View of the Rivet Hole With a Small Groove 6-12

6-12 Optical Micrographs for Specimen U26s: View of the Faying Surface, View of the Crack Growth, and View of the Rivet Hole With a Small Groove 6-13

LISTS OF TABLES


| Table | | Page |
|---|---|---|
| 3-1 | Material Property Parameters Used in FE Models | 3-3 |
| 3-2 | Comparison of Rivet Head Deformation as Predicted by the FE Method to Experiment Measurements | 3-4 |
| 4-1 | Results From the Mesh Refinement Study | 4-3 |
| 4-2 | Parametric Variations | 4-10 |
| 4-3 | Comparison of Radial and Hoop Stresses for Different Parameters | 4-14 |
| 4-4 | Summary of Residual Hoop Stress Variations With Sealant | 4-17 |
| 5-1 | Summary of Results From the Parametric Studies | 5-9 |
| 6-1 | Complete Test Matrix | 6-2 |
| 6-2 | Summary of Mean Cycles to Failure | 6-11 |

LIST OF ACRONYMS

| | |
|---|---|
| 2D | Two-dimensional |
| 3D | Three-dimensional |
| DAL | Delta Airlines |
| DSG | Design service goal |
| FAA | Federal Aviation Administration |
| FE | Finite element |
| FML | Fiber metal laminate |
| H | Height |
| IR | Infrared |
| LTR | Load transfer ratio |
| SIF | Stress-intensity factor |
| SWT | Smith-Watson-Topper |
| TSA | Thermographic Stress Analysis |

# EXECUTIVE SUMMARY

Aircraft fuselage splices are fatigue-critical structures, and the damage associated with these structures has been widely recognized as a safety issue that needs to be addressed in the structural integrity of aging aircraft. Airframe teardown inspections and laboratory fatigue testing of lap joint specimens is an effective means of obtaining essential data for fatigue cracking and structural evaluation of airworthiness of aging aircraft. The Federal Aviation Administration and Delta Airlines teamed in an effort to conduct destructive evaluation, inspection, and extended fatigue testing of a retired Boeing 727-232 (B727) passenger aircraft near its design service goal.

Preliminary visual inspection revealed a large number of cracks in the aircraft fuselage lap joint emanating from the rivet/skin interface. Most of these cracks were observed in the lower skin such that they could not be detected under an operator's routine maintenance. The presence of these cracks was attributed to the sharp gradients of stress arising from contact between the installed rivet and rivet holes. The residual-stress field generated during the rivet installation has a strong impact on the nucleation and propagation of fatigue cracks at and around the rivet/skin interface. The main objective of this research was to establish a link between critical riveting process parameters and the potential of fatigue damage in the joint.

From an analytical perspective, the significance of contact and plasticity in the riveting process made the problem well suited to a finite element (FE) modeling solution. In addition to the need to understand the mechanics of the process, there was also a need to understand how manufacturing process variations affect the residual-stress state produced in the joint. Both objectives were addressed in this research.

The investigation conducted herein was carried out in four phases. In the first phase, a two-dimensional axisymmetric model of the riveting process was developed using the ABAQUS/Standard FE solver, which was designed to simulate previous experiments conducted by a team of Canadian researchers involving force-controlled riveted specimens. A quarter-symmetry, quasi-static, three-dimensional (3D) model of the process was then analyzed using ABAQUS/Explicit FE tools to simulate previous experiments conducted by a team of French researchers. From a modeling standpoint, the experimental comparisons offered a good set of validation measurements obtained under well-controlled laboratory conditions to establish solver capabilities. Additionally, the analyses also showed the difference in capabilities of the two solvers in simulating the same process. Overall, the prediction quality of the models was good and generated confidence in the ability to accurately capture the residual-stress state from such a complex forming process.

The second phase of this investigation used the FE model approaches and the lessons learned from the first phase to specifically focus on the development of a 3D displacement-controlled riveting process model for the B727 lap joint configuration. Effects such as rivet hole defects, presence of sealant, presence of debris, and rivet interference were considered using the developed model. The analyzed models demonstrated a strong dependence of the residual hoop stress on process variations. Effect of underdriven rivets was observed to be especially critical in altering the residual-stress state qualitatively as well as quantitatively.

In the third phase of this investigation, the residual stress and strain results already generated from the riveting process models served as an input to a global three-rivet lap joint model designed to approximate the in-service loading experienced by the B727 fuselage splice. As evident from the teardown inspection, a good comparison of the state of damage observed around the rivet holes to the critical stress location predicted by the FE model provided excellent validation to the analysis.

In the fourth phase of this research, experimental fatigue testing of riveted lap joint specimens was conducted with the specific goal of forging a link between rivet installation and hole-quality effects on fatigue performance of the joint. A comparison of the surface strains predicted by the FE models to the surface strains of the tested specimen captured through thermal imaging techniques offered an additional source of validation to the analysis. An observed correlation between the fatigue lifetimes of the tested specimens and controlled parameters showed under-driven rivets to be the most threatening in reducing the fatigue life of the joint.

# 1. INTRODUCTION.

The fuselage of an aircraft consists of sheet panels, stringers, and stiffeners held together by riveted lap joints. Although different joining techniques exist, the skin panels are typically fastened together with rivets. Numerous rivets are required to join the skin completely. Flight fatigue loading is due to the pressurization and depressurization of the fuselage, which occurs once every flight. The concentrated stress state at the rivet/skin interface combined with a large number of loading cycles is a primary cause of crack initiation at and around the rivet/skin interface. The 1988 Aloha Airlines flight 243 incident, in which an extensive section of the fuselage ripped off from the aircraft while in flight, demonstrates the importance of aircraft fastener hole fatigue. The incident was attributed to linking up of cracks at different rivet holes, caused by a combination of fatigue and corrosion.

Airframe teardown inspections and laboratory fatigue testing of lap joint specimens is an effective means of obtaining essential data for fatigue cracking and structural evaluation of airworthiness of aging aircraft. The Airworthiness Assurance Working Group (AAWG) under the Federal Aviation Administration (FAA) is currently using published technical rulemaking recommendations to develop programs that monitor and prevent such long-term damage effects [1]. The destructive testing and analysis of aircraft structures will provide the aviation community with comprehensive guidelines for a structural maintenance program to assist the FAA in issuing rules, policy, and advisory circulars to ensure continued safety.

For the primary focus of characterizing fatigue damage in aircraft fuselage structure, the FAA and Delta Airlines (DAL) collaborated in a 3-year effort to conduct destructive evaluation, finite element (FE) analysis, fatigue testing, and inspection of nine lap-spliced panels obtained from a retired Boeing 727-232 (B727) airplane near its design service goal (DSG) [2]. This study is part of the effort and is primarily concerned with the effects of the riveting process and subsequent load transfer on fatigue life of the airframe lap joints.

## 1.1 DESCRIPTION OF FINDINGS.

The aircraft selected for this program was a Boeing 727-232 (B727). The airplane was placed into service in 1974 and retired in 1998. During that time, the airplane accumulated 59,497 flight cycles and 66,412 flight hours and was near its DSG. The airplane was owned and operated exclusively by DAL and had a well-documented service history. Throughout the operation of the aircraft, the average operating pressure was 8.6 psi [2]. Figure 1-1 shows a picture of the aircraft. Nine fuselage lap joint areas susceptible to widespread fatigue damage were removed from the aircraft. Out of these, five were destructively evaluated and four were subjected to extended fatigue testing at the FAA Full-Scale Aircraft Structural Test Evaluation and Research (FASTER) facility located at the William J. Hughes Technical Center, New Jersey. Figure 1-2 shows the aircraft with the fuselage panels removed for inspection. Prior to removal, all target sections were labeled with boundaries and identification marks to indicate the location and orientation of the section with respect to the aircraft [2].

Figure 1-1. Aircraft Selected for the FAA/DAL Teardown Program

Figure 1-2. Aircraft With Panels Removed for Damage Characterization

A field inspection was also performed at the storage site to catalogue the condition of the aircraft and target structure. Detailed visual inspections and nondestructive evaluations were conducted using mid-frequency eddy current and external low-frequency eddy current methods. After the site inspections, the target structure was removed and transported to the analysis site at DAL in Atlanta, GA, for postremoval inspections [2]. Figure 1-3 shows the schematic of the removed panels and the fuselage lap joint.

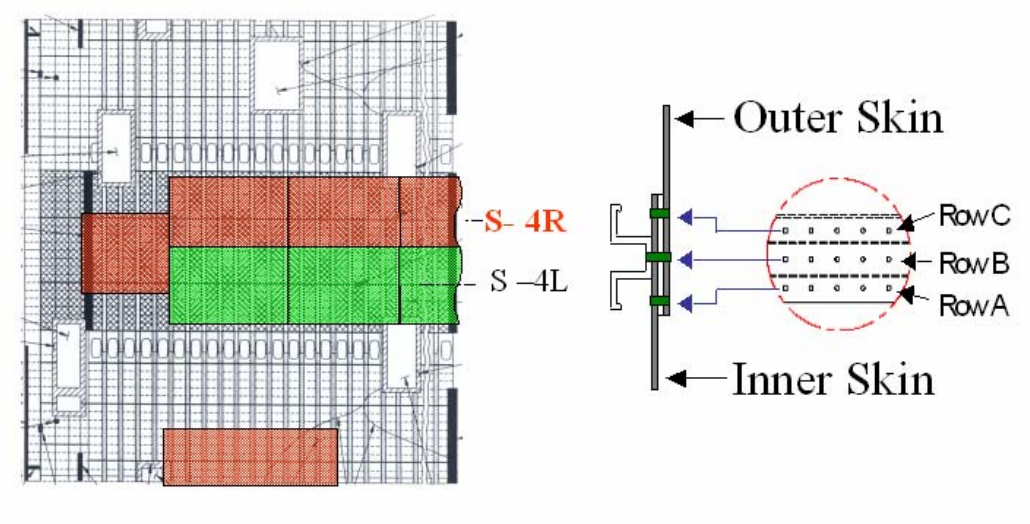


Figure 1-3. Schematic of the Removed Panels and the Fuselage Lap Joint

Preliminary findings from the inspection included the following:

- Several cracks were observed along the S-4R panel (hereafter referred to as the right-hand side panel), inner skin, and outer row A.

- Each crack had several origins, and the general direction of the cracks was normal to the hoop circumferential direction. The primary origin of the cracks was at the corner of the hole and the faying surface (figure 1-4). While hole quality was not uniformly good, the defects in the holes were generally in the circumferential direction (figure 1-5). Fracture surfaces appeared to be free of corrosion and any gross mechanical fretting damage.

- Sixty percent of the rivets along the right-hand side panel were observed to be underdriven (final installed rivet head diameter less than specifications).

- Significant variations in rivet interference were observed through the rivet rows along the right-hand side panel, combined with presence of embedded drill shavings in the sealant (figure 1-6).

- Very few crack indications were observed along the S-4L panel (hereafter referred to as the left-hand side panel).

- Quality of installed rivets along the left-hand side panel was significantly better (figure 1-7).

- The right-hand side panel used a different quality sealant than the left-hand side panel.

- The right-hand side panel rivet spacing along the lap joint was different than that along the left-hand side panel.

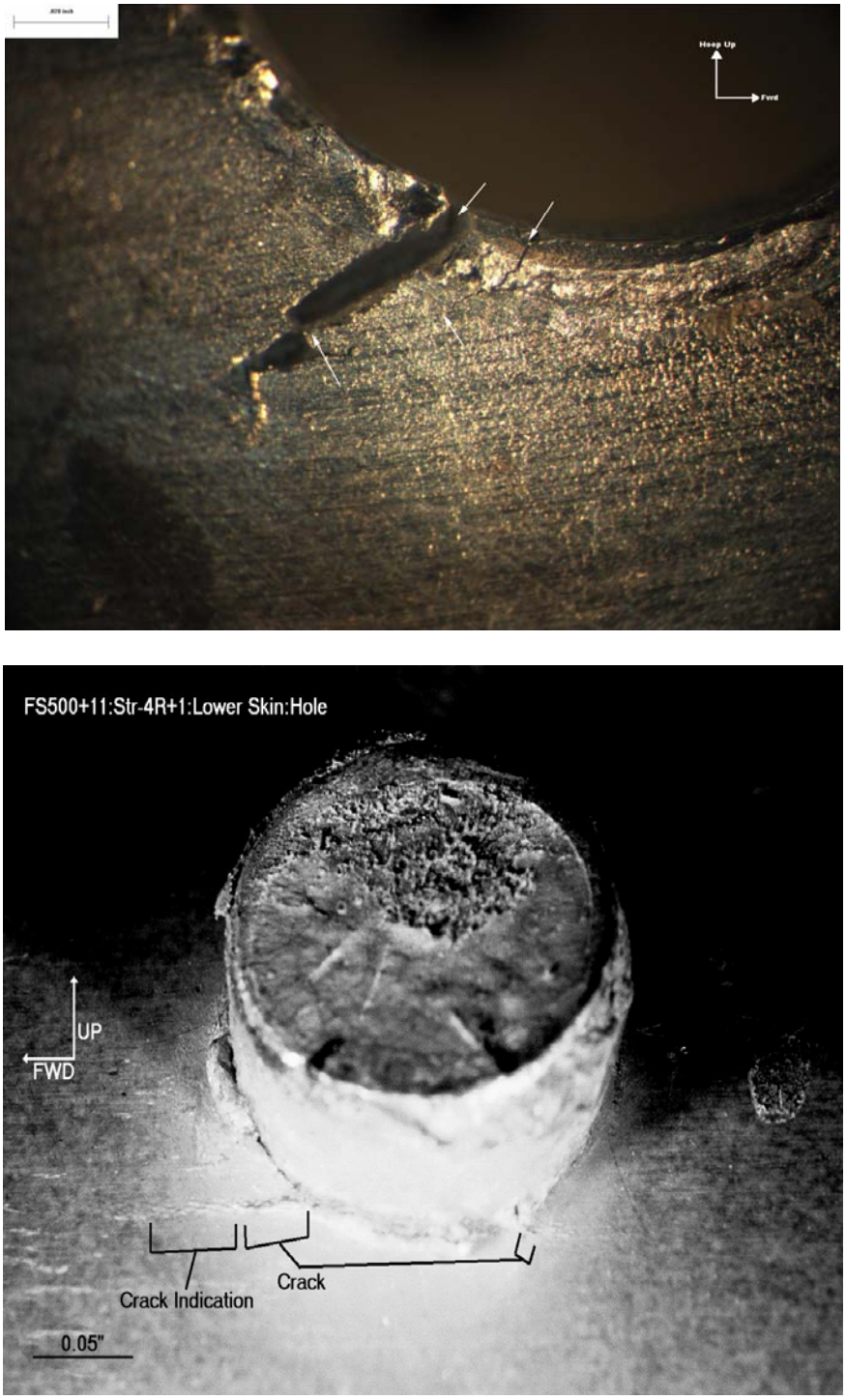


Figure 1-4. Example of Crack Indications at the Rivet Holes in the Right-Hand Side Panel

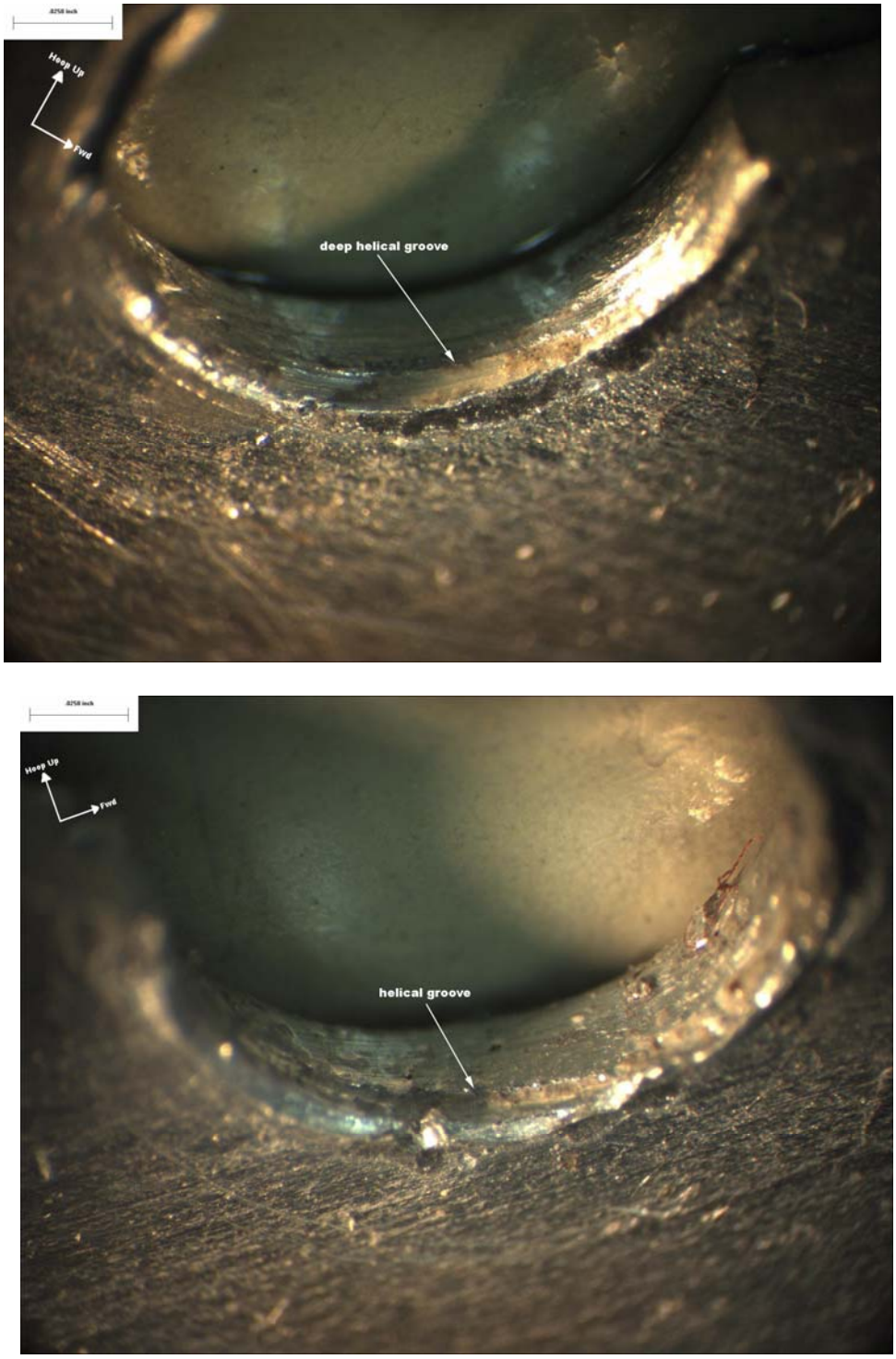


Figure 1-5. Example of the Rivet Hole Defects in the Right-Hand Side Panel

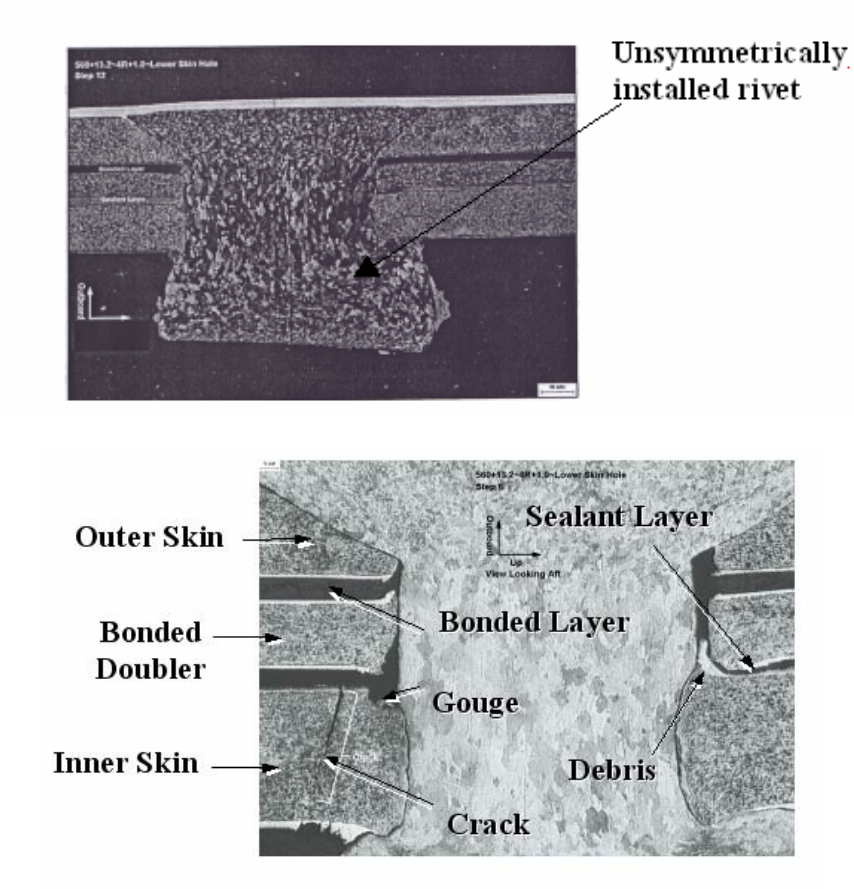


Figure 1-6. Microscopy of Riveted Sections Along the Right-Hand Side Panel (Differences in rivet interference, deformation of sealant and presence of drill shavings are evident.)

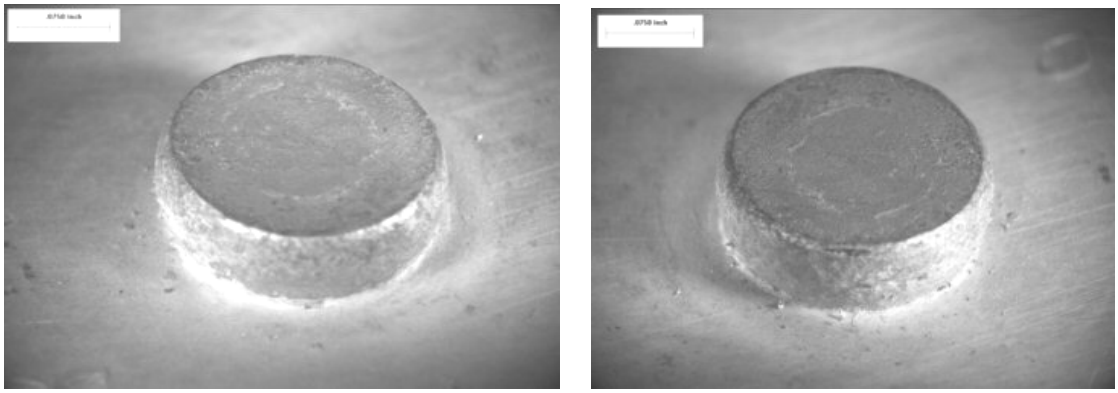

Figure 1-7. View of the Installed Rivets Along the Left-Hand Side Panel

It is clear there is a need for an accurate understanding of the initial interference effects induced by rivet installation and the resulting residual-stress field around the periphery of the hole. The nature of this residual-stress field can have a profound impact on the nucleation and subsequent propagation of fatigue cracks emanating from near the edge of the hole. Motivated by teardown inspections and laboratory nondestructive examinations of the fuselage lap joint, this research targeted analyzing the localized stress conditions at the rivet/skin interface resulting from rivet installation and subsequent load transfer.

## 1.2 APPROACH.

The adopted approach for this research is shown in figure 1-8 with a brief summary following.

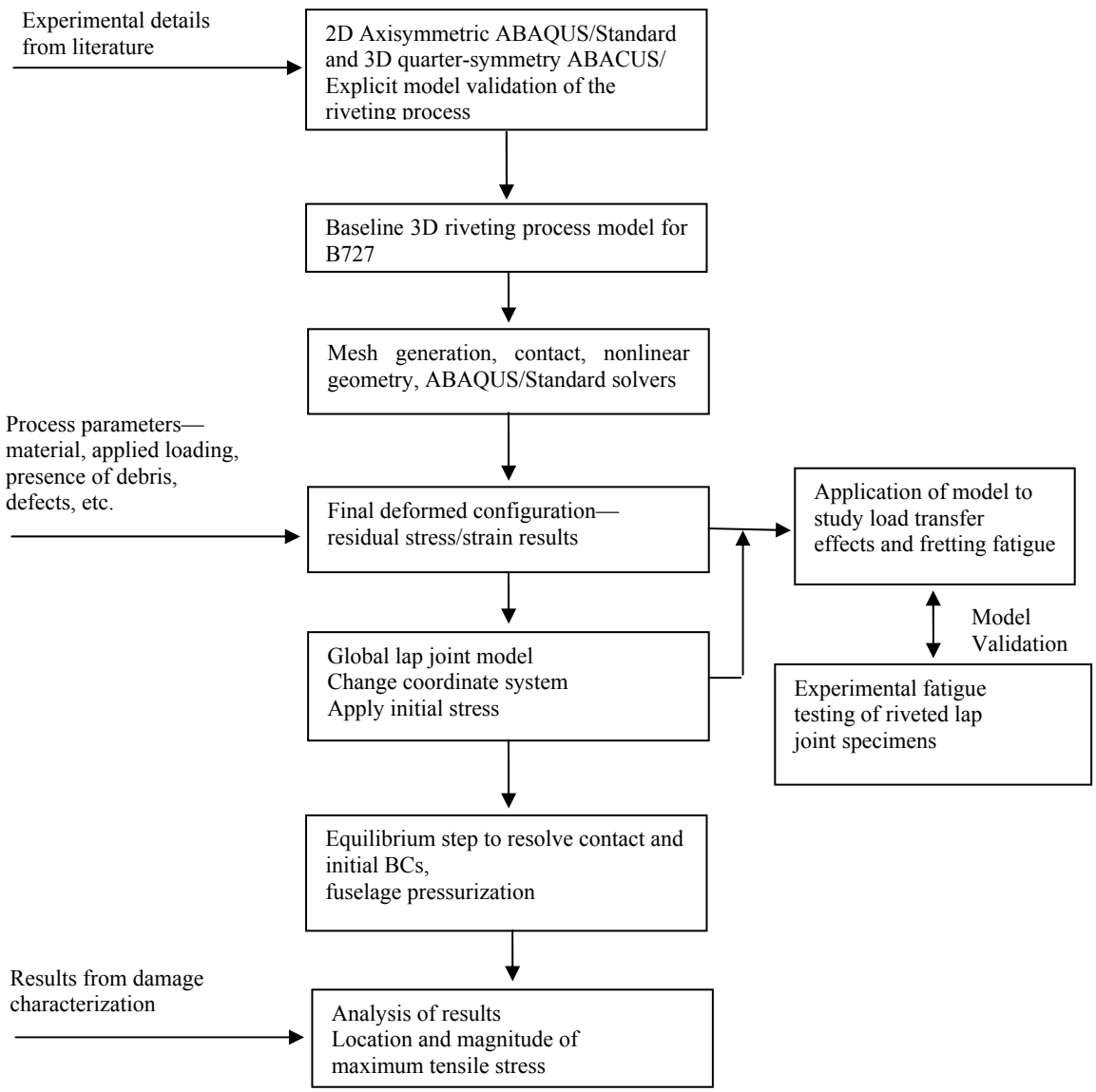


Figure 1-8. Flowchart Outlining the Approach of This Research

1.2.1 Development of a Two-Dimensional Axisymmetric Force-Controlled Rivet Installation Simulation Using ABAQUS/Standard™.

The purpose of this analysis was to establish ABAQUS/Standard simulation capabilities and check the extent of the accuracy of numerical tools in predicting the residual stresses. This was achieved by comparing the force-displacement curves, the rivet deformation parameters, and strains from the simulation with experimental data for a range of installation forces.

1.2.2 Three-Dimensional Quasi-Static Rivet Installation Simulation Using ABACUS/Explicit™.

From three-dimensional (3D) quasi-static rivet installation simulation using ABAQUS/Explicit, general observations on rivet installation show that the rivets were all uniformly installed with little or no tilt in the tail buttons and no offsets of the buttons' axes with respect to the rivet shank axes. The purpose of this analysis was to investigate the accuracy of ABAQUS/Explicit FE tools in simulating the forming process. This was achieved by comparing the force-displacement curves and strains from the simulation to those measured by experiment.

The complex contact interactions and large deformations pose a significant problem in performing rivet simulations even for a commercial FE program. Another approach of this work was to provide detailed generalized documentation on element library, material behavior, contact formulations of the code, and overcoming convergence difficulties (appendix D). Particular emphasis was placed on specific capabilities of the code (ABAQUS/Standard and ABAQUS/Explicit) in correctly modeling such forming processes (appendix D).

1.2.3 Development of a Baseline 3D Model Based on the Data Available From DAL for the B727 Rivet Configuration.

The 3D model has the capability of representing the manufacturing process variations more accurately and can be implemented for modeling subsequent load transfer effects. The results from the baseline model serve as a comparison for parametric variations. The effect of some critical process parameters on the residual-stress state in the skin were analyzed using the developed model. The simulated process variations as observed from the teardown inspection included presence of hole defects such as gouges, presence of drill shavings, presence of sealant, varying hole sizes, and varying rivet interferences. The developed 3D model was also implemented to investigate the effects of different percentages of load transfer on the stress state in the lap joint. The results were compared to the stress state predicted without taking into account initial rivet interference.

The results from the rivet installation models were input to a global lap joint model representing a three-rivet row joint. The initial residual-stress state was applied to the rivet installation models. This was followed by application of the in-service loads to observe the resulting stress state at and around the rivet holes. The model served to demonstrate the importance of load transfer through the fuselage splice. The model results were compared to the damage characterization results available from DAL. The effects of variation in interference through the rivet row, variation in friction and presence of sealant on load transfer, and resulting stress state on the joint were also analyzed using the developed model.

### 1.2.4 Experimental Fatigue Testing of Riveted Lap-Joint Specimens.

The goal of the experimental fatigue testing with riveted lap joint specimens was to form a link between rivet installation, nucleation of fatigue damage, and subsequent fatigue performance of these joints. The goal can be summarized as: manufacture lap joint specimens for critical parameters under controlled conditions; fatigue test joints under a range of loads representative of fuselage structure; identify critical areas of fatigue crack nucleation sites; and correlate the process parameters with observed failure mechanisms to identify critical variables in nucleation of cracks.

## 1.3 RESEARCH OUTCOMES.

The research work:

- provided a relationship between the impact of riveting process parameters on potential fatigue damage in aircraft structural joint that can be implemented by aircraft fatigue designers to assist in retarding fatigue damage.

- provided a comparison of the effectiveness of the FE models, ABAQUS/Standard and ABAQUS/Explicit methods to model the riveting process, particularly the sealant analysis.

- provided stress/strain results that can be applied in crack growth analyses software programs such as FASTRAN.

- provided an observation on the effects of interference on the mechanics of load transfer and resulting stress state in the rivet rows for the fuselage splice joint.

- provided a database to the FAA of the critical parameter models, recommendations, and problem-solving methodology, which will assist in improving structural integrity of aircraft structures.

## 2. BACKGROUND AND LITERATURE REVIEW.

A riveted single lap joint is formed by joining two sheets together with rivets. The process is accomplished by driving the rivet shank with a rigid bucking bar while a rigid tool constrains the head of the rivet. This is illustrated in figure 2-1. The bucking bar may be driven hydraulically, pneumatically, or manually. When aircraft skin panels are joined with an interference fit, a residual-stress field is created. With increased interference, plasticity strain hardening occurs. When the skin panels are subjected to in-service cyclic loads, load transfer takes place locally at the rivet/skin interface. The resulting contact stresses at the rivet/skin interface play a primary role in propagation of fatigue cracks at and around the rivet/skin interface. The primary goal of this investigation was to develop a model that accurately characterizes the residual-stress state from the riveting process and implement the model to study the effects of critical manufacturing process variations.

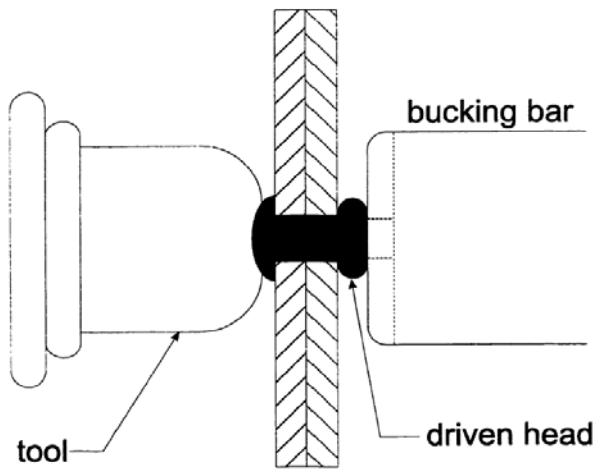


Figure 2-1. Schematic of Rivet Installation [3]

To date, there has not been any comprehensive research published in open literature that addresses manufacturing process variations (such as hole quality and sealant issues combined with rivet interference) in the riveting process. Despite its complex nature, when this problem separated into the general engineering issues that are germane to the application one can find much pertinent published research. Once all the contributing subjects to the problem have been identified, a survey of the previous research in each of these areas can be done before tackling the more specific problem. What follows is an extensive survey of significant research conducted on crack growth in riveted lap joints, which includes the implementation of analytical and experimental tools to characterize riveted lap-joint residual stresses, study of fatigue life in riveted joints, and development of analytical models to predict fatigue crack growth in lap joints.

## 2.1 ANALYTICAL STUDY OF RESIDUAL STRESSES AROUND FASTENER HOLES.

The rivet deformation is analogous to cold working of holes with an expanding mandrel. By squeezing the rivet, a radial outward in-plane pressure $p$ is applied inside the fastener hole in an infinite sheet. The elastic solution for the stress field near the hole is

$$\sigma_r = -p\left(\frac{r}{R_o}\right)^{-2} \tag{2-1}$$

$$\sigma_\theta = p\left(\frac{r}{R_o}\right)^{-2} \tag{2-2}$$

where $r$ is the distance from the center of a hole with radius $R_o$ .

Increasing the internal pressure can lead to plastic deformation of the sheet material. A relationship between the plastic deformation and stress distribution of elastic-perfectly plastic materials was shown by Park and Atluri [4]:

$$\sigma_r = -p + \sigma_y \ln\left(\frac{r}{R_o}\right) \qquad R_o \le r \le r_y \tag{2-3a}$$

$$\sigma_r = \frac{-\sigma_y}{2}\left(\frac{r_y}{r}\right)^2 \qquad r > r_y \tag{2-3b}$$

$$\sigma_\theta = (\sigma_y - p) + \sigma_y \ln\left(\frac{r}{R_o}\right) \qquad R_o \le r \le r_y \tag{2-4a}$$

$$\sigma_r = \frac{\sigma_y}{2}\left(\frac{r_y}{r}\right)^2 \qquad r > r_y \tag{2-4b}$$

where $\sigma_y$ is the material yield stress, $r_y$ is the radius of the plastic region.

Park and Atluri obtained the residual-stress field by subtracting the elastic stress field of equations 2-1 and 2-2 from equations 2-3 and 2-4 after releasing rivet squeeze force. Limitations of this analytical model were pointed out by Muller [5] as (1) the model does not include strain hardening, (2) the model is one-dimensional and neglects hole expansion variation through the thickness, and (3) a 3D stress state results from the driven rivet head exerting a pressure on the sheets.

## 2.2 EXPERIMENTAL MEASUREMENTS OF RESIDUAL STRESSES AROUND FASTENER HOLES.

Strain gage methods, ultrasonics, x-ray techniques, and magnetics are some of the methods that can be used to measure residual stresses. However, the structural peculiarities of riveted joints make it an extremely tenuous task to implement any of these methods for nondestructive determination of residual stresses on the surface, or in the immediate vicinity of a hole.

Langrand, et al. [6] applied a strain gage method to measure radial sheet strains during and after riveting. The method was applied to circular and square-shaped sheets. A single rivet was present in each specimen with an applied crushing velocity of 2 mm/min, slow enough to be considered quasi-static. They observed more than 20% compressive strain levels near the crushing edge and lower than 1% strain levels away from the edge while riveting. After riveting, the residual strains were similar to maximum observed during the process. The strain levels near the punching edge could not be observed accurately due to damage to the strain gage. Furthermore, the strain gages only measured the radial strain. The residual strain through-the-thickness and inside the sheet could not be detected.

The x-ray technique was applied by Fitzgerald and Cohen [7] to determine residual stresses around rivets in clad aluminum alloy (Al) plates. They assumed an in-plane stress state over the depth of penetration. This technique was limited such that the entire residual-stress state at and around the rivet/skin interface could not be measured. Only residual stresses close to the sheet surface could be calculated. The implemented technique was documented thoroughly in their research.

The riveted joint interference can improve the lap joint's ability to resist fatigue. Nepershin and Knigin [8] suggested an interference of 2% to 3%, while Yarkovets, et al. [9] recommend an interference value of 2.2% to 3.4% for passenger aircraft. Demina and Volkov [10] define interference as

$$\delta = \frac{d_1 - d}{d} \times 100\% \tag{2-5}$$

where $d_1$ is the deformed rivet diameter and $d$ is the hole diameter.

Ryzhova [11] applied a nondestructive ultrasonic inspection method to determine rivet/hole interference. The ultrasonic method was based on echo signal amplitudes, which are a function of interference. Experimental data was used to establish a correlation between the interference and the mean value of ultrasonic signal amplitude. Ryzhova [11] also established a linear correlation of the average echo signal amplitude value and the average residual stress along the rivet height based on the least-squares method. However, the ultrasonic method could only determine radial residual stresses along rivet height at the rivet/hole interface by using the relation between the rivet residual stresses and interference. No results for hoop or radial stresses in the sheets were reported in this study. A labor-intensive destructive method was used to measure residual stresses in the rivet body.

Muller [5] used photoelasticity, rivet-sheet springback, and microhardness to determine residual stress at the panel-mating surface. The experiments were however unsuccessful, and it was concluded that experimental measurement of residual stresses was not a simple task.

## 2.3 FINITE ELEMENT METHODS TO CHARACTERIZE RESIDUAL STRESSES AROUND FASTENER HOLES.

The FE method is a powerful numerical tool to simulate complex forming problems. Review of the literature showed that this method was applied to study riveted joints since the 1990s. A force-controlled two-dimensional (2D) axisymmetric model consisting of two circular pieces of sheet metal connected by a single rivet was implemented to simulate the rivet installation in majority of prior research. The axisymmetric FE analysis models a one-quarter joint configuration with geometric, contact, and material nonlinearity.

Slater [12] analyzed this model for a noncountersunk configuration. He investigated the results (interference, residual stresses) for only one value of squeeze force. Based on this model, Muller [5] studied the residual stresses for a range of squeeze forces. He used PATRAN (preprocessor) and ABAQUS (solver) for his analysis. A slug-type rivet (driven head on both sides) and a countersunk configuration were analyzed in his research. An elastic-linearly plastic material behavior was assumed in the model. Muller concluded that a force-controlled rivet installation provided a more accurate control for the process. The results of residual stresses at the hole wall and along the mating surface, as well as clamping stress (in thickness direction), were given and discussed in Muller's work. His conclusions for the slug and countersunk models can be summarized as follows [5]:

- Slug model: The residual tangential stresses along the mating surface become compressive from tensile in the vicinity of the hole as a result of the increasing squeezing force. Tensile residual stresses increase with distance away from the hole. Residual radial compressive stresses occur on the wall of the hole, but are not homogeneous through the thickness of the sheet. The maximum compressive residual stress occurs away from the rivet hole. For large squeeze forces, significant compressive radial residual stresses occur at a considerable distance from the hole edge. With a larger driven head, significant clamping stresses can be induced. These are generated by increasing the squeeze force.

- Countersunk model: In the FE simulation, only one value of squeeze force was applied. A reduction of the hole expansion towards the rivet flush head was observed from Muller's FE results. The average rivet expansion was smaller for the countersunk sheet than for the noncountersunk sheet. The residual stresses at the hole edge (both the tangential and radial compressive residual stresses) were larger for noncountersunk sheets than for countersunk sheets.

Muller's research was limited by the effects of material properties and the residual-stress field. Szolwinski and Farris [13] implemented a strain-hardening material model for the rivet and the plates to analyze the riveting process. The material model was based on experimental compression testing of 2117-T4 alloy rivet shanks. Squeeze forces ranging from 2500 to 5000

pounds force were considered in the analysis. Szolwinski and Farris [13] observed that an increasing value of squeeze force pushed the zone of tensile hoop stress away from the hole and resulted in a larger driven-head size. A noncountersunk model was analyzed. A through-the-thickness gradient of residual stresses was observed in the model with a compressive hoop zone dominating near the hole periphery and tensile hoop zone away from the hole. Their investigation showed that an increase in fatigue life could be obtained with larger squeeze force. None of the cases analyzed indicated appreciable levels of residual clamping pressure through-the-thickness, contrary to that of Muller's [5] findings for a slug-type rivet with a driven head on both ends. Their results were consistent, however, with modeling results conducted by Fawaz [14]. Comments were also made regarding the relationship between the riveting process parameters and trends in observed failures of riveted lap joint test articles. Their study showed that fatigue life increases with larger squeeze forces, and decreases with an increase in fatigue load.

A large number of aircraft manufacturers use rivet-tail shape parameters, such as tail height and tail diameters, as a means of determining whether a joint will operate successfully in service. Displacement-controlled riveting is the main method of determining this. A displacement-controlled riveting process was analyzed theoretically by Nepershin and Knign [8]. The analysis primarily characterized the interference and residual stresses in a riveted joint using a rigid, plastic body model. A finite difference approach was applied to replace differential equations using Tresca plasticity conditions in the principal stress plane to analyze the plastic flow due to the upsetting of the rivet head. The formation process was solved by using a sequence of Cauchy, Riemann, and mixed boundary-value equations defined by (1) the shape of the free side surface of the rivet head being formed, (2) the boundaries of the tool, and (3) the plastic-friction coefficient at the boundaries between the plastic region, the tool, and the package. Though similar to the FE method, FEs provide an easier tool for analysis.

Nepershin, et al. [8] also performed nonlinear FE simulations by using the previous finite difference model to form a riveted joint and by using the force boundary conditions of stack loading on offset rivet heads. The results for interference distribution across joint packages were compared with experimental data, and a linear approximation for calculating interference values at certain positions, based on riveting stress, was also proposed. The authors also discussed comparisons between the calculated interference and the experimental results determined by measuring the rivet diameter after cutting the package. Significant discrepancies were observed between the calculated and experimental results.

Langrand, et al. [6] conducted 3D FE simulations of rivet forming. Circular and square sheet geometries were analyzed and experimental residual strain data were used to validate the FE model. The crushing velocity applied in the simulation was slow enough to be considered quasi-static. They applied a strain hardening material model for both the rivet and sheet based on experimental data. The FE simulations agreed with the experiment, but full residual stress/strain fields around the hole were not found.

The residual clamping stress exerted by the rivets on the joint was studied by Deng and Hutchinson [15]. Relation between the clamping and applied force was analyzed using FE methods in the small strain framework. Full finite strain formulation was used for re-

computation of some results. The results were analyzed for an elastic-perfectly plastic material model for both the rivets and sheet, and effects of strain hardening on the residual clamping stress were also discussed.

Ryan and Monaghan [16] simulated rivet installation with an elasto-plastic axisymmetric model for fiber laminate and typical aluminum alloy countersunk panels. A large deformation, nonlinear quasi-static analysis was conducted since sheet materials, 2024-T3, fiber metal laminate (FML), rivet, 2117-T3 alloy are not strain rate sensitive at room temperature. They concluded from the models that the localized compressive hoop stress after the riveting process increases fatigue life of panels. It was also observed that FML could extend fatigue life of the riveted joint as compared to monolithic aluminum alloys. They also noted that the behavior of aluminum alloy relative to FML panels was very different, hence the squeezing load should be reduced while installing rivets in FML panels. Tail height and tail diameters cannot be used successfully as a means of comparing the behavior of various panel materials.

Swenson, et al. [17] analyzed an FE model of crack growth in a riveted lap joint. The panels were modeled as 2D layers connected by elastic shear springs. The rivet was modeled as a disk in each layer connected by an adhesive. Automatic remeshing was implemented to model crack growth. However, the model lacked sufficient similarity to a riveted lap joint and the rivet was only realistic as a noncountersunk one without any heads.

Weissberg, et al. [18] performed 3D linear elastic FE analysis of a bolted lap joint using NASTRAN. They investigated the compliance of riveted joints experimentally and found reasonable agreement between the two results. A major conclusion from the work was that the compliance measurements showed considerable scatter due to unknown values of interference and clamping force.

Sundarraj, et al. [19] studied 3D effects in double-shear single rivet lap joints via axisymmetric FE models. However, the model was only applicable in the absence of frictional forces and for limited number of loads. Ekvall [20] modeled a four-rivet-row lap joint with bar elements connected at node points offset from the rivet location. The model was linear elastic.

In a recent study conducted at the National Research Council, Canada, Li, et al. [21 and 22] presented 2D and 3D numerical techniques to characterize the stress state for a one-rivet joint through the entire loading history (rivet expansion and tensile loading). Their numerical results predicted that the residual stress induced by the rivet squeeze force had a considerable effect on the stress variations in the tensile loading stage.

Imanaka [23] has experimentally analyzed the fatigue strength of adhesive-rivet lap joints for riveted lap joints with sealant. He has also investigated the stress distribution in the riveted joint for a high-modulus adhesive using the FE method. Similar analysis was also conducted by Liu and Sawa [24] to evaluate the strength of single lap adhesive joints with rivets, subjected to external bending moments. Dechwayukul, et al. [25] presented a thin adhesive layer analysis FE method to investigate the effects of thin sealant layers on the fatigue performance of riveted countersunk and noncountersunk lap joints. They compared their results to riveted lap joints without sealant and observed a reduction in the stress concentration factor at the rivet/skin

interface. The analysis however does not take into account plasticity and the nonuniform interference produced by rivet installation.

## 2.4 OTHER METHODS TO CHARACTERIZE RESIDUAL STRESSES AROUND FASTENER HOLES.

The interference stresses resulting from the riveting process can be analyzed using other methods, such as the misfit method. In this method, radial and rivet height conformity is forced between an initially oversized ratio of rivet shank and hole and an undersized ratio of shank height over panel depth. Fung and Smart [26] employed a thermal expansion method by varying the temperature of the rivet shank to reduce its length and expand it in the radial direction. Their interference values were typically lower than those observed in practice. Bellinger, et al. [27] and Shi, et al. [28] implemented a method by applying squeeze force at two heads of the rivet followed by external loads to predict stress distribution.

## 2.5 MECHANICAL PROPERTIES OF RIVET MATERIALS.

Most rivets are made from 2117, 2024, and 7075 aluminum alloy, and most sheets are made from 2024-T3 aluminum alloy. The extra weight penalty of the riveted joint is imposed by the offset rivet head. Aluminum riveting provides several advantages to the aviation industry, such as low manufacturing cost, low material cost, and fuel economy. The majority of aerospace manufacturers currently adopt the MS20426 type of rivet to assemble the fuselage section. The rivet's mechanical property is also an important component in the structure. Patronelli, et al. [29] investigated rivet performance in actual service conditions. They developed an original microtensile test rig to test rivet specimens. The rig was first implemented to test 7050 aluminum alloy specimens with 5% compressive residual strains corresponding to a driven rivet head. The results indicate that the 7050 alloy shows a kinematic hardening behavior.

## 2.6 STUDY OF FRETTING FATIGUE.

Fretting is a type of damage arising from a combination of wear, corrosion, and fatigue. It is a contact mechanism driven by micromotion and stresses at the contact zone. Early analyses conducted by Mindlin [30] revealed the division of contact into stick and slip, relevant to fretting damage. Fretting damage was commonly observed on roller bearings, riveted lap joints, and even in artificial hip joints. In riveted lap joints, fretting was shown to be a primary cause of crack initiation [31-34]. In engineering materials, fretting is a three-stage mechanism [35]:

1. A thin layer of oxide is removed from the surface of the material through wear.

2. In the first few cycles as the oxide degrades, the underlying material forms micro-welds through an adhesive process causing wear debris between the contacting surfaces [36]. As the fretting contact cycles increase, the coefficient of friction increases with wear debris accumulation [37 and 38].

3. As the cycles accumulate, plastic deformation takes place near the surface promoting wear and oxide formation.

This plastic deformation is a source of crack nucleation, and fretting fatigue is a result of these microcracks penetrating into the bulk of the material. The damage caused by fretting can reduce fatigue strength by 18 times [39]. Iyer, et al. [40] conducted 3D FE simulations and experimental fretting wear tests. They observed that rivet tilt and panel local bending enhanced fatigue crack growth. They also noted that fretting wear was more pronounced at the panel interface than at rivet/panel interface. This process was promoted by a countersunk head and low friction.

Szolwinski and Farris [32 and 33] assessed the applicability of conventional multiaxial fatigue theories to fretting. Szolwinski's and Farris's [32 and 33] predictions were in good agreement with the experiments of Nowell and Hills [41].

Socie [42 and 43] successfully applied multiaxial fatigue models to correlate crack nucleation observation in strain-controlled tension and torsion tests of AISI type 304 stainless steel tubular specimens. In 1993, he provided an excellent summary of work done on multiaxial fatigue, which was used to develop life models for two nucleation behaviors observed in the multiaxial loading of various materials. They were (1) cracks nucleating and growing on planes of maximum cyclic shear strain and (2) high-cycle fatigue behavior in which crack formation on shear planes consumes the majority of the fatigue life.

On a general side, Swalla [44] conducted a detailed investigation on the application of different multiaxial fatigue theories for prediction of fretting crack damage in PH 13-8 Mo stainless steel. The advantages and disadvantages of the different criteria in fatigue crack prediction are discussed in detail below using FE and experimental methods.

## 2.7 STUDY OF FATIGUE CRACKING IN LAP JOINTS.

Fung and Smart [26] used the Coffin-Manson [45 and 46] strain-life law along with the Walker [47] equation, which relates effective stress to fatigue life for prediction of the fatigue life of riveted joints. They applied a thermal expansion method for computing the local total strain range and effective stress. The method, however, assumes an artificially induced level of uniform through-the-thickness interference. Park and Atluri [4] and Beuth and Hutchinson [48] investigated multiple-site cracking in fuselage lap joints; however, the effects of rivet installation and interaction of the rivet with the surrounding material were not considered. Muller [5] studied fatigue life of riveted Al-to-Al and laminates-to-fiber metal laminate lap joints. Vlieger and Ottens [49] conducted uniaxial and biaxial fatigue tests for Al-to-Al riveted lap joints for countersunk configurations. Effects of different bonding qualities of the riveted joints on fatigue performance were investigated in their research. They observed that bonding quality was a major quality in fatigue life such that life increased with an improved quality of the bonded joint.

Fawaz, et al. [50] conducted crack growth predictions by applying the Newman and Raju [51] equations for partially through- and through-cracks with crack shapes. From the point of view of crack growth prediction, if the cracks are nucleating and growing at the hole edge, then the new Newman and Raju [51] equations (ellipse crack shape considered) are applicable. If the cracks are not nucleating and growing from the hole edge, then the solution is not applicable. No residual stress was involved in the prediction model, and the Newman and Raju [51] solution

overestimates the value of stress-intensity factor (SIF) *K*. As a result, accurate theoretical work still needs to be done.

Piascik [52] conducted destructive and nondestructive examinations on a bay part with several row of rivets. Cracks were found to originate in the skin with the loading end closest to the extreme rows. In between, cracks were found to originate in both skins. The mating surfaces, rivet hole surfaces, and rivet hole corners were all found to be sites of crack nucleation (figure 2-2). At the extreme rows, however, the mating surface was found to be a major site of crack initiation. He also observed that a large quantity of fretting damage at a particular hole did not necessarily result in crack initiation.

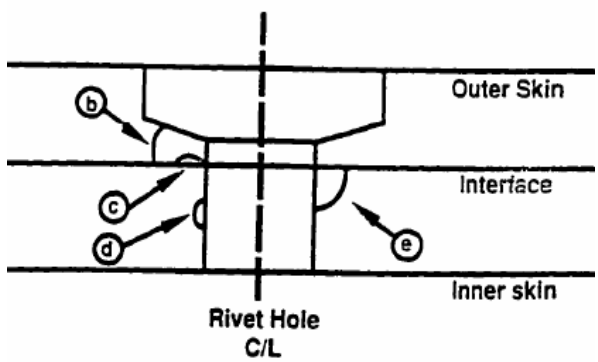


Figure 2-2. Locations of Crack Origins in the Experimental Tests Conducted by Piascik [52]

Experimental studies conducted by Piascik, et al. [52] showed that fatigue crack initiation occurred in regions of high-stress concentration factors located at or near the rivet holes. They found cracks initiated at rivet hole corners, burrs, dents, and fretted surfaces. In separate studies, Wang [53] and Potter and Yee [54] report crack nucleation at inclusions and tool marks. Small surface damage, which might have been induced by poor drilling techniques, was found to be a significant cause of fatigue damage.

Lucas, et al. [55] conducted experimental fatigue testing and damage characterization of riveted lap joint bays to assess multiple-site damage effects. They concluded that the associated residual stresses and the joint eccentricity due to bending stresses result in a complex 3D stress distribution. They noted that fatigue crack initiation occurred at regions of high-stress concentration at or near rivet holes.

The environment also plays an important role. Fatigue cracks tend to initiate earlier and crack growth tends to be faster in moist environments [56]. Sealant applied to the faying surfaces and rivets prior to assembly can keep moisture out of the splice. Surface chemical treatments tend to slow its effects. Visual and high-frequency eddy-current techniques are currently used for inspecting fuselage skin splices. These techniques cannot reliably detect cracks until they are through the sheet and clear of the rivet head. Initiation is often considered the appearance of a crack of size 0.02 in. [57]. At this size, the crack generally just emerges from under a typical fastener head and becomes inspectable. The crack initiation stage and early crack growth (up to visible cracks) may cover the major part of the fatigue life [58]. Striation counts on the Aloha Airline B737 provided evidence of crack growth underneath rivet heads for at least 25% of the

total airframe fatigue life [59], while cracks have appeared beyond rivet heads during full-scale tests after approximately 50% of airframe life [60]. In regard to the distribution in initiation life, Eastaugh, et al. [56] reported that there was a relation between the uniformity of cracks within a multiple-site damage cluster and the growth period from first link-up to critical length. In the B747, this period seems to vary from about 10,000 pressurization cycles for a small, nonuniform cluster of cracks down to 1000 cycles for a larger, more uniform cluster of cracks spanning most of the frame bay [56].

Liao, et al. [61] implemented 3D FE models for fuselage splices to derive analytical expressions for the local stress at the rivet hole. They introduced a response surface technique to develop the expressions as a function of friction and squeeze force. A major finding from their study was that the squeezing force had a more significant effect on fatigue life distribution of the joint than the coefficient of friction and material properties. Their model simulated a three-rivet-row flat lap joint with only one cycle constant amplitude in-plane loading to determine the final stress state. Another important observation from their investigation was that cracks mainly initiated at the rivet holes in the countersunk skin (figure 2-3).

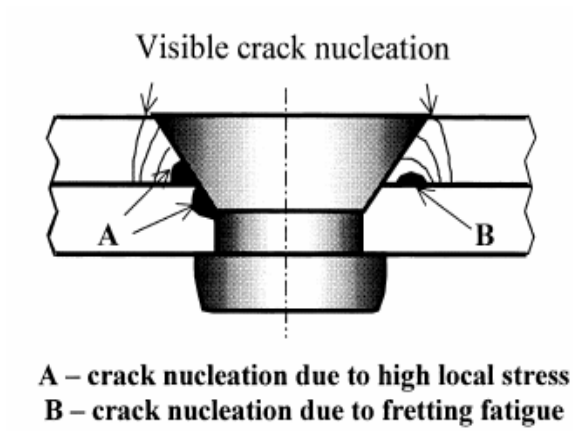


Figure 2-3. Locations of Crack Origins Observed by Liao, et al. [61]

Based on an extensive experimental database from detailed teardown examinations of fatigue cracks at rivet holes, Harris, et al. [62] developed a comprehensive analysis methodology to predict the onset of widespread fatigue damage in lap joints of fuselage structure. In their study, several computer codes (such as FASTRAN) were enhanced with specialized capabilities to conduct the various analyses that make up the comprehensive methodology. The authors have questioned all aspects of the analysis methods to determine computational rigor required to produce accurate numerical predictions. Their study led to the development of a practical engineering approach of predicting fatigue crack growth in riveted lap joints, which has been widely implemented by other researchers. Figure 2-4 shows an example of models developed by the researchers to predict fatigue crack growth.

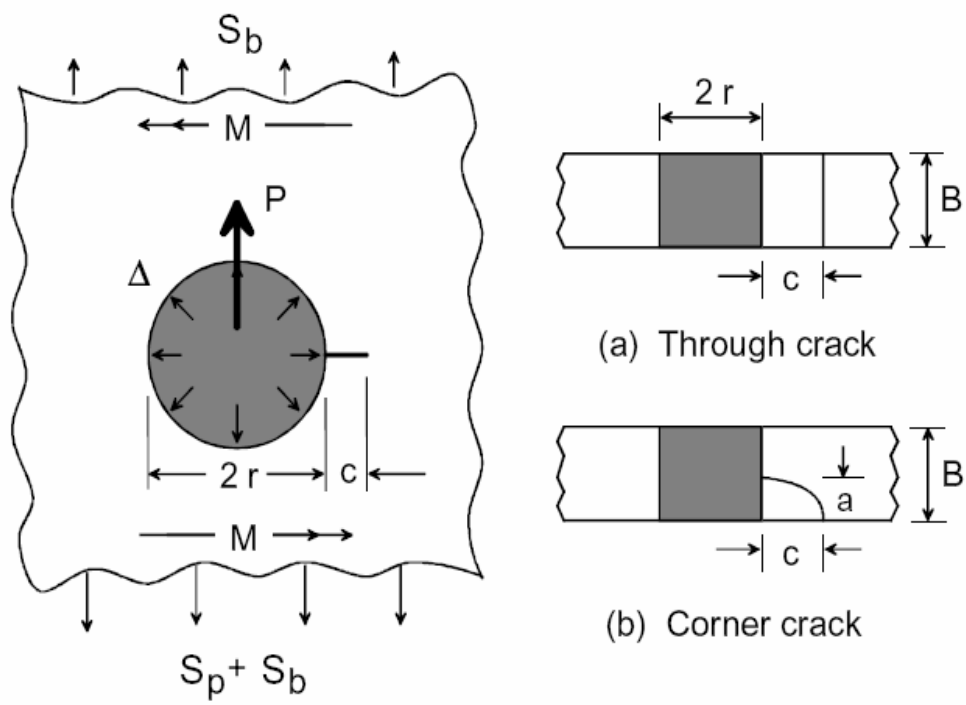


Figure 2-4. An Example of Models Developed by Harris, et al. to Predict Fatigue Crack Growth in Riveted Lap Joints [65]

## 2.8 SUMMARY.

This section began with a review of the state-of-the art in characterization of residual-stresses in riveted lap joints. Due to the complicated 3D residual-stress state induced by the riveting process, it is impossible to apply analytical theories to obtain the stress distribution at the rivet hole. Different experimental techniques implemented to date to predict residual stresses in the joint were then discussed. A review of the results obtained from these techniques led to the conclusion that their implementation was very complex and numerical tools were necessary to pursue the problem more rigorously.

A review of the literature pertinent to application of finite element methods to characterize the residual stresses revealed that the majority of work conducted was on noncountersunk configurations and based on 2D axisymmetric models. The most significant results from the studies of Muller, and Szolwinski and Farris, demonstrated the importance and complexity of the residual-stress state in the skin resulting from rivet expansion. Their studies (conducted separately) also showed the influence of increasing squeeze force on extending the fatigue life of riveted lap joints. In more recent numerical trade studies conducted by Li, et al., it was observed that the residual stress induced by the rivet squeeze force had a considerable effect on the stress variations in the tensile loading stage.

The final stage of the literature review focused on the mechanics of crack initiation in the joint. It was noted that fretting was a major cause of initiation at the mating surface of the joint. It was also worthy to note the successful application of multiaxial fatigue theories to predicting fretting

fatigue crack growth in riveted joints. The results of extensive experimental lap joint testing conducted by researchers, such as Piascik and Lucas, were reviewed. Their investigation concluded that fatigue crack initiation occurred at multiple sites of stress concentrations in the lap joint. A similar investigation conducted by Liao, et al. showed the countersunk skin more susceptible to cracking than the straight shank skin. Finally, the comprehensive methodology of crack growth analyses developed by Harris, Piascik, and Newman was reviewed. It was noted that their study presented a significant development in predicting fatigue crack growth in riveted lap joints, and their computational methods could be applied in conjunction with local FE analysis to predict crack growth curves and SIFs for different types of cracks arising at the rivet holes.

## 3. INITIAL MODEL VALIDATION.

One of the earliest goals of the research was to establish ABAQUS [63] capabilities to simulate the complex forming process. As such, the literature review revealed that a Canadian research team at the National Research Council, Canada, led by Li [21] conducted an experimental study in which 20 riveted lap joints were designed, manufactured, and tested. Variations of the driven rivet head compressive displacement versus the applied squeeze force were measured experimentally in their investigation. In a separate study, Langrand, et al. [6] at the University of Valenciennes conducted quasi-static experimental tests and numerical simulations to characterize the local strains resulting from the rivet expansion. This section provides background of the investigation followed by details of the FE models, and the experimental results are compared with those predicted by the numerical simulations.

### 3.1 ABAQUS/STANDARD MODEL VALIDATION.

As previously stated, the riveting process is accomplished by driving the rivet shank with a rigid bucking bar, while a rigid tool constrains the head of the rivet. The specimen configuration analyzed in ABAQUS/Standard is shown in figure 3-1. It consisted of two 76.2 mm x 76.2 mm bare 2024-T3 Al alloy sheets, each 2 mm thick, and one 2117-T4 Al alloy countersunk type rivet MS20426AD8-9. The rivet had a total length of 14.2 mm and a shank diameter (D) of 6.35 mm. The mean inner sheet hole diameter was 6.4 mm. The rivet's mean protruding length below the inner sheet surface was 9.9 mm.

The material properties for the sheet and the rivet were implemented from the parameters obtained by uniaxial tensile tests on 2024-T3 and 2117-T4 aluminum alloy, respectively. Table 3-1 shows the material property parameters for both the Al alloy sheet and the rivet used in the FE models. Based on experimental data, a tabular input of the data was provided in ABAQUS/Standard using equation 3-1. The material model assumed isotropic hardening, with linear interpolation of data points performed by ABAQUS.

$$\sigma_{true} = C(\varepsilon_{true}^{m}) \tag{3-1}$$

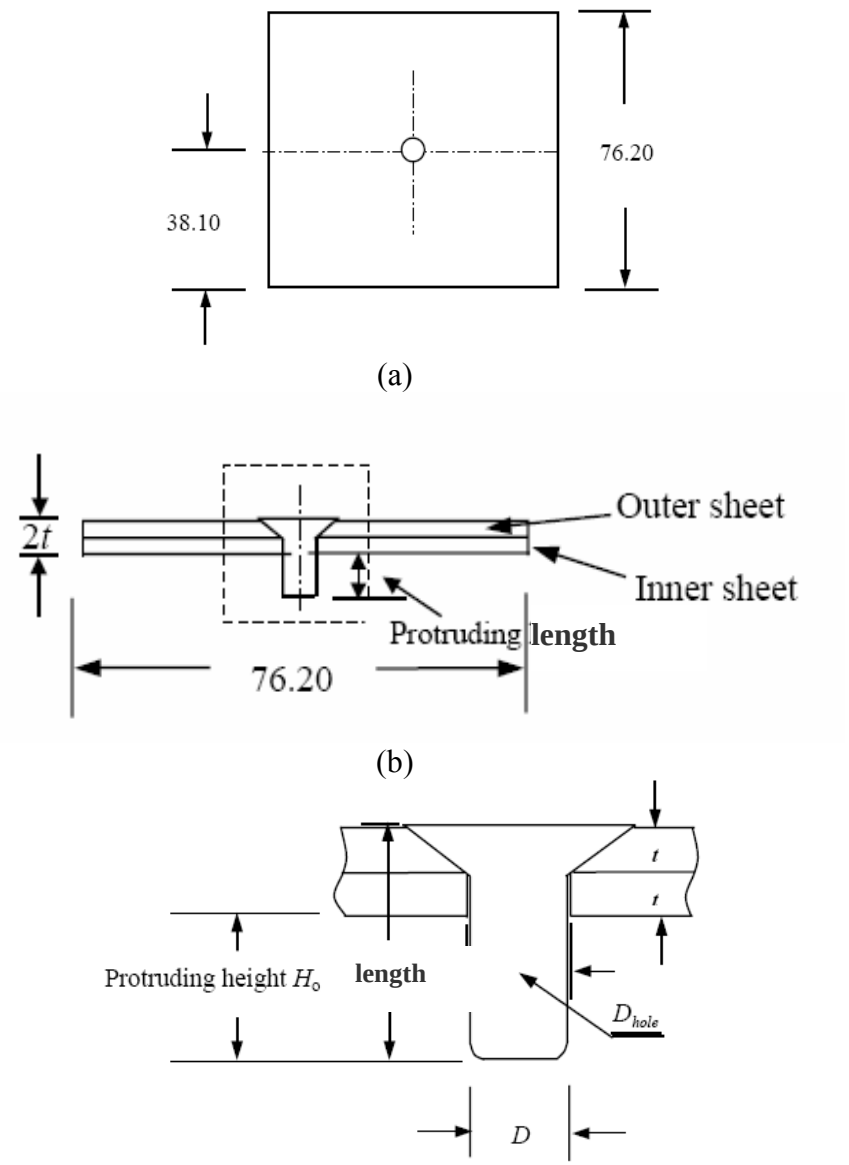


D = diameter

Figure 3-1. Specimen Configuration Analyzed in ABAQUS/Standard [21] (a) View Above Joint Inner Sheet Surface, (b) Side View of Specimen, and (c) Close-Up of Rivet

Table 3-1. Material Property Parameters Used in FE Models [6 and 21]

| Material | Elastic Properties | | Flow Stress Parameters | | |
|---|---|---|---|---|---|
| | E [GPa] | ν | | C [MPa] | m |
| Al 2024-T3 | 72.4 | 0.33 | $\varepsilon_y \leq \varepsilon_{true} \leq 0.02$ | 765 | 0.14 |
| | | | $0.02 \leq \varepsilon_{true} \leq 0.1$ | 744 | 0.164 |
| Al 2117-T4<br>Al 2017-T4 | 71.7 | 0.33 | $\varepsilon_y \leq \varepsilon_{true} \leq 0.02$ | 544 | 0.23 |
| | | | $0.02 \leq \varepsilon_{true} \leq 0.1$ | 551 | 0.15 |
| | | | A [MPa] | B [MPa] | n |
| Al 2024-T351 | 74 | 0.33 | 350 | 600 | 0.502 |
| Al 7050 | 74 | 0.33 | 312.5 | 290.5 | 0.25 |

A detailed view of the meshed axisymmetric FE model and the applied boundary conditions is shown in figure 3-2. The model, which had 8214 nodes and 7254 elements, was generated using ABAQUS/CAE 6.4-1 with CAX4R reduced integration 4-node axisymmetric elements. Three deformable bodies, two sheets and a rivet, and one rigid pusher were defined in the model. Geometric and surface interaction nonlinearities were included in the model. Surface interactions were defined as contact pairs using the master-slave algorithm available in ABAQUS/Standard with the finite sliding option. The surface contact was defined as the areas between the rivet and skin, rivet and the rigid tool, and between the upper and lower skin surfaces. The constraint applied by the tool to the head of the rivet was modeled indirectly using boundary conditions, which improved convergence as well as saved computational time. The contact interaction was modeled with the Coulomb friction model, and a coefficient of friction of 0.2 was specified for all surface interactions. Formulation of the elemental stiffnesses based on current configurations from deformed nodal positions was provided using the NLGEOM option, which is a geometric nonlinear analysis. Since the model undergoes large displacements, the calculated stresses were the true stresses.

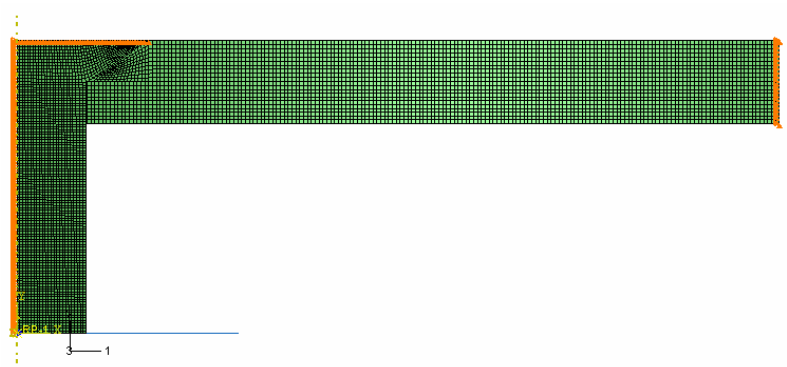

Figure 3-2. The 2D Axisymmetric FE Model With Three Deformable Bodies and One Rigid Pusher

The skin edge surfaces on one end were constrained in the x direction, with the y-direction nodes constrained at the top and bottom to prevent rigid-body motion. The rivet displacement was fixed at the head, while the squeeze force was applied at the rigid tool in contact with the rivet shank. The process was simulated in two steps: (1) a loading step in which the rivet was

deformed by the applied force and (2) an unloading step in which the rivet was allowed to spring back. The final deformed driven rivet head diameter and final deformed rivet head height predicted by the FE analysis was compared with experimental measurements for the range of squeeze forces. Figure 3-3 shows these parameters, while table 3-2 shows the comparison. Figure 3-4 shows the final rivet deformations after unload for a range of applied squeeze forces.

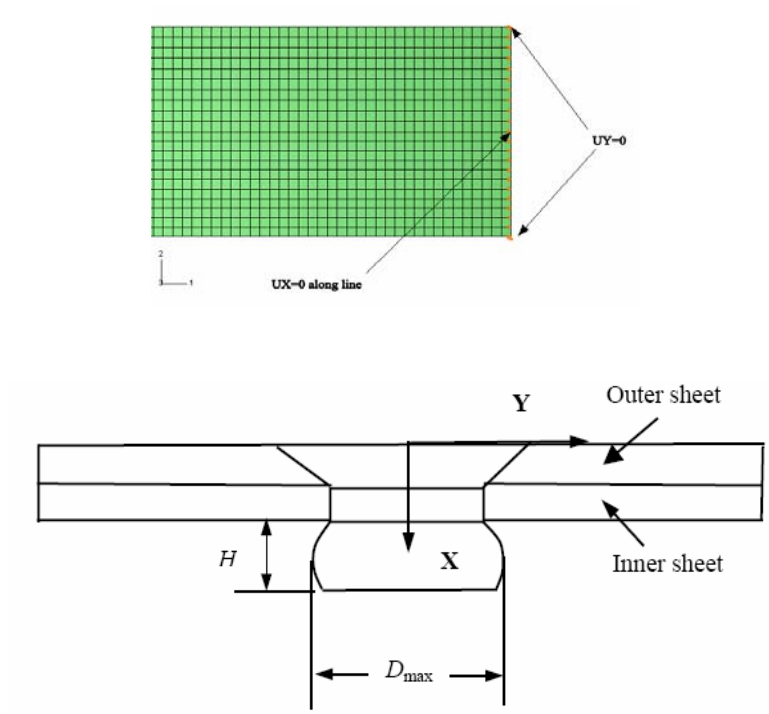


Figure 3-3. Deformed Rivet Parameters

Table 3-2. Comparison of Rivet Head Deformation as Predicted by the FE Method to Experiment Measurements [21]

| Squeeze Force (kN) | $D_{max}$ (mm) FEM | $D_{max}$ (mm) Experiment | % Diff | H (mm) FEM | H (mm) Experiment | % Diff |
|---|---|---|---|---|---|---|
| 26.69 | 8.001 | 8.559 | 3.4 | 5.79 | 5.796 | 0.7 |
| 35.56 | 9.09 | 9.525 | 1.6 | 4.546 | 4.59 | 0.9 |
| 44.48 | 9.931 | 10.16 | 2 | 4.0463 | 4 | 1.3 |
| 53.37 | 10.61 | 10.795 | 1.5 | 3.484 | 3.49 | 0.362 |

FEM = Finite element method

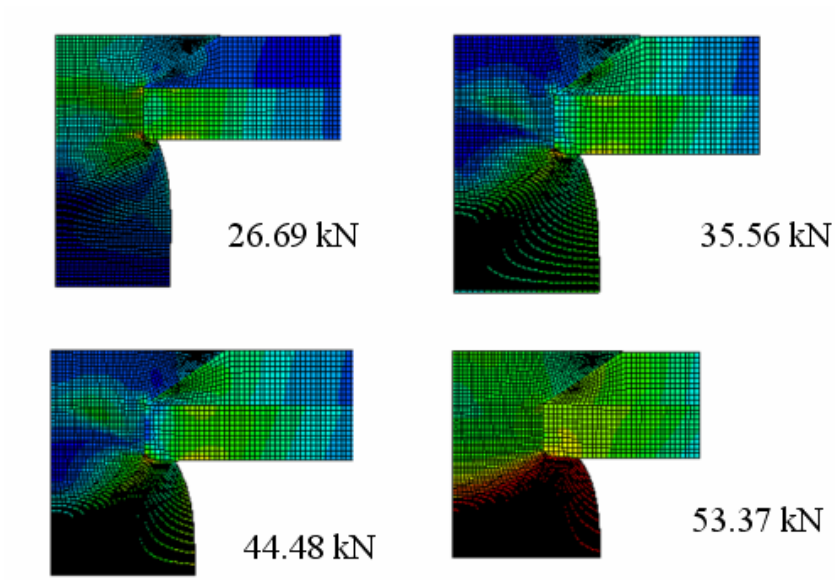


Figure 3-4. Deformed Configuration for a Range of Applied Squeeze Forces

A maximum difference of 3.4% was observed for the final deformed rivet diameter, while a maximum difference of 1.3% was observed for the final rivet height. Figure 3-5 compares the measured and predicted force-displacement curves. A slight discrepancy can be observed at unload and also at higher squeeze forces. The differences in the curves and the rivet deformation parameters can be attributed to geometry surfaces (which the FE model assumes perfect), numerical errors, and errors associated with experimental uncertainties. Taking into account these uncertainties, the FE predictions are observed to be in good comparison with the experiment.

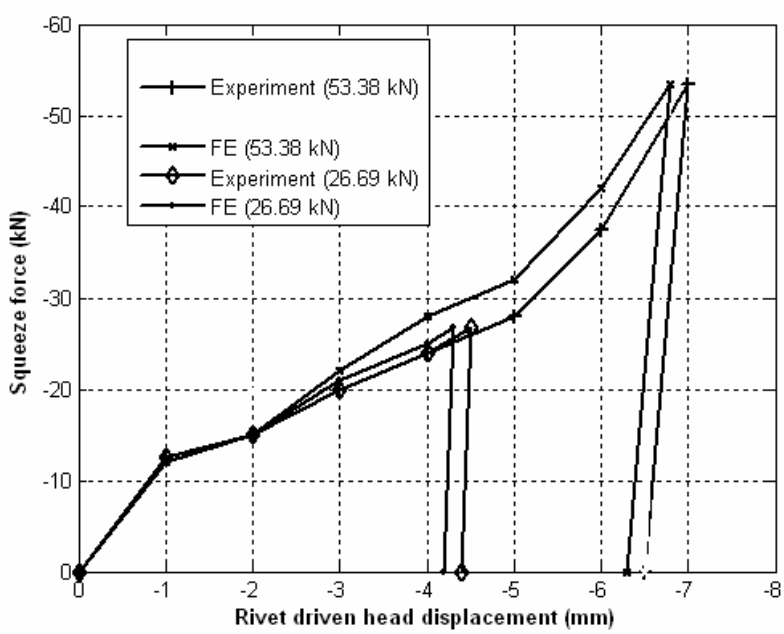


Figure 3-5. Comparison of Force-Displacement Curves

## 3.2 EXPLICIT MODEL VALIDATION.

The specimen configuration analyzed in ABAQUS/Explicit is shown in figure 3-6. It consisted of two 15 by 15 mm bare 2024-T351 Al alloy sheets, each 1.6 mm thick, and one 7050 Al alloy countersunk rivet. The rivet had a total length of 8 mm. The material properties for the sheet and the rivet were implemented from the parameters obtained by experimental characterization of 2024-T3 and 2117-T4 aluminum alloy respectively [6] (table 3-1). Based on experimental data, a tabular input of the data was provided in ABAQUS/Standard 6.4-1 using equation 3-2.

$$\sigma(\varepsilon_p) = A + B\varepsilon_p^{\,n} \tag{3-2}$$

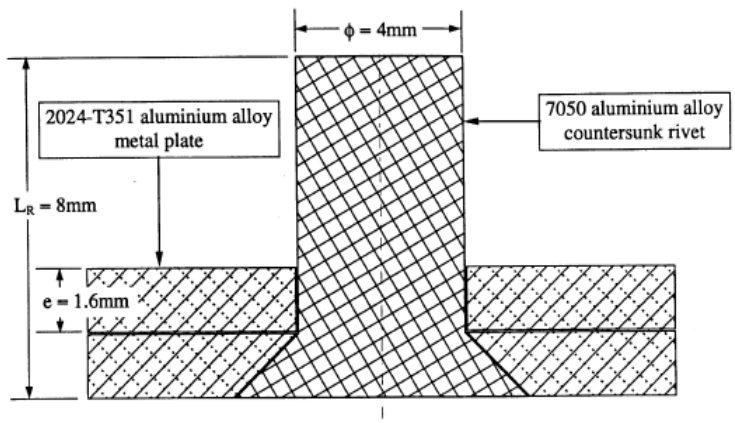


Figure 3-6. Riveted Joint Parameters for Model Validation in ABAQUS/Explicit [6]

The quarter-symmetry model, which had 31,541 nodes and 22,771 elements, was generated using ABAQUS/CAE 6.4-1 with C3D8R reduced integration eight-node solid continuum elements. Three deformable bodies, two sheets and a rivet were defined in the model. The kinematic predictor-corrector algorithm was implemented in defining the surface interactions with a balanced master-slave approach. Using this approach with hard kinematic contact, surface penetrations that might occur during the process were minimized. The surface contact was defined between the rivet and skin and between the upper and lower skin surfaces. The constraint applied by the tool that constrains the head of the rivet was modeled indirectly using boundary conditions. The contact interaction was modeled with the Coulomb friction model with a coefficient of friction of 0.2 assumed for all interactions. The skin edge surfaces on one end were constrained in the x direction, with the y-direction nodes constrained at the top and bottom to prevent rigid-body motion. A crushing velocity of 2 mm/min was applied to the rivet shank. Figure 3-7 shows the boundary conditions.

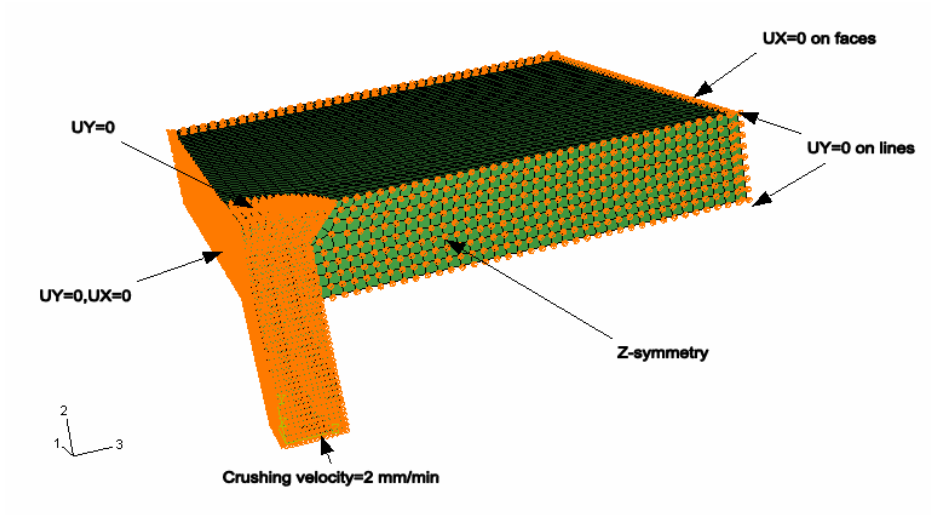


Figure 3-7. Boundary Conditions for ABAQUS/Explicit Model Validation

In ABAQUS/Explicit, the driven rivet head displacement was applied using a smooth step loading amplitude function. A small amount of material damping was also introduced in the ABAQUS/Explicit analysis to obtain a smoother kinetic energy response. Since ABAQUS/Explicit solutions typically require large run times compared to its ABAQUS/Standard counterpart, it was not feasible to analyze both the loading and unloading steps in one analysis. Hence, for all of the ABAQUS/Explicit problems, the rivet loading was analyzed in the solver, and the unloading step was completed in ABAQUS/Standard using the *IMPORT option provided by ABAQUS. Mass scaling was implemented in the ABAQUS/Explicit solution to speed up the solution time by artificially scaling the density of the materials. A mass scaling factor of 10 was found to be appropriate to obtain solutions in reasonable run times without introducing excessive spikes in the expended kinetic energy.

The simulation was validated using three criteria. (1) The von Mises stress of the deformed configuration and equivalent plastic strain at the end of analysis (after unloading) was compared to that predicted by the simulations conducted by Langrand, et al. [6]. (2) The residual strains after riveting as predicted by the FE were compared to values recorded by strain gauges along the length of the skin. (3) The force-displacement response of the FE solution was compared to the experimental response. The von Mises stress predicted by the ABAQUS/Explicit solver (figure 3-8) was observed to be slightly lower than that predicted by Langrand, et al. [6]. The equivalent plastic strain, which provides a measure of the plasticity in the model, showed that the plastic strains in the rivet reached a range of 1.2 (figure 3-8). This is consistent to that reported by Langrand, et al. [6].

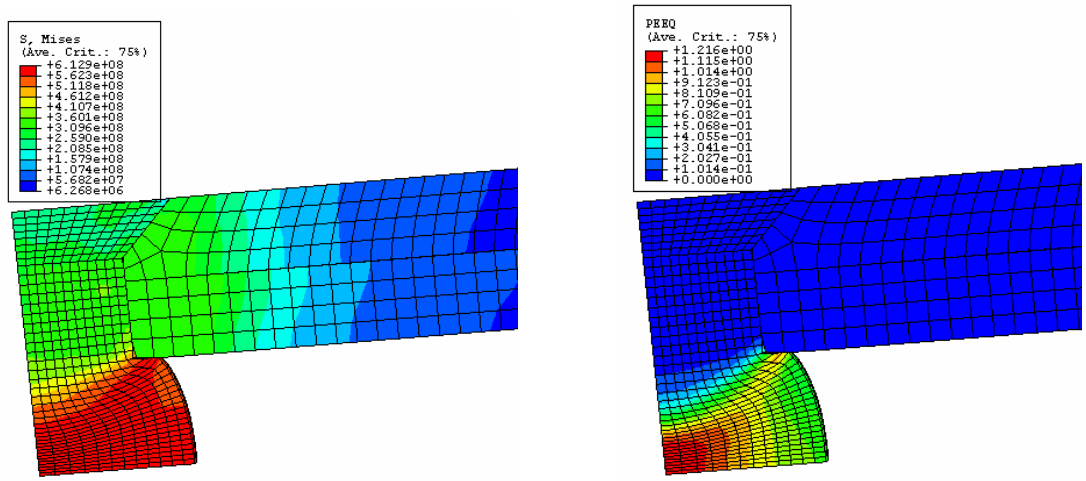


Figure 3-8. von Mises Stress Contour in MPa (Left) and Equivalent Plastic Strains at End of the Riveting (Right)

From comparisons of the residual strains (figure 3-9), it was observed that the measurements and the FE results were essentially in agreement. The ABAQUS/Explicit predicted force-displacement curve compared to the experiment shown in figure 3-10 also showed reasonable agreement. The FE model predicted lesser elastic recovery than observed in the experiment for both the ABAQU/Standard and ABAQUS/Explicit solutions.

| Gauge No. | Residual Strain- Expt. | Residual Strain - Finite Element |
|---|---|---|
| 1 | 0.01e-02 | 0.018e-02 |
| 2 | 0.04e-02 | 0.05e-02 |
| 3 | -0.28e-02 | -0.32e-02 |

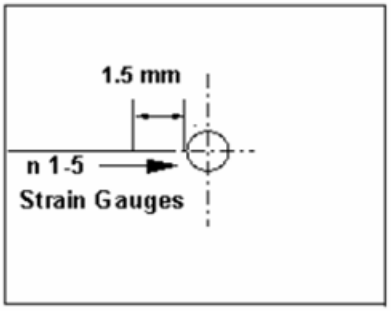


Figure 3-9. Comparison of Residual Strains

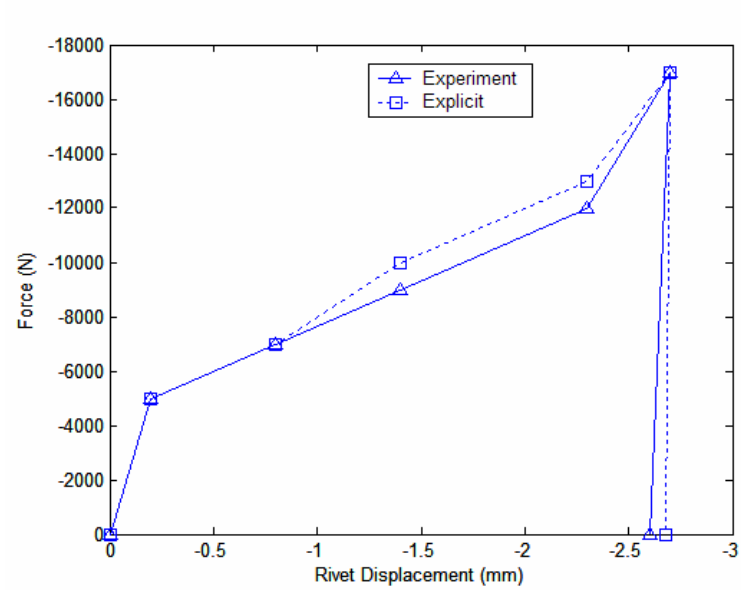


Figure 3-10. Comparison of Force-Displacement Diagram for the ABAQUS/Explicit Solution

As previously stated, the ABAQUS/Explicit solution is a true dynamic solution algorithm developed to model events in which inertia plays a significant role. Figure 3-11 compares the energy response at the end of the riveting process. It was ensured that the kinetic energy was small enough in comparison to the internal energy for the solution to be considered quasi-static. An identical analysis was also conducted in ABAQUS/Standard to compare the residual stresses and plastic strains to those predicted by ABAQUS/Explicit. Figures 3-12 and 3-13 show the comparison of equivalent plastic strain contours and residual stresses in the skin after unloading, for the ABAQUS/Standard and ABAQUS/Explicit solutions.

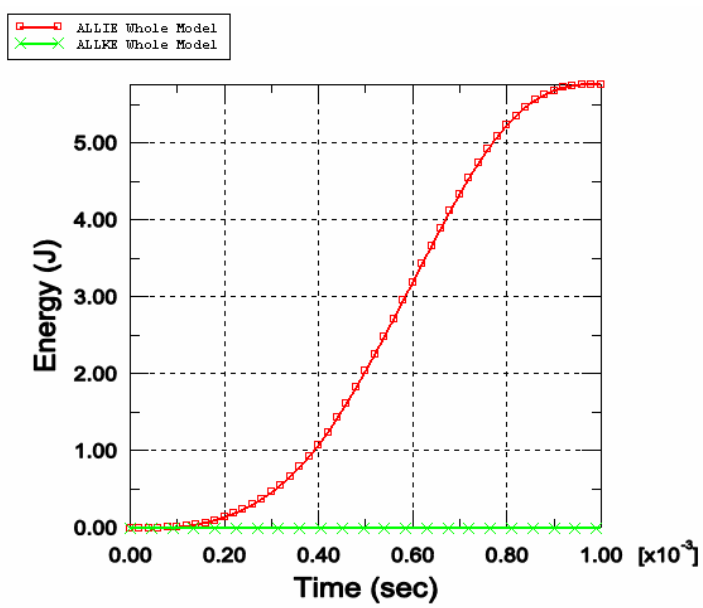


Figure 3-11. Energy Response in the Model

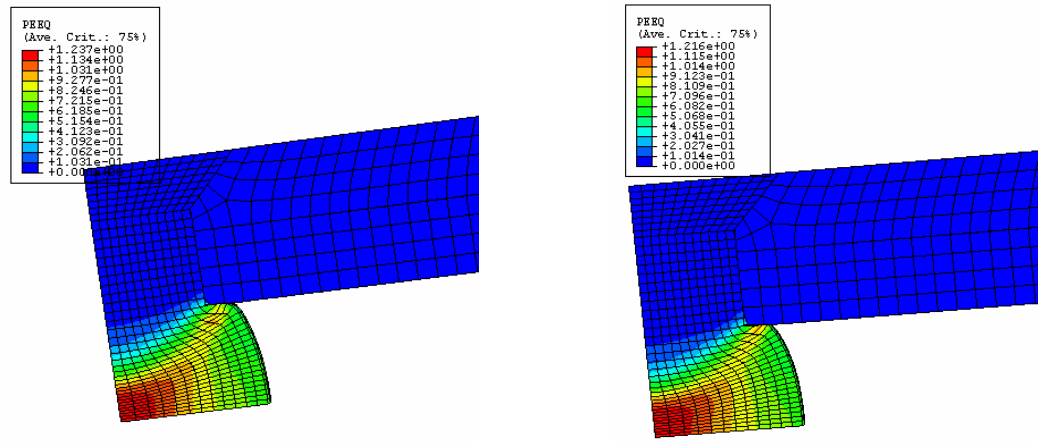


Figure 3-12. Equivalent Plastic Strain Contours for the ABAQUS/Standard (Left) and ABAQUS/Explicit (Right) Analyses

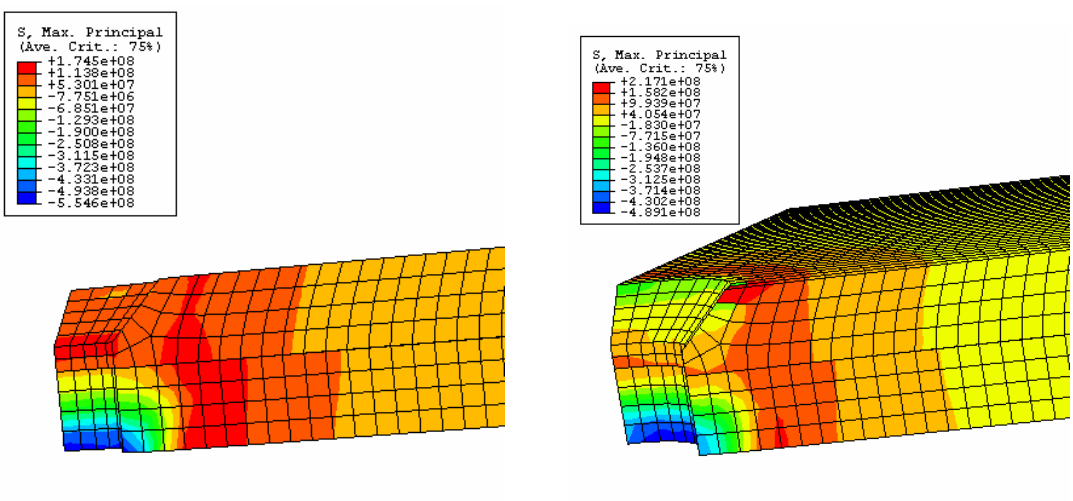


Figure 3-13. Residual-Stress Contours in MPa for the ABAQUS/Standard (Left) and ABAQUS/Explicit (Right) Analyses

The results show a good agreement, indicating the ability of the dynamic solver to model the quasi-static problem. The residual stresses are qualitatively the same, but quantitatively, the ABAQUS/Explicit solution shows around 20% greater values than that predicted by ABAQUS/Standard solution. The difference in values must be taken in light of the dynamic nature of the solver based on stress wave propagation. Even though the analysis was ensured to be quasi-static, some inertia effects in the solution always exist that lead to the observed difference in residual stresses from the true quasi-static solution. Different forming quasi-static analyses (such as indentation of a foam and forging with sinusoidal dies) were also conducted separately, based on examples provided in the ABAQUS manuals, to confirm this trend.

As the rivet head was formed in the joint, friction between the skin and the rivet head led to the formation of a lug (material flow) trapped by the driven rivet head. The lug was visualized in the specimen sectioning conducted by Langrand, et al. [6]. The FE analysis and Langrand [6] did

not show this lug formation, indicating the limitations of numerical tools in simulating forming processes. Figure 3-14 compares the driven rivet head from specimen sectioning to the one from the FE analyses.

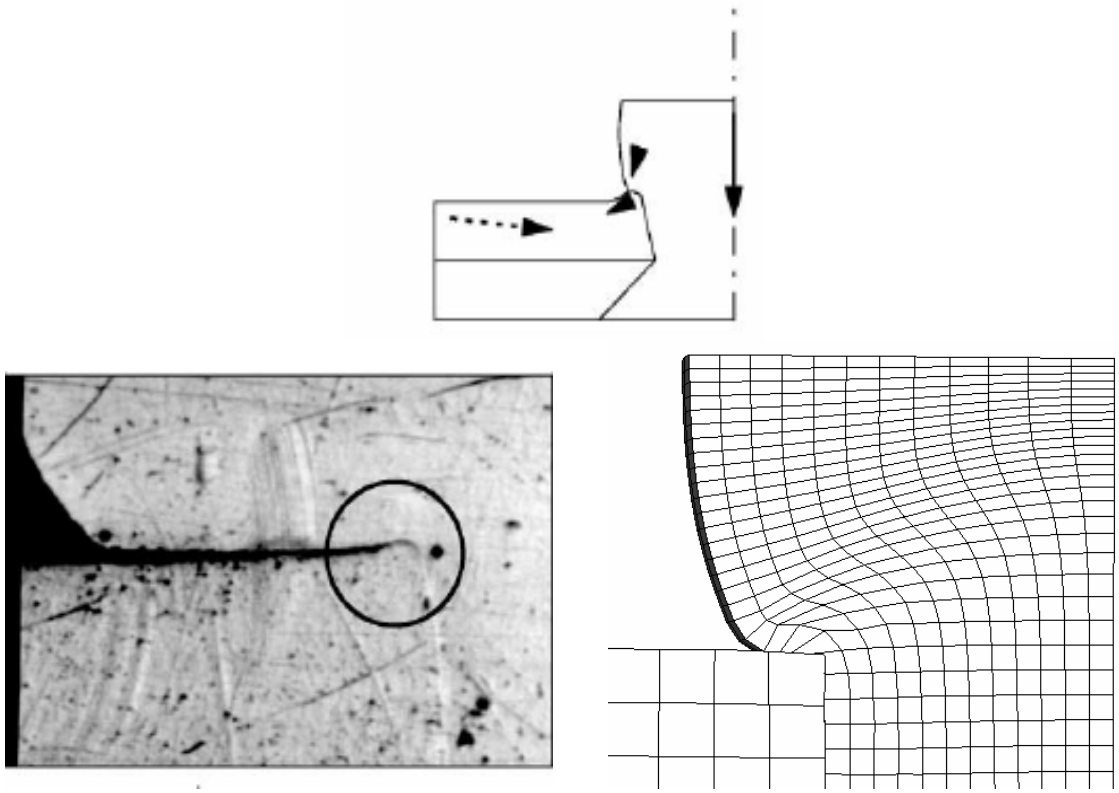

Figure 3-14. Comparison of Rivet Head Deformation From Experiment [6] to the FE Analyses (A 'lug' formation was observed in the experiment [6].)

## 3.3 SUMMARY.

This section presented the verification and validation approach of the ABAQUS FE code used to simulate the riveting process. This approach was accomplished through comparisons with a carefully obtained set of experimental results previously generated in separate investigations conducted by Li and Langrand. A review of the details of the experimental specimens including the material models implemented for the analysis was presented for both the investigations.

A 2D axisymmetric representation was used to model the riveted lap joint of Li [64]. The rivet deformation and force-displacement curves predicted by the simulations were compared to the experimental measurements. A reasonable comparison was observed for both, taking into account effects of numerical and experimental uncertainties and thus establishing the capabilities of ABAQUS/Standard in simulating this process.

A quarter-symmetry 3D model was constructed to model the configuration used by Langrand, et al. The simulation was conducted quasi-statically invoking the "more forgiving" ABAQUS/Explicit solver to emulate the analysis and experiments. Although a good comparison

was observed between the simulations and experiment, the simulation did not show the lug formation observed in the experiments. Finally, a comparison was made between the residual stresses predicted by ABAQUS/Explicit and those predicted by the less forgiving ABAQUS/Standard solver. It was observed that approximately 20% differences in residual-stress predictions must be taken into account due to the inherent differences in the nature of the two solvers.

## 4. PARAMETRIC STUDIES.

Section 3 demonstrated the viability of FE simulations in analyzing the riveting process. While those results provided the necessary validation of the modeling approach and pointed out simulation limitations, they did not implement the developed models to simulate actual service variations. As such, the present investigation was focused on a more realistic scenario to simulate the residual-stress state in the riveting process. In conducting this investigation, a baseline 3D model was established to capture the unsymmetrical residual-stress state resulting from variations and rivet buckling. The model was then implemented to compare the effects of hole quality, sealant, and load transfer effects on the residual-stress state. The effect of the variations was analyzed separately for the baseline driven rivets and underdriven rivets. The different parameters considered in this section were based on actual service variations observed in the B727 teardown. As such, a full design of experiments optimization was not established for the parametric studies.

### 4.1 BASELINE MODEL.

Figure 4-1 shows the joint parameters modeled in this study. The specimen configuration consisted of two 2024-T3 25 mm x 25 mm Al alloy sheets. The upper skin was 1.5 mm thick and the lower skin was 1 mm thick. The 2017-T4 Al alloy countersunk type rivet had a total length of 7.8 mm and a shank diameter of 3.9 mm. The lower skin hole diameter was 4 mm and the upper skin hole diameter was 6 mm at the top of the countersunk edge. The depth of the countersunk part measured from the top of the plate edge ($h_c$) was 0.09 mm. A coefficient of friction of 0.2 was assumed for lubricated contact and 1.1 for dry contact. The same friction coefficient was applied for both rivet-skin and skin-skin contact. The FE study was conducted as a quasi-static process (low-speed). Any thermal and inertial effects were ignored.

A detailed view of the meshed, symmetric 3D FE model and the applied boundary conditions is shown in figure 4-2. The model, which had 6457 nodes and 3947 elements, was generated using ABAQUS/CAE 6.4-1 with C38DR reduced integration eight-node linear solid brick elements.

The modeled riveting configuration was from the end of a three-row lap joint. The skin edge surfaces on one end were constrained in the x direction with the y-direction nodes constrained at the top and bottom to prevent rigid-body motion. The skin surfaces on the opposite end were unconstrained. The rivet displacement was fixed at the head, while a displacement of 3.3 mm (baseline) was applied at the driven rivet head surface. Symmetric boundary conditions were imposed in the z direction for both the rivet and the skin surfaces. The process was simulated in two steps: (1) a loading step in which the rivet is deformed by an applied displacement and (2) an unloading step in which the rivet was allowed to spring back. The unloading step was important, as at the end of the loading step the stress state was above yield at the rivet/skin interface, but after unloading, most of these locations showed a stress state below yield.

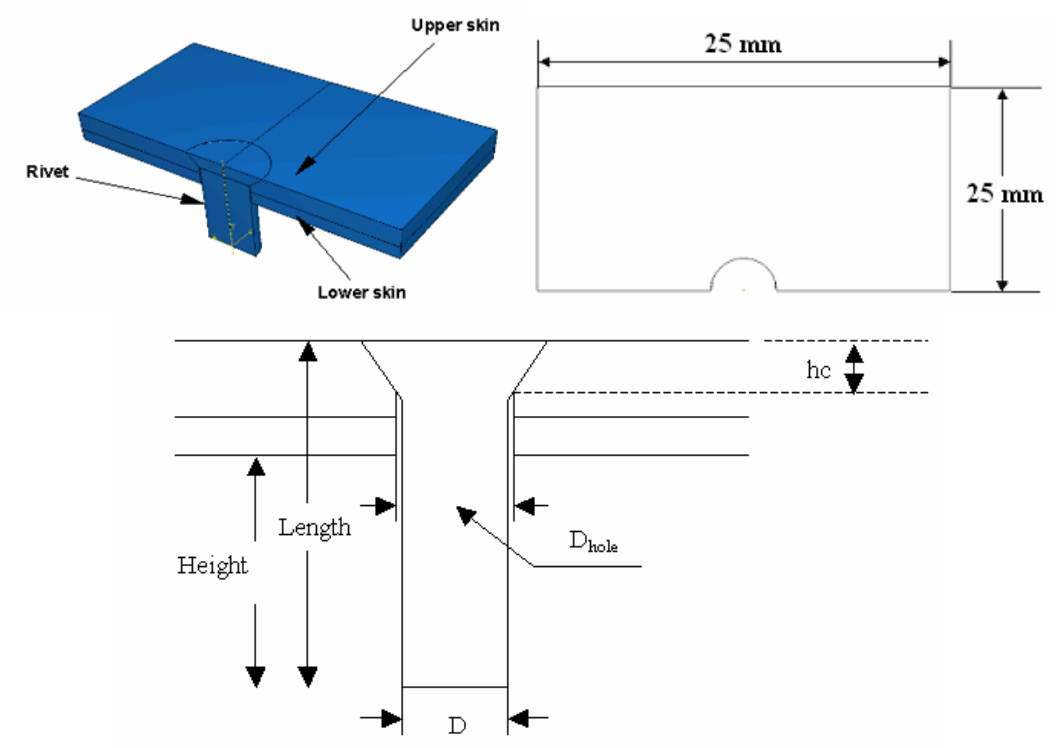


Figure 4-1. Geometry Parameters for the Baseline Model

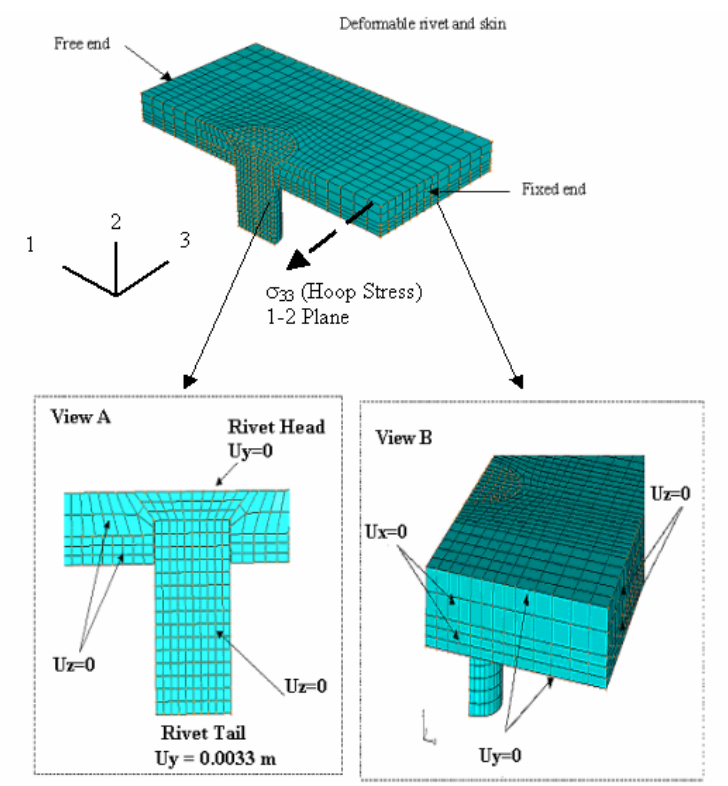


Figure 4-2. Boundary Conditions

Several meshing techniques available in ABAQUS/CAE were tested, namely, Free, Edge by Number, and Edge Biased. Since the riveting process presents a complex contact problem, the mesh around the holes, as well as the rivet, needed to be refined to obtain a converged solution. The sought mesh in each of the latter techniques was hard to find in terms of a generalized expression, but with Free meshing, one mesh criterion was obtained. In Free meshing, a Global Element Size has to be suggested by the user. By using the same global element size for both the skins, one can define

$$\text{Mesh Ratio} = \frac{\text{global element size in the rivet}}{\text{global element size in the plates}} \tag{5-1}$$

A mesh ratio of 0.7 was found to be suitable to carry out the analysis successfully. Several mesh configurations were implemented based on the above ratio to analyze the problem. The mesh ratio was decreased iteratively until no appreciable difference was observed in the residual hoop stress in the skin. Table 4-1 summarizes the results from the mesh refinement study.

Table 4-1. Results From the Mesh Refinement Study

| Elemement Size (Skin) | No. of Elements | No. of Nodes | Tensile Nodal Residual Hoop Stress in Lower Skin (MPa) |
|---|---|---|---|
| 0.050″ | 1324 | 2417 | 68.947 |
| 0.025″ | 5318 | 8962 | 110.316 |
| 0.020″ | 9989 | 15538 | 137.895 |
| 0.008″ | 32681 | 44327 | 144.789 |

The stresses shown in the contour plots of this study represent the nodal averaged stresses (stresses extrapolated from the element integration points and averaged over all the elements containing the specific node). These stresses were compared separately to the stresses reported at the element integration points for the different meshes. The nodal maximum residual stress for the upper skin was 68.754 MPa, while the element maximum was 65.562 MPa (4% difference). The nodal maximum residual stress for the lower skin was 138.895 MPa versus the corresponding 146.527 MPa element maximum (4.5% difference) stress. The excellent agreement between these values also demonstrates the adequacy of the mesh in closely approximating the continuum being modeled.

Figure 4-3 shows the deformed plot and contours of residual hoop stress induced in the upper and lower skins after unloading in the original baseline ABAQUS/Standard model. The residual hoop stresses (shown for the baseline model and further simulations) are on the face of the skin only (1-2 plane). During the process, the rivet expands against the hole and the contact pressure exceeds the yield point of the material ($\sigma_{11} < \sigma_y$). The material deforms so that $\sigma_{33} < 0$. This compressive hoop stress is analogous to cold working of holes with an expanding mandrel to prevent fatigue cracks that might initiate at the holes. The elastic deformation energy is not allowed full release after the process due to the large plastic deformation of the rivet. This leads to both compressive and tensile residual stresses in the skin. The compressive zone is balanced

by the tensile zone away from the hole edge. This tensile hoop stress is critical for fatigue cracks that may initiate at the faying surface.

| Maximum Hoop Stress (MPa) | Upper | Lower |
|---|---|---|
| Tensile | 68 | 137 |
| Compressive | -199 | -351 |

(a)

(b)

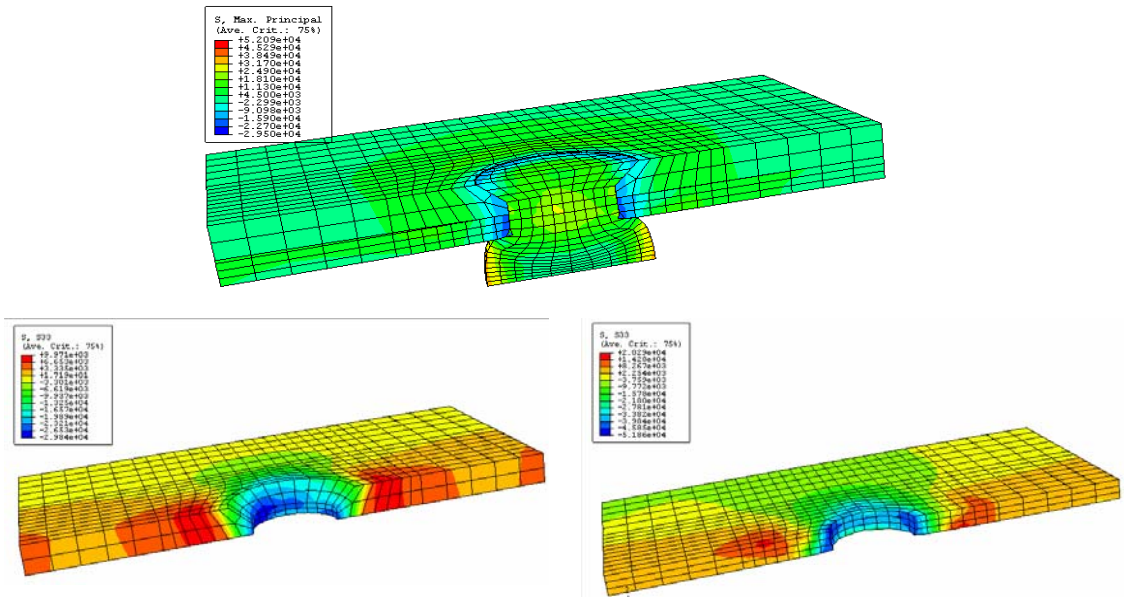


Figure 4-3. (a) Deformed Shape and (b) Residual Hoop Stress Contours in the Skin After Unload in ABAQUS/Standard Analysis

The resulting interference is an indicator of the quality of the riveted joint. A high interference means a tighter connection between the rivet and the skin. A larger compressive stress was observed for both the hoop and radial stresses in the lower skin than in the upper skin. As a result, the lower skin and the rivet will have a tighter connection as compared to the upper skin. The residual stresses showed an unsymmetrical distribution and a through-the-thickness variation as shown in figures 4-4 and 4-5. A variation in the resulting interference was also observed.

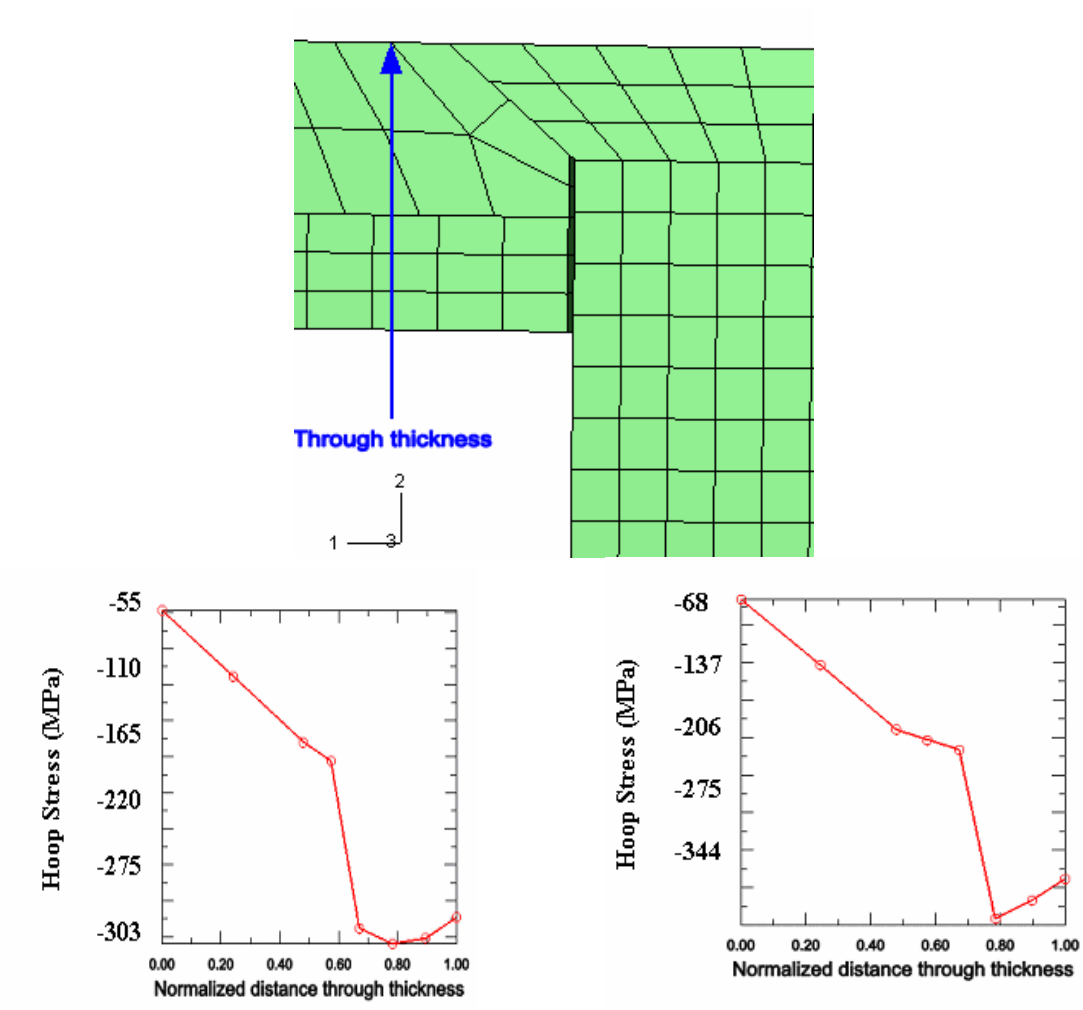


(a) (b)

Figure 4-4. An Example of the Through-the-Thickness and Unsymmetrical Variation of the Hoop Stress: (a) Constrained Side (b) Unconstrained Side

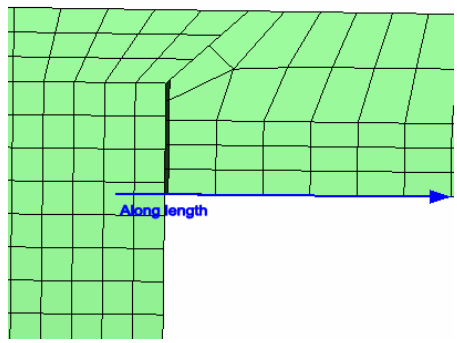


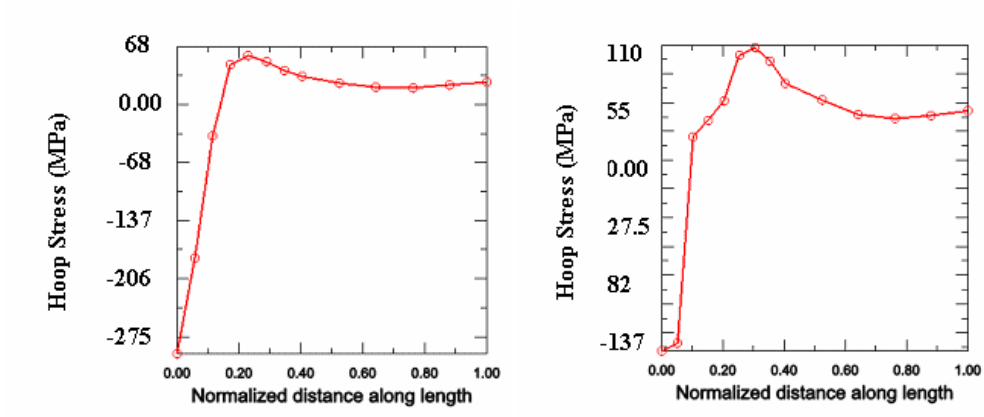


(a) (b)

Figure 4-5. An Example of the Unsymmetrical Variation of the Hoop Stress Along the Length of the Skin: (a) Constrained Side (b) Unconstrained Side

A separate analysis was also conducted to demonstrate the unsymmetrical nature of the local residual-stress state that must be taken into account while analyzing process variations. In this analysis, the rivet deformation was simulated without any initial clearance between the rivet and the skin. Figure 4-6 shows the residual hoop stress contours in the model after unloading. The resulting symmetric deformation of the rivet without the initial hole clearance can be clearly observed from the contours.

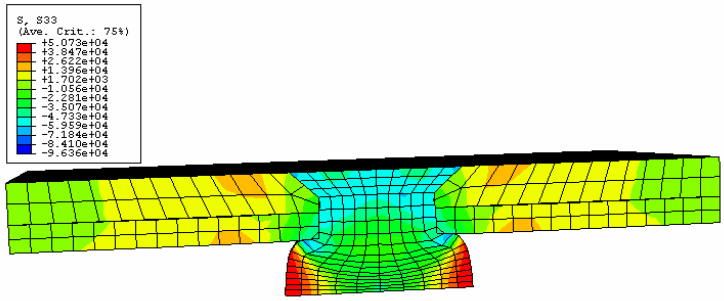


Figure 4-6. Symmetric Stress State Resulting From Zero Clearance Between Rivet and Hole

In ABAQUS/Explicit the rivet-driven head displacement was applied using the smooth step loading amplitude function. Preliminary analysis showed that a time period of 0.001 second was appropriate to obtain a quasi-static solution and achieve computational efficiency. Additional analyses were also conducted over a time period of 0.01 and 0.1 second to ensure that there was no significant difference in the residual-stress values. In all analyses, it was ensured that the kinetic energy was negligible in comparison to the internal energy in the model. A small amount of material damping was also introduced in the ABAQUS/Explicit analysis to obtain a smoother kinetic energy response. For all of the ABAQUS/Explicit problems the rivet loading was analyzed in the solver and the unloading step was completed in ABAQUS/Standard using the *IMPORT option provided by ABAQUS. Figure 4-7 compares the equivalent plastic strain in the ABAQUS/Standard and ABAQUS/Explicit analysis. Figure 4-8 shows the kinetic energy plot for the ABAQUS/Explicit analysis. The results show a good agreement, indicating the ability of the dynamic solver to model the quasi-static problem. Figure 4-9 shows the residual-stress state in the skin predicted by the ABAQUS/Explicit analysis. The tensile and compressive zone locations predicted by ABAQUS/Explicit were observed to be similar to the ones predicted by ABAQUS/Standard. In comparison of the reported nodal values between the two solvers, the ABAQUS/Explicit values were noted to be approximately 20% greater than those computed by ABAQUS/Standard.

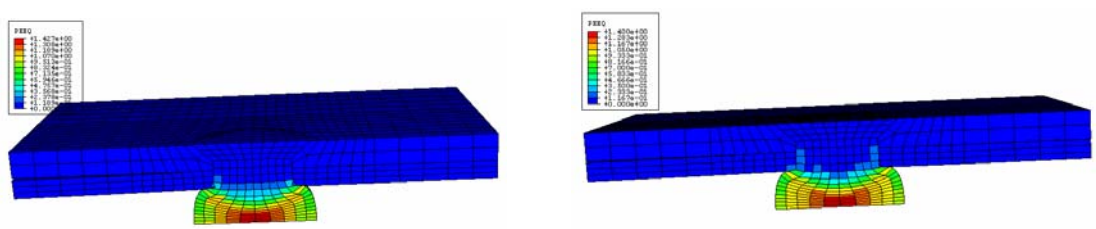

Figure 4-7. Comparison of the Equivalent Plastic Strain Contours From the ABAQUS/Standard (Left) and ABAQUS/Explicit (Right) Analyses

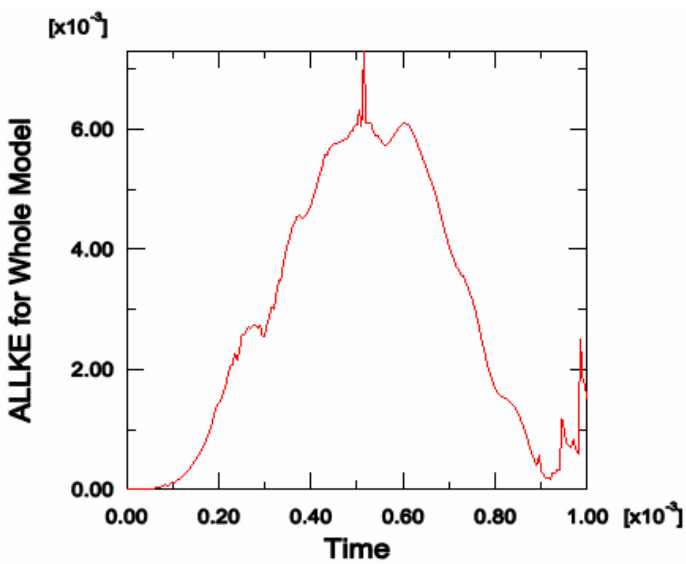


Figure 4-8. Kinetic Energy Plot for the Whole Model
(A small amount of material damping results in a relatively smooth response.)

| Maximum Hoop Stress (MPa) | Upper | Lower |
|---|---|---|
| Tensile | 89 | 144 |
| Compressive | -420 | -599 |

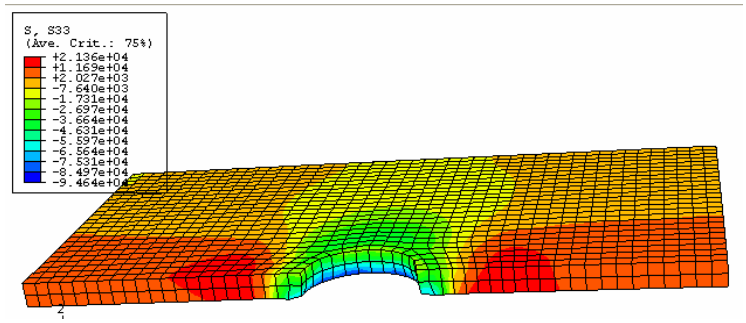


Figure 4-9. Residual Hoop Stress Contours in Upper and Lower Skin as Predicted by ABAQUS/Explicit Analysis

## 4.2 RIVET DEFORMATION.

The deformed model configuration for a range of rivet-head displacement is shown in figure 4-10. As the applied displacement increased, the rivet head increased in size. The crimping in the free ends of the skin was also observed to increase significantly for the range of applied displacement. The maximum rivet shank deformation ($D_{max}/D$) and the final rivet head height ($H$) are shown in figure 4-11 as a function of the applied displacement. An applied rivet displacement above 3.3 mm corresponds to an overdriven rivet, while an applied rivet displacement below that corresponds to an underdriven rivet. $D_{max}/D$ and H were fitted with the linear regression curve and power law regression equations expressed below.

Linear regression equations:

$$D_{max}/D = 0.1019d + 1.3452 \qquad R^2 = 0.9971 \qquad (4\text{-}1)$$

$$H = -0.0002d + 0.0026 \qquad R^2 = 0.9951 \qquad (4\text{-}2)$$

Power-law:

$$D_{max}/D = 1.4154d^{0.1632} \qquad R^2 = 0.9302 \qquad (4\text{-}3)$$

$$H = 0.0026d^{-0.323} \qquad R^2 = 0.9269 \qquad (4\text{-}4)$$

$R^2$ is the data-fit parameter (from 0 to 1) and $d$ is the rivet head displacement in the range of 3.3 to 4 mm. A similar equation for a squeeze-force controlled process has been presented by Li and Shi [21]. The above equations and the rivet deformation trends observed in figure 4-11 are meant as a means to achieve the desired riveting quality. It should be noted that the equations presented above are for the particular configuration analyzed in this research. Similar equations can be developed for different geometries. Large $D_{max}/D$ (larger rivet expansion) values are

observed to increase the compressive zone near the hole edge while enhancing the probability of fatigue cracks at the faying surface.

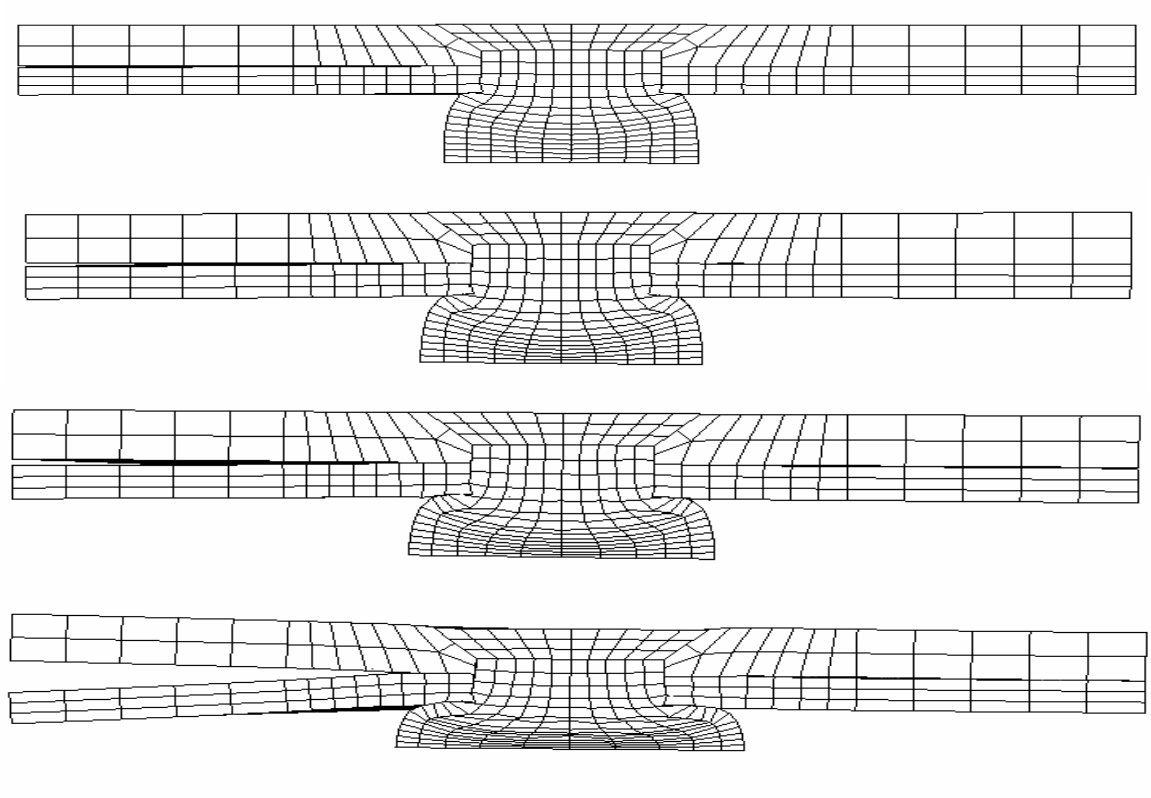

Figure 4-10. Deformed Configuration for an Applied Displacement of 0.0027 m (0.11 in.), 0.0033 m (0.13 in.) (Standard), 0.0035 m (0.14 in.), 0.004 m (0.16 in.) Top to Bottom, Respectively

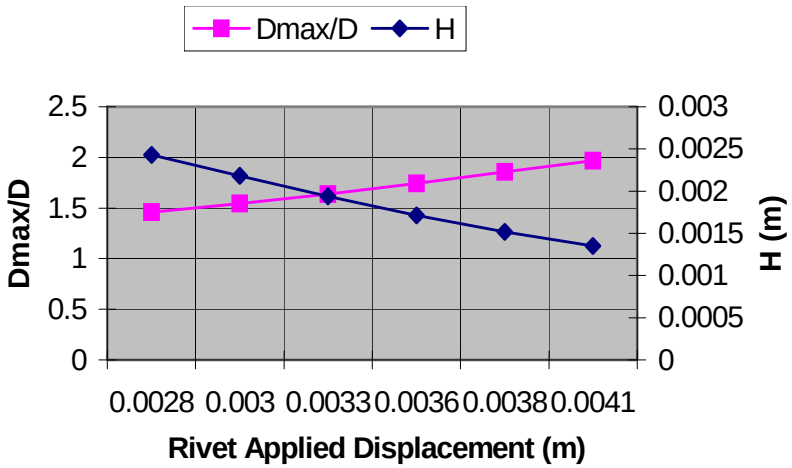


Figure 4-11. Rivet Head Deformation Compared With Applied Displacement (where $D_{max}$ is the Maximum Deformed Diameter, $H$ is the Deformed Tail Height, and $D$ is the Original Rivet Diameter)

## 4.3 EFFECT OF VARIATIONS ON BASELINE MODEL.

Parametric studies were conducted to observe the effects of varying friction, increased hole clearance, a misaligned assembly of upper and lower skin, faying surface hole defects, and presence of debris on the residual-stress state in comparison with the original model [11]. Again, the tensile hoop stress ($\sigma_{33}$) is only on the faces of the upper and lower skin in the 1-2 plane. This is the critical stress of interest. The geometry parameters of the variations are specified in table 4-2. A view of the FE models is shown in figure 4-12.

Table 4-2. Parametric Variations

| Parameter | Description |
|---|---|
| Friction effect | Varying coefficient of friction (0.2 to 1.1) |
| Clearance effect | Varying hole clearance (0.19 mm to 2 mm) |
| Misalignment effect | Holes same size by misaligned (0.04572 mm) |
| Geometry effect I | Lower plate hole size larger (0.20955 mm) |
| Geometry effect II | Upper plate hole size larger (0.20955 mm) |
| Defects effect I | Lower plate material removed in middle (scar-like) |
| Defects effect II | Lower plate material removed at interface |
| Defects effect III | Lower plate increased material removed at interface |
| Debris effect | Plates separated by debris |
| Increased displacement | Displacement of rivet increased from 3.3 mm (standard) to 4 mm |

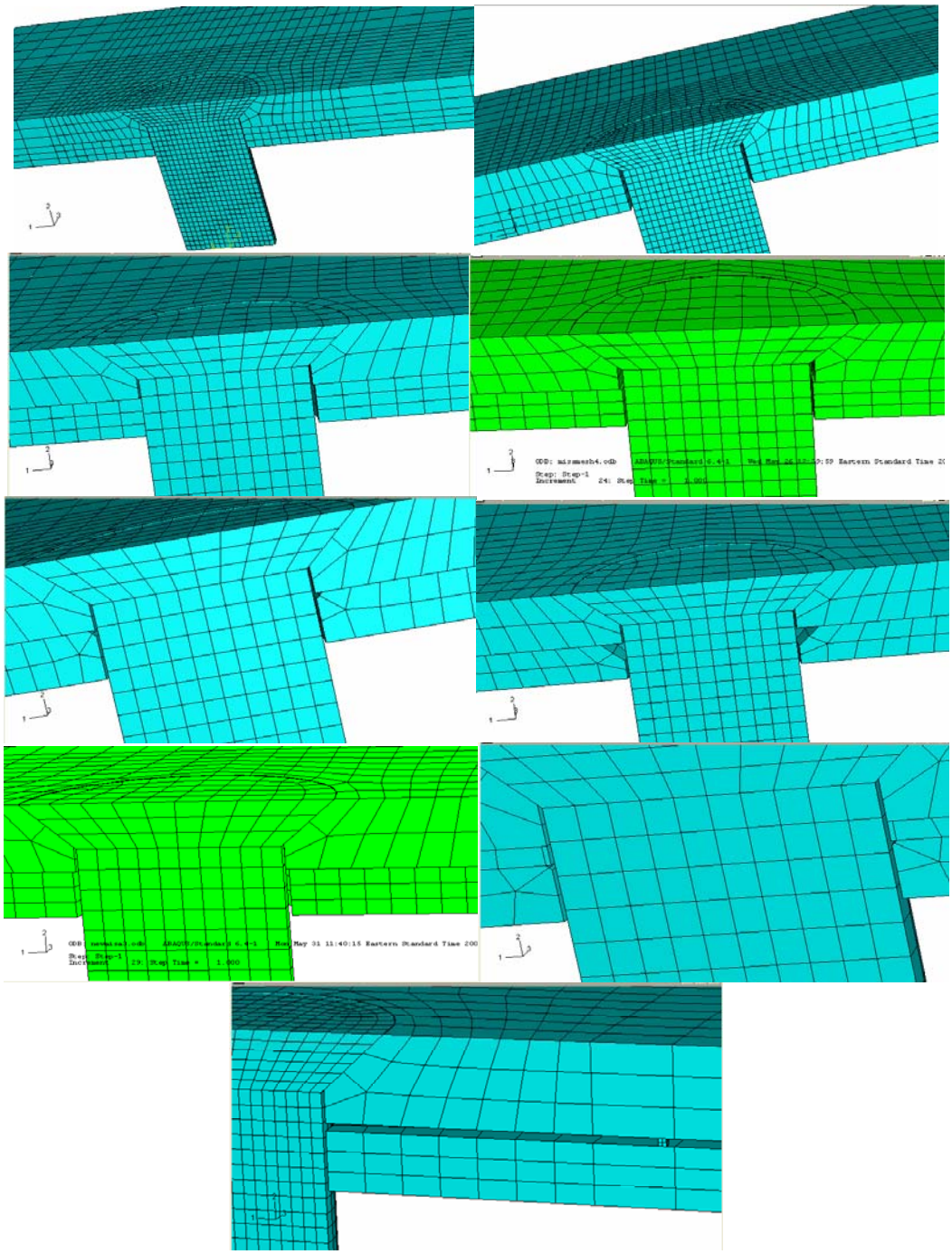

Figure 4-12. A View of the Models Showing Reduced Hole Size, Increase Hole Size, Lower Skin Misalignment, Increased Upper Skin Hole Size, Hole Defects Such as Scars and Gouges, Increased Lower Skin Hole Size, and Presence of Debris

4.3.1 Increased Rivet Displacement (Overdriven Rivet).

An increase in the applied rivet displacement leads to a larger rivet-hole expansion, consequently leading to an increase in both the compressive radial and hoop stresses around the hole periphery. A tighter interference can be achieved with an increase in the applied displacement.

Also, the fatigue performance can be improved by retarding crack growth near the hole edges. The tensile hoop stress is pushed away from the hole edge, but an increase in magnitude is observed in both the outer (52%) and the inner (25%) skin. This increases the potential for initiation and fatigue crack propagation at the faying surface.

4.3.2 Increased Coefficient of Friction.

Increased friction leads to large frictional energy dissipation. A larger amount of the load is transferred at the faying surface. As a result, the upper skin shows an increase in the compressive hoop stress balanced by an increase in the tensile stress (22%). The tensile stress zone is also observed to move near the hole edge. The lower skin shows a decrease in the compressive hoop stress around the hole edge. The tensile hoop stress showed a decrease in magnitude (33%) but is also observed to increase in area.

4.3.3 Hole Misalignment.

Hole misalignment increases the unsymmetrical deformation of the rivet. As the rivet expands, contact is established first with the lower skin unconstrained side. After full contact is made with the hole, the expansion proceeds normally. The misalignment effect leads to a larger rivet expansion against the upper skin, increasing the compressive hoop stress and consequently the tensile (22%) stress. The lower skin shows a decreased compressive stress, but the decrease is not significant so that the tensile hoop stress variation is affected by about 1%.

4.3.4 Decreased Lower Skin Hole Size.

With a decrease in the lower skin hole size, the rivet expansion is larger in the lower skin leading to an increase in the compressive residual hoop stress near the hole edge and a tensile hoop stress increase (5%) at the faying surface. Due to the different hole sizes, the rivet does not contact the upper skin uniformly leading to a localized compressive hoop stress that causes an increase (33%) of tensile hoop stress at the mating surface.

4.3.5 Decreased Upper Skin Hole Size.

With a decrease in the upper skin hole size, the rivet expansion is larger in the upper skin leading to an increase in the compressive and tensile hoop (11%) residual stresses. The rivet shows a "bulging" type deformation shape as it achieves contact with the lower skin. As a result, the rivet does not contact the lower skin completely and the compressive hoop stress is greater near the lower portion of the hole edge. The tensile hoop stress increases slightly (1%), but no change in location is observed. An example of the rivet deformation for such geometric variations is shown in figure 4-13.

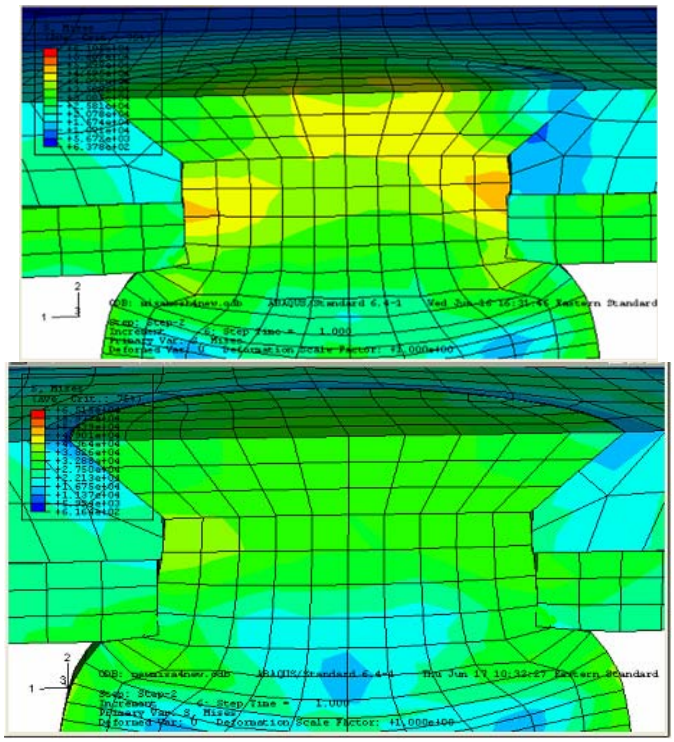

Figure 4-13. An Example of the Rivet Bulging Resulting From Effects Such as Skin Misalignment and Varying Hole Sizes

4.3.6 Presence of Debris.

The presence of debris at the faying surface decreases the rivet expansion against the lower skin hole edge. Part of the rivet deformation results in the faying surface contact closing the debris gap. Reduction in rivet expansion shows a reduced compressive hoop stress near the lower skin hole edge and a reduced tensile hoop stress away from the hole edge (20%). The upper skin shows an average reduction in the compressive hoop stress. However, a local tensile hoop stress increase of 44% is observed near the inner surface of the hole on the constrained side.

4.3.7 Decreased Hole Clearance.

A decrease in the hole clearance leads to a greater rivet expansion. This causes a compressive hoop stress increase in both the upper and lower skin. The compressive zone also increases in size. The upper skin shows an overall increase in the tensile hoop stress of 22%. The lower skin shows a local increase in the tensile hoop stress but an overall decrease (20%). This effect requires a more detailed analysis.

4.3.8 Decreased Rivet Displacement (Underdriven Rivet).

A decrease in the applied rivet displacement leads to a reduced rivet-hole expansion and consequently a “neat-fit” rivet connection. The underdriven rivet analysis showed the biggest threat to potential for fatigue damage. The underdriven rivet leads to not only an increase in the tensile hoop stress but leads to concentration of the hoop tension at the hole for both the upper

and lower skins. This residual hoop tension, especially with the effect of the sharp countersunk hole, will prove to be a critical site for fatigue damage.

A comparison of the residual-stress variations for the parametric studies is shown in table 4-3. For the simulations summarized in the table, a strong quantitative variance in the residual hoop stress was observed for some parameters. Qualitatively, the tensile hoop stress remains concentrated away from the hole for both the upper and lower skin.

Table 4-3. Comparison of Radial and Hoop Stresses for Different Parameters

| | Hoop Stress (MPa) | | | | Radial Stress (MPa) | | | |
|---|---|---|---|---|---|---|---|---|
| | Upper Skin | | Lower Skin | | Upper Skin | | Lower Skin | |
| Baseline model | 68 | -199 | 137 | -351 | 117 | -206 | 158 | -379 |
| Overdriven rivet | 131 | -448 | 193 | -468 | 179 | -441 | 186 | -448 |
| Increased friction | 75 | -248 | 103 | -372 | 110 | -199 | 144 | -386 |
| Hole misalignment | 75 | -234 | 139 | -344 | 110 | -199 | 172 | -344 |
| Reduced lower skin hole | 82 | -282 | 144 | -393 | 124 | -234 | 172 | -399 |
| Reduced upper skin hole | 68 | -213 | 140 | -386 | 110 | -227 | 165 | -372 |
| Presence of debris | 89 | -234 | 110 | -351 | 110 | -199 | 144 | -365 |
| Reduced hole clearance | 68 | -248 | 110 | -372 | 117 | -248 | 151 | -372 |

## 4.4 EFFECT OF HOLE-QUALITY VARIATIONS WITH UNDERDRIVEN RIVETS.

The previous analyses were also conducted to assess the potential threat of underdriven rivets. It was observed from the analyses that underdriven rivets do not significantly change the hoop stresses quantitatively, but it remains concentrated at holes for both the upper and lower skin. An example is shown in figure 4-14.

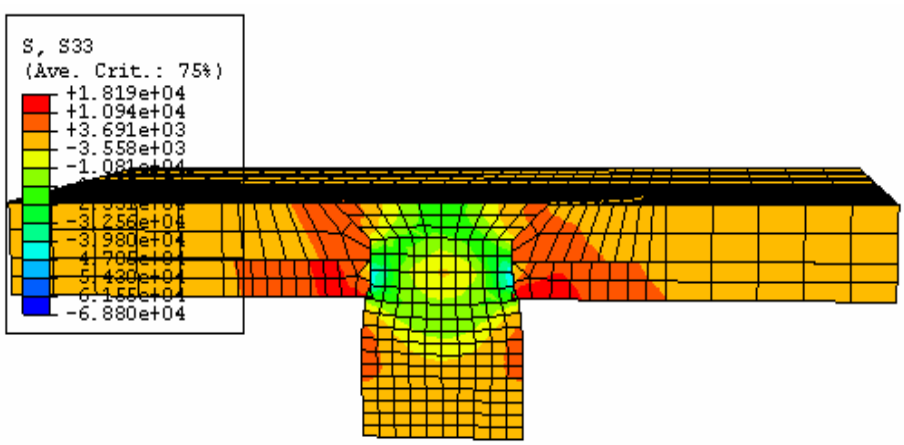


Figure 4-14. Underdriven Rivets and Effects Such as Skin Misalignment

Figure 4-15 shows a plot of the maximum tensile residual hoop stress as a function of rivet interference for the countersunk and the straight shank skin. The plot shown is only for variation in rivet interference. Other parameters, such as debris and sealant, were not considered in the analysis. The plot shows that as the rivet interference increases (going from underdriven to overdriven), a shift in location of the maximum tensile hoop stress occurs with an increase in magnitude.

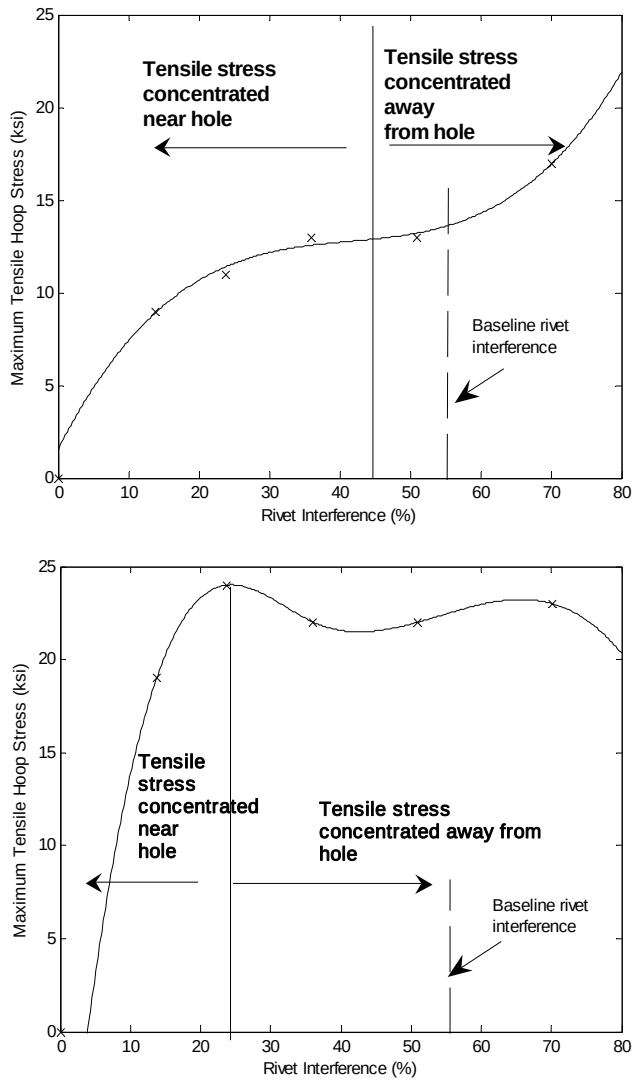


Figure 4-15. Maximum Tensile Hoop Stress as a Function of Rivet Interference, Countersunk Skin (Top), and Straight-Shank Skin (Bottom)

## 4.5 EFFECT OF VARIATIONS ON BASELINE MODEL WITH SEALANT.

As previously stated, the sealant analysis presented a large distortion problem. The element distortions that occur during the analysis, combined with the nonlinear material model, presented a significant difficulty for the ABAQUS/Standard solver leading to ABAQUS/Explicit considerations. The sealant was modeled as a low stiffness linear elastic adhesive material

(E = 0.85 GPa, ν = 0.31) [64] in ABAQUS/Standard. In ABAQUS/Explicit, the sealant was modeled as a nonlinear hyperelastic material. The stress-strain data for the material [63] and an example of evaluation of test data for different strain energy functions is shown in figure 4-16.

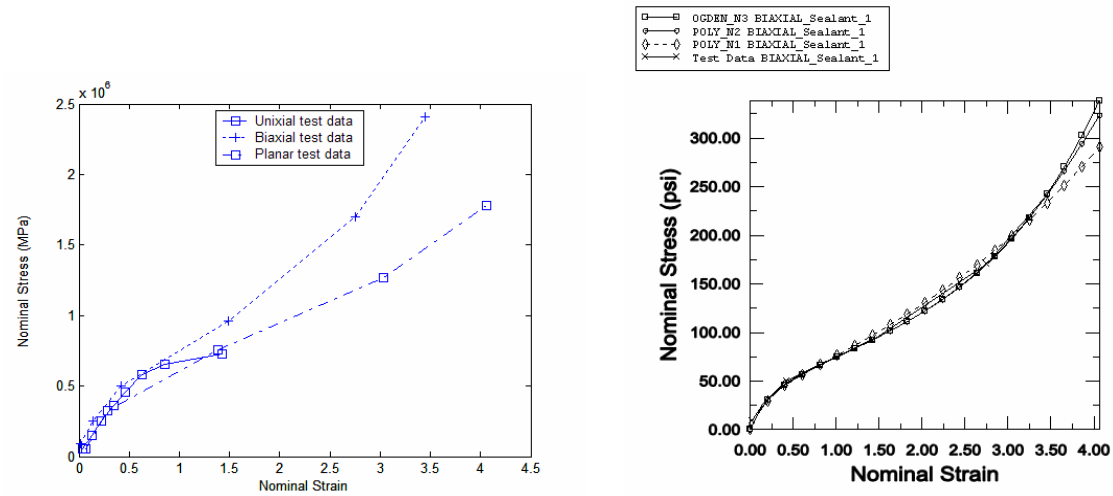


Figure 4-16. Stress-Strain Data for Hyperelastic Material Model

Elastomeric sealants are essentially incompressible materials. However, ABAQUS/Explicit requires a small amount of compressibility in the analysis. The amount of sealant compressibility becomes important when the material is confined between adjacent stiffer components. Larger compressibility ratios introduce high-frequency noise in the solution, leading to excessively small time increments that produce infeasible results. Trial analyses were conducted for Poisson's ratio ranging from 0.475 to 0.4999. A Poisson's ratio of 0.495 introduces the required compressibility in the solution without excessive run times.

The test data was evaluated for the different strain energy functions. Evaluating the strain energy function was important because the material model could become unstable at certain strain magnitudes leading to convergence issues. A first-order polynomial strain energy potential was found to be stable for all strains and hence, was implemented in the analysis. Figure 4-17 shows a view of the model with sealant. The sealant was modeled as a thin layer with a thickness of 0.127 mm. The sealant was constrained on one side while it was allowed to flow on the other side to capture the true effect. The sealant was modeled with C3D8R elements with enhanced hourglassing options and distortion control to model the sealant deformation. Near the hole where significant deformations were expected, the sealant was modeled with a refined mesh through-the-thickness to minimize numerical errors. The model was implemented to observe the effects of interference and the presence of drill shavings on the residual stress state. For each case, two simulations were conducted: one with the baseline interference, where the rivet was driven as per the specified standards, and one with low interference, where the rivet was underdriven as observed in the teardown inspection. The summary of residual stress variations with sealant are shown in table 4-4.

Table 4-4. Summary of Residual Hoop Stress Variations With Sealant

| Model | Residual Hoop Stress (MPa) | | | | | | | |
|---|---|---|---|---|---|---|---|---|
| | ABAQUS/Standard | | | | ABAQUS/Explicit | | | |
| | Upper Skin | | Lower Skin | | Upper Skin | | Lower Skin | |
| Baseline | 75 | -206 | 144 | -324 | 89 | -420 | 144 | -599 |
| Baseline interference with sealant | 96 | -206 | 172 | -344 | 213 | -393 | 179 | -565 |
| Baseline interference, sealant, and drill shavings | 82 | -165 | 151 | -344 | 193 | -517 | 213 | -482 |
| Baseline interference and sealant coverage variation | N/A | N/A | N/A | N/A | 158 | -468 | 172 | -579 |
| Low interference | 55 | -124 | 96 | -268 | 75 | -206 | 117 | -420 |
| Low interference with sealant | 75 | -154 | 151 | -303 | 137 | -310 | 151 | -386 |
| Low interference, sealant, and drill shaving | 89 | -144 | 137 | -303 | 158 | -324 | 172 | -399 |
| Low interference and sealant coverage variation | N/A | N/A | N/A | N/A | 158 | -468 | 172 | -579 |
| Rivet tilt and sealant | 144 | -220 | 158 | -282 | 179 | -310 | 193 | -420 |

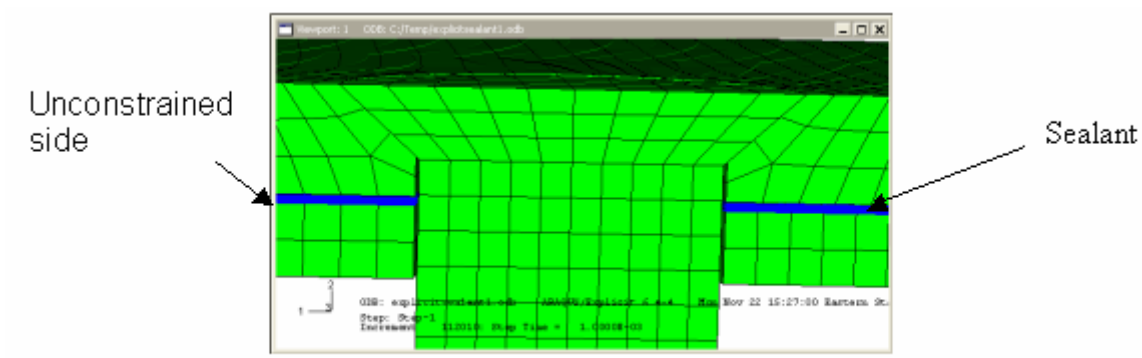


Figure 4-17. A View of the Model With the Sealant

4.5.1 Baseline Interference and Sealant.

Figure 4-18 shows the final deformed plot for both the ABAQUS/Standard and ABAQUS/Explicit analysis. The ABAQUS/Explicit results show the true sealant deformation near the hole, as seen from the microscopy of rivet installation. Figures 4-19 and 4-20 show the residual hoop stress in the upper and lower skin for both the analyses. For both the ABAQUS/Standard and ABAQUS/Explicit cases, a quantitative increase in the tensile hoop stress for the upper skin (28% and 139%) and for the lower skin (19% and 24%) was observed. Qualitatively, the lower skin showed similar results while the upper skin showed a concentrated tensile stress near the countersunk edge.

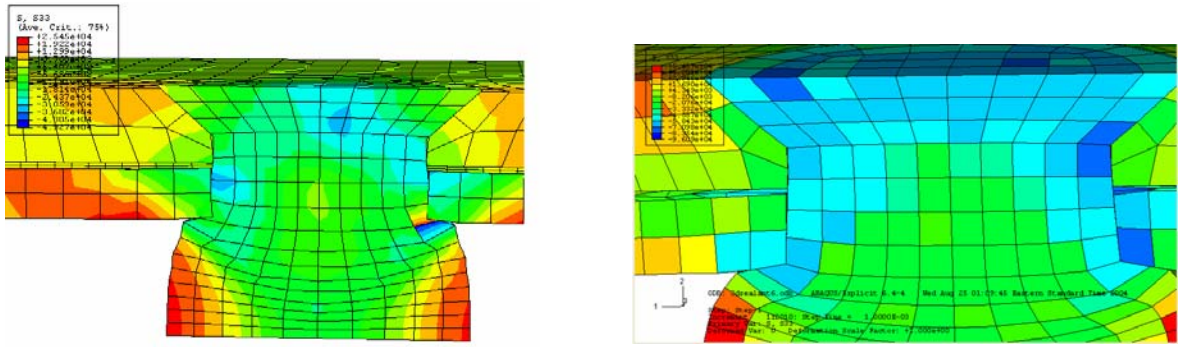

Figure 4-18. Final Deformed Shape With Sealant: ABAQUS/Standard (Left) and ABAQUS/Explicit (Right)

| Maximum Hoop Stress (MPa) | Upper | Lower |
|---|---|---|
| Tensile | 96 | 172 |
| Compressive | -165 | -344 |

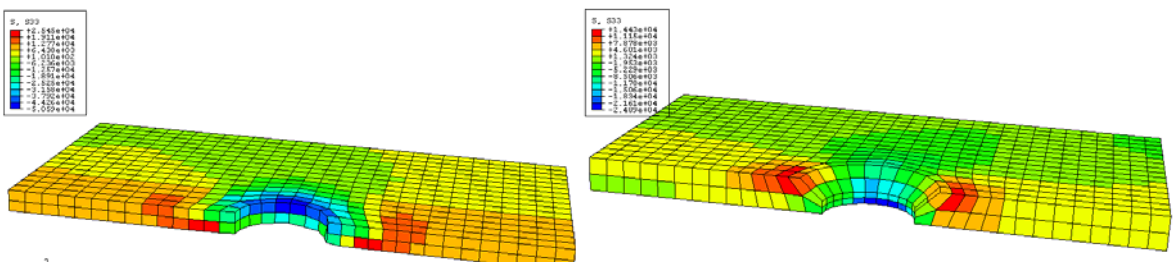

Figure 4-19. Residual Hoop Stress Contour in ABAQUS/Standard for the Upper and Lower Skin

| Maximum Hoop Stress (MPa) | Upper | Lower |
|---|---|---|
| Tensile | 213 | 179 |
| Compressive | -393 | -572 |

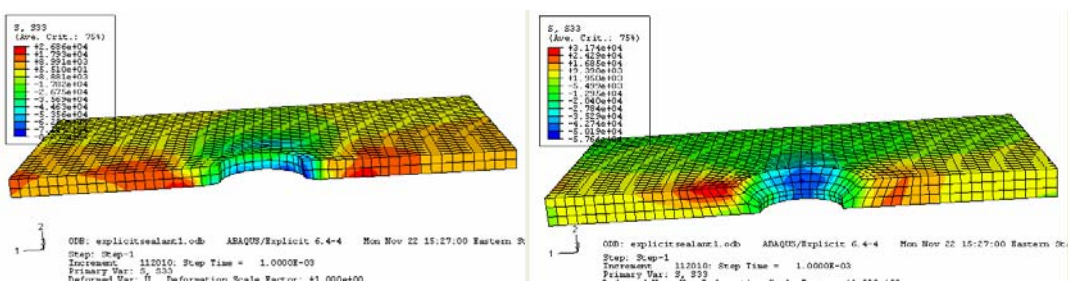

Figure 4-20. Residual Hoop Stress Contour in ABAQUS/Explicit for the Upper and Lower Skin

4.5.2 Baseline Interference and Sealant Coverage Variation.

The sealant coverage was reduced in an area next to the hole to observe the effect on the residual-stress state (figure 4-21). For the baseline interference, no contact between the upper and lower skin was observed at the reduced sealant coverage area due to sealant flow during the riveting process. The upper skin showed a shift in the tensile hoop stress near the countersunk edge. An increase in the tensile hoop stress was also observed for both the upper (76%) and lower skin (13%). For the ABAQUS/Standard analysis, a converged solution could not be obtained.

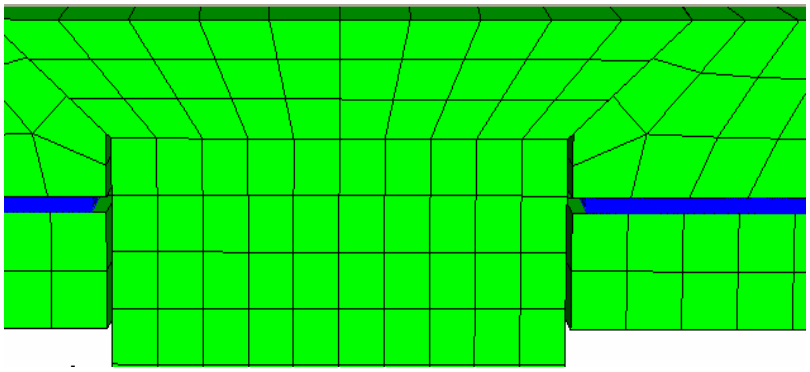

Figure 4-21. Model with Sealant Coverage Reduced Near Hole

4.5.3 Baseline Interference, Sealant, and Drill Shavings.

Microscopy of the riveted lap joints revealed skin drill shavings embedded in the sealant. An analysis was conducted to observe the effects of baseline interference with embedded drill shavings present in the sealant. Figure 4-22 shows the FE model along with a representative rivet section. The drill shaving prevents the sealant flow near the hole and strongly affects the rivet deformation. For both the ABAQUS/Standard and ABAQUS/Explicit cases, a quantitative increase in the tensile hoop stress for the upper skin (9% and 116%) and for the lower skin (5% and 47%) was observed.

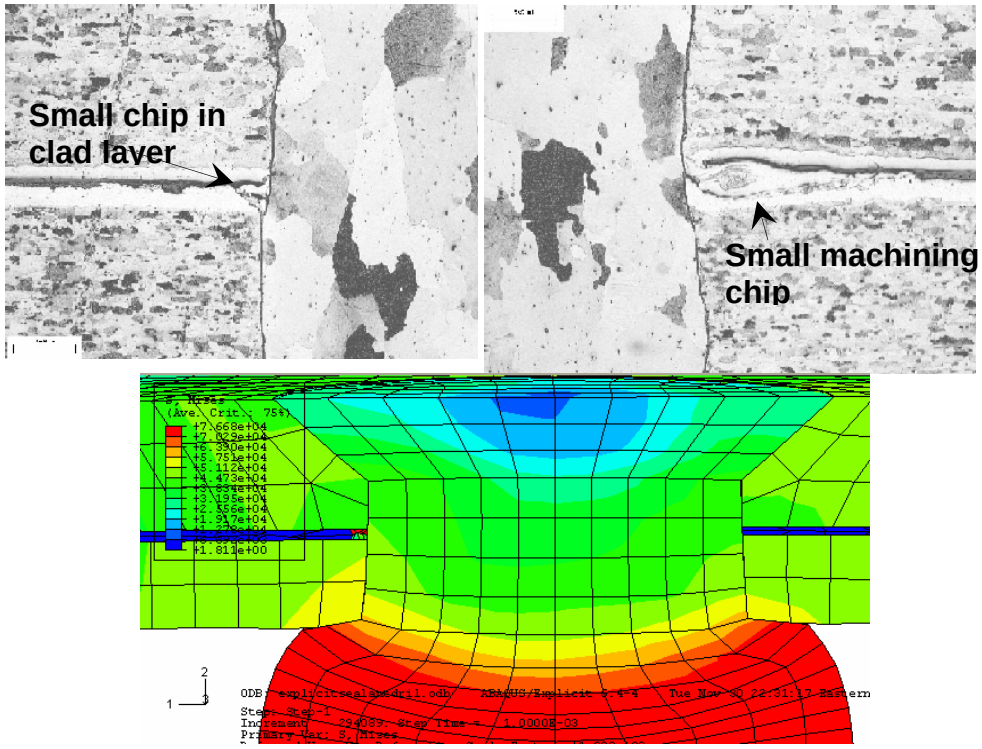


Figure 4-22. Rivet Section Showing Drill Shaving and Deformed Plot of Representative FE Model in ABAQUS/Explicit

4.5.4 Low Interference and Sealant.

Figure 4-23 shows the final deformed plot for the ABAQUS/Standard and ABAQUS/Explicit analyses. In this case, the rivet was underdriven to obtain the effect of reduced interference. Both ABAQUS/Standard and ABAQUS/Explicit analyses show a dominant tensile hoop stress near the hole edge for the upper and lower skin. The ABAQUS/Explicit analysis showed a stronger tensile zone at the faying surface unconstrained side. In both analyses, a quantitative increase was observed for the tensile hoop stress in the upper (ABAQUS/Standard-37.5% and ABAQUS/Explicit-81%) and lower skin (ABAQUS/Standard-57% and ABAQUS/Explicit-29%) in comparison with the analysis for low interference without sealant (not shown).

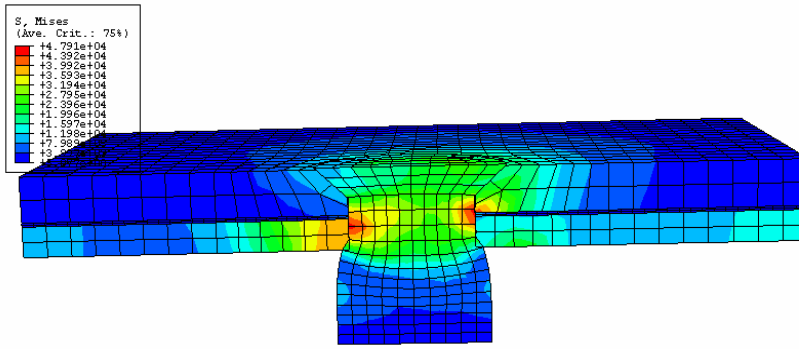


Figure 4-23. Final Deformed Shape With Sealant and Low Interference in ABAQUS/Standard

4.5.5 Low Interference, Sealant, and Drill Shavings.

An analysis was conducted to observe the effects of low interference with embedded drill shavings present in the sealant. The tensile residual hoop stress remained concentrated near the holes at the rivet/skin interface with a quantitative increase of the residual tension in the upper skin (ABAQUS/Standard-62% and ABAQUS/Explicit-109%) and in the lower skin (ABAQUS/Standard-45% and ABAQUS/Explicit-47%).

4.5.6 Low Interference and Sealant Coverage Variation.

In this case, the effect of low interference was analyzed by reducing the sealant coverage near the holes to observe the effect on the residual-stress state. Even for low interferences, the skin did not come into contact with areas where the sealant coverage was reduced because of sealant flow during the riveting process. Along with a quantitative increase in the tensile hoop stress for both the upper (109%) and lower skins (47%), the tensile zone was also observed to shift inside the hole. For the ABAQUS/Standard analysis, even for the linear elastic adhesive model, a converged solution could not be obtained.

4.5.7 Rivet Tilt and Sealant.

To simulate the rivet tilt (variation in rivet head deformation on the opposite side of the hole) observed from rivet microscopy, the applied rivet head displacement varied in magnitude across the straight shank rivet head (point of application). Figure 4-24 shows an example of the rivet section and representative FE model. This method gives a first approximation of analyzing the residual-stress state with an interference variation on both sides of the rivet hole. The residual hoop tension is observed to increase largely on one side of the hole for both the upper and lower skin.

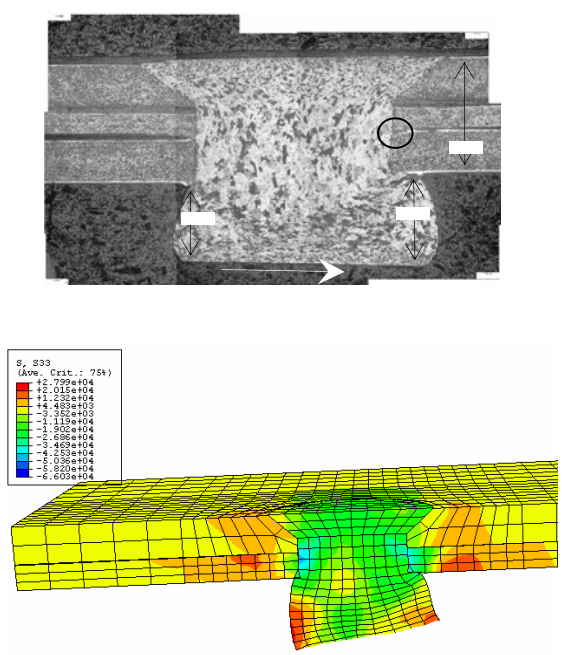


Figure 4-24. Rivet Section Showing Rivet Tilt and Deformed Plot of Representative FE Model in ABAQUS/Standard

## 4.6 EFFECT OF LOAD TRANSFER ON COUNTERSUNK JOINTS.

Joining the two skins provides a path for load transfer. The load transfer ratio (LTR) is defined as the ratio of the load transferred to the upper skin to the load applied to the lower skin (figure 4-25). To analyze the effect of load transfer on the stress state in the model, four different LTRs were analyzed (0%, 25%, 50%, and 100%). Based on the remote tension experienced by the joint from fuselage pressurization, the applied stress (P1) was 96 MPa. The cases were analyzed for both low and high interferences (figures 4-26 and 4-27).

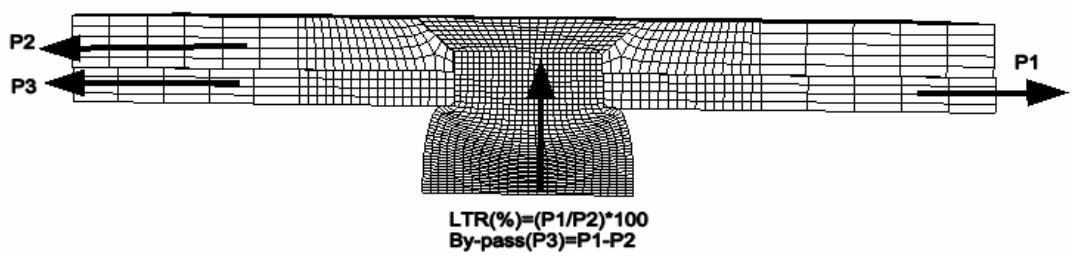


Figure 4-25. Definition of LTR in Riveted Lap Joints

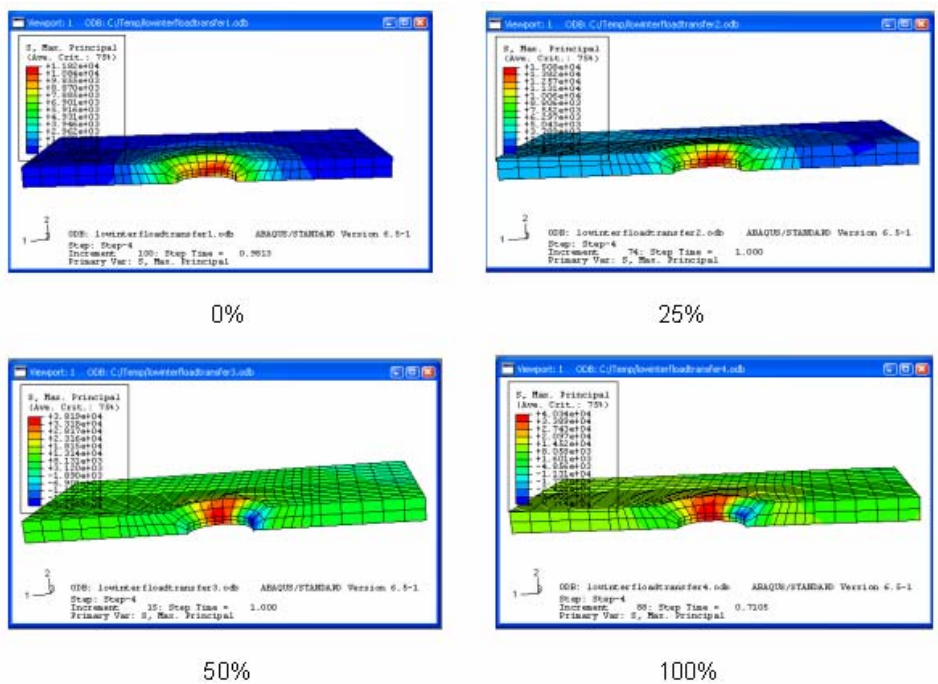


Figure 4-26. Effect of LTR on Maximum Principal Stress State in the Upper Skin for Underdriven Rivets

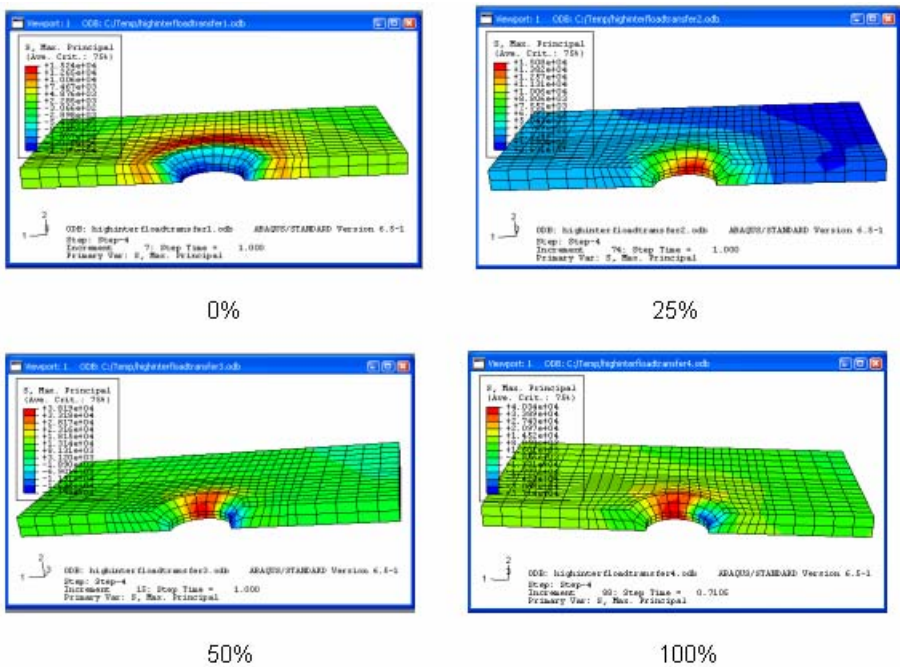


Figure 4-27. Effect of LTR on Maximum Principal Stress State in the Upper Skin for Overdriven Rivets

Park [65] performed a similar study but did not account for the residual-stress distribution resulting from rivet expansion. He observed that the maximum principal stress state moves away from the countersunk region of the upper skin to the straight shank region of the upper skin as the LTR exceeds 20%. Based on these results, Park concluded that surface cracks would initiate at the intersection or the straight bore for low load transfer, while edge corner cracks would develop in the higher load transfer case. It is interesting to note that for low interference, the maximum principal stress state remains concentrated near the bottom of the countersunk hole. As the LTR increases, the stress concentration moves to the entire hole surface. For high interference and low load transfer, the countersunk hole shows a strong compressive zone with the tensile stress concentrated at the faying surface. As the load transfer increases, the stress state moves and remains concentrated at the countersunk hole.

## 4.7 APPLICATION OF MODELS TO FRETTING FATIGUE.

In an airframe, load transfer takes place on a local scale at the rivet/skin interface. The global loading induced normal and shear loading at the rivet, causing normal pressure and shear traction at the interface. The contact region consists of a stick/slip zone. Small relative displacement in the slip zone results in increasing stress intensity at the edge of contact favoring the nucleation of cracks. The microslip between the skin and the rivet causes wear, and the associated cyclic stress nucleates small cracks. The high tangential stress can then propagate one or more of these cracks in to the bulk of the skin. This is the basic mechanism of fretting fatigue. Thus, the emergence of cracks from fastener holes can be attributed to fretting fatigue among other possible mechanisms of nucleation. The fretting fatigue behavior of contacting components depends on the contact geometry, contact pressure, and slip amplitude at the interface, material factors, and environmental factors. The material pair and surface environment determine the

friction coefficient and the tangential stresses generated at the interface. Presence of corrosion also plays an important role in crack initiation.

Fretting wear has been expressed in terms of volume of material abraded, V ($2NWf\delta$), or the average depth of the fretting damage also known as wear scar, y ($2NWfp\delta$) [65]. Here, N is the number of fretting cycles, f is the normal contact force, p is the contact pressure, W is the specific wear rate, and $\delta$ is the local slip amplitude. Fretting wear is favored by large values of W, p, and $\delta$. The amount of fretting wear is not proportional to the risk of critical crack formation. At large slip amplitudes, cracks may be abraded resulting in material loss. Efforts to understand fretting fatigue are divided into mechanistic and fretting map approaches. The mechanistic approach links interfacial shear stresses, slip amplitudes, and underlying bulk stresses to crack initiation. The fretting map approach [66] characterizes the nature of material degradation at the interface under various slip amplitude, normal load, number of cycles, etc. This approach proves to be more empirical as it involves repeated testing for different material pairs under different fretting conditions.

For the mechanistic approach, Ruiz, et al. [67] proposed two design parameters to predict fretting fatigue crack initiations. The first one is $F_1=\tau\delta$, defined as the product of interfacial tangential shear stresses and slip amplitude. This parameter is a measure of the work expended per unit contact area. This parameter will fall to zero in the stick zone or outside the area of contact. The second parameter, $F_2=\sigma_{\theta\theta} F_1$, is defined as the product of $F_1$ and the tensile stress just beneath the contacting surface. The peak of this parameter has been observed to coincide with crack initiation sites in dovetail joints. Conceptually, this parameter is similar to the multiaxial fatigue theory, which involves the product of maximum normal stress and strain amplitude as a basis for crack initiation.

In this study, the mechanistic fretting fatigue parameters were integrated with the FE simulations to demonstrate the application of the models in predicting fretting fatigue. Analyses were conducted for low rivet interference and large rivet interference. The analyses were conducted in three steps with the same mesh as the baseline model: (1) a rivet loading step, (2) a rivet unloading step, and (3) the application of remote cyclic tensile load. The applied stress (P1) was 96 MPa, which was consistent with the remote tension on the joint imposed by the 55 kPa fuselage pressurization. A 37% load transfer ratio was assumed since the joint modeled was from a three-rivet-row configuration [62]. The remote loads were cycled for two cycles after which the model settled into a shakedown state. To enforce accurate stick/slip behavior in the model, the Lagrange multiplier was invoked for the contact interactions between the different surfaces. However, convergence proved to be difficult. Due to increase in the computational cost and preclusion of the contact convergence (oscillating behavior) caused by the algorithm, the contact constraint was switched to the default penalty method. Finally, the two slip parameters, CSLIP1 and CSLIP2, computed by ABAQUS were combined to obtain an overall estimate of the slip magnitude. For a countersunk configuration, there are four locations where fretting might be of concern: between the rivet shank and hole surface (A), between the two skins (B), between the rivet head and the skins (C), and between the countersunk rivet head and countersunk hole surface (D). These locations are identified in figure 4-28.

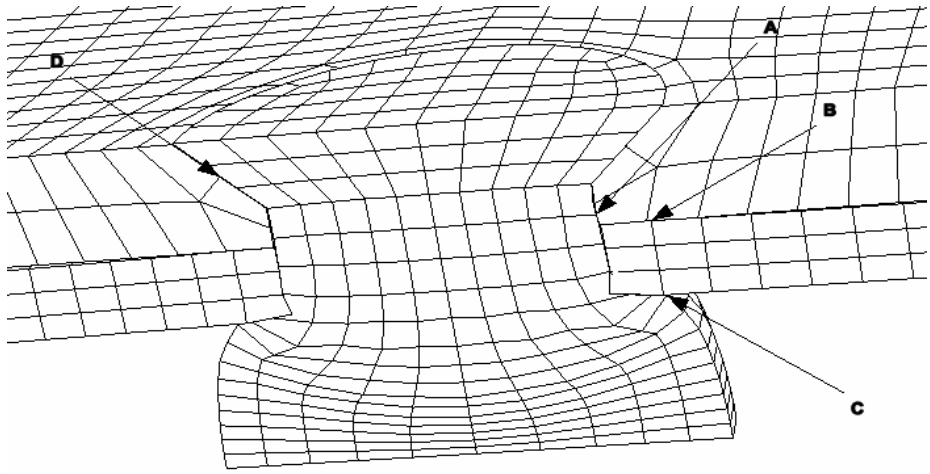


Figure 4-28. Possible Locations Susceptible to Fretting in Riveted Lap Joints

Fretting field A arises from the in-plane slip between the hole surface and rivet shank. Fretting field B is responsible for the in-plane load transfer to the rivet. Fretting damage in this region can be severe but the compressive bulk stress might prevent this plasticized volume from crack initiation. Fretting field B is caused by in-plane slips between the panel surface and opposite panel hole edge and is present at symmetric 90 and 90° locations (figure 4-29). Fretting field C arises from the contact between the rivet head and skin. Fretting field D arises from the rubbing of the sharp chisel countersunk edge against the countersunk hole surface.

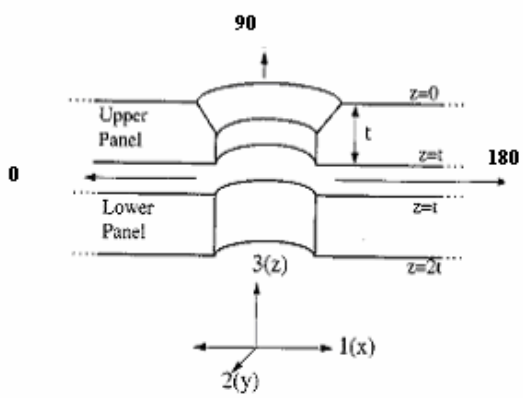


Figure 4-29. Angular Locations and Depth in the FE Model

Figure 4-30 shows the angular variations of contact pressure at the rivet/hole interface (z=t) for different rivet interferences. This contact pressure and the parameters discussed next are plotted at the faying surface (z=t) around the hole to characterize primarily the skin-skin fretting. An increase in the applied rivet displacement increases the clamping provided by the formed rivet head, which leads to greater contact pressures. The damage parameter $F_1$ is also plotted for all three cases.

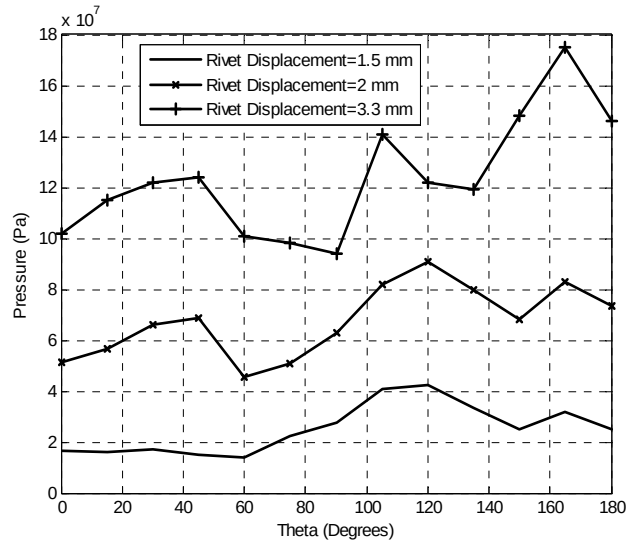


Figure 4-30. Angular Variations of Contact Pressure at Faying Surface for Different Rivet Interferences

This parameter gives no warning of crack initiation but indicates the contact area that might be subjected to severe fretting. For low rivet interferences (rivet displacement-1.5 mm), a peak is observed at θ=120° and another at θ=150° (figure 4-31). At larger rivet interferences (rivet displacement-2 mm, 3.3 mm), the first peak shifts to θ=90°. Figures 4-32 and 4-33 show a view of the faying surface for selected hole sections cut from the right-hand side panel. In most of the figures, it is shown that the general location of observed fretting is close to the peaks of the $F_1$ parameter. Figure 4-34 shows a plot of the tangential stress at the faying surface and a plot of the $F_2$ parameter around the hole. The low interference cases indicate a peak at θ=90°. This is the possible location of crack initiation. At high interferences, the bulk stress is compressive around the hole. This reduces the probability of crack initiation due to fretting at the rivet/skin interface but away from the hole at θ=90°. A presence of the bulk tensile zone is the primary cause of crack initiation. The shift in the location of the damage parameters demonstrates the application of design tools for maximizing life of the structure.

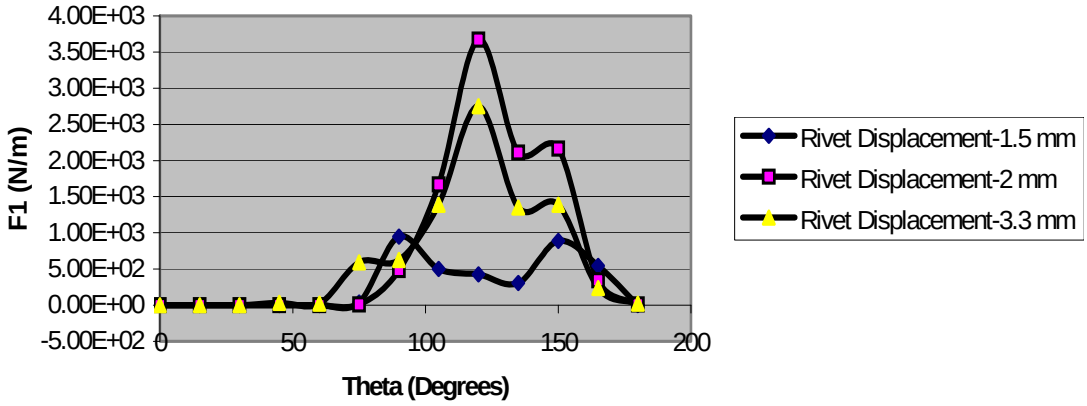


Figure 4-31. Angular Variations of Damage Parameter $F_1$ at Faying Surface (z=t) for Different Rivet Interferences

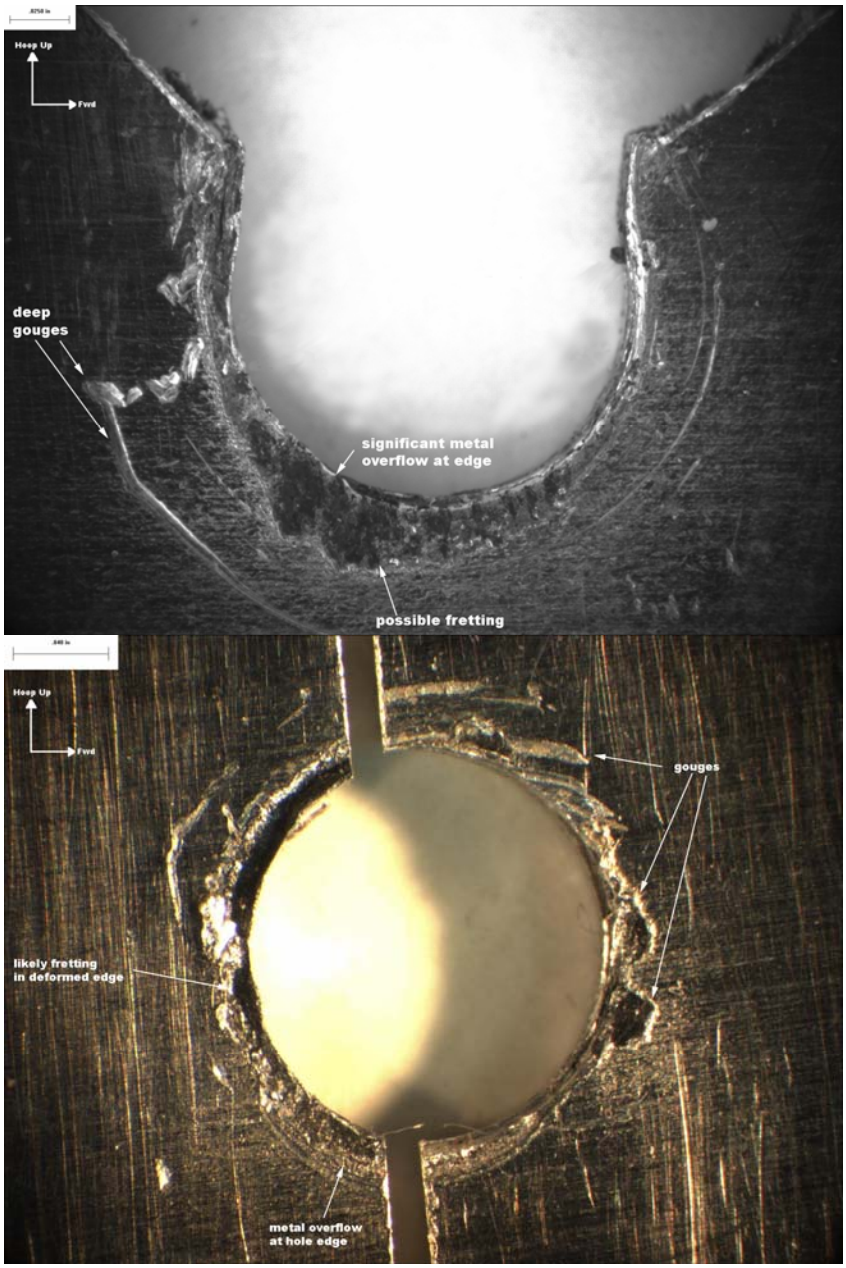


Figure 4-32. Example 1 of Fretting Damage Observed for Some Rivet Holes From the Teardown Inspection (Faying Surface, Right-Hand Side Panel Joint)

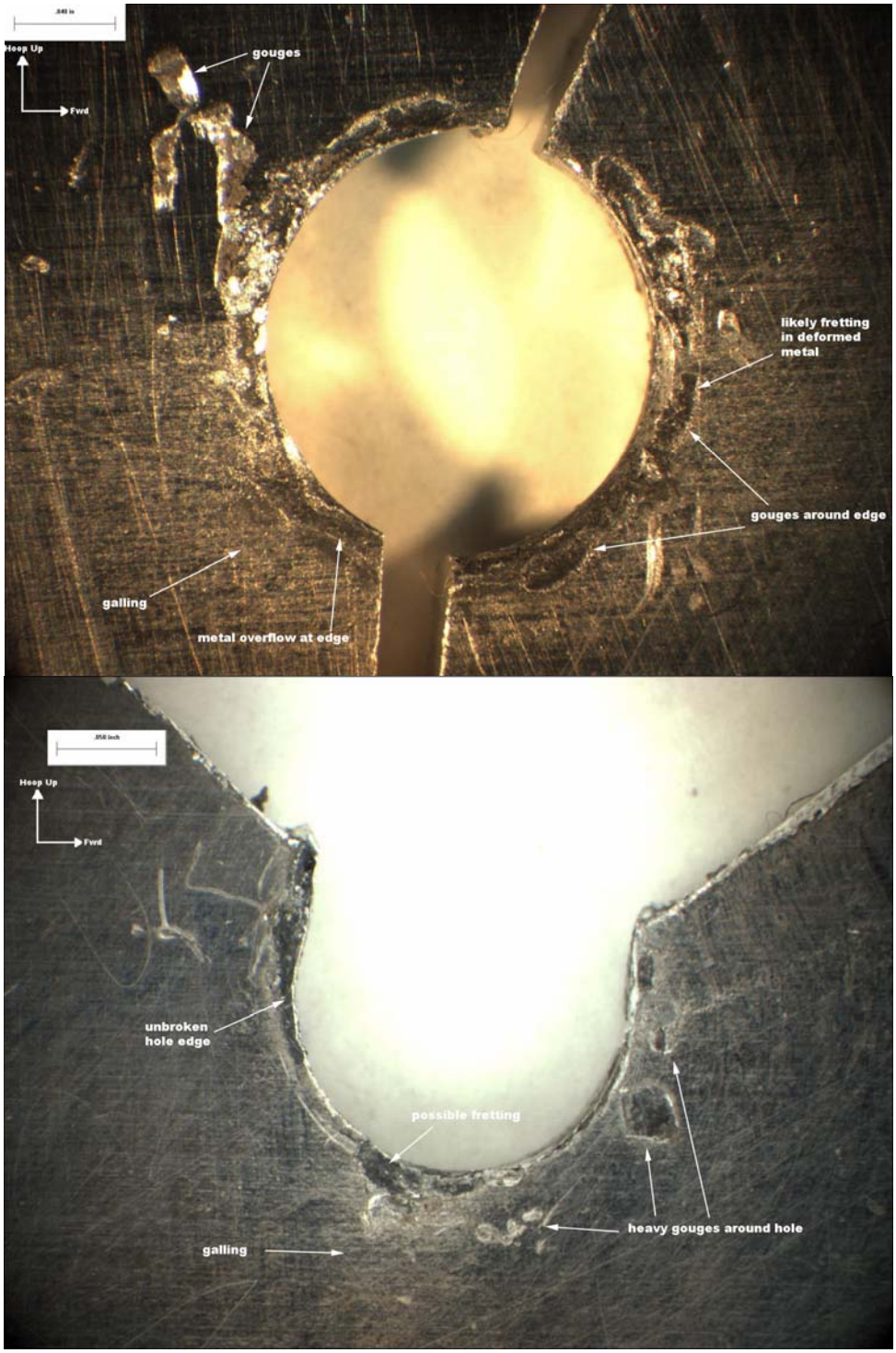


Figure 4-33. Example 2 of Fretting Damage Observed for Some Rivet Holes From the Teardown Inspection (Faying Surface, Right-Hand Side Panel Joint)

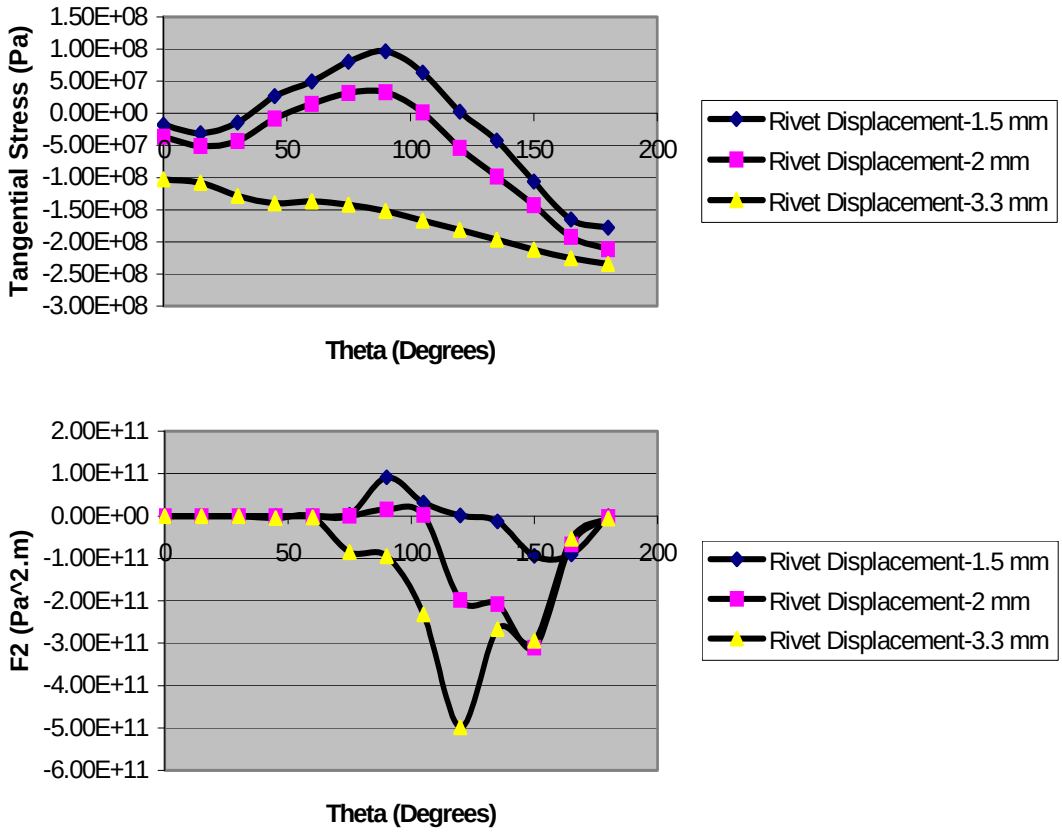


Figure 4-34. Angular Variations of Tangential Stress and Damage Parameter $F_2$ at the Faying Surface (z=t) for Different Rivet Interferences

## 4.8 SUMMARY.

Section 4 examined the effect of manufacturing process variations on the residual-stress state generated in aircraft riveted lap joints. The investigation was performed implementing a quasi-static FE approach similar to the one presented in section 3. This section demonstrated the development of a baseline 3D riveted joint model designed to duplicate the end row of a three-rivet-row B727 fuselage joint. Before establishment of the model, several mesh designs had to be numerically evaluated. During those evaluations, a mesh ratio of 0.7 was found to be successful in simulating the problem. The baseline model analysis showed a string compressive residual-stress state around the rivet holes balanced by a tensile zone away from the hole. This stress distribution in the joint was found to be highly unsymmetric in nature. A separate analysis conducted on the same model without assuming any initial rivet hole clearance also demonstrated the unsymmetrical nature of the stress state. A similar baseline analysis conducted in ABAQUS/Explicit followed. Though the analysis was simulated quasi-statically, comparison of residual-stress results predicted by the two solvers showed a 20% difference between the values. This disparity was attributed to the inherently different nature of the two solvers.

Additional FE analyses were conducted to investigate the difference in residual-stress state, if any, resulting from variations such as hole clearance, hole defects, sealant, and debris. Comparison of the results for these models with the baseline showed that the process variations

affected the residual hoop tension quantitatively to some extent. Qualitatively, underdriven rivets were observed to create a stress concentration at the hole. In summary, of the observation of process variations on the residual-stress state, underdriven rivets proved to be the biggest threat by creating a tensile stress concentration at the hole; this stress concentration was observed to be 40% greater in value than that for the baseline model. The FE models were also implemented to demonstrate the importance of taking into account initial rivet interference when predicting the final stress state. This was achieved by observing the variation in stress state at the countersunk hole for different percentages of load transfer.

The FE models were then used in conjunction with traditional fatigue damage parameters to predict the location of potential fretting damage in the joint. For this purpose, the fatigue damage parameters were plotted at the rivet/skin surface for underdriven and baseline installed rivets. The peaks of the damage parameters agreed with the general location of fretting damage observed around the rivet holes.

## 5. GLOBAL FUSELAGE LAP JOINT ANALYSIS.

Section 4 discussed the results from the development and implementation of 3D one-rivet FE models to investigate the effects of manufacturing process variations on the residual-stress state in the skin. While those models demonstrated the sensitivity of residual stresses to process variations, they did not take into account the uneven load transfer and secondary bending resulting in the lap joint. As such, the present investigation focused on development of a global three-rivet fuselage lap joint, which accounts for the residual stresses resulting from rivet installation and in-service fuselage loads. The model behavior was designed to approximate the loading experience by the fuselage splices removed in the teardown inspection. Available results from the B727 teardown damage characterization provided validation to the analysis. Finally, the global models were implemented in conjunction with crack growth analysis to predict the approximate number of cycles to grow a crack of 0.2 inch at the critical holes.

### 5.1 BACKGROUND.

Observation of the influence of rivet installation process variables on fatigue damage in fuselage splices depends on accurate determination of the local stress distribution. The local stress state in a fuselage lap joint depends on rivet/skin, skin/skin contact, residual stress resulting from installation, fuselage pressurization, friction, and secondary bending effects. The load transfer in the splice is a difficult matter. This load transfer is done by rivet shear and through friction between the sheets. This gives rise to a complex 3D stress distribution at the hole. Eastaugh, et al. [56] illustrated this in a photoelastic stress image. They concluded that the stress was a cause of several loading conditions, such as clamping stress applied by rivet, biaxial tension in sheet, internal pressure applied by rivet expansion, out-of-plane bending due to joint eccentricity, pin loading at hole due to load transfer through rivet shear, and surface shear within the clamping zone of rivet due to load transfer through friction.

### 5.2 ANALYSIS.

A schematic of the lap joint is shown in figure 5-1. The joint joins two skins that are typically 5,000-10,000 mm long. A fuselage frame is fastened to the skin every 5000 mm, dividing the lap joint into 5000 mm bays. The three-row lap joint is the structure typically susceptible to multiple-site damage. As shown, in figure 5-1, the skins at the lap joint have two critical areas; the outer skin at the top row of fastener holes, and the inner skin at the bottom fastener row. At both rows, the fastener hole is loaded by far-field and hole-bearing stresses and is susceptible to accelerated crack initiation and growth.

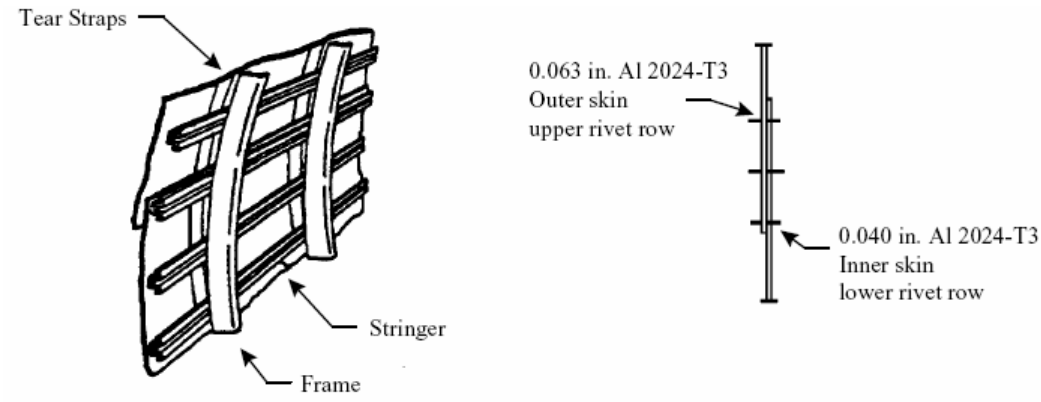


Figure 5-1. Schematic of Lap Joint Typically Susceptible to Widespread Fatigue Damage

Figure 5-2 shows a typical three-rivet fuselage splice. Fuselage pressurization is the main fatigue load on the lap joint (55 kPa once per flight). As stated previously, the flight load subjects the lap joint to hoop tension, longitudinal tension, out-of-plane bending, and secondary bending. Out-of-plane bending causes distortion and pillowing of the skin between the stiffeners. This is also known as secondary bending caused by the action of hoop tension on the eccentricity inherent in single lap joints. Fatigue cracks start in or near the rivet holes. Determination of the stress distribution at the hole is thus of prime importance. The stress distribution is a combination of biaxial tension in the skin, clamping load applied by rivet, residual stresses due to rivet installation, out-of-plane bending, and load transfer due to friction.

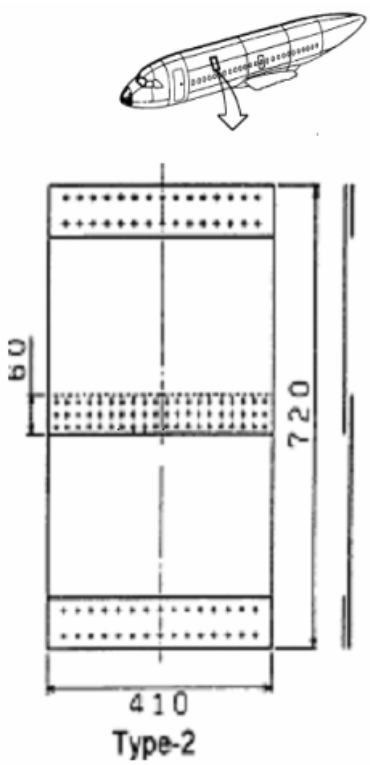


Figure 5-2. Typical Three-Rivet Fuselage Splice [62]

Figure 5-3 shows the geometry of the fuselage splice in the current study and the developed FE model. The model, which had 27,660 nodes and 21,641 elements (93,645 DOF), was generated using ABAQUS/CAE 6.4-1 with C38DR, reduced integration, 8-noded linear, solid-brick elements with a few triangular elements interspersed in the mesh. Spring elements with a stiffness of 175 kN/m connected to the middle rivet were used to represent the stringer. Symmetric boundary conditions were used and surface interactions were defined as contact pairs using the master-slave algorithm available in ABAQUS/Standard with the finite sliding option. The contact interaction was modeled with the Coulomb friction model. Formulation of the elemental stiffnesses based on current configurations from deformed nodal positions was provided using the NLGEOM option. Nonlinear material data was implemented from table 3-1.

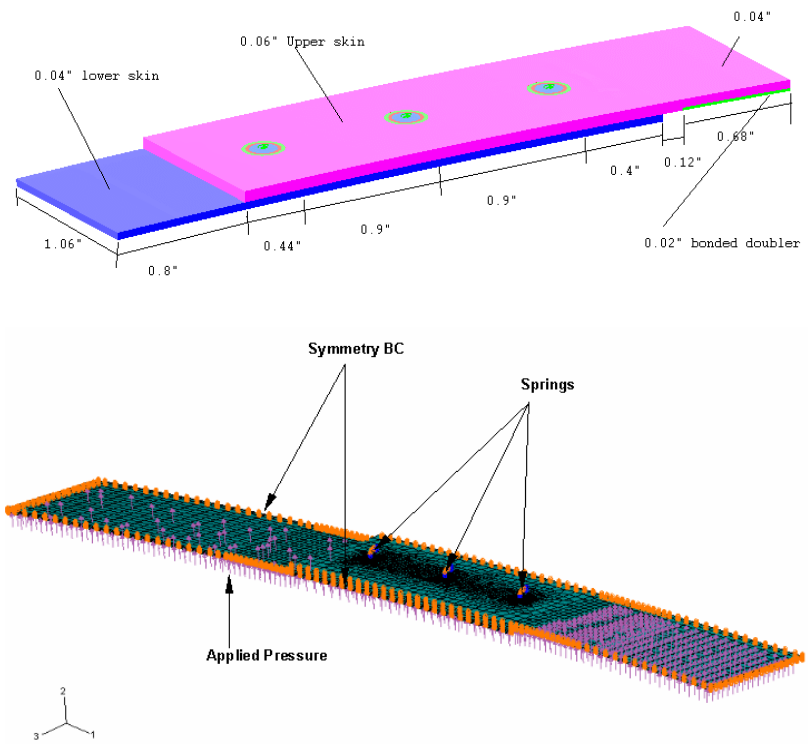


Figure 5-3. Geometry of the Fuselage Lap Joint Model and FE Model Analyzed in This Study

The analysis was done in two steps. In the first step, three rings of elements at the rivet holes in the global model were oriented in their respective local cylindrical coordinate system. Eight element sets were created through-the-thickness for each rivet hole. The residual stresses at the end of unloading from the riveting model were computed at the centroid of each element for the three rings of elements around the rivet holes. The residual stresses were mapped from the riveting model to the element sets around the rivet holes for the global lap joint model as initial conditions. An equilibrium step was performed to resolve the contact conditions and check for consistency with the riveting model. This ensured that the global model had the residual stresses and plastic strains consistent with the riveting model and also allowed ABAQUS to check for equilibrium and iterate if necessary to achieve equilibrium. The results of the first step confirmed that the approach was correct and the contact conditions were resolved accurately. Once this step was completed successfully, the fuselage pressure loading (55 kPa) was applied to

duplicate the loading experienced in service. The loads were applied for three cycles. After two cycles, the model settled into a periodic solution known as the shakedown state. A coefficient of friction of 0.2 was assumed in the baseline analysis. The final stress state from rivet installation is the only input to the global model. Hence, it does not recognize the past loading history and assumes a lesser work hardening than what may be occurring in service.

In the second step, a mesh refinement study, similar to the riveting process model study, was conducted. The mesh was refined around the three rivet holes and through-the-thickness to generate a model with 65,000 elements. The maximum principal stress at the critical rivet holes at the end of all the loading cycles showed a 1% difference in comparison to the original model, indicating numerical convergence. The stresses reported at the nodes around the rivet holes were compared to the stresses at the integration points of the elements to ensure there was no significant difference between the two values.

Figure 5-4 shows the deformed plot (exaggerated) at the end of the application of residual stress and the cyclic pressure loading. The stress state in the inner and outer skin is shown in figure 5-5. The maximum principal stress is located at the lower row hole in the inner skin (row A in figure 5-5) and upper row hole in the outer skin (row C in figure 5-5). The observation of the maximum principal stress at the lower row hole inner skin is consistent to the observed fatigue damage at the same location from the teardown inspection. Figure 5-6 shows the comparison of the stresses in both rows. The stress varies around the hole as well as through-the-thickness for each hole, illustrating the complexity of distribution, as shown in figure 5-7.

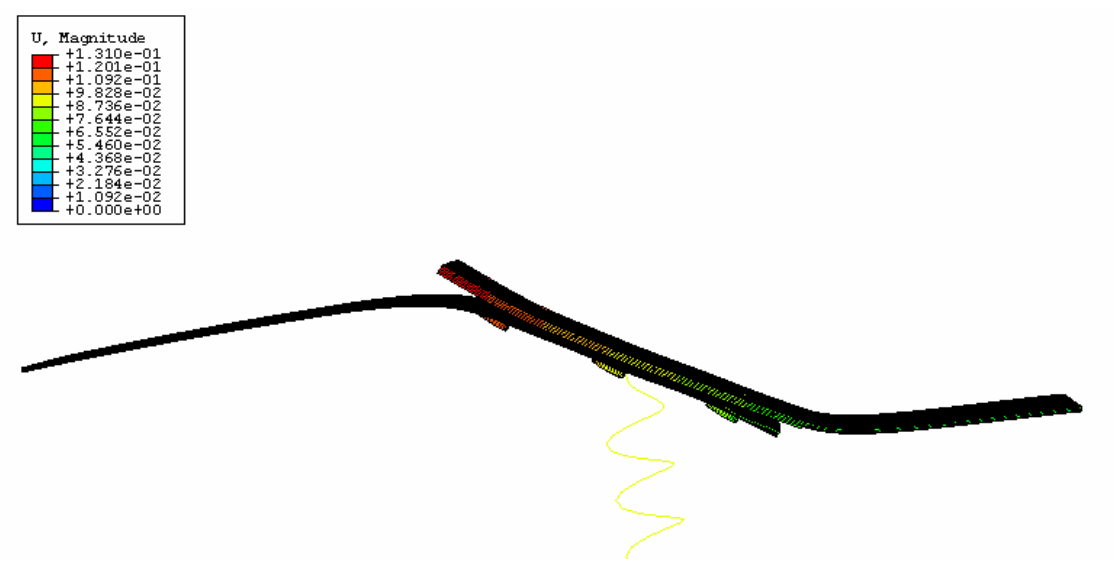


Figure 5-4. Deformed Plot (Exaggerated 20 Times) of Fuselage Splice After Residual Stress Application and Cyclic Pressurization

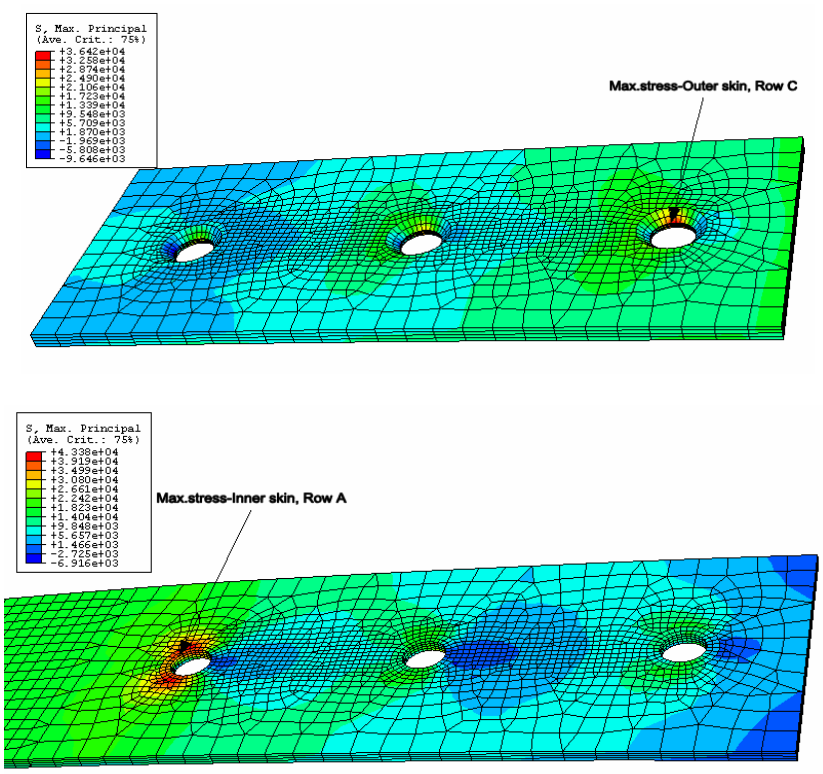


Figure 5-5. Maximum Principal Stress State in Inner and Outer Skins

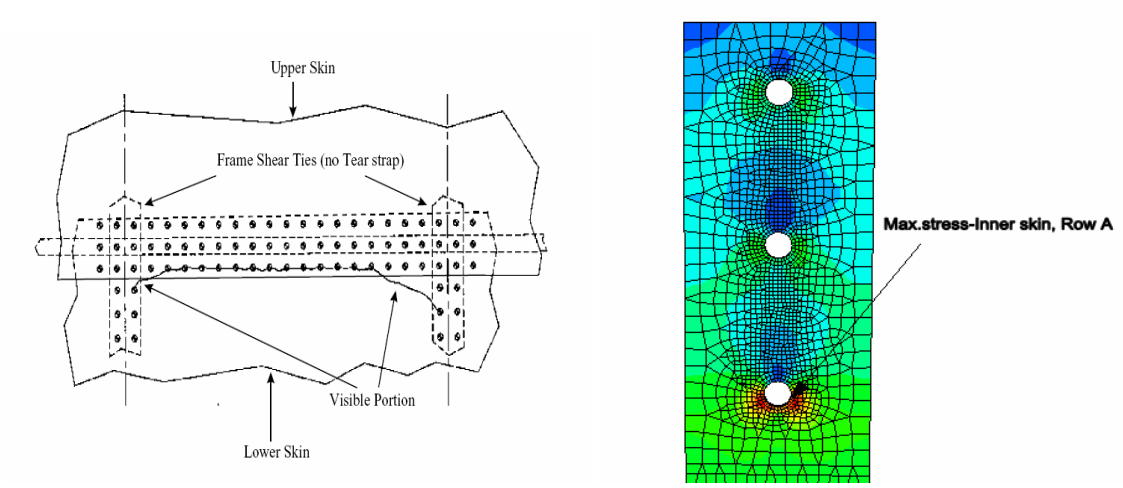


Figure 5-6. Comparison of Cracking Observed in Teardown Inspection and Stress State Predicted by the FE Analysis in the Lap Joint

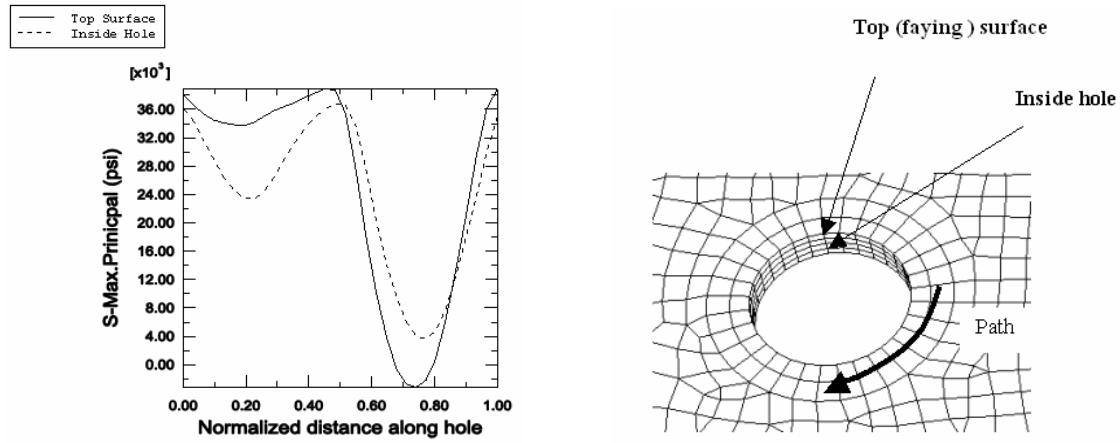


Figure 5-7. Complexity of Stress Distribution at the Inner Skin Lower Row Rivet Hole (Row B)

A major finding from the teardown inspection was the right-hand and the left-hand side panels had been installed with different rivet spacing. The right-hand side panel joint had an average rivet spacing (22.479 mm), as shown in figure 5-1. The left-hand side panel joint had a slightly larger rivet spacing (27.94 mm) between the lower and the middle rows. It was speculated that the difference in the spacing dimensions might reduce the bending stress at the lower rows, leading to better fatigue lives for the left-hand side panel joint. To analyze this effect, a fuselage splice model of the left-hand side panel joint was constructed in ABAQUS/CAE. The model had 65,000 hexahedral elements and applied loading similar to the right-hand side panel analysis. Figure 5-8 shows the model. The analysis, however, showed no difference in the stress state at the critical rivet row in the inner skin (figure 5-9), indicating that the slightly increased rivet spacing did not significantly affect the stress state for either of the skins.

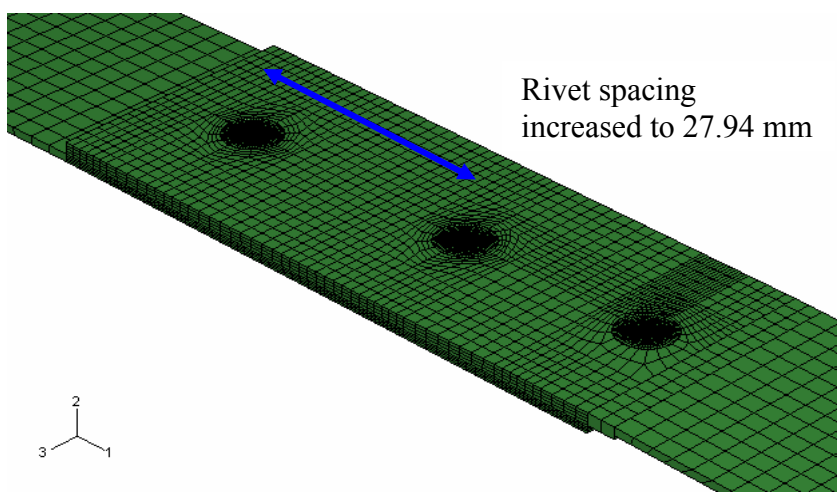


Figure 5-8. Fuselage Splice Model for the Left-Hand Side Panel Joint With Modified Rivet Spacing

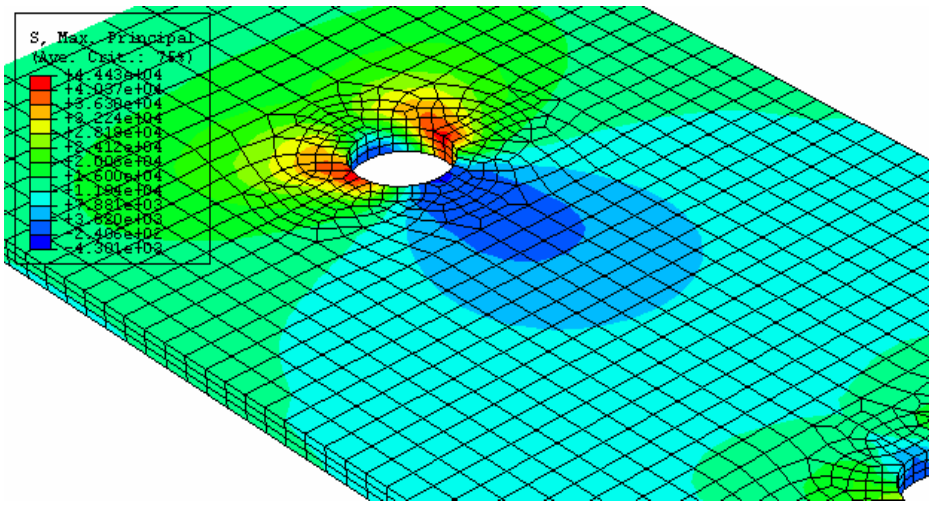


Figure 5-9. Stress State at the Critical Hole for the Inner Skin (Left-Hand Side Panel Joint)

## 5.3 FATIGUE CRACK GROWTH ANALYSIS.

Visual and high-frequency eddy current are some of the techniques used to inspect the lap joint for cracks. These techniques cannot reliably detect cracks until they are a certain length. Initiation is typically considered as the appearance of a crack of 0.02 in. The strain-life model, Smith-Watson-Topper (SWT), can be applied to predict the crack nucleation at rivet holes in the lap joints. Smith, et al. [68] first proposed the SWT model in 1970, which incorporated both cyclic strain range and maximum stress. The SWT model was selected because it had the capability to predict multiaxial fatigue life (fatigue life due to complex stress states where the three principal stresses are nonproportional or whose directions change during the loading cycle). The SWT model only used uniaxial fatigue properties and had the capability to predict fretting fatigue life.

Work related to the development of the final SWT equation can be also found in the papers of Manson [46] and Coffin [47]. The applications of the SWT model to fretting can be found in the papers by Szolwinski, Harish, and Farris [32, 33, and 69-71]. According to the SWT criterion (equation 5-1), a minimum nucleation life $2Nf$ corresponds to a maximum value of $\Gamma$, as the exponents are less than zero.

The SWT model is expressed as

$$\Gamma = \sigma_{max}\left(\frac{\Delta\varepsilon}{2}\right) = \frac{(\sigma'_f)^2}{E}(N_N)^{2b} + \sigma'_f\,\varepsilon'_f(N_N)^{b+c} \tag{5-1}$$

where

$\Gamma$ = SWT parameter

$\frac{\Delta\varepsilon}{2}$ = maximum principal strain amplitude

$\sigma_{max}$ = maximum stress on the maximum principal strain plane
$E$ = elastic modulus
$N_N$ = number of cycles to crack nucleation under a certain stress and strain level
$\sigma'_f$ = fatigue strength coefficient (843 MPa)
$\varepsilon'_f$ = fatigue ductility coefficient (0.174)
$B$ = fatigue strength exponent (-0.096)
$C$ = fatigue ductility exponent (-0.644)

and the values for the parameters are based on uniaxial strain fatigue tests. Using the stress and strain results from the FE analysis and the material parameters, the cycles $N_N$ to nucleate a crack of 0.5 mm was related to the SWT model. Figure 5-10 shows a plot of the SWT parameter plotted with the number of cycles to crack nucleation $N_N$.

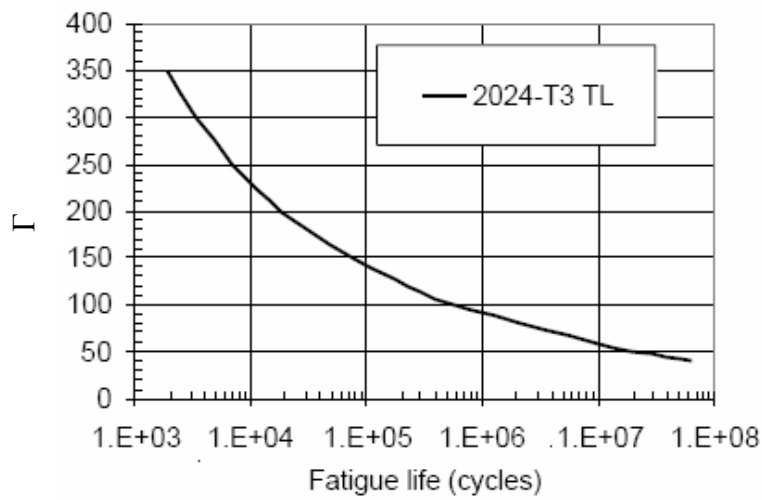


Figure 5-10. The SWT Parameter Plotted With the Number of Cycles to Crack Nucleation $N_n$

The crack growth analysis determined the subsequent crack growth after the crack was nucleated to a certain length. The AFGROW software package was employed to perform this crack growth analysis. The crack growth analysis was performed using the classic model of a corner crack at a straight hole in AFGROW and a combination of bypass tension, bearing, and bending loading (figure 5-11). For typical lap joints with 2, 3, and 4 rivet rows, FE analyses produced rivet loading (top rivet row) in terms of the local stress as 0.5, 0.37, and 0.29, respectively. For example, for the three-rivet row, 37% of the load is carried by the rivet loading and 63% of the load is the bypass loading [62]. The applied remote stress (S) was 96 MPa with a 37% rivet stress and 67% bypass stress ($S_b$). The results from the analysis in which the number of cycles ($N_G$) to grow a crack from 0.5 mm to 1.27 mm was determined. Using this approach the total number of cycles to nucleate and grow a crack to a length of 1.27 mm was determined to be 76,361 for the baseline model.

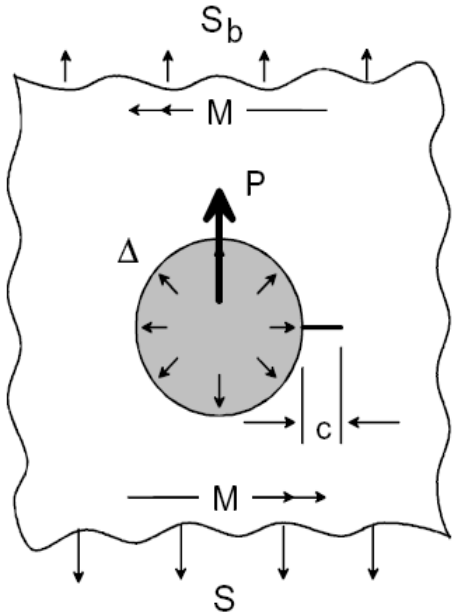


Figure 5-11. Schematic of Model Used for Crack Growth Analysis [62]

## 5.4 ANALYSIS OF CRITICAL PROCESS VARIATIONS.

With confidence established in the developed model to predict the stress state at the hole, the analysis was implemented to observe the effect of process variations on the stress state at the hole and cycles to crack growth. Again, these process variations investigated are based on actual observed service conditions. Hence, a full factorial design of experiments was not established for the parametric variations. A summary of the results from this study is given in table 5-1.

Table 5-1. Summary of Results From the Parametric Studies

| Parameter | Maximum Principal Stress at Critical Row in Lower Skin (MPa) | Number of Cycles to Grow a Crack of Length 1.27 mm ($N_T$) |
|---|---|---|
| Baseline analysis | 296 | 76,361 |
| Underdriven rivets | 337 | 41,548 |
| Overdriven rivets | 303 | 66,361 |
| Variation in interference | 303 | 66,361 |
| Sealant analysis | 310 | 60,761 |
| Sealant and underdriven rivets | 330 | 44,761 |
| Sealant, drill shavings, and underdriven rivets | 337 | 41,548 |
| Friction effect | 289 | 90,761 |

### 5.4.1 Effect of Underdriven Rivets.

The teardown inspection revealed that 60% of the rivets in the lap joint were underdriven. The average measured driven rivet head diameter in this case was documented to be 5.334 mm. To observe the effect of underdriven rivets on the fuselage, the riveting process was analyzed iteratively by applying different displacements to the rivet to obtain approximately the same driven head diameter and importing the residual-stress state to the fuselage splice model. Underdriven rivets reduced the rivet expansion leading to a tensile residual-stress state at the rivet/skin interface. This caused a stress increase of approximately 15% at the critical rivet row A. The outer skin showed a stress increase at the critical row C as well as at the middle and bottom row of approximately 18%. This effect will reduce the life to crack nucleation in both outer and inner skins as well as create a multiple-site damage scenario for the outer skin where cracks could originate from all three rivet holes.

### 5.4.2 Effect of Overdriven Rivets.

The average measured driven rivet head diameter in this case was documented to be 6.096 mm. To observe the effect of overdriven rivets on the fuselage, the riveting process was analyzed iteratively by applying different displacements to the rivet to obtain approximately the same driven head diameter and importing the residual-stress state to the fuselage splice model. Overdriven rivets increase the rivet expansion leading to a strong compressive zone at the rivet/skin interface but increasing the tensile stress away from the hole. The maximum principal stress at row B rivet/skin interface was reduced by approximately 30%. The maximum tensile stress was observed slightly away from the hole approximately 10% higher than the baseline. The outer skin also showed a reduction in stress (10%) with a slight stress concentration only at row C. This will increase the nucleation life for cracks arising from hole-quality issues particularly for the outer skin. The major threat in this case will be the tensile zone at row A that might be a potential site for fatigue damage.

### 5.4.3 Variation in Rivet Interference.

To observe the effect of rivet interference variations along the rivet rows, the residual stresses from both the under- and overdriven analyses were used. The residual stress generated by the overdriven rivet was applied to row A, while the residual stress generated by the underdriven rivet was applied to the middle and bottom row. For the lower skin, the maximum stress, which occurs away from the hole at row A, remains the same. A stress concentration can be observed at the bottom and middle holes. For the upper skin, row A and the middle row show a strong stress concentration at the rivet hole with an 18% increase in stress, while the top row shows a dominant compressive zone. Such variations of rivet interference might increase the propensity of fatigue damage combining any arising at overdriven holes with strong stress concentrations at underdriven or nonuniformly installed rivets.

### 5.4.4 Effect of Sealant.

The sealant analysis presents a large distortion problem. The sealant was modeled as a low stiffness linear elastic adhesive material (E = 0.85 GPa, ν = 0.31) [64] and a thin layer with a thickness of 0.127 mm. The sealant was constrained on one side and allowed to flow on the other side. The sealant was modeled with C3D8R elements using enhanced hourglassing options to model its deformation. The presence of sealant showed a quantitative increase in the residual stresses. Qualitatively, the tensile zone remained concentrated away from the hole. For the inner skin, the maximum principal stress showed a slight increase (5%) at row A. The outer skin row C showed a 13% increase in the stress. A strong stress concentration was also observed at the middle row countersunk hole with a stress increase of almost 34%. This increase can be attributed to residual stress increase as well as higher load transfer to the outer skin.

### 5.4.5 Effect of Sealant And Underdriven Rivets.

To observe the effect of underdriven rivets with sealant on the fuselage, the sealant model was analyzed by applying 2.54-mm displacement to the rivet and importing the residual-stress state to the fuselage splice model. The presence of sealant showed an increase in residual stresses with the tensile stress concentrated at the rivet/skin interface in comparison to the underdriven rivet without sealant. Compared to the analysis with underdriven rivets, both the outer and inner skin showed similar stress concentrations with a slight increase in the maximum principal stress (5%).

### 5.4.6 Effect of Sealant, Drill Shavings, and Underdriven Rivets.

Microscopy of the riveted lap joints revealed skin drill shavings embedded in the sealant. An analysis was conducted to observe the effects of low interference with embedded drill shavings present in the sealant. The drill shaving was modeled next to the hole with the sealant using the same material model of the skin. The drill shaving prevented the sealant flow near the hole and strongly affected the rivet deformation causing an increase in the residual stresses. Compared to the underdriven rivet analysis, both the outer and inner skins showed similar stress concentrations with a slight increase in the maximum principal stress (5%).

### 5.4.7 Effect of Friction.

To observe the effect of friction on the baseline model, residual stresses from the riveting process were imported to the fuselage splice model followed by cyclic pressurization. A coefficient of friction of 1.1 between the outer and inner skins was used. Increase in friction between the skins led to lower load influence on the rivet, with the remaining load manifesting as the interfacial friction. The maximum stress at row A was reduced only slightly (2%).

## 5.5 SUMMARY.

This section provided a brief background of the loads experienced by a typical lap joint, which led to a complex stress state at the rivet holes. Based on the splice geometry of the B727, a three-rivet row model was constructed to simulate the loading experience by the joint in service. The results from the analysis of this model showed excellent correlation between the location of the cracking observed in the teardown inspection and the critical stress site indicated by the FE

model. An important implementation of this model was to investigate the effect of different rivet spacing on the stress state at the critical hole. A comparison of the two previous analyses showed that slight differences in the rivet spacing did not significantly affect the stress state at the critical hole. This indicated that rivet spacing was not a cause of the differences in fatigue lives observed for either the right-hand side or the left-hand side panel joints.

Finally, the global splice model was used to observe the effects of underdriven rivets, sealant, and friction on the stress state at the critical hole. The results from the analyses were used in subsequent crack growth analyses to obtain an approximation to grow a 1.27-mm crack. Comparison of the results indicated that underdriven rivets in combination with sealant and drill shavings are the biggest threat to the propensity of fatigue damage at the critical rivet holes.

## 6. EXPERIMENTAL FATIGUE TESTING.

A formulation of the mechanics of the riveting process allowed for the characterization of the conditions associated with fatigue. Of particular interest were the sharp gradients of tensile stress tangential to the surface at the edge of contact. Exact assessment of the contact conditions hinged on accurate 3D FE modeling of the riveting process and subsequent in-service load transfer. This characterization of the residual-stress fields in the lap joint highlighted the potential dichotomous effects of the riveting process on the fatigue of the joint.

The pursuit of interpreting the manufacturing process variations into improved joint performance motivated experimental fatigue testing of riveted lap joint specimens with the specific goal of forging a link between rivet installation and hole-quality effects on fatigue performance of the joint. This section provides the background of the experimental study. Following this, the experimental results are compared to the FE simulations through techniques such as Thermographic Stress Analysis (TSA) (appendix A). Some microscopic observations are presented regarding the nucleation of fatigue damage in the tested specimens. A comparison of the fatigue performance of the specimens is presented based on rivet installation and hole-quality issues.

### 6.1 FATIGUE TEST MATRIX.

The matrix tested three parameters that showed high sensitivity in the FE analysis runs. These were evident in the destructive evaluation and were practical to control in specimen preparation as follows:

- Rivet Installation: either (1) underdriven, (2) baseline per specifications, or (3) overdriven.

- Hole Preparation/Debris Removal: either (1) drilled and deburred prior to assembly or (2) sealed first, then drilled.

- Hole Quality: either (1) piloted, then drilled or (2) single-step drilling

A fractional factorial matrix allowed for fewer experiments by not testing some interactions. It was critical that the interactions with rivet installation be fully tested, including all three levels of rivet installation. The least critical interaction was between hole preparation and hole quality. These tests were removed in the proposed test matrix. The advantage of the fractional factorial test matrix was that it allowed three tests per configuration with only 27 total experiments. This advantage likely outweighed the disadvantage of neglecting hole preparation versus hole-quality interactions. Other test matrix parameters that were considered included:

- Rivets installed with surface sealant wet, dry, or absent: could have been fabricated but was omitted only to reduce the size of the test matrix. Whether the sealant was wet or dry during the B727 lap joint assembly was not discerned from teardown. Also, assembly without sealant was not found.

- Gap between sheets present/absent: such a gap would have been difficult to control during specimen preparation without causing artificial stress concentrations not represented in actual manufacture.

- Debris between sheets present/absent: addressed somewhat by the hole preparation. Debris inclusion beyond that was difficult to control during specimen preparation, or to make representative. Table 6-1 gives details of the full factorial test matrix.

Table 6-1. Complete Test Matrix

| No. | Test Type | No. of Specimens | ID | Brief Manufacturing Description |
|---|---|---|---|---|
| 1 | Rivet underdriven, sealant 26 single-step drilling | 3 | U26S<br>Min. driven-head thickness-2.3 mm | Fabricate specimen, drill holes, deburr faying surface, seal surface, allow to dry, install rivet underdriven |
| 2 | Rivet underdriven, sealant 95, piloted and drilled | 3 | U95P<br>Min. driven-head thickness-2.3 mm | Fabricate specimen, seal surface, drill pilot holes without curing sealant, no deburr, drill holes, no deburr, install rivet underdriven |
| 3 | Rivet underdriven, sealant 95, single-step drilling | 3 | U95S<br>Min. driven-head thickness-2.3 mm | Fabricate specimen, seal surface, drill holes without curing sealant, no deburr, install rivet underdriven |
| 4 | Baseline, sealant 26 single-step drilling | 3 | B26S<br>Min. driven-head thickness-1.7 to 2.3 mm<br>Min. driven-head diameter-5.5 mm | Fabricate specimen, drill holes, deburr faying surface, seal surface, allow to dry, install rivet-baseline |
| 5 | Baseline, sealant 95, piloted and drilled | 3 | B95P<br>Min. driven-head thickness-1.7 to 2.3 mm<br>Min. driven-head diameter-5.5 mm | Fabricate specimen, seal surface, drill pilot holes without curing sealant, no deburr, drill holes, no deburr, install rivet-baseline |
| 6 | Baseline, sealant 95, single-step drilling | 3 | B95S<br>Min. driven-head thickness-1.7 to 2.3 mm<br>Min. driven-head diameter-5.5 mm | Fabricate specimen, seal surface, drill holes without curing sealant, no deburr, install rivet-baseline |
| 7 | Rivet overdriven, sealant 26, single-step drilling | 3 | O26S<br>Min. driven-head thickness-1.2 to 1.7 mm<br>Min. driven-head diameter-5.5 mm | Fabricate specimen, drill holes, deburr faying surface, seal surface, allow to dry, install rivet-overdriven |
| 8 | Rivet and overdriven, sealant 95, piloted and drilled | 3 | O95P<br>Min. driven-head thickness-1.2 to 1.7 mm<br>Min. driven-head diameter-5.5 mm | Fabricate specimen, seal surface, drill pilot holes without curing sealant, no deburr, drill holes, no deburr, install rivet-overdriven |
| 9 | Rivet overdriven, sealant 95, single-step drilling | 3 | O95S<br>Min. driven-head thickness-1.2 to 1.7 mm<br>Min. driven-head diameter-5.5 mm | Fabricate specimen, seal surface, drill holes without curing sealant, no deburr, install rivet-overdriven |
| | Total no. of specimens | 27 | | |

## 6.2 SPECIMEN AND TEST DETAILS.

The lap joint specimens used in the series of tests were composed of two Al skins with the dimensions specified in figure 6-1. The specimens were based on NASM 1312-4 (figure 6-2). The sheets were Al 2024-T3 with 3.968-mm countersunk rivets, as in the B727 joint. The top (countersunk) sheet was 1.524 mm, as required to prevent a knife-edge condition at the countersink. This configuration modeled the 1-mm outer skin bonded to a 0.5-mm doubler as in the B727 joint. The lower sheet was 1 mm, as in the B727 lap joint. Faying surface was sealed and assembled wet. A set of grip tabs were attached to the end of the joint to enable the specimens to be mounted securely in the load train of a 97.8 KN servohydraulic MTS test frame. Figure 6-3 shows a schematic of the assembled specimen. Rivet installation was accomplished with a quasi-static displacement controlled machine. All specimens were assembled and riveted at the DAL facility in Atlanta, Georgia. Figure 6-4 shows a picture of the final specimens. The levels of installation were based on the FE simulations and observations from the teardown inspection. The goal of the varied installation was to provide a wide range of interference and driven-head clamping constraint, to generate varying modes of fatigue failure in the joint. Figure 6-5 compares an underdriven and baseline specimen. The difference in the formed rivet head diameter is evident.

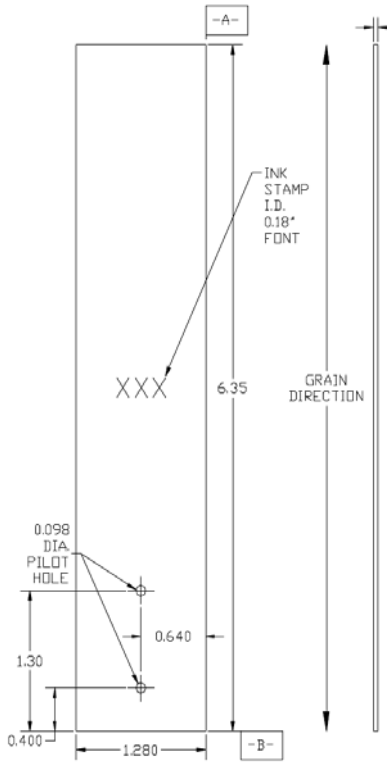


Figure 6-1. Specification of the Joint

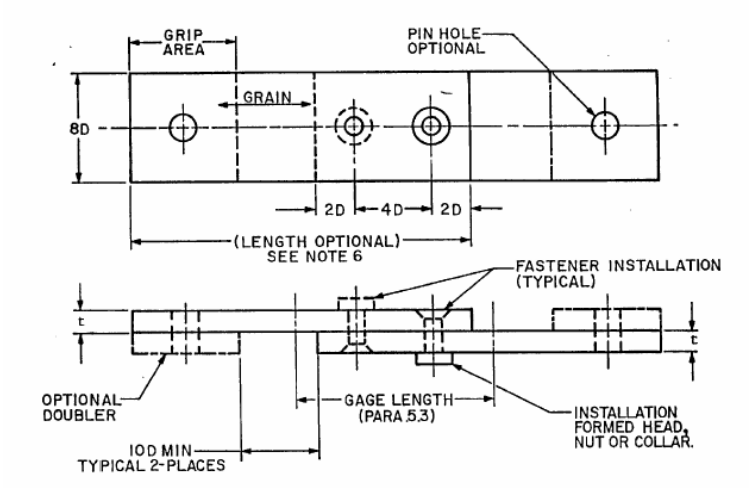


Figure 6-2. Schematic of the Specimen Based on NASM

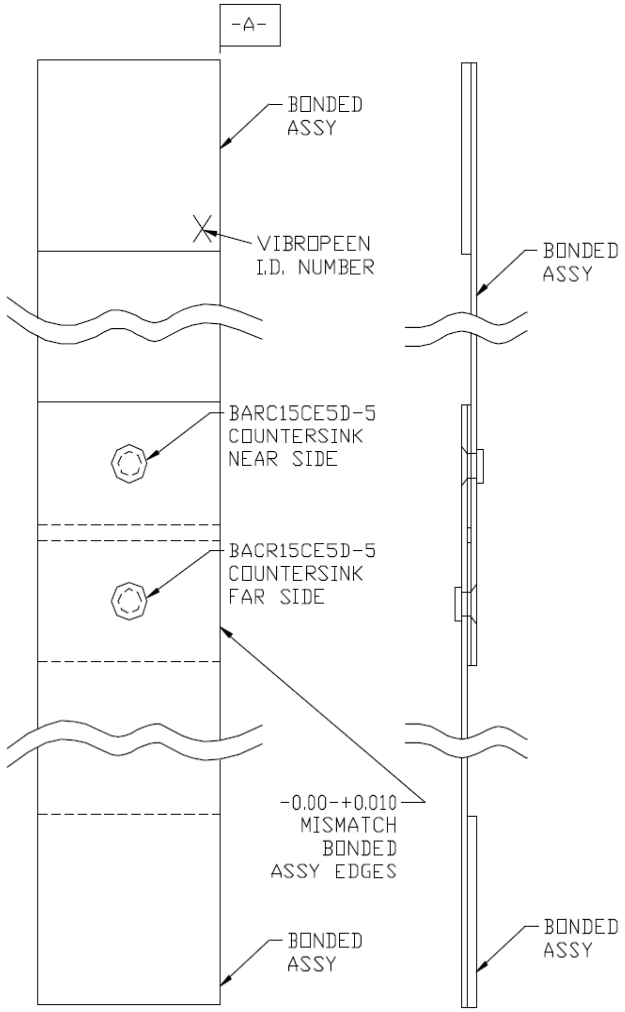


Figure 6-3. Schematic of the Assembled Joint

Figure 6-4. Final Assembled and Riveted Specimens

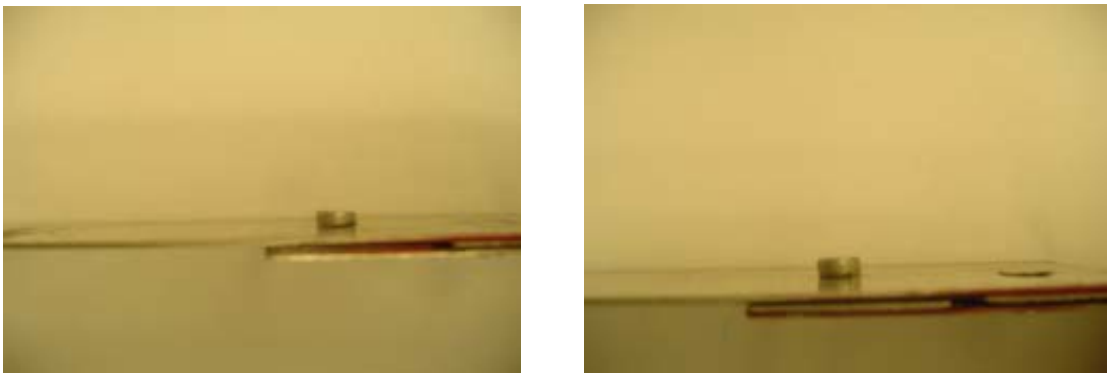

Figure 6-5. Comparison of Baseline (Left) and Underdriven (Right) Specimens
(The difference in tail diameters is evident.)

## 6.3 TEST SETUP.

Twenty-one specimens were tested employing a 97.8 kN servohydraulic MTS test frame. The tests were conducted in a laboratory atmosphere (figure 6-6) with a constant-amplitude stress level of 124 MPa with an R ratio of 0.1 and a frequency of 10 Hz. The stress level was based on testing of four dummy specimens at 96, 103, 117, and 124 MPa. The 124 MPa stress level was observed to be appropriate in terms of obtaining failure within a reasonable number of cycles. For each test, the rivet head diameters and tail heights were recorded to ensure they were within specifications. The remaining six specimens were tested implementing a thermal imaging technique. The setup and results obtained from the thermographic test are discussed in appendix A.

Figure 6-6. Fatigue Test Setup

## 6.4 FATIGUE TEST RESULTS.

Each specimen was inspected carefully upon failure to characterize the damage at and around the rivets. The process relied on optical microscopy and photographic cataloguing of the faying surface damage and interior of the rivet holes. Failure in each specimen occurred, without exception, at the driven rivet head side either on the top or bottom rivet, consistent with 50% load transfer (figure 6-7). Correlation was noted between fatigue lifetimes and the controlled experimental parameters. A comparison of these fatigue lifetimes for the three different parameters is shown in figures 6-8, 6-9, and 6-10. The summary of the fatigue lifetimes reveals some trends:

- Fatigue life increased with increasing rivet interference.
- No significant difference in fatigue life was observed at medium to high rivet interferences.
- No significant difference was observed in the fatigue life of the joints in comparison of the two sealants. For both the sealants, a reduction in the adhesive quality was observed at the end of the test. Since sealants are used more as a corrosion inhibitor (in the absence of corrosion), the less observed difference in the fatigue lives is not surprising.
- In comparing fatigue lives based on hole quality, again, underdriven rivets show the maximum difference in life. Rivet deformation, which might lead to negation of hole-quality issues (such as stress concentrations due to drilling procedures), might be less in this case.

- After testing, the hole surfaces of both the single-step and piloted specimens were examined. There seemed to be no obvious differences between them in terms of surface quality. That is, the circumferential grooves observed in the holes were not limited to just single-step or piloted specimens. The majority of both type of specimens showed circumferential grooves. Detailed viewgraphs are presented in appendix D. A measurement of surface roughness of the holes was beyond the scope of this work and hence is not presented in this report.

- The TSA was unable to detect the cycles to initiation of cracks in all the tested specimens. Cracks were identifiable only after 70,000-80,000 cycles. The detailed results of the TSA testing are discussed in appendix A.

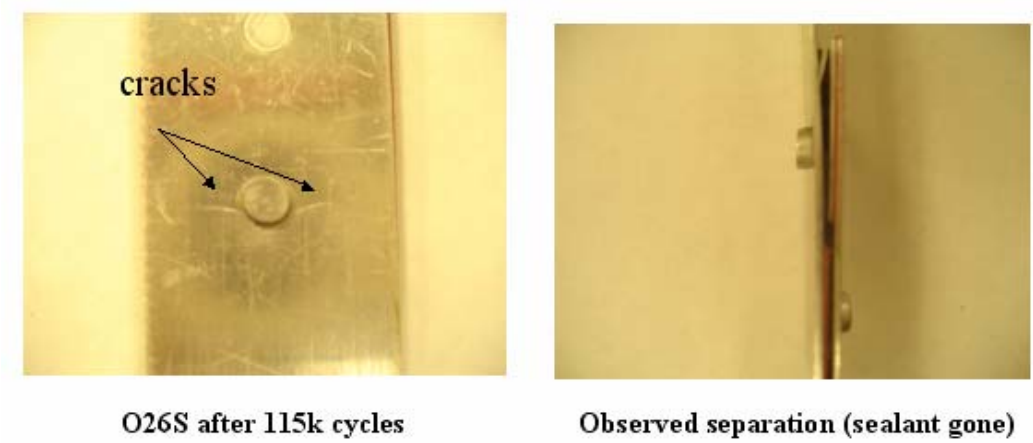


Figure 6-7. Observed Failure Location for Specimens (Left) and Sealant Separation (Right)

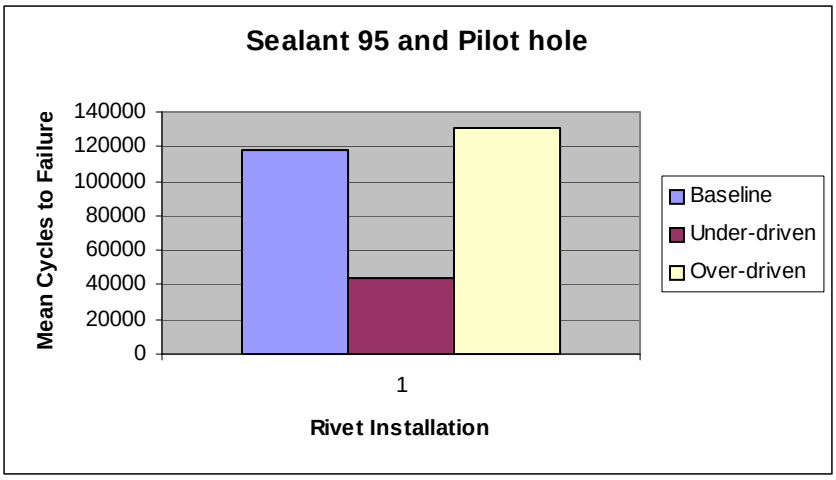


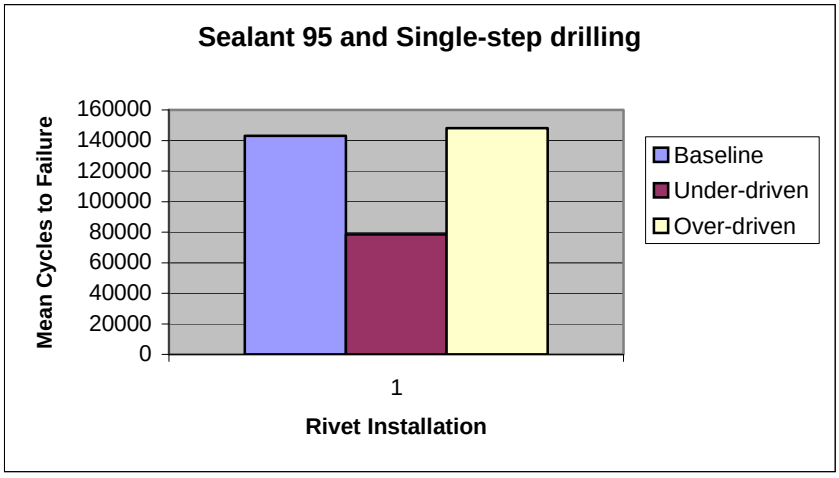


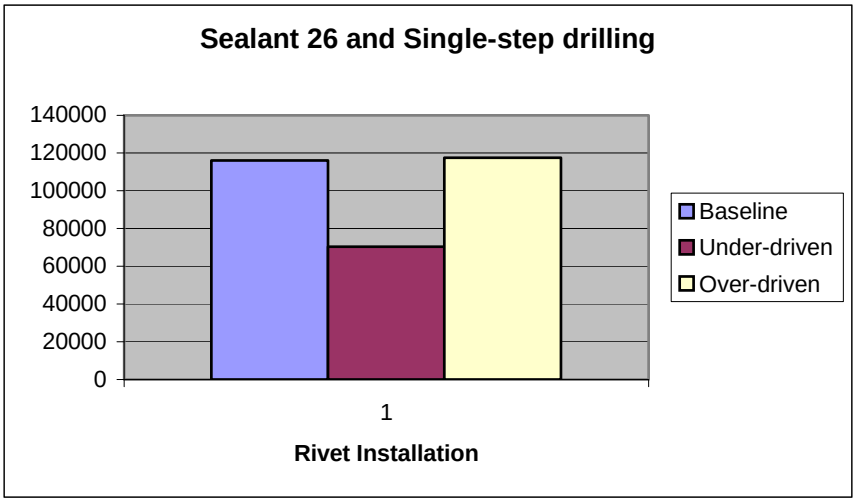


Figure 6-8. Comparison of Fatigue Lifetimes for Rivet Installation

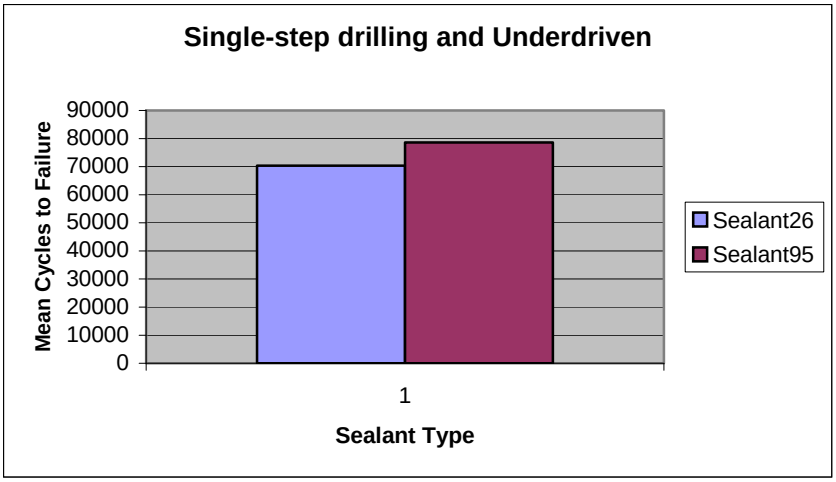


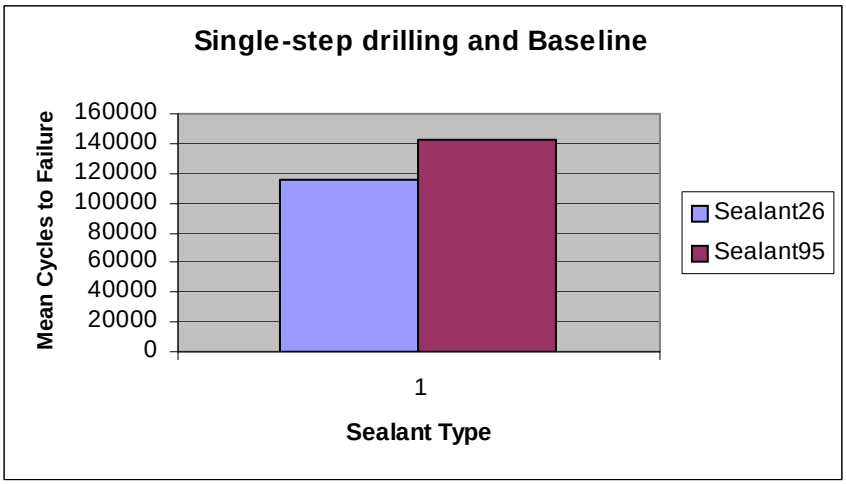


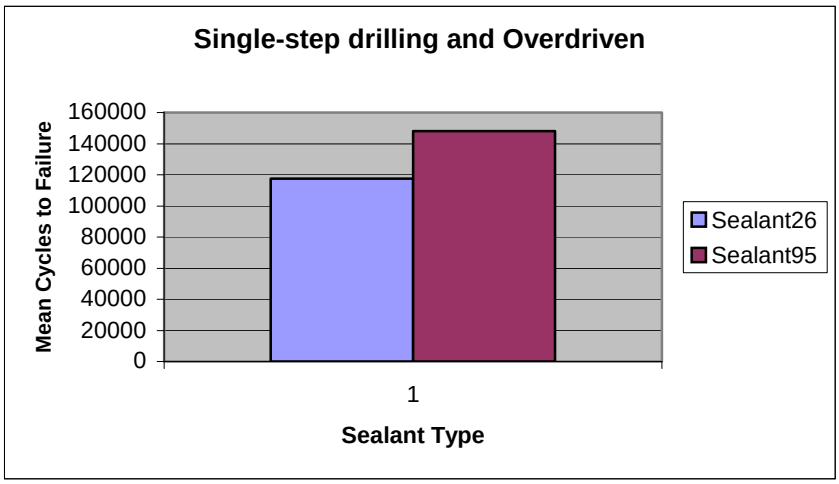


Figure 6-9. Comparison of Fatigue Lifetimes for Sealant Type

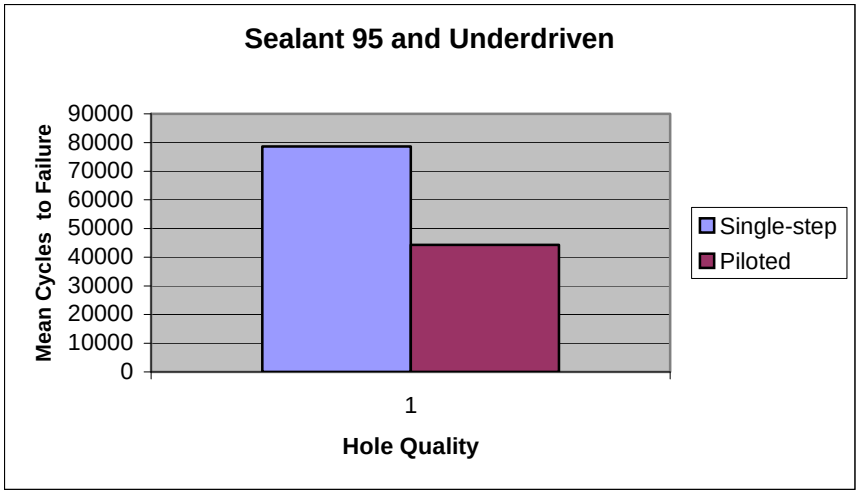


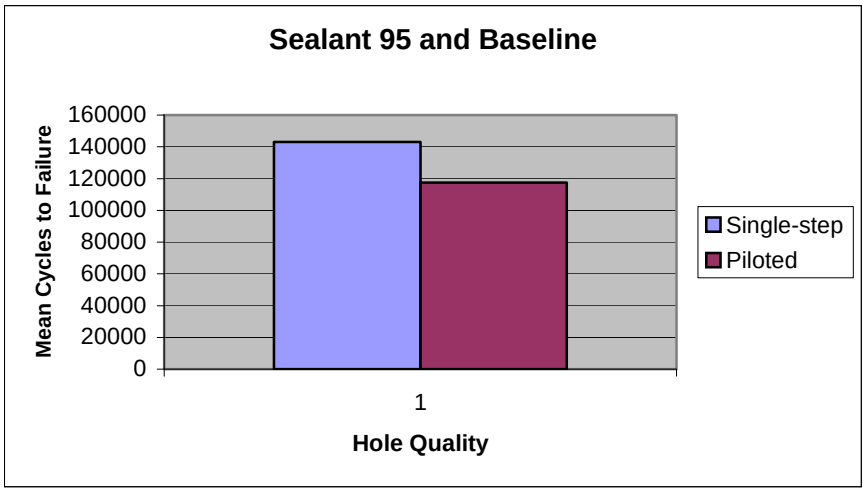


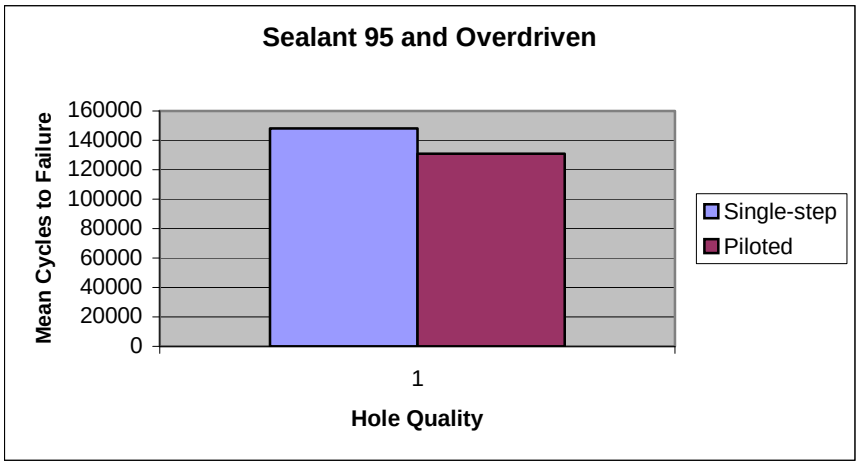


Figure 6-10. Comparison of Fatigue Lifetimes for Hole Quality

Concurrently, a characteristic state of damage was observed at and around the rivet holes based on the rivet interference. Figures 6-11 and 6-12 show photographs of the state of damage for around and near the rivet holes. The first specimen was baseline (B26S), which failed after 125,000 cycles. The second specimen was underdriven (U26S) and failed after 80,000 cycles, which is a 1.5 times shorter fatigue life. Table 6.2 shows the summary results of mean cycles to failure of the specimens. A part of this difference can be attributed to the compressive residual stress generated from increased rivet expansion in the baseline specimen. The faying surface of the baseline specimen showed signs of fretting debris at the rivet hole. Evidence of fretting debris was noted by black oxide deposited on the faying surface around the rivet hole.

Table 6-2. Summary of Mean Cycles to Failure

| Specimen Type | ID | Cycles to Failure (Mean Test Life) |
|---|---|---|
| Baseline, sealant 26, single step | B26S | 116,039 |
| Underdriven, sealant 26, single step | U26S | 70,300 |
| Overdriven, sealant, 26, single step | O26S | 117,566 |
| Baseline, sealant 95, single step | B95S | 142,983 |
| Underdriven, sealant 95, single step | U95S | 78,622 |
| Overdriven, sealant 95, single step | O95S | 148,094 |
| Baseline, sealant 95, pilot | B95P | 117,500 |
| Underdriven, sealant 95, pilot | U95P | 44,371 |
| Overdriven, sealant 95, pilot | O95P | 130,815 |

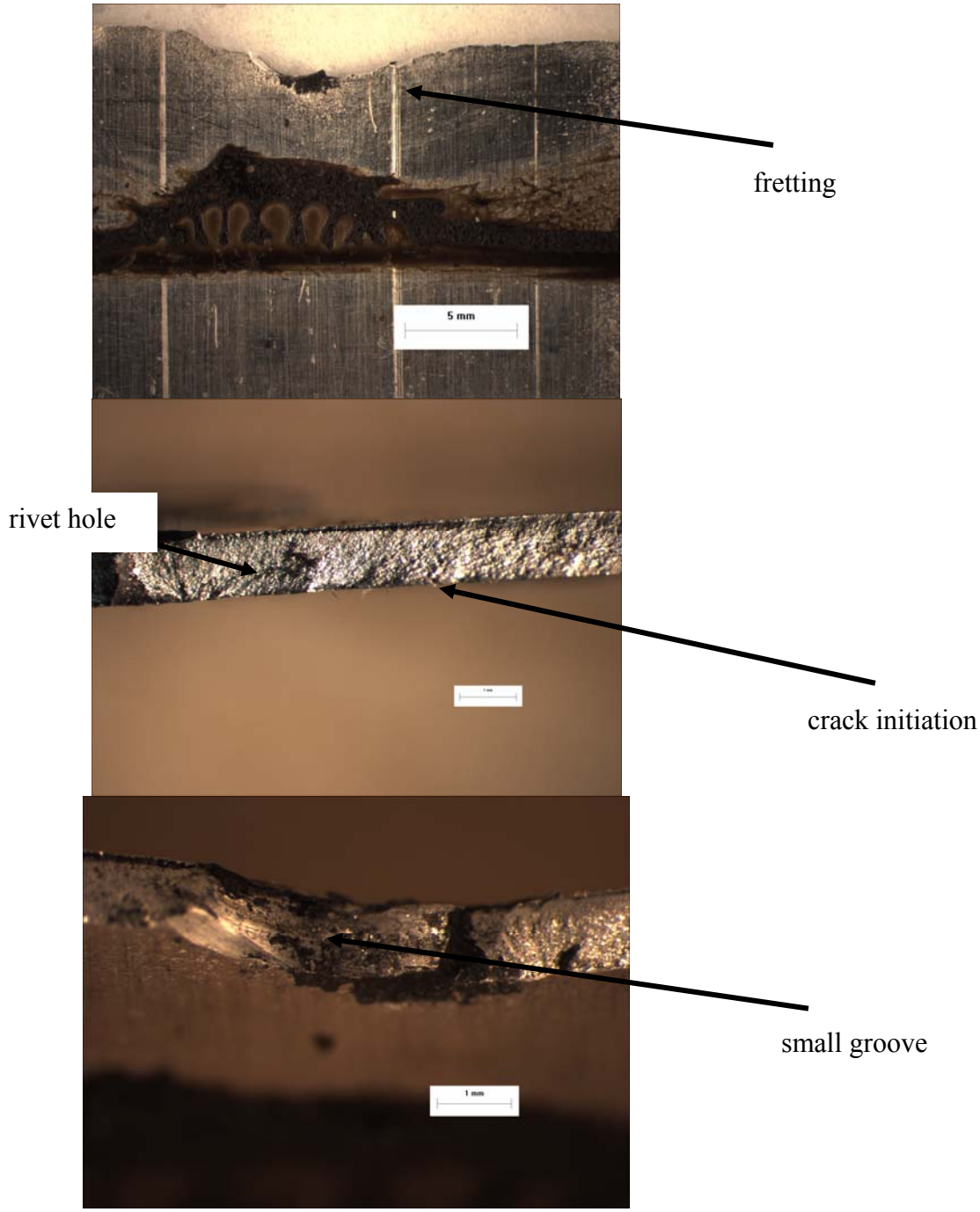


Figure 6-11. Optical Micrographs for Specimen S26s: View of the Faying Surface (Top) View of the Crack Growth Away From the Hole (Middle) View of the Rivet Hole With a Small Groove (Bottom)

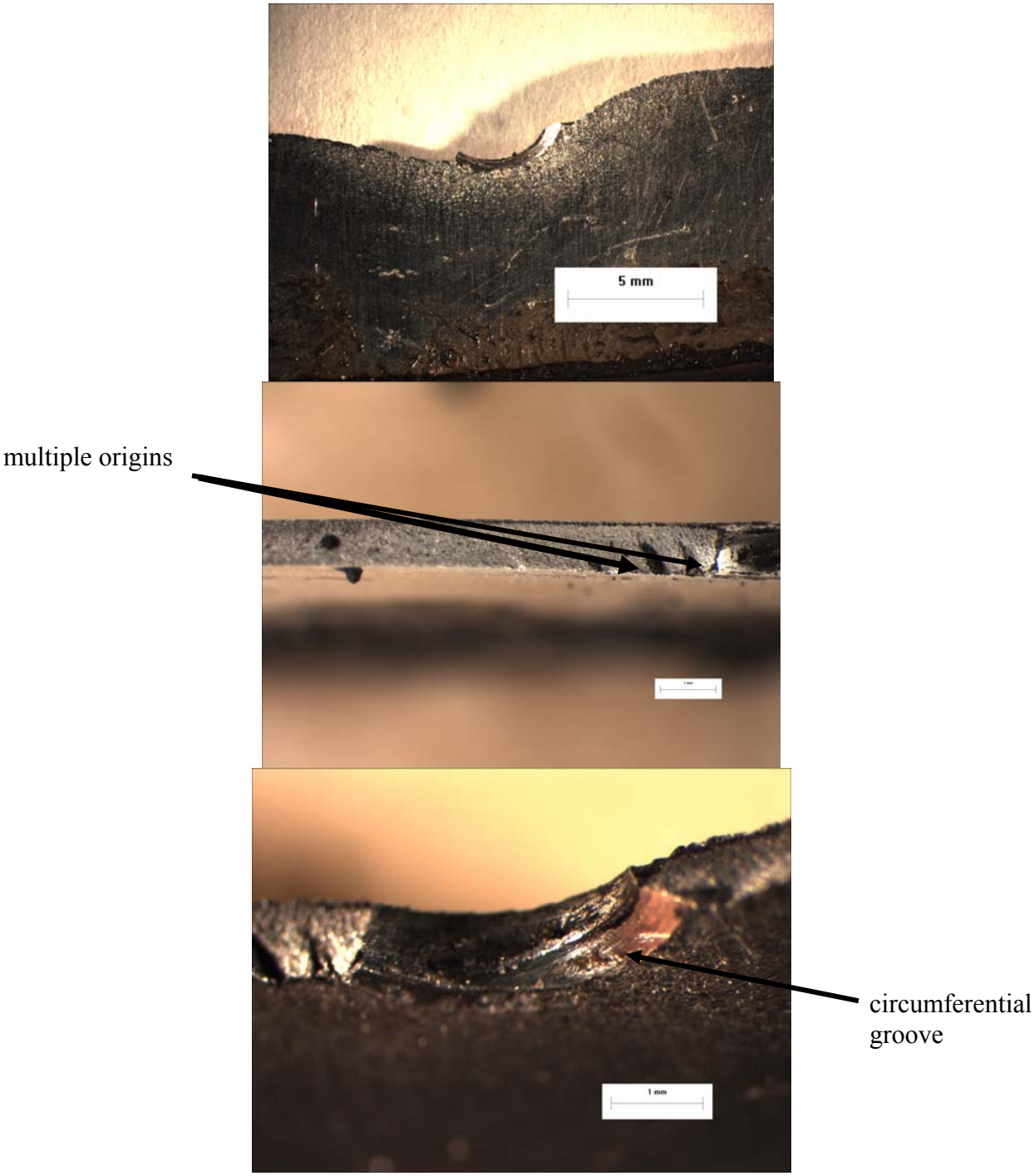


Figure 6-12. Optical Micrographs for Specimen U26s: View of the Faying Surface (Top), View of the Crack Growth (Middle), View of the Rivet Hole With a Small Groove (Bottom)

Similar debris was observed in the underdriven specimen, but the amount of debris present was smaller than that of the baseline. This is consistent with Szolwinski's [13] observed state of damage for tested joints. Increased clamping provided by larger driven heads leads to a large load transfer via friction at the faying surface. No direct correlation was observed for the state of

fatigue damage for the specimens, that is, fretting alone was not a cause of crack initation. Effects of hole quality might have been dominant in crack initiation. The majority of the rivet holes were observed to have circumferential grooves. These grooves were similar to the ones observed in the teardown inspection for the right-hand side panel joint holes and are estimated to originate from the drilling process. Effects of such drilling variations on open-hole specimens are discussed in reference 71. These hole-quality issues, especially for the underdriven rivets, might have been a cause for crack initiation.

Nuclei were observed on the fracture surface of many fatigue cracks, ridges, and several crack initiations. It seemed as if one crack was composed of several initiated cracks that had grown on different levels independently of each other. The role of fretting was not clear. It may be the result, or the cause, of cracking, which increases the local stress and hence, the crack driving force during early crack growth. The detailed damage characterization of the tested specimens showed faying surface crack origin for the baseline and overdriven rivets. The majority of the underdriven specimens showed hole surface crack origins. Recalling the results of the FE simulations conducted previously, this was an excellent validation of the developed models. For baseline and overdriven models, the tensile hoop stress was at the faying surface away from the hole, consistent with the cracking pattern observed in the experiments. For underdriven models, the tensile hoop stress was concentrated at the hole surface, which is also consistent with the nucleation of cracks in the underdriven specimens.

Observations from the damage characterization of the specimens revealed the link between riveting process parameters and the lap joint fatigue. It is noted that this test program, although not exhaustive, such as efforts by Piascik and Willard [52], attempted to establish a conclusive link between rivet installation, hole-quality issues, and the effect of these parameters on the propensity for fatigue damage at the faying surface of the riveted lap joint.

## 6.5 SUMMARY OF FATIGUE TEST RESULTS.

Section 6 began with a brief review of the previous work presented and an outline of the goals for experimental fatigue testing. This was followed by details of the tested specimens and a summary of the parameters under consideration. It was noted that parameters such as debris were difficult to produce consistently in the lap joint specimens, and hence, were not considered in the test matrix.

Details of the fatigue lifetimes for the tested specimens were also presented. A 2.5 to 3 times reduction in fatigue lives was noted for underdriven specimens in comparison to baseline and overdriven specimens. For the effect of fretting on crack initiation, although not clear, it was observed that hole-quality issues appeared to be a cause of initiation. The experimental fatigue tests showed that underdriven lap joints have a significantly shorter fatigue life than overdriven or baseline riveted joints. The effects of hole-quality were also observed to be dominant for underdriven rivets. The damage characterization showed faying surface crack origins for baseline and overdriven rivets, while hole surface origins for underdriven rivets, which are consistent to the location of the tensile stresses, are predicted by the finite element simulations.

Finally, observations from the damage characterization of the specimens re-emphasized the link between riveting process parameters and fatigue of the lap joint.

## 7. SUMMARY.

The overall investigation of the FE simulation of the riveting process and fatigue lives was conducted in four distinct phases, all of which were successful in achieving their stated goals. In the first phase, the goals were to verify and validate the intended quasi-static FE modeling approach by demonstrating it could accurately predict the residual-stress state that occurred in a previous investigation. This portion of this study carefully measured the deformation, residual strains, and force-displacement data for a force-controlled rivet configuration. Additionally, the model results were also compared for both ABAQUS/Standard and ABAQUS/Explicit solvers.

The second phase of this investigation used the FE modeling approach from the first phase to address the more practical problem of predicting the residual-stress state in the riveted joint subjected to process variations. A 3D baseline model was developed for this purpose. The specifications of the model were the same as that of the B727 joint. The goal of this investigation was to predict the differences in residual-stress state for critical process variations. In conducting this investigation, five main process variables were analyzed to observe their qualitative and quantitative effect on the residual-stress state, namely: rivet interference, presence of sealant, presence of debris, hole quality effects, and geometry effects.

The third phase of this investigation focused on development of a global three-rivet fuselage lap joint, which takes into account the residual stresses resulting from rivet installation and in-service fuselage loads. The model behavior was designed to approximate the loading experience by the fuselage splices removed in the teardown inspection. Available results from the B727 teardown damage characterization provided validation to the analysis.

The pursuit of interpreting manufacturing process variations into improved joint performance motivated the final phase of experimental fatigue testing of riveted lap joint specimens. The investigation was conducted with the specific goal of forging a link between rivet installation and hole quality effects on fatigue performance of the joint.

## 8. CONCLUSIONS.

A number of finite element (FE) simulations were conducted for the riveting process using different techniques, and the results were presented in previous sections. It can be concluded that with the correct implementation of FE tools, the riveting process can be successfully simulated to obtain an accurate representation of the residual stresses resulting from the riveting process.

The rivet expansion in the baseline analysis led to both compressive and tensile residual stresses in the skin. The tensile hoop stress observed away from the hole is critical for fatigue cracks that may initiate at the faying surface.

An increase in the applied rivet displacement led to a larger rivet-hole expansion, consequently causing an increase in both the compressive radial and hoop stresses around the hole periphery. This indicated that the fatigue performance could be improved by retarding crack growth near the hole edges. The tensile hoop stress was pushed away from the hole edge, but an increase in magnitude was observed in both the outer (52%) and the inner (25%) skin. This meant an increase in the potential for initiation and fatigue crack propagation at the faying surface.

Effects such as skin misalignment, hole defects, and hole geometry increased the unsymmetrical deformation of the rivet. A significant quantitative increase in the tensile hoop stress was observed because of rivet bulging.

A decrease in the applied rivet displacement led to a reduced rivet-hole expansion and, consequently, a neat-fit rivet connection. The underdriven rivet analysis proved to be the biggest potential threat for fatigue damage. The underdriven rivet caused not only an increase in the tensile hoop stress but also a stress concentration of the hoop tension at the hole for both the upper and lower skins. This residual hoop tension, especially with the effect of the sharp countersunk hole, proved to be a critical site for fatigue damage.

The analyses with sealant showed an increase in residual hoop tension for both the upper (20%-80%) and lower skins (20%-60%). For example:

- In cases where the rivet was driven as-specified (baseline), the upper skin showed a shift in the tensile zone near the countersunk edge, which might be a probable location for fatigue cracking. For the lower skin, the tensile zone remained concentrated at the faying surface (away from the hole). For low interference or underdriven rivets with the sealant, an increase in tensile hoop stress was observed with the tensile zone concentrated near the rivet/skin interface for both the upper and lower skins.

- Rivet tilt also showed a similar tensile zone concentrated largely on one side of the hole due to the unsymmetric rivet deformation. For this type of installed rivet, the stress distribution seems to suggest that both the upper and lower skins would be susceptible to fatigue damage at the rivet/skin interface. Also, for such cases, the presence of sealant might not show any beneficial effects.

- Presence of drill shavings in the sealant showed a large increase in the tensile hoop stress for both the upper (40%-60%) and lower (50%-110%) skins. The tensile hoop stress remained concentrated at the rivet/skin interface for low interferences. Rivets installed with low interference (underdriven) with drill shavings might be a major cause of fatigue crack initiation at the rivet/skin interface.

- The presence of sealant showed an increase in the residual tensile stress state compared to without sealant. For rivets that are installed per specifications (baseline), the effect of sealant on any fatigue damage might not be significant. For cases where rivets are underdriven or tilted, the effects of sealant combined with any drill shavings might increase the propensity for fatigue crack nucleation at the rivet/skin interface.

Damage parameters were implemented in conjunction with the FE models to predict the location of fretting damage in the joint. For low rivet interferences, a peak was observed at $\theta=120°$ and another at $\theta=150°$. At larger rivet interferences, the first peak shifted to $\theta=90°$. In most cases, it was observed that the general location of fretting noted in the teardown damage characterization was close to the peaks of the $F_1$ parameter. The low interference cases indicated a peak at $\theta=90°$ for the damage parameter $F_2$, which indicates the potential for crack initiation. This is the possible location of crack initiation. At high interferences, the bulk stress was observed to be compressive around the hole. This reduces the probability of crack initiation due to fretting at the rivet/skin interface, but away from the hole at $\theta=90°$, a presence of the bulk tensile zone could be the primary cause of crack initiation.

The maximum principal stress at the end of the load application was located at the lower row hole in the inner skin and upper row hole in the outer skin (row C in figure 1-3). The observation of the maximum principal stress at the lower row hole of the inner skin was consistent with the observed fatigue damage at the same location from the teardown inspection.

A major finding from the teardown inspection was that the right-hand and the left-hand side panel lap joints had been installed with different rivet spacing. The right-hand side panel joint had an average rivet spacing (22.479 mm). The left-hand side panel joint had a slightly larger rivet spacing (27.94 mm) between the lower and the middle rows. It was speculated that the difference in these spacings might reduce the bending stress at the lower rows leading to the better fatigue lives observed for the left-hand side panel joint. To analyze this effect, a fuselage splice model of the left-hand side panel joint was constructed in ABAQUS/CAE. The analysis, however, showed no difference in the stress state at the critical rivet row in the inner skin, indicating that the slightly increased rivet spacing did not significantly affect the stress state for either of the skins.

The global splice model was then implemented to observe the effects of underdriven rivets, sealant, and friction on the stress state at the critical hole. Results from the analyses were used in subsequent crack growth analyses to obtain an approximation to grow a crack of 1.27 mm. Comparison of the results indicated that underdriven rivets in combination with sealant and drill shavings are the biggest threat to the propensity of fatigue damage at the critical rivet holes.

The observed fatigue lifetimes for the tested specimens revealed (1) fatigue life increased with increasing rivet interference, (2) no significant difference in fatigue life was observed at medium to high rivet interferences, (3) no significant difference was observed in the fatigue life of the joints when comparing the two sealants. Since sealants are applied as a corrosion inhibitor, in the absence of corrosion, the less observed difference in the fatigue lives was not surprising, and (4) in comparing of fatigue lives based on hole quality, again, underdriven rivets show the maximum difference in life. Rivet deformation, which might lead to negation of hole-quality issues (such as stress concentrations due to drilling procedures), might be less in this case.

Evidence of fretting debris was noted by black oxide deposits on the faying surface around the rivet hole. No direct correlation was observed for the state of fatigue damage for the specimens, that is, fretting alone was not a cause of crack initation. Effects of hole quality might have been dominant in crack initiation.

The damage characterization showed faying surface crack origins for baseline and overdriven rivets, while hole surface origins for underdriven rivets, which are consistent with the location of the maximum tensile hoop stress, were predicted by the finite element simulations.

## 9. RECOMMENDATIONS FOR RIVET INSTALLATION.

In light of the influence rivet installation has on the residual-stress state in the skin, it is strongly recommended that rivets installed with less than 35%-40% (underdriven) interference (55% being the baseline) should not be used in service. These rivets would tend to promote fatigue damage much earlier than rivets installed with a much higher interference. It is also recommended that the interference plots be used as a rough guideline in installing rivets to ensure at least a small compressive zone around the holes especially for the sharp countersunk skin. A rivet interference ranging from 50%-70% is recommended in service. At much higher interferences, the rivet clamping might lead to a much higher load transfer, increasing the probability of fretting crack initiation in the tensile hoop stress zone away from the holes at the faying surface.

## 10. FUTURE WORK.

The combined results of the computational and experimental investigations provided a great deal of insight into how the residual-stress state affects the proclivity for fatigue damage in riveted lap joints. To further improve preserving the structural integrity of aging aircraft, a sequence of recommendations based on the results from this work follows, with the ABAQUS/Standard assumption that some or all could, and eventually should, integrate numerical and experimental tools.

Residual stress is complicated by hole-quality effects. A model is needed that relates the SIF to the gouge mark geometry. The model would need to take into account size and shape of the gouge. Implementing the already developed FE models into SIF determination would be an excellent initial start.

The exact cause of gouging observed both in the teardown and the tested specimens is still a mystery. Determining exactly which factors in the hole drilling technique cause this gouging would be a worthy study.

This study focused on fatigue testing of a limited number of specimens. An exhaustive program based primarily on fatigue testing of specimens with underdriven/baseline rivets and hole-quality issues (such as gouging) should be established. This will ensure to eliminate any scatter associated with the testing as well as provide a database of effect of hole-quality issues on fatigue behavior of riveted lap joints.

## 11. REFERENCES.


1. Airworthiness Assurance Working Group (AAWG) report, "Recommendations for Regulatory Action to Prevent Widespread Fatigue Damage in the Commerical Airplane Fleet," revision A, June 29, 1999, J. McGuire and J. Foucault, Chairpersons.

2. Bakuckas, J.G. and Carter, A., "Destructive Evaluation and Extended Fatigue Testing of Retired Aircraft Fuselage Structure: Project Update," *Proceedings of the 7th Joint DoD/FAA/NASA Conference on Aging Aircraft*, New Orleans, Louisiana, 2003, pp. 1-12.

3. Reithmaeir, L., *Standard Aircraft Handbook*, Tab AERO, Blue Ridge Summit, 5th ed., 1991.

4. Park, J.H. and Atluri, S.N., "Fatigue Growth of Multi-Cracks Near a Row of Fastener-Holes in a Fuselage Lap-Joint," *Computational Mechanics*, 13, 1993, pp. 189-203.

5. Muller, R.P., "An Experimental and Analytical Investigation on the Fatigue Behavior of Fuselage Riveted Lap Joints," Ph.D. Thesis, Delft University of Technology, Delft, The Netherlands, 1995.

6. Langrand, B., Deleotombe, E., Markiewicz, E., and Drazetic, P., "Riveted Joint Modeling for Analysis of Airframe Crashowrthiness," *Finite Elements in Analysis and Design*, Vol. 48, 2001, pp. 21-44.

7. Fitzgerald, T.J. and Cohen, J.B., "Residual Stresses in and Around Rivets in Clad Aluminum Alloy Plates," *Materials Science and Engineering*, A188, 1994, pp. 51-58.

8. Nepershin, R.I. and Knigin, V.V., "Interferences and Residual Stresses in Riveted Joints," *Journal of Machinery, Manufacture and Reliability*, No. 5, 1992, pp. 47-51.

9. Yarkovets, A.I., Sirotkin, O.S., Firsov, V.V., and Kisilev, N.M., "Processes for Ensuring Long Life of Riveted and Bolted Joints in Aircraft Structures," *Mashinostroyeniye*, Moscow, 1987.

10. Demina, N.I. and Volkov, A.K., "The Influence of the Interference of a Rivet on the Mechanical Properties of D16 Alloy Sheet in Biaxial Tension," Cambridge Science Abstracts, Aluminum Industry Abstracts, Accession No. 01901145-0483, Vol. 21, No. 3, ISSN 0039-2316, March 1989, pp. 407-409.

11. Ryzhova, T.B., "Estimation of the Reliability of Ultrasonic Quality Control of Riveted Joints with Clearance," *Russian Journal of Nondestructive Testing*, Vol. 30, 1994, pp. 418-421.

12. Slater, W.J., "Static Strength of Riveted Joints in Fiber Metal Laminates," Ph.D. Thesis, Delft University of Technology, Delft, The Netherlands, 1994.

13. Szolwinski, M.P. and Farris, T.N., "Linking Riveting Process Parameters to the Fatigue Performance of Riveted Aircraft Structures," *Journal of Aircraft*, Vol. 37, No. 1, 2000, pp. 130-137.

14. Fawaz, S.A., "Fatigue Crack Growth in Riveted Joints," Ph.D. Thesis, Delft University of Technology, Delft, The Netherlands, 1997.

15. Deng, X. and Hutchinson, J.W., "The Clamping Stress in a Cold Driven Rivet," *International Journal of Mechanical Sciences*, Vol. 40, 1998, pp. 683-694.

16. Ryan, L. and Monaghan, J., "Failure Mechanism of Riveted Joint in Fibre Metal Laminates," *Journal of Materials Processing Technology*, Vol. 103, 2000, pp. 36-43.

17. Swenson, D.V., Chieh-Chien, C., and Derber, T., "Analytical and Experimental Investigation on Fatigue of Lap Joints, Advances in Fatigue Lifetime Predictive Techniques," ASTM STP 1122, 1992, pp. 449-459.

18. Weissberg, V., Wander, K., and Ithzakov, R., "A New Approach to Load Transfer in Bolted Joints," *16th Congress of the International Council for Aeronautical Sciences*, Jerusalem, Israel, Vol. 1, 1988, pp.96-101.

19. Sundarraj, M., Dattaguru, B., and Ramamurthy, T.S., "Analysis of a Double Shear Lap Joint With a Interference Fit Pin," *Computers and Structures*, Vol. 55, No. 2, 1995, pp. 357-363.

20. Ekvall, J.C., "Fatigue of Riveted Metallic Joints," ASTM Special Technical Publication, 927, 1986, pp. 172-189.

21. Li, G. and Shi, G., "Effect of the Riveting Process on the Residual Stress in Fuselage Lap Joints," *Canadian Aeronautics and Space Journal*, Vol. 50, No. 2, 2003, pp. 91-105.

22. Li, G., Shi, G., and Bellinger, N.C., "Studies of Residual Stress in Single-Row Countersunk Riveted Lap Joints," *46th AIAA Structures, Structural Dynamics and Materials Conference*,18-21 April 2005, Austin, TX, AIAA 2005-2024.

23. Imanaka M., "Fatigue Strength of Adhesive/Rivet Combined Lap Joints," *Journal of Adhesion*, Vol. 49, 1995, pp. 197-209.

24. Liu J. and Sawa T., "Stress Analysis and Strength Evaluation of Single-Lap Adhesive Joints Combining Rivets Subjected to External Bending Moments," *Reliability, Stress Analysis, and Failure Prevention Issues in Adhesive and Bolted Connections*, *ASME Proceedings*, Vol. 105, 1999.

25. Dechwayukul, C., Rubin, C., and Hahn, G., "Analysis of the Effects of Thin Sealant Layers on Aircraft Structural Joints," *AIAA Journal*, Vol. 41, No. 11, 2003, pp. 2216-2228.

26. Fung, C-P and Smart, J., "An Experimental and Numerical Analysis of Riveted Single Lap Joints," *Proc. Instn. Mech. Engrs.–G- J. of Aerospace Engineering*, Vol. 208, No. 2, 1994, pp. 79-90.

27. Bellinger, N.C., Krishnakumar, S., and Komorowski, J.P., "Modeling of Pillowing due to Corrosion in Fuselage Lap Joints," *Canadian Aeronautics and Space Journal*, Vol. 40 (3), 1994, pp. 125-130.

28. Shi, G., Bellinger, N., and Xiong, Y., "Three-Dimensional Nonlinear Finite Element Modeling and Analysis of Riveted Lap Joints With Corrosion Pillowing," *Advances in Computational Engineering & Science*, Vol. II, Atluri, S.N. and Brust, F.W., eds., Tech Science Press, 2000, pp. 1542-1547.

29. Patronelli, L., Langrand, B., Deletombe, E., Markiewicz, E., and Drazétic, P., "New Experimental Procedure for Analysis of Rivet Material Mechanical Properties," *ONERA, TP, No. 2000-32*, 2000.

30. Mindlin, R.D., "Compliance of Elastic Bodies in Contact," *Journal of Applied Mechanics*, 1949, pp. 259-268.

31. Hoeppner, D.A., III, Elliot, C.D., and Moesser, M.W., "The Role of Fretting Fatigue on Aircraft Rivet Hole Cracking," FAA report DOT/FAA/AR-96/10, October 1996.

32. Szolwinski, M.P., Harish, G., and Farris, T.N., "Experimental Observation of the Effect of Contact Parameters on Fretting Fatigue Crack Nucleation," *Proceedings of the 1995 USAF Structural Integrity Program Conference*, San Antonio, Texas, 1995.

33. Szolwinski, M.P. and Farris, T.N., "Observation, Analysis and Prediction of Fretting Fatigue in 2024-T352 Aluminum Alloy," *Wear*, Vol. 221, 1998, pp. 24-36.

34. Finney, J.M. and Evans, R.L., "Extending the Fatigue Life of Multi-Layer Metal Joints," *Fatigue and Fracture of Engineering Materials and Structures*, 1995, pp. 1231-1247.

35. Hurricks, P.L., "Mechanism of Fretting," *Wear*, Vol.15, 1970, pp. 389-409.

36. Waterhouse, R.B. and Taylor, D.E., "The Initiation of Fatigue Cracks in a 0.7% Carbon Steel by Fretting," *Wear*, Vol. 17, 1971, pp. 139-147.

37. Nishioka, K. and Hirakawa, K., "Fundamental Investigations of Fretting Fatigue," Part 3, *Bulletin of JSME*, Vol. 12(51), 1969, pp. 397-407.

38. Endo, K. and Goto, H., "Initiation and Propagation of Fretting Fatigue Cracks," *Wear*, Vol. 38, 1976, pp. 311-324.

39. Hills, D.A., Nowell, D., and O'Connor, J.J., "On the Mechanics of Fretting Fatigue," *Wear*, Vol. 125, 1988, pp. 129-146.

40. Iyer, K.A., "Three-Dimensional Finite Element Analyses of the Local Mechanical Behavior of Riveted Lap-Joints," Ph.D. Thesis, Materials Science and Engineering, Vanderbilt University, Nashville, Tennessee, 1997.

41. Nowell, D. and Hills, D.A., "Crack Initiation Criteria in Fretting Fatigue," *Wear*, Vol. 136, 1990, pp. 329-343.

42. Socie, D., "Multiaxial Fatigue Damage Models," *J. Eng. Mater. Technol*., Vol. 109, 1987, pp. 292-298.

43. Socie, D., "Critical Plane Approaches for Multiaxial Fatigue Damage Assessment," in *Advances in Multiaxial Fatigue—ASTM STP 1191*, ASTM, PA, 1993, pp. 7-36.

44. Swalla, D., *Fretting Fatigue Damage Prediction Using Multiaxial Fatigue Criteria*, MS Thesis, Georgia Institute of Technology, Atlanta, Georgia, 1999.

45. Coffin, L.F. Jr., "A Study of the Effects of Cyclic Thermal Stresses on a Ductile Metal," *Trans. ASME*, Vol. 76, 1954, pp. 931-950.

46. Manson, S.S., "Behavior of Materials Under Conditions of Thermal Stress," *Heat Transfer Symposium*, University of Michigan Engineering Research Institute, 1953, pp. 9-75.

47. Walker, K., "The Effect of Stress Ratio During Crack Propagation and Fatigue for 2024-T3 and 7075-T6 Aluminum," *Effects of Environment and Complex Load History on Fatigue Life, ASTM STP 462*, American Society of Testing and Materials, Philadelphia, Pennsylvania, 1970, pp. 1-14.

48. Beuth, J.L. and Hutchinson, J.W., "Fracture Analysis of Multi-Site Cracking in Fuselage Lap Joints," *Computational Mechanics*, Vol. 13, 1994, pp. 315-331.

49. Vlieger, H. and Ottens, H.H., "Uniaxial and Biaxial Tests on Riveted Fuselage Lap Joint Specimens," FAA report DOT/FAA/AR-98/33, October 1998.

50. Fawaz, S.A., Schijve, J., and de Koning, A.U., "Fatigue Crack Growth in Riveted Joints, ICAF 97—Fatigue in New and Aging Aircraft," *Proceedings of the 19th ICAF Symposium*, Edinburgh, UK, Vol. 1, June 18-20, 1997, pp. 553-574.

51. Newman, J.C., Jr. and Raju, I.S., "Stress Intensity Factor Equations for Cracks in Three-Dimensional Finite Bodies Subjected to Tension and Bending Loads," NASATP-85793, 1985.

52. Piascik, R.S., Willard, S.A., and Miller M., "The Characterization of Widespread Fatigue Damage in Fuselage," NASA 95N14920, 1994.

53. Wang, D.Y., "A Study of Small Crack Growth Under Transport Spectrum Loading," AGARD-CP-328, paper 14, 1983, shorter version in ASTM STP 761, American Society for Testing and Materials, 1982, pp. 181-211.

54. Potter, J.M. and Yee, B.G.W., "Use of Small Crack Data to Bring About and Quantify Improvements to Aircraft Structural Integrity," AGARDCP-328, paper 4, 1983.

55. Lucas, F.M., Silva, Goncalves, J.P.M., Oliveira, F.M.F., and de Castro, P.M.S.T., "Multiple Site Damage in Riveted Lap-Joints: Experimental Simulation and Finite Element Prediction," *International Journal of Fatigue*, Vol. 22, 2000, pp. 319-338.

56. Eastaugh, G.F., Simpson, D.L., Straznicky, P.V., and Wakeman, R.B., "A Special Uniaxial Coupon Test Specimen for the Simulation of Multiple Site Fatigue Crack Growth and Link-Up in Fuselage Skin Splices," NASA 96N24261, 1995.

57. Pitt, S. and Jones, R., "Multiple-Site and Widespread Fatigue Damage in Aging Aircraft," *Eng. Failure Anal*., Vol. 4 (4), 1997, pp. 237-257.

58. Schijve, J., "Fatigue of Aircraft Materials and Structures," *Int. J.Fatigue*, Vol. 16 (1), 1994, pp. 21-32.

59. Part 2 of the U.S. National Transportation Safety Board Report on the Fuselage Failure of an Aloha Airlines Boeing 737-200 in April 1988, *Aviation Week and Space Technology*, 4-15 September 1989.

60. Maclin, J.R., "Performance of Fuselage Pressure Structure," *International Conference on Aging Aircraft and Structural Airworthiness*, NASA CP 3160, 1991, pp. 67-74.

61. Liao, M., Shi, G., and Xiong, Y., "Analytical Methodology of Predicting of Predicting Fatigue Life Distribution of Fuselage Splices," *International Journal of Fatigue,* 2001, pp. 177-185.

62. Harris, C.E., Piascik, R.S., and Newman, J.C., "A Practical Engineering Approach to Predicting Fatigue Crack Growth in Riveted Lap Joints," NASA ICAF-CEH, 1999.

63. Hibbitt, Karlsson and Sorensen, Inc., "ABAQUS/Standard 6.3/6.5 User's Manual," Hibbitt, Karlsson and Sorensen, Inc., Pawtucket, Rhode Island, 2003.

64. Li, G. and Sullivan, P.L., "Finite Element and Experimental Studies on Single-Lap-Joints in Tension," *Journal of Adhesion and Adhesives*, Vol. 21, 2001, pp. 211-220.

65. Waterhouse, R.B., "Avoidance of Fretting Fatigue Failures," *Fretting Fatigue*, Applied Science Publishers Limited, 1981, pp. 221-240.

66. Vingsbo, O. and Soderberg, S., "On Fretting Maps," *Wear*, Vol. 126, 1981, pp. 131-147.

67. Ruiz, C., Boddington, P., and Chen, K., "An Investigation of Fatigue and Fretting in Dovetail Joints," *Exp. Mech*., Vol. 24, No. 3, 1984, pp. 208-217.

68. Smith, K.N., Watson, P., and Topper, T.H., "A Stress-Strain Function for the Fatigue of Metals," *J. Mater.,* Vol. 5(4), 1970, pp. 767-778.

69. Harish, G. and Farris, T.N., "Modeling of Skin/Rivet Contact: Application to Fretting Fatigue, *AIAA/ASME/ASCE 38th Structural Dynamics and Materials Conference,* Vol. 4, AIAA/Reston, Virginia, 1997, pp. 2761-2771.

70. Harish, G. and Farris, T.N., "Effect of Fretting Contact Stresses on Crack Nucleation in Riveted Lap Joints," *AIAA,* paper 98-1746, 1998.

71. Harish, G. and Farris, T.N., "An Integrated Approach for Prediction of Fretting Crack Nucleation in Riveted Joints," *AIAA,* paper 99-1340, April 1999.

APPENDIX A—THERMOGRAPHIC STRESS ANALYSIS

To characterize the near-surface response driving fatigue damage, a thermal imaging system capable of capturing sequences of temperature profiles was implemented in conjunction with a fatigue testing setup. The thermographic testing was conducted in collaboration with the research group of Dr. Rami Haj-Ali in the Georgia Institute of Technologies School of Civil Engineering. The experimental procedure used was modeled closely from the work of El-Hajjar [A-1]. The thermal measurements were acquired with a Delta Therm DT 1500 thermoelasticity measurement system, which uses a liquid nitrogen-cooled infrared camera. The Thermographic Stress Analysis (TSA) system operates by recording the temperature change of the specimen under fatigue loading as shown in figure A-1. A focal plane array in the infrared (IR) camera is employed to detect the incident radiant energy emitted from the specimen's surface during testing and convert it to an electrical signal [A-1]. The software in the system coordinates a reference signal from the test frame load cell to ensure that only true temperature changes are monitored. Hundreds of cycles are collected and averaged to improve the signal to noise ratio. To properly track stress states in the material, strain gages or other means should be used to correlate the received IR information to a known stress value.

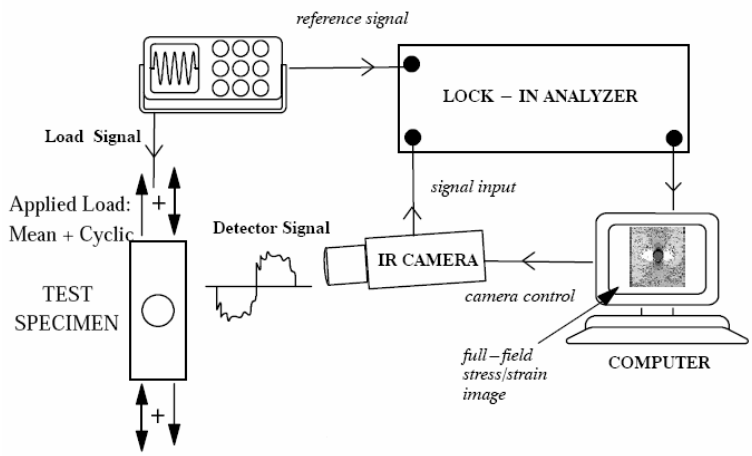


Figure A-1. Schematic TSA System [A-2]

The goal of this investigation was to establish TSA capabilities for such riveted lap joints to detect crack initiation and compare the in-plane strains predicted by the finite element (FE) models to those predicted by the TSA. The test frame employed for these tests was a MTS 810 servohydraulic test system 22.5 kN with 76-mm SURFALLOY grips. The specimens had to be tabbed prior to testing to conform to the larger grips. Also, a thin coat of Krylon Ultra Flat black paint was applied to the surface of the HTCL specimen to cut down on environmental noise and improve surface emissivity. The specimen was then centered in the grips to eliminate off-axis loading and testing was initiated. The IR signal from the coat is measured while the specimen is loaded, and a combined material factor ($k_\varepsilon$), comprised of mechanical and thermal properties, is calibrated such that the measured IR signal can be related to the sum of the in-plane direct strains (equation A-1). The theoretical derivation of this new method assumes adiabatic conditions and applies a thermomechanical theory. Complete details of the derviation can be found in reference A-2.

$$\Delta\varepsilon_{aa} = k_{\varepsilon}S \quad a = 1,2 \tag{A-1}$$

Six specimens were tested at a frequency of 5 Hz. Since the fatigue testing machine employed for the TSA technique was setup for thicker specimens, the amplitude had to be adjusted to obtain the same stress levels (124 MPa) as those applied to the 21 specimens tested in the Material Properties Research Laboratory.

Figure A-2 shows a thermographic image taken at the start of the test (10 cycles). Figure A-3 shows images after 90,000 and 120,000 cycles, respectively. The tips of the cracks are clearly visible in the pictures. For all the tested specimens, the cracks were visible only after 70,000-80,000 cycles. No clear indication of cycles to initiation was obtained. The setup of the specimen dictated a load transfer ratio (LTR) of approximately 50%. This meant that the cracks could initiate on either side, limiting the use of TSA. In one case, the specimen was coated on both sides and thermal images were captured by flipping the specimen after a certain number of cycles.

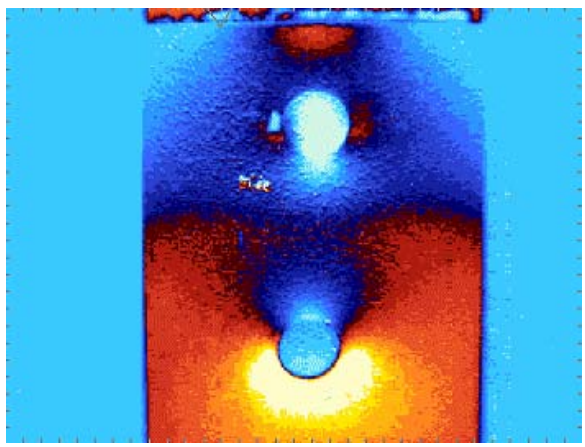

Figure A-2. Thermal Image of Specimen (B26S) After 10 Cycles

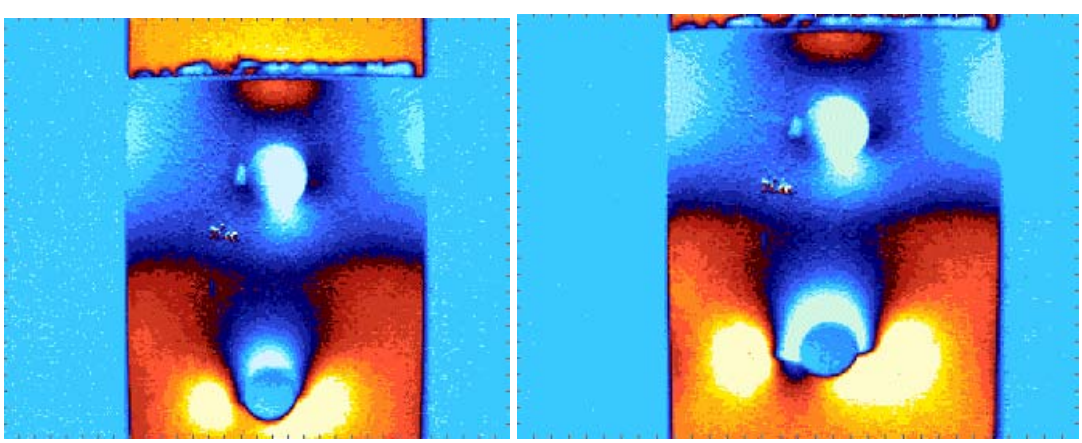

Figure A-3. Thermal Image of Specimen (B26S) After 90,000 Cycles (Left) and 120,000 Cycles (Right) (Tips of the cracks are clearly visible.)

A detailed view of the meshed, symmetric three-dimensional FE model and the applied boundary conditions designed to simulate the specimen is shown in figure A-4. The model, which had 6457 nodes and 3947 elements, was generated using ABAQUS™/CAE 6.4-1 with C38DR, reduced integration, 8-noded linear, solid-brick elements. The process was simulated in three steps: (1) a loading step in which the rivet was deformed to achieve the appropriate driven head size, (2) an unloading step in which the rivet was allowed to springback, and (3) followed by the 124 MPa tensile loads, assuming 50% load transfer. Figure A-5 shows the direction of measurement of surface strains taken to validate with the TSA results.

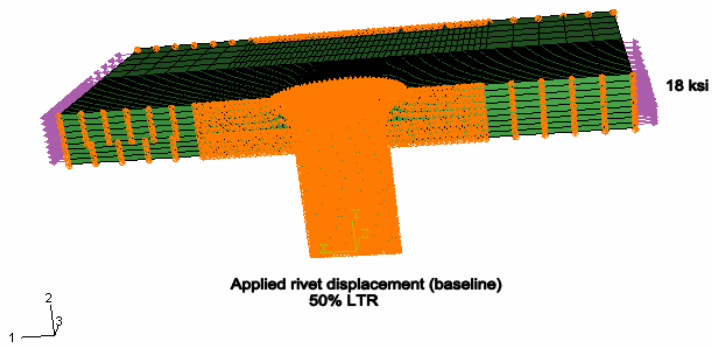


Figure A-4. Finite Element Model of Specimen

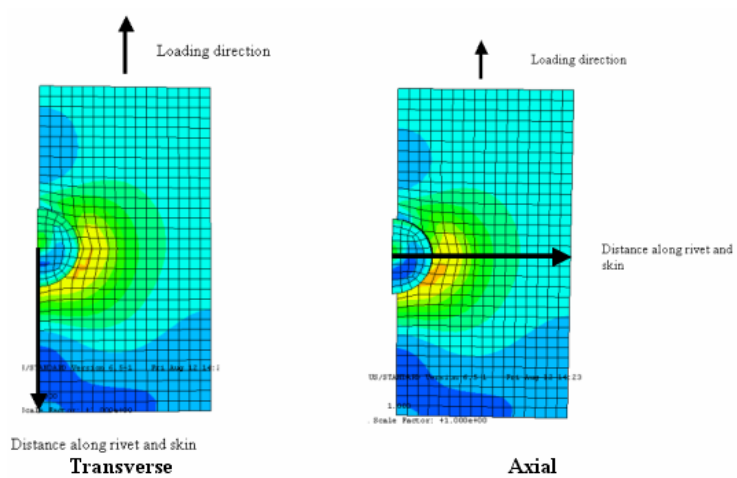


Figure A-5. Direction of Mmeasurement of Strain Values Extracted From the FE Model to Compare to the TSA Predictions

Figure A-6 shows a comparison of the strains from the FE to the TSA for both the transverse and axial directions. The transverse measurement shows a good comparison. A discrepancy can be observed for the axial measurement at the bottom of the rivet head. It is uncertain whether the inaccuracies in the FE modeling or the TSA or both are responsible for the observed discrepancy.

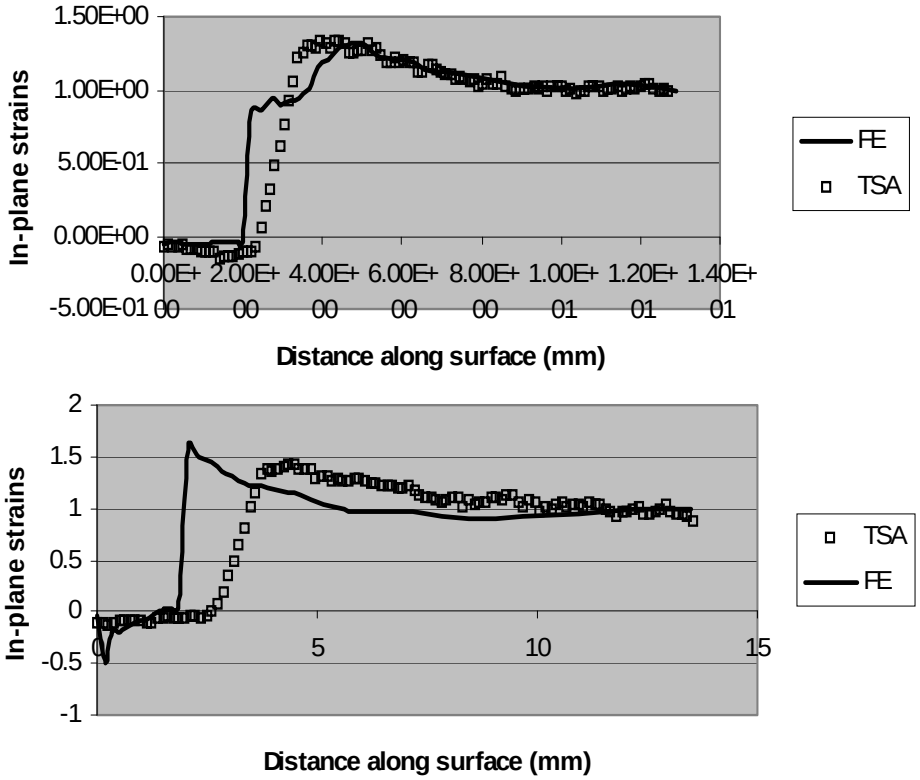


Figure A-6. Comparison of the Surface Strains Predicted by the FE Model to Those Measured by the TSA (Transverse Direction (Top) and Axial (Bottom))

REFERENCES.

A-1. El-Hajjar, R.F., "Experimental Study and Analytical Modeling of Translayer Fracture in Pultruded FRP Composites," Ph.D. Thesis, Georgia Institute of Technology, Atlanta, Georgia, 2004.

A-2. Carter, R., "Assessment of Hole Drilling Procedures on Resulting Fatigue Lives," M.S. Thesis, Georgia Institute of Technology, Atlanta, Georgia, 2003.

APPENDIX B—SOME MODELING CONSIDERATIONS

Different analyses techniques were attempted for the riveting models and their solutions were compared. An analysis conducted with full integration assumed for the linear elements showed no difference in the stress solution but consumed twice the run time required for the analysis with reduced integration. An analysis conducted with fixed time incrementation failed to converge even for time increments as low as 6.25e-03. Automatic time incrementation should always be applied for such nonlinear problems. A three-dimensional, force-controlled riveting model was simulated at the National Research Council, Canada using MSC.MARC near the end of this work [B-1]. This model was an extension of the axisymmetric analysis [B-2] conducted by the same researchers (figure B-1). The model had 5560 linear reduced integration elements and 7431 nodes (figure B-2). Three steps were defined in the analysis: (1) a range of squeeze forces from 35.59 kN to 53.39 kN was applied with a rigid pusher to the rivet head, (2) the force was then reduced to zero (unload), and (3) 98.5 MPa of joint tensile loading was then applied at the right end.

It is very interesting to note that the same analysis conducted in ABAQUS™ with 32,186 reduced integration linear elements and 43,468 nodes failed to converge in the third (tensile loading) step (figure B-3). The analysis aborted at the same time increment for the range of applied squeeze forces. It was ensured that the contact areas near the rivet hole had a much finer mesh. Stabilization techniques were also attempted but did not show any success. Equivalent displacement control loading was implemented to replace the force-control loading, but the analysis still did not converge. The skin-skin bending during the tensile loading stage led to excessive penetration of the skin surfaces near the rivet holes, causing ABAQUS to cut back and abort.

The analysis can be attempted with a much more refined mesh for the upper skin, especially for the sharp countersunk edge along with automatic tolerances to obtain convergence. This analysis, however, would require more powerful computing facilities and, hence, was not attempted in this study.

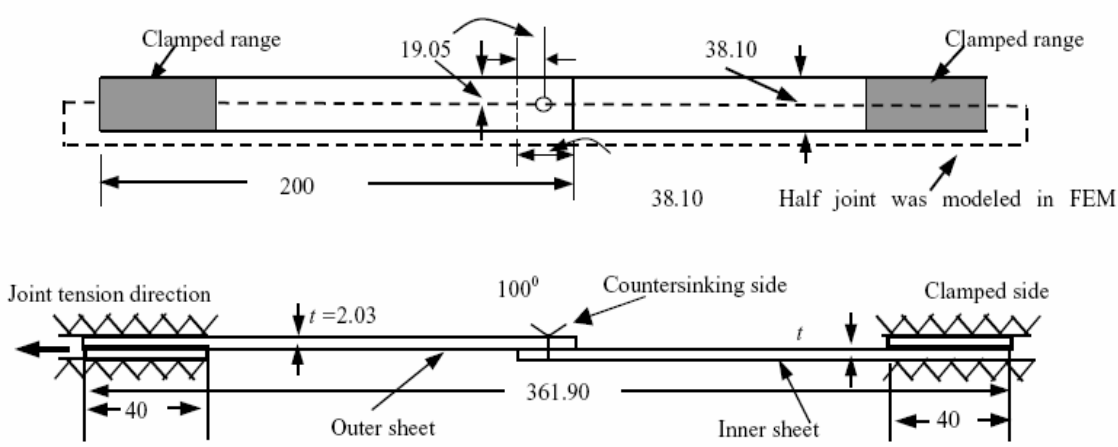


Figure B-1. Geometric Configuration of Rivited Joint Analyzed by Li, et al. [B-1]

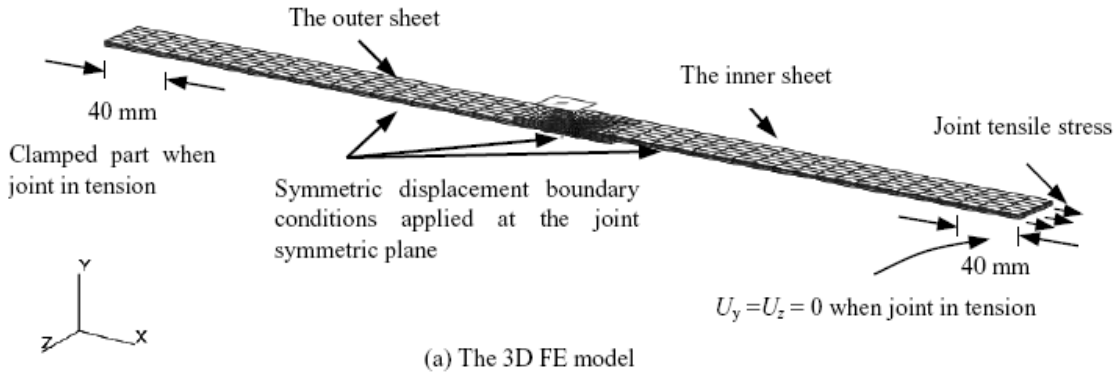


Figure B-2. Finite Element Model and BCs of the Three-Dimensional Riveted Joint Model Analyzed by Li, et al. [B-1]

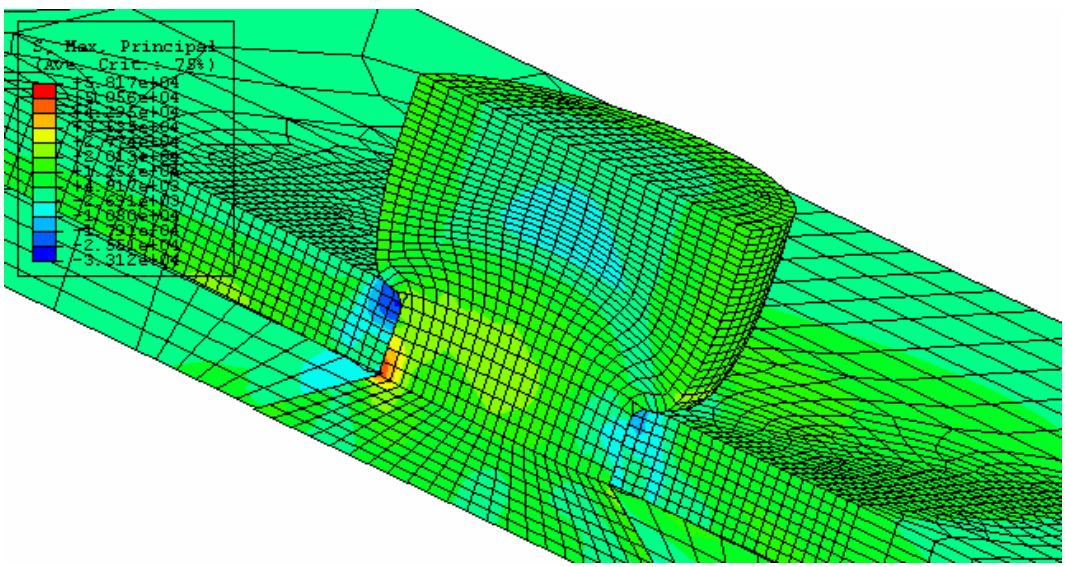


Figure B-3. Same Model Analyzed in ABAQUS
(The picture shows the stress state for a solution that aborted at a time increment of 0.27 in the tensile loading stage.)

REFERENCES.

B-1. Li, G., Shi, G., and Bellinger, N.C., "Studies of Residual Stress in Single-Row Countersunk Riveted Lap Joints," *46th AIAA Structures, Structural Dynamics and Materials Conference*, 18-21 April 2005, Austin, Texas, AIAA 2005-2024.

B-2. Li, G. and Shi, G., "Effect of the Riveting Process on the Residual Stress in Fuselage Lap Joints," *Canadian Aeronautics and Space Journal*, Vol. 50, No. 2, 2003, pp. 91-105.

# APPENDIX C—ABAQUS CAPABILITIES

The ABAQUS™ [C-1] finite element code was chosen to perform all the simulations conducted throughout these investigations. ABAQUS is a general-purpose code that has been successfully implemented to solve a wide variety of problems in the areas of structural analysis and other disciplines of mechanical engineering. Additionally, ABAQUS allows certain interactions among multiple engineering disciplines, such as thermal-electrical and thermal-structural coupled-field problems. This appendix provides highlights of the workings of the code [C-1], including its element library, contact capabilities, material constitutive behaviors, and nonlinear solution capabilities. Particular emphasis is placed on the specific qualities of the code with regard to correctly accounting for the structural phenomena that comprise the simulations conducted in this work.

## C.1 ELEMENT LIBRARY.

A wide range of elements are available in ABAQUS. This extensive element library provides the user with a powerful set of tools for solving many different problems. Each element in ABAQUS is characterized by family, degrees of freedom, number of nodes, formulation, and integration.

Family refers to the element in a particular type of analysis, such as continuum (solid), beam, shell, thermal, and spring. Degrees of freedom are the fundamental variables calculated in the analysis. These might be translations in the 1,2,3 directions for a structural analysis or temperature for a heat transfer analysis. The number of nodes of an element determines the order of interpolation. The variables in the analysis are computed at the nodes of the element. At any other point in the element, the variables are interpolated. Elements that have nodes only at the corners, such as an 8-noded brick, use linear interpolation in each direction. Such elements are called linear or first-order elements. Elements that have midside nodes in addition to the nodes at the corners, such as a 20-noded brick element, use quadratic interpolation in each direction. Such elements are called quadratic or second-order elements. An element's formulation refers to the mathematical theory used to define the element's behavior. All of the stress/displacement elements in ABAQUS are based on the Lagrangian or material description of behavior: the material associated with an element remains associated with the element throughout the analysis, and material cannot flow across element boundaries. In the alternative, Eulerian or spatial description, elements are fixed in space as the material flows through them. ABAQUS uses numerical techniques to integrate various quantities over the volume of each element. Using Gaussian quadrature for most elements, ABAQUS evaluates the material response at each integration point in each element. When using continuum elements, the user must choose between full or reduced integration, a choice that can have a significant effect on the accuracy of the element for a given problem. An example of a continuum element in ABAQUS is shown in figure C-1.

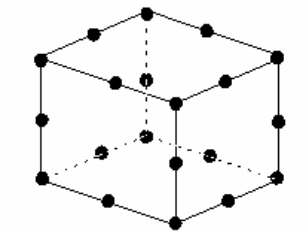

Figure C-1. C3D20 Continuum Element in ABAQUS [C-1]

C.2 CONTINUUM ELEMENTS.

Continuum or solid elements can be used to model a wide variety of components. Continuum elements model small blocks of material in any component. This stress/displacement family of elements is one of the most comprehensive element libraries available in ABAQUS. For three-dimensional (3D) elements, the user has a choice of hexahedrons, tetrahedrons, and wedges; for two-dimensional elements, the choice is between triangles and quadrilaterals. There are linear and quadratic versions for each of these basic element shapes. The user has a choice between full and reduced-integration elements for hexahedrons and quadrilaterals.

C.3 ELEMENT INTEGRATION.

The expression "full integration" refers to the number of Gauss points required to integrate the polynomial terms in an element's stiffness matrix exactly when the element has a regular shape as shown in figure C-2(a). A regularly shaped hexahedral or quadrilateral element is one in which: the edges of the element are straight, the edges meet at right angles, and any edge nodes are at midpoint of the edge. Fully integrated linear elements use two integration points in each direction, while quadratic elements use three integration points in each direction. Reduced integration can only be used with quadrilateral and hexahedral elements (figure C-2(b)). Reduced integration linear elements have one integration point located at the centroid of the element.

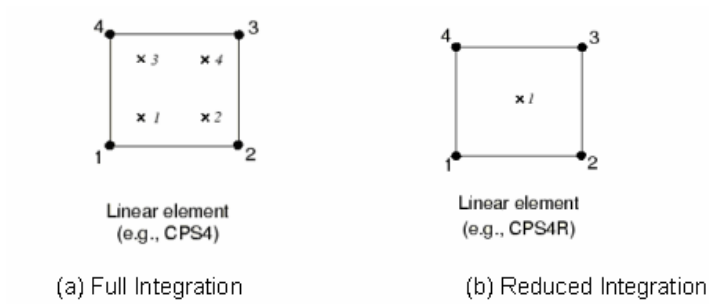


Figure C-2. Integration Points in Two-Dimensional Linear Elements [C-1]

## C.4 ELEMENT TYPES AND SELECTION.

Table C-1 gives an overview of the continuum elements available in ABAQUS for structural analysis. Based on this overview, particular solid elements are chosen and discussed in light of the specific needs of this investigation.

Table C-1. ABAQUS Solid Element Types

| Element | Description | Active DOF |
|---|---|---|
| CPE3 | 3-node linear plane strain | 1,2 |
| CPE6 | 6-node quadratic plane strain | 1,2 |
| CPS3 | 3-node linear plane stress | 1,2 |
| CPS6 | 6-node quadratic plane stress | 1,2 |
| C3D4 | 4-node linear tetrahedron | 1,2,3 |
| C3D6 | 6-node linear triangular prism | 1,2,3 |
| C3D8 | 8-node linear brick | 1,2,3 |
| C3D10 | 10-node quadratic tetrahedron | 1,2,3 |
| C3D15 | 15-node quadratic triangular prism | 1,2,3 |
| C3D20 | 20-node quadratic brick | 1,2,3 |
| CAX3 | 3-node linear axisymmetric | 1,2 |
| CAX4 | 4-node bilinear axisymmetric | 1,2 |
| CAX6 | 6-node quadratic axisymmetric | 1,2 |

DOF = Degree of Freedom

### C.4.1 CHOOSING BETWEEN FIRST- AND SECOND-ORDER ELEMENTS.

The continuum elements in ABAQUS can be used for linear analysis and for complex nonlinear analyses involving contact, plasticity, and large deformations. In first-order plane strain, generalized plane strain, axisymmetric quadrilateral, hexahedral solid elements, and cylindrical elements, the strain operator provides constant volumetric strain throughout the element. This constant strain prevents mesh "locking" when the material response is approximately incompressible. The fully integrated elements (such as C3D8) exhibit shear locking (excessive stiffness in bending), and hence, should be avoided for bending dominated problems. The reduced integration elements exhibit hourglassing (no stiffness in bending). A refined mesh of the reduced integration elements should be used for bending dominated problems to obtain accurate results.

Second-order elements in ABAQUS provide several features, including: (1) higher accuracy than first-order elements for problems that do not involve complex contact conditions, impact, or severe element distortions, (2) effective representation of stress concentrations, and (3) effective modeling of curved surfaces with fewer elements. The fully integrated elements (such as C3D20) do not exhibit shear locking, as their edges are able to curve, hence avoiding the formation of spurious shear stresses. The reduced integrated elements also show hourglassing, but using a sufficiently refined mesh produces accurate results.

First-order triangular and tetrahedral elements are overly stiff and exhibit slow convergence with mesh refinement. A fine mesh may be needed to obtain results of sufficient accuracy. ABAQUS provides a modified version of these triangular and tetrahedral elements (such as C3D10M). They are recommended for contact problems because the contact forces are consistent with the direction of contact. These elements also perform better in analyses involving impact, in analyses involving nearly incompressible material response, and in analyses requiring large element distortions.

### C.4.2 CHOOSING BETWEEN FULL AND REDUCED INTEGRATION ELEMENTS.

Reduced integration uses a lower-order integration to form the element stiffness. Solution run time can be drastically decreased with reduced-integration elements, especially for 3D problems. For example, an analysis with C3D20 element, which has 27 integration points versus the C3D20R element that has only 8; element assembly is approximately 3.5 times more costly for the former. The user can choose between full and reduced-integration only for quadrilateral and hexahedral elements. First-order, reduced-integration elements, such as C3D8R, can display hourglassing. This means that the elements can distort in such a way that the computed strains at the single integration point are zero. This leads to uncontrolled mesh distortion. These elements do have the capability of hourglass control, but this is effective only with fine meshes.

Second-order, reduced-integration elements (excluding C3D27R and C3D27RH) do not have the same difficulty and can be used in all cases when the solution is expected to be smooth. First-order elements should be used when large strains or very high strain gradients are expected.

In ABAQUS, the fully integrated elements do not exhibit hourglassing. However, they might display shear or volumetric locking. Shear locking is possible in first-order, fully integrated elements subjected to bending. The internal formulation of these elements causes spurious shear strains, making the elements too stiff in bending. For problems involving incompressibility in the solution, second-order, fully integrated elements may exhibit volumetric locking when the plastic strains are on the order of the elastic strains. The first-order, fully integrated quadrilaterals and hexahedra use reduced integration on the volumetric terms and do not lock with almost incompressible materials. Reduced-integration, second-order elements exhibit volumetric locking for almost incompressible materials only after significant straining occurs. Volumetric locking can be accompanied by hourglassing in such cases. A refined mesh in the regions of high plastic strains may resolve the issue.

### C.4.3 CHOOSING BETWEEN QUADRILATERAL, TRIANGULAR, AND TETRAHEDRAL ELEMENTS.

Many automatic-meshing algorithms use triangular and tetrahedral elements because of their versatility. These elements increase user convenience to mesh complex shapes. However, a solution obtained from these elements is very costly compared to using hexahedra. Some other advantages that quadrilaterals and hexahedra offer in comparisons to triangles and tetrahedra are better convergence rate and less sensitivity to mesh orientation. However, triangles and tetrahedra are less sensitive to initial element shape, whereas first-order quadrilaterals and hexahedra perform better if their shape is approximately rectangular. The elements become much less accurate when they are initially distorted. Fully integrated, first-order triangles and

tetrahedra also exhibit volumetric locking. The recommended use of these elements is only as a filler material.

The modified elements display much better performance in complex analyses. However, they are more expensive computationally than lower-order quadrilaterals and hexahedra. They may sometimes require a more refined mesh for the same level of accuracy. In ABAQUS/Explicit they are provided as an attractive alternative to the lower-order triangles and tetrahedron to take advantage of automatic triangular and tetrahedral mesh generators. One more disadvantage of the modified triangular and tetrahedral elements is incompatibility with the regular second-order solid elements in ABAQUS/Standard, and hence, these elements should not be connected together in a mesh.

### C.4.4 HYBRID ELEMENTS.

Hybrid elements are available only in ABAQUS/Standard. Their primary purpose is to model incompressible and almost incompressible material behavior. When the material response is incompressible, the solution to a problem cannot be obtained in terms of the displacement history only, since a purely hydrostatic pressure can be added without changing the displacements. Linear elastic materials, which have a bulk modulus much greater than the shear modulus, exhibit nearly incompressible material behavior. Extremely large changes in pressure are obtained with small variations in displacements. A pure displacement solution in this case is numerically very sensitive to problems such as computer round-off errors. Hence, the stress caused by the pressures is treated as an independently interpolated basic solution variable coupled to the displacement solution through constitutive and compatibility conditions. This internal formulation forms the groundwork for hybrid elements. Since these elements have more internal variables, they are more computationally expensive.

### C.4.5 CHOOSING ELEMENTS FOR PROBLEMS WITH PLASTICITY.

Incompressibilty imposed by plasticity in metals limits the type of elements that can be used for elastic-plastic simulations. This limitation arises from the kinematic constraint imposed on element behavior, namely, constrainment of constant volume at the element integration point. In some cases, this actually makes the element overconstrained. Elements that cannot resolve this contraint suffer from volumetric locking, that is, overly stiff response. Fully integrated, second-order, solid elements are very susceptible to volumetric locking in elastic-plastic simulations. The ABAQUS fully integrated, first-order, solid elements do not suffer from volumetric locking because ABAQUS actually uses a constant volume strain in these elements. Reduced-integration, solid elements have fewer integration points at which the incompressibility constraints must be satisfied. Therefore, they are not overconstrained and can be used for most elastic-plastic simulations. In simulations with plastic strains exceeding 20%-40% second-order, reduced integration elements should be used cautiously and with fine meshes.

### C.4.6 RIGID BODIES.

In ABAQUS, a rigid body is a collection of nodes and elements whose motion is governed by the motion of a single node, known as the rigid body reference node. The shape of the rigid body is defined as an analytical surface or discrete rigid body. The analytical surface is obtained by

revolving or extruding a two-dimensional geometric profile. A discrete rigid body is obtained by meshing the component with nodes and elements. The shape of the rigid body remains constant during an analysis. The body can undergo large rigid body motions. Computation of mass and inertia for a discrete rigid body can be based on contributions from its elements. It can also be assigned specifically.

Boundary conditions governing the motion of a rigid body are applied to the rigid body reference node. Contact and nodal connections are used for interaction of rigid bodies and deformable elements. Rigid bodies are typically used to model very stiff components. These components may be fixed or undergoing large rigid body motions. In forming analyses, rigid bodies are an excellent choice for modeling components such as punches, dies, and rollers. The computational efficiency provided by rigid bodies is the primary reason for choosing them above deformable elements. Element-level computations are avoided, and relatively small effort is required to update the motion of the nodes and assemble concentrated/distributed loads.

## C.4.7 MATERIAL MODELS.

The material library in ABAQUS allows most engineering materials to be modeled, including metals, plastics, rubbers, foams, composites, granular soils, rocks, and plain and reinforced concrete. This section only discusses three of the most commonly used material models: linear elasticity, metal plasticity, and rubber elasticity.

## C.4.8 CLASSICAL METAL PLASTICITY.

The yield and inelastic flow of a metal at relatively low temperatures, where creep effects are not important and loading is relatively monotonic, can typically be described with the classical metal plasticity. Standard von Mises or Hill yield surfaces with associated plastic flow are implemented in ABAQUS for this purpose. Perfect plasticity and isotropic hardening definitions are both available in the classical metal plasticity models. The von Mises and Hill yield surfaces assume that yielding of the metal is independent of the equivalent pressure stress. The von Mises yield surface is used to define isotropic yielding. It is defined by giving the value of the uniaxial yield stress as a function of uniaxial equivalent plastic strain, temperature, and field variables on the data lines or by defining the yield stress in user subroutines.

The Hill yield surface allows anisotropic yielding to be modeled. A reference yield stress must be given, and the user must define a set of yield ratios. ABAQUS provides two types of work hardening: perfect plasticity and isotropic hardening. In perfect plasticity, the yield stress does not change with plastic strain, while isotropic hardening means the yield surface changes size uniformly in all directions such that the yield stress increases (or decreases) in all stress directions as plastic straining occurs.

If isotropic hardening is defined, the yield stress can be defined in tabular form or described through user subroutines. If the tabular form is used, the yield stress must be given as a tabular function of plastic strain and, if required, of temperature or other predefined field variables. The yield stress at a given state is simply interpolated from this table of data, and it remains constant for plastic strains exceeding the last value given as tabular data. Associated plastic flow is used. Therefore, as the material yields, the inelastic deformation rate is in the direction of the normal to

the yield surface (the plastic deformation is volume invariant). ABAQUS optionally allows for plastic dissipation to result in the heating of a material. The option is typically used in the simulation of bulk metal forming or high-speed manufacturing processes involving large amounts of inelastic strain where the heating of the material caused by its deformation is an important effect. The option is applicable only to adiabatic thermal stress analysis or fully coupled temperature-displacement analysis. Only a von Mises yield surface can be used in an adiabatic analysis.

When defining plasticity data in ABAQUS, the user must provide true stress and true strain. ABAQUS requires these values to interpret the data in the input file correctly. ABAQUS approximates the smooth stress-strain behavior of the material with a series of straight lines joining the given data points. Any number of points can be used to approximate the actual material behavior; therefore, it is possible to use a very close approximation of the actual material behavior. The material data defines the true yield stress of the material as a function of true plastic strain. The first piece of data given defines the initial yield stress of the material and, therefore, should have a plastic strain value of zero.

C.4.9 HYPERELASTICITY.

The hyperelastic material model is isotropic and nonlinear. The material model is valid for materials that exhibit instantaneous elastic response up to large strains. Rubbers and elastomers are typical examples of materials that are modeled with hyperelastic formulation. This model requires the use of nonlinear geometry since it is intended for finite strain applications. The shear flexibility of most elastomers is large compared to its compressibility. In applications where the material is not highly confined, it is quite satisfactory to assume that the material is fully incompressible. In cases where the material is highly confined, the compressibility must be modeled correctly to obtain accurate results.

The hyperelastic material model can be used with continuum elements. For continuum elements, hyperelasticity can be used with the pure displacement formulation elements or with the hybrid (mixed formulation) elements. Because elastomeric materials are usually almost incompressible, fully integrated pure displacement method elements are not recommended for use with this material, except for plane stress cases. If fully or selectively reduced-integration displacement method elements are used with the almost incompressible form of this material model, a penalty method is used to impose the incompressibility constraint in anything except plane stress analysis. The penalty method can sometimes lead to numerical difficulties; therefore, the fully or selectively reduced-integrated hybrid formulation elements are recommended for use with hyperelastic materials.

ABAQUS describes hyperelastic materials in terms of a "strain energy potential," $U(\varepsilon)$, which defines the strain energy stored in the material per unit of reference volume (volume in the initial configuration) as a function of the strain at that point in the material. There are several forms of strain energy potentials available in ABAQUS to model approximately incompressible isotropic elastomers: the Arruda-Boyce form, the Mooney-Rivlin form, the neo-Hookean form, the Ogden

form, the polynomial form, the reduced polynomial form, the Yeoh form, and the Van der Waals form. The polynomial form of the strain energy potential is most commonly used. Its form is

$$U = \sum_{i+j=1}^{N} C_{ij}(\overline{I_1} - 3)^i (\overline{I_2} - 3)^j + \sum_{i=1}^{N} \frac{1}{D_i}(J_{el} - 1)^{2i} \tag{C-1}$$

where $U$ is the strain energy potential; $J_{el}$ is the elastic volume ratio; $\bar{I}_1$ and $\bar{I}_2$ are measures of the distortion in the material; and $N$, $C_{ij}$, and $D_i$ are material parameters, which may be functions of temperature. The $C_{ij}$ parameters describe the shear behavior of the material, and the $D_i$ parameters introduce compressibility. All zero values for $D_i$ means that the material is fully incompressible. If the number of terms, $N$, is one, the initial shear modulus, $\mu_0$ , and bulk modulus, $K_o$, are given by

$$\mu_0 = 2(C_{01} + C_{10}) \text{ and } K_0 = \frac{2}{D_1} \tag{C-2}$$

If the material is also incompressible, the equation for the strain energy density is

$$U = C_{10}(\overline{I_1} - 3) + C_{01}(\overline{I_2} - 3) \tag{C-3}$$

This expression is commonly referred to as the Mooney-Rivlin material model. If $C_{01}$ is also zero, the material is called neo-Hookean.

The user must provide ABAQUS with the relevant material parameters to use a hyperelastic material. For the polynomial form, these are $N$, $C_{ij}$ , and $D_i$. ABAQUS can also accept test data directly and calculate the material parameters using a least squares fit. The experimental tests for which ABAQUS can fit data are Uniaxial tension and compression, Equibiaxial tension and compression, Planar tension and compression (pure shear), and Volumetric tension and compression. Unlike plasticity data, the test data for hyperelastic materials must be given to ABAQUS as nominal stress and nominal strain values. Volumetric compression data only need to be given if the material's compressibility is important.

The quality of the results from a simulation using hyperelastic materials strongly depends on the material test data provided to ABAQUS. It is common for the material model determined from the test data to be unstable at certain strain magnitudes. ABAQUS performs a stability check to determine the strain magnitudes where there is unstable behavior. The user should check this information carefully since the simulation may not converge if any part of the model experiences strains beyond the stability limits. The stability checks are done for specific deformations, so it is possible for the material to be unstable at the strain levels indicated if the deformation is more complex. Likewise, it is possible for the material to become unstable at lower strain levels if the deformation is more complex.

C.4.10 NONLINEAR ANALYSIS.

A nonlinear structural problem is one in which the structure's stiffness changes as it deforms. In a nonlinear analysis, the stiffness matrix of the structure has to be assembled and inverted many times during the course of the analysis, making it much more expensive to solve than a linear analysis. Since the response of a nonlinear system is not a linear function of the magnitude of the applied load, superposition cannot be applied to obtain the solution. Each load case must be defined and solved as a separate analysis.

There are three sources of nonlinearity in structural mechanics simulations:

- Material nonlinearity: Most metals have a fairly linear stress-strain relationship at low strain values, but at higher strains, the material yields, at which point the response becomes nonlinear and irreversible.

- Boundary nonlinearity: This occurs if the boundary conditions change during the analysis. Boundary nonlinearities are extremely discontinuous when (1) contact occurs during a simulation and (2) there is a large and instantaneous change in the response of the structure.

- Geometric nonlinearitiy: Geometric nonlinearity occurs whenever the magnitude of the displacements affects the response of the structure. This may be caused by large deflections or rotations, snap through, and initial stresses or load stiffening. If the deflection is small, the analysis can be considered as being approximately linear. However, if the deflections are large, the shape of the structure and, hence, its stiffness changes. In addition, if the load does not remain perpendicular to the structure, the action of the load on the structure changes significantly. Both of these effects contribute to the nonlinear response of the structure. Incorporating the effects of geometric nonlinearity in an analysis requires only minor changes to the input file. The user just needs to add the NLGEOM parameter to the *STEP option.

C.4.11 SOLUTION OF NONLINEAR ANALYSIS.

The nonlinear load-displacement curve for a structure is shown in figure C-3.

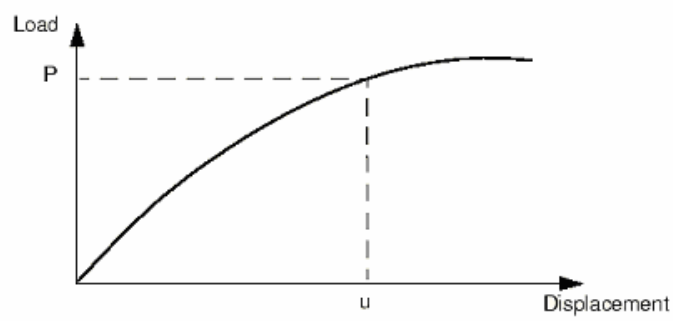


Figure C-3. Nonlinear Load-Displacement Curve [C-1]

ABAQUS implements the Newton-Raphson method to obtain solutions for nonlinear problems. In a nonlinear analysis, the solution cannot be calculated by solving a single system of equations, as in a linear problem. Instead, the solution is found by applying the specified loads gradually and incrementally working toward the final solution. Therefore, ABAQUS breaks the simulation into a number of load increments and finds the approximate equilibrium configuration at the end of each load increment. It often takes ABAQUS several iterations to determine an acceptable solution to a given load increment. The sum of all the incremental responses is the approximate solution for the nonlinear analysis.

Consider the external forces, $P$, and the internal (nodal) forces, $I$, acting on a body (figure C-4). The internal loads acting on a node are caused by the stresses in the elements that contain the node. For the body to be in equilibrium, the net force acting at every node must be zero. Therefore, the basic statement of equilibrium is that the internal and external forces must balance each other: $P\text{-}I = 0$.

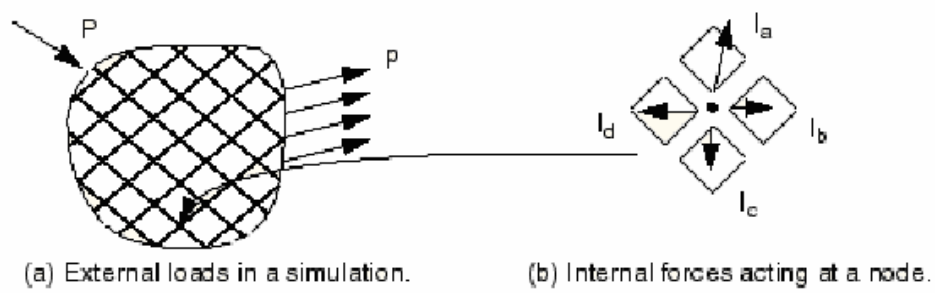


Figure C-4. Internal and External Loads on a Body [C-1]

It is important for the user to understand the difference between an analysis step, a load increment, and iteration. The load history for a simulation consists of one or more steps. The user defines the steps, which generally consist of an analysis procedure and loading. Different BCs and analysis procedure options can be specified in each step. An increment is part of a step. In nonlinear analyses, the total load applied in a step is broken into smaller increments so that the nonlinear solution path can be followed. The user suggests the size of the first increment, and ABAQUS automatically chooses the size of the subsequent increments. At the end of each increment, the structure is in (approximate) equilibrium. An iteration is an attempt at finding an equilibrium solution in an increment. If the model is not in equilibrium at the end of the iteration, ABAQUS tries another iteration. With every iteration, the solution ABAQUS obtains should be closer to equilibrium; sometimes ABAQUS may need many iterations to obtain an equilibrium solution. When an equilibrium solution has been obtained, the increment is complete. The nonlinear response of a structure to a small load increment, $\Delta P_0$, is shown in figure C-5. ABAQUS uses the structure's initial stiffness, $\Delta K_0$, which is based on its configuration at $u_0$ and $\Delta P$ to calculate a displacement correction, $c_a$, for the structure. Using $c_a$, the structure's configuration is updated to $u_a$.

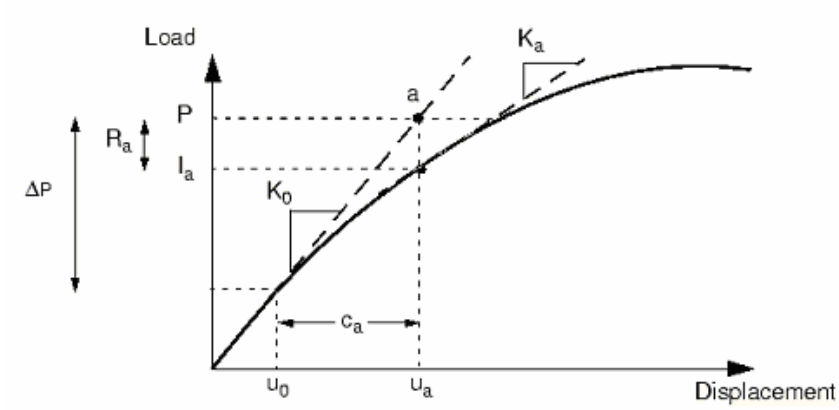


Figure C-5. First Iteration in an Increment [C-1]

ABAQUS forms a new stiffness, $K_a$, for the structure, based on its updated configuration, $u_a$. ABAQUS also calculates the structure's internal forces, $I_a$, in this updated configuration. The difference between the total applied load, $P$, and $I_a$ can now be calculated as $R_a = P - I_a$, where $R_a$ is the force residual for the iteration. At every degree of freedom in the model, if $R_a$ becomes zero, point $a$ in figure C-5 would lie on the load-deflection curve, and the structure would be in equilibrium. In a nonlinear problem, it is almost impossible to have $R_a$ equal zero. Hence, ABAQUS compares the computed value to an initial tolerance. If $R_a$ is less than this force residual tolerance, ABAQUS accepts the structure's updated configuration as the equilibrium solution. This tolerance value is set to 0.5% of an average force in the structure, averaged over time. The spatially and time averaged force are automatically computed during the analysis. If $R_a$ is less than the current tolerance value, $R_a$ and $P_a$ are in equilibrium, and $R_a$ is a valid equilibrium configuration for the structure under the applied load. This, however, is not the only check performed by ABAQUS. The code also checks that the displacement correction, $c_a$, is small, relative to the total incremental displacement, $\Delta u = u_a - u_0$. Both convergence checks must be satisfied before a solution is said to have converged for that load increment. The exception to this rule is a linear increment, which is defined as any increment in which the largest force residual is less than $10^{-8}$ times the time-averaged force. Another (or several) iterations may be performed by ABAQUS if the solution from the iteration does not converge. This second iteration uses the stiffness, $K_a$, calculated at the end of the previous iteration together with $R_a$ to determine another displacement correction, $c_b$ that brings the system closer to equilibrium.

For each iteration in a nonlinear analysis, the model stiffness matrix needs to be assembled and a system of equations needs to be solved. Each iteration is equivalent to conducting a complete linear analysis. For ease and efficient solution of nonlinear problems, ABAQUS automatically adjusts the size of the load increments. Only an initial increment is suggested by the user. ABAQUS applies all the loads defined in the first increment if no initial increment size is suggested by the user. For problems with dominant nonlinearity, ABAQUS will have to reduce the increment size repeatedly, resulting in wasted computer processing time. Hence, the user should provide a reasonable initial increment size.

The number of iterations needed to find a converged solution for a load increment will vary, depending on the degree of nonlinearity in the system. If the solution has not converged within 16 iterations, or if the solution appears to diverge, ABAQUS abandons the increment and starts again with the increment size set to 25% of its previous value. ABAQUS then attempts to find a solution with this smaller increment. This increment size is reduced repeatedly, in case ABAQUS fails to obtain convergence. A maximum of five reductions of increment size for each increment is performed before the analysis aborts.

The user may also add the INC parameter to specify the maximum number of increments allowed during the step. ABAQUS terminates the analysis if more than the set-limit number of increments is needed to complete the step. The default number of increments for a step is 100, but if significant nonlinearity is present in the simulation, the analysis may require more increments.

In a nonlinear analysis, a step takes place over a finite period of time. This time has no physical meaning in a purely static solution (without inertial effects or rate-dependent behavior). The data line on the procedure option used in the step specifies the initial time increment and the total time for the step. For example

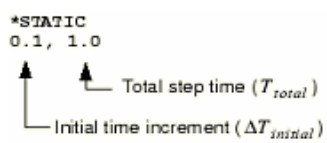


defines a static analysis that occurs over 1.0 unit of time and has an initial increment of 0.1. These data also specify the proportion of load applied in the first increment. The initial load increment is given by:

$$\frac{\Delta T_{initial}}{T_{total}} \times \text{Load magnitude}$$

The choice of initial time increment can be critical in certain nonlinear simulations, but for most analyses, an initial increment size that is 5% to 10% of the total step time is usually sufficient. The total step time is set to 1.0 in static simulations. With this time, 50% of the total load is applied when the step time is 0.5. An analysis is terminated if a large number of cutbacks (due to convergence problems) reduce the increment size below the minimum allowable time increment, $\Delta T_{\min}$, which is $10^{-5}$ times the total step time. The user may want to specify different minimum or maximum allowable increment sizes on the basis of the problem under consideration.

C.4.12 LINEAR EQUATION SOLVERS.

Linear equation solution in ABAQUS is obtained by direct Gauss elimination method using a sparse solver. This part of the analysis is often the most time-consuming. A large part of disk space is consumed by the storage of the equations. If the system of equations has a sparse

structure, a multifront technique is used that reduces the computational time. The sparse solver can be executed in parallel to reduce the solution time for large problems.

C.4.13 BOUNDARY NONLINEARITY.

Many engineering problems involve contact between two or more components. In these problems, a force normal to the contacting surfaces acts on the two bodies when they touch each other. If there is friction between the surfaces, shear forces may be created that resist the tangential motion (sliding) of the bodies. Contact simulations are typically conducted to identify the areas on the surfaces that are in contact and to calculate the contact pressures generated.

Contact conditions are a special class of discontinuous constraint, because forces are applied only when the two surfaces are in contact. When the two surfaces separate, no constraint is applied. The finite element code has to be able to detect when two surfaces are in contact. Then it must apply the required constraints. It must also detect separation of surfaces and enforce subsequent removal of constraints.

The distance separating two surfaces is called the clearance. With zero clearance between the surfaces, the contact constraint is applied. There is no limit in the contact formulation on the magnitude of contact pressure that can be transmitted between the surfaces. The contact constraint is removed when the contact pressure between the surfaces becomes zero or negative. This surface interaction behavior is referred to as hard contact.

The change in contact pressure that occurs when a contact condition changes from open (positive clearance) to closed (clearance equal to zero) sometimes makes it difficult to complete contact simulations. In contact simulations, ABAQUS should detect contact at a particular point and calculate sliding between the two contacting surfaces. Since this is a complex computation, ABAQUS separates simulations based on the magnitude of sliding, namely small-sliding analysis or finite-sliding analysis. Small sliding is difficult to define, but it is typically used to refer to problems where a point contacting a surface does not slide more than a small fraction of a typical element dimension. This is a relatively less expensive computation.

ABAQUS establishes the relationship between the slave nodes and the master surface at the beginning of the simulation, as in the small-sliding analysis case. ABAQUS determines which segment on the master surface will interact with each node on the slave surface. It maintains these relationships throughout the analysis, never changing which master surface segments interact with which slave nodes. If geometric nonlinearity is included in the model by using the NLGEOM parameter on the *****STEP option, the small-sliding algorithm accounts for any rotation and deformation of the master surface and updates the load path through which the contact forces are transmitted. In contrast to small sliding, the finite-sliding contact formulation requires that ABAQUS constantly determine which part of the master surface is in contact with each slave node. This results in a complex computation, whereby the level of complexity increases for the contact between deformable bodies.

The analysis may need to take into account frictional resistance if the two interacting surfaces are rough. Coulomb friction is a common friction model used to describe the interaction of contacting surfaces. The model characterizes the frictional behavior between the surfaces using

a coefficient of friction, $\mu$. The product $\mu p$, where $p$ is the contact pressure between the two surfaces, gives the limiting frictional shear stress for the contacting surfaces. The contacting surfaces will not slip (slide relative to each other) until the shear stress across their interface equals the limiting frictional shear stress, $\mu p$. For most surfaces, $\mu$ is normally less than unity. The solid line in figure C-6 summarizes the behavior of the Coulomb friction model: there is zero relative motion (slip) of the surfaces when they are sticking (the shear stresses are below $\mu p$).

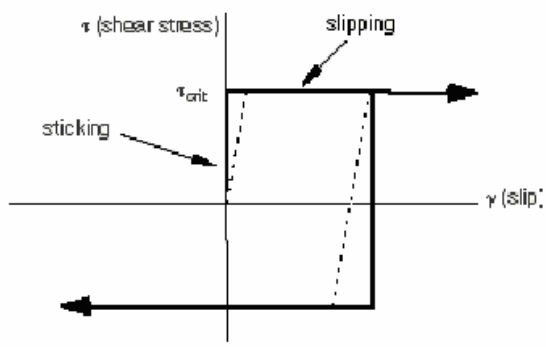


Figure C-6. Frictional Behavior [C-1]

Convergence problems are often caused by discontinuous stick-slip behavior. Since simulation of ideal friction behavior is very difficult, a penalty friction formulation with an allowable elastic slip, shown by the dotted line in figure C-6, is used by ABAQUS. The elastic slip is defined as the small amount of relative motion between the surfaces that occurs when the surfaces should be sticking. The penalty stiffness (the slope of the dotted line) is chosen automatically by ABAQUS. This results in an allowable elastic slip that is a very small fraction of the characteristic element length. For most applications, this penalty formulation is sufficient to model any frictional behavior. When ideal stick-slip frictional behavior must be included (such as fretting problems) the Lagrange friction formulation can be used. The Lagrange friction formulation uses more computer resources because of additional variables imposed by ABAQUS for each surface node with frictional contact. The Lagrange formulation also exhibits a slower rate of convergence.

The inclusion of friction in a model adds unsymmetric terms to the system of equations being solved. For values of $\mu$ less than approximately 0.2, the magnitude and influence of these terms are quite small and the symmetric solver is sufficient for the analysis. For higher coefficients of friction, the unsymmetric solver is invoked automatically by ABAQUS, which improves the convergence rate. The user has the flexibility of selecting the unsymmetric solver by including the UNSYMM=YES parameter on the *STEP option. It should be noted, however, that the unsymmetric solver requires twice as much computer memory and scratch disk space compared to its symmetric counterpart.

ABAQUS uses a pure master-slave contact algorithm: nodes on one surface (the slave) cannot penetrate the segments that make up the other surface (the master). The algorithm does not place any restrictions on the master surface. The master surface can penetrate the slave surface between slave nodes, as shown in figure C-7.

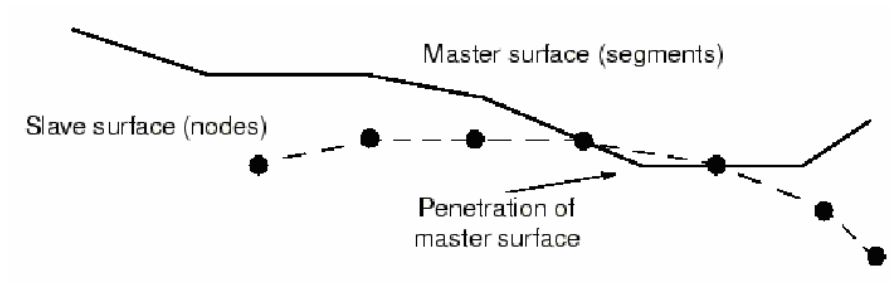


Figure C-7. The Master Surface can Penetrate the Slave Surface [C-1]

The order of the two surfaces given in the *CONTACT PAIR option is very important. This order determines which surface is the master surface and which is the slave surface. The first surface is taken to be the slave surface, and the second is the master surface. The user must carefully select the slave and master surfaces to achieve the best possible contact simulation. Typically, the following rule applies: the slave surface should be the more finely meshed surface, and if the mesh densities are similar, the slave surface should be the surface with the softer underlying material.

First-order elements should be typically selected for the slave surface. Second-order elements can cause problems in contact simulation. This is due to the way in which consistent nodal loads are calculated for these elements for a constant pressure. The consistent nodal loads for a constant pressure, *P*, on second-order, two-dimensional elements, with area A, are shown in figure C-8.

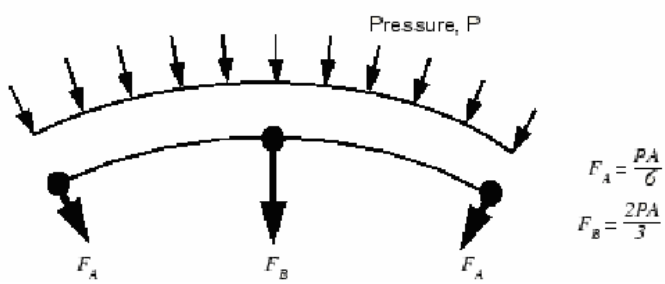


Figure C-8. Equivalent Nodal Loads for a Constant Pressure on a Two-Dimensional, Second-Order Element [C-1]

Important decisions are based by the contact algorithms, depending on the forces acting on the slave nodes. The algorithms find it difficult to distinguish if the force distribution represents a constant contact pressure or an actual variation across the element. Equivalent nodal forces for a three-dimensional, second-order brick element prove to be more confusing because they do not have the same sign for a constant pressure. This creates problems for the algorithm, especially for nonuniform contact simulations. To avoid such problems, ABAQUS automatically adds a mid-face node to any face of a second-order, three-dimensional brick or wedge element that defines a slave surface. For a second-order element face with a mid-face node, the equivalent nodal forces have the same sign for a constant pressure. They still differ considerably in magnitude.

The equivalent nodal forces for applied pressures on first-order elements always have a consistent sign and magnitude. The contact algorithm, therefore, faces no ambiguity about the contact state that a given distribution of nodal forces represents. If the geometry is complicated and requires using an automatic mesh generator, the modified second-order tetrahedral elements (C3D10M) in ABAQUS should be used. These elements are designed for use in complex contact simulations. Regular second-order tetrahedral elements (C3D10) have zero contact force at their corner nodes. This leads to poor predictions of the contact pressures. The modified second-order tetrahedral elements can calculate the contact pressures accurately.

ABAQUS/Standard implements the Newton-Raphson technique for the contact algorithm. The state of all contact pairs is examined: the start of each increment to establish whether slave nodes are open or closed. In figure C-9, *P* denotes the contact pressure at a slave node and H denotes the penetration of a slave node into the master surface. If a node is closed, ABAQUS determines whether it is sliding or sticking. A constraint is applied by ABAQUS for each closed node and any constraint is removed from any node where the contact state changes from closed to open. An iteration is then carried out and the model configuration updated based on the calculated corrections.

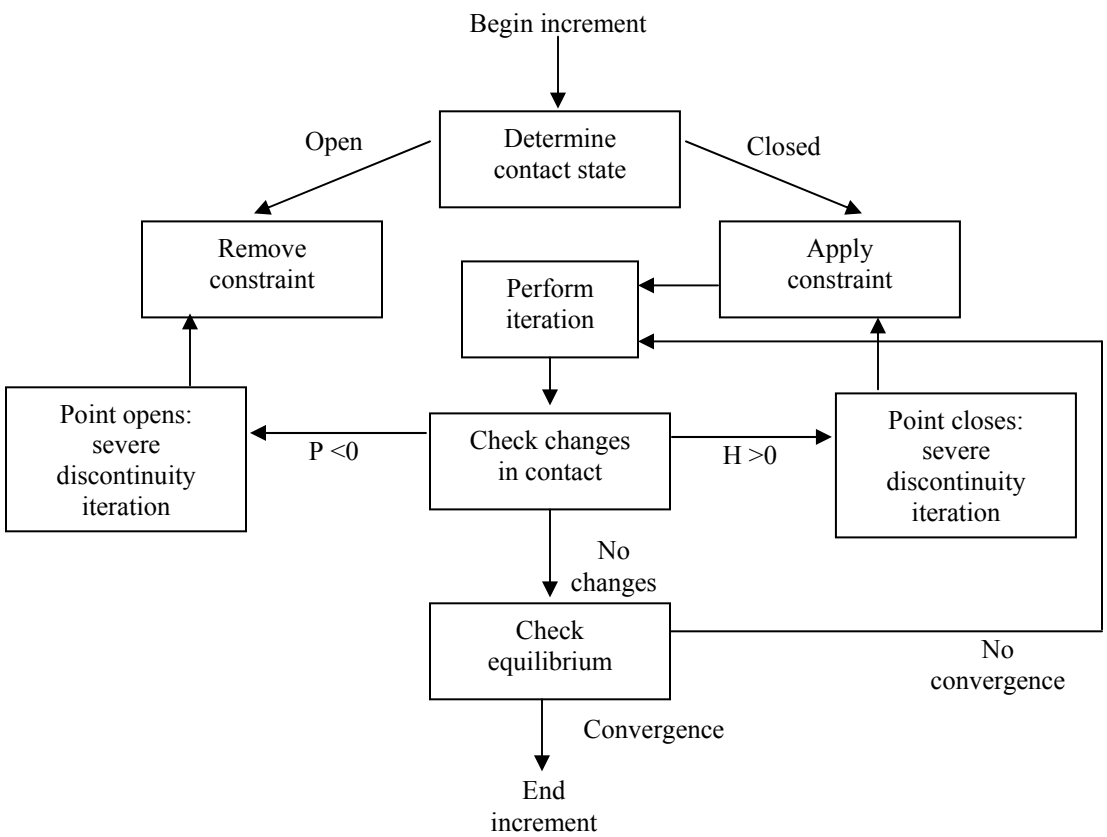


Figure C-9. Contact Logic [C-1]

Before checking for equilibrium of forces or moments, checks are performed for changes in the contact conditions at the slave nodes. Any node where the clearance after the iteration becomes negative or zero has changed status from open to closed. Any node where the contact pressure

becomes negative has changed status from closed to open. If any contact changes are detected in the current iteration, ABAQUS labels it a severe discontinuity iteration and no equilibrium checks are performed.

The contact constraints are modified to reflect the change in contact status after the first iteration. A second iteration is then attempted by ABAQUS. This procedure is repeated until there are no changes in contact status. This iteration becomes the first equilibrium iteration, and ABAQUS performs the normal equilibrium convergence checks. Another iteration is performed if the convergence checks fail. The internal count of equilibrium iterations is reset to zero for every severe discontinuity iteration. This iteration count is used to determine if an increment should be abandoned due to a slow convergence rate. The entire process is repeated until convergence is achieved.

The user can separate the two types of iterations to see how well ABAQUS is coping with the contact calculations and how well it is achieving equilibrium. If the number of severe discontinuity iterations is high but there are few equilibrium iterations, ABAQUS is having difficulty determining the proper contact conditions. Any increment needing more than 12 severe discontinuity iterations is abandoned and a cutback occurs. If there are no severe discontinuity iterations, the contact state is not changing from increment to increment.

C.4.14 ABAQUS/EXPLICIT SOLVERS.

A wide variety of nonlinear solid mechanics problems can be solved with the ABAQUS/Explicit dynamics procedure in ABAQUS. This method is sometimes complimentary to an ABAQUS/Standard analysis (ABAQUS/Standard). From a user's standpoint, the distinguishing characteristics of the ABAQUS/Explicit and ABAQUS/Standard methods are:

- ABAQUS/Explicit methods require a small time increment size. The size depends on the highest natural frequencies of the model and is independent of the type and duration of loading. Simulations generally take on the order of 10,000 to 1,000,000 increments, but the computational cost per increment is relatively small.

- In ABAQUS/Standard methods, increment size is generally determined from accuracy and convergence considerations. ABAQUS/Standard simulations typically take orders of magnitude fewer increments than ABAQUS/Explicit simulations. Since a global set of equations must be solved in each increment in ABAQUS/Standard methods, the cost per increment is far greater than an ABAQUS/Explicit method.

The ABAQUS/Explicit method is designed for solving high-speed dynamic events that require many small increments to obtain a high-resolution solution. If the duration of the event is short, the solution can be obtained efficiently. Formulation of contact conditions is extremely easy in the ABAQUS/Explicit method and can be enforced on a node-by-node basis without iteration. The nodal accelerations can be adjusted to balance the external and internal forces during contact. The ABAQUS/Explicit method displays the lack of a global tangent stiffness matrix, which is required with ABAQUS/Standard methods. Iterations and tolerances are not required since the state of the model is advanced explicitly.

With the ABAQUS/Explicit method, the state of the model is advanced through an increment of time, $\Delta t$. This is based on the state of the model at the start of the increment at time $t$. The amount of time that the state can be advanced and still remain an accurate representation of the problem is typically quite short. The increment will exceed a stability limit if it is larger than this maximum amount of time. Exceeding the stability limit might lead to numerical instability and, consequently, an unbounded solution. The stability limit has a great effect on reliability and accuracy. Hence, a consistent and conservative estimate is necessary. For computational efficiency, ABAQUS/Explicit chooses the time increments to be as close as possible to the stability limit without exceeding it.

ABAQUS/Explicit adjusts the time increment size throughout the analysis so that the stability limit, based on the current state of the model, is never exceeded. The stability limit is a mathematical concept resulting from the numerical model. It is directly proportional to element size and inversely proportional to the wave speed of the material. The wave speed of the material, in turn, is directly proportional to the stiffness and, inversely, proportional to density. Thus, the mass density influences the stability limit. Scaling the mass density can increase analysis efficiency. Models might typically have regions containing few localized small or poorly shaped elements that control the stability limit. By scaling the mass of only these elements, the stability limit can be increased without affecting the overall dynamic behavior of the model. There are two approaches used in mass scaling: the user can define a scaling factor directly or define a desired element-by-element stable time increment for the elements whose mass is to be scaled. However, the user should be cautious when employing mass scaling, since significantly changing the mass of the model may change the physics of the problem.

The material model affects the stability limit through its effect on the dilatational wave speed. In a linear material, the wave speed is constant. The only changes in the stability limit during the analysis are a result of changes in the smallest element dimension during the simulation. In a nonlinear material, such as a metal with plasticity, the wave speed changes as the material yields and the stiffness of the material changes. The effective wave speed in the model is monitored by ABAQUS/Explicit throughout the analysis, and the current material state in each element is used for stability estimates. After yielding, the stability limit increased due to a decrease in the stiffness.

Since the stability limit is roughly proportional to the shortest element dimension, it is advantageous to keep the element size as large as possible. However, accurate analyses typically require a fine mesh. To obtain the highest possible stability limit while using the required level of mesh refinement, a uniform mesh should be used. Even a single, small, or poorly shaped element can reduce the stability limit drastically.

## C.4.15 COMPARISON OF ABAQUS/STANDARD AND ABAQUS/EXPLICIT SOLVERS.

ABAQUS/Explicit and ABAQUS/Standard are capable of solving a wide variety of problems. The characteristics of ABAQUS/Standard and ABAQUS/Explicit procedures dictate which method is appropriate for a given problem. For those problems that can be solved with either method, the question of which analysis tool to use has a direct bearing on the efficiency with which the problem is solved.

Each iteration in an ABAQUS/Standard analysis requires solving a large system of linear equations. This leads to large computational and memory requirements. As the problem size increases, the equation solver requirements grow very rapidly. The maximum size of an ABAQUS/Standard analysis that can be solved on a given computer often is dictated by the amount of disk space and memory available on the computer.

ABAQUS/Standard must iterate to determine the solution to a nonlinear problem. In contrast, ABAQUS/Explicit determines the solution without iterating by explicitly advancing the kinematic state from the previous increment. A static analysis may typically require a large number of time increments using the ABAQUS/Explicit method. However, the analysis can be more efficient and less expensive in ABAQUS/Explicit than using ABAQUS/Standard. ABAQUS/Explicit requires much less disk space and memory than ABAQUS/Standard for the same simulation.

Using the ABAQUS/Explicit method, the computational cost is proportional to the number of elements and, roughly, inversely proportional to the smallest element dimension. Mesh refinement, therefore, increases the computational cost by increasing the number of elements and reducing the smallest element dimension.

There are certain static or nearly static problems that can be simulated well with either solver. Typically, these problems would be solved with ABAQUS/Standard. But since they may have difficulty converging because of contact or material complexities, ABAQUS/Explicit might be a feasible option.

### C.4.16 QUASI-STATIC ANALYSIS CONSIDERATIONS.

Obtaining the solution of quasi-static problems with ABAQUS/Explicit requires some special considerations. A static solution is, by definition, a long-time solution. It is often computationally impractical to analyze the simulation in its natural time scale since it would require a large number of small increments. To obtain an economical solution, the event must be accelerated in some way. As the event is accelerated, the state of static equilibrium evolves into a state of dynamic equilibrium in which inertial forces become more dominant. The process must be modeled in the shortest time period in which inertial forces are negligible.

Performing an analysis in natural time for a quasi-static process will probably produce accurate static results. The user can increase the loading rate so that the same physical event occurs in less time, as long as the solution remains nearly the same as the true static solution and dynamic effects remain insignificant.

Applied loading in a quasi-static analysis should be as smooth as possible to obtain an accurate solution. Stress waves can be caused by sudden, jerky movements leading to noise. Negligible acceleration variations between increments, ensures smooth loading. If the acceleration is smooth, it follows that the changes in velocity and displacement are also smooth. ABAQUS has a simple, built-in type of amplitude called SMOOTH STEP that automatically creates smooth loading amplitude. The user defines time-amplitude data pairs using *AMPLITUDE, DEFINITION=SMOOTH STEP. ABAQUS/Explicit then automatically connects each of the provided data pairs with curves. The first and second derivatives of the curves are smooth, and

slopes are zero at each of the provided data points. Thus, the user can apply a displacement loading with SMOOTH STEP using only the initial and final data points. (The intervening motion will be smooth.) A quasi-static analysis can then be performed without generating waves due to discontinuity in the rate of applied loading.

In a static analysis, the lowest mode of the structure usually dominates the response. Using the period of the lowest mode, the user can estimate the time required to obtain the proper static response. Typically, the user should increase the loading time to 10 times the period of the lowest mode to be certain that the solution is truly quasi-static.

Artificially increasing the speed of forming events is necessary to obtain an economical solution. The suggested approach to determining an acceptable velocity involves running a series of analyses at various speeds. The user should perform the analyses from fastest to slowest, since the solution time is inversely proportional to the velocity. The user should examine the results of each analysis, specifically if the deformed shapes, stresses, and strains vary with speed. At some point the solutions should converge to steady state. This is an indication that, as inertial effects become less significant, differences in simulation results also become less significant.

Springback is often an important part of a forming analysis because the springback analysis determines the shape of the final, unloaded part. Forming simulations can be simulated well with ABAQUS/Explicit. However, springback poses some difficulties. The main problem with performing springback simulations within ABAQUS/Explicit is the amount of time required to obtain a steady-state solution. Typically, the loads must be removed very carefully, and damping must be introduced to make the solution time reasonable.

Springback typically involves no contact and usually includes only mild nonlinearities. Hence, ABAQUS/Standard can be used to solve springback problems much faster than ABAQUS/Explicit. The approach is to solve forming analysis in ABAQUS/Explicit and then import the completed forming model from ABAQUS/Explicit into ABAQUS/Standard.

### C.4.17 MASS SCALING.

Mass scaling enables an analysis to be performed economically without artificially increasing the loading rate. For simulations involving a rate-dependent material or rate-dependent damping, such as dashpots, the solution can be obtained economically only with mass scaling. Increasing the loading rate is not an option in such cases. This is because material strain rates increase by the same factor as the loading rate. As the properties of the model change with the strain rate, artificially increasing the loading rate artificially changes the process.

### C.4.18 ENSURING QUASI-STATIC ANALYSIS RESULTS.

The most standard means of evaluating whether or not a simulation is producing an appropriate quasi-static response involves studying the various model energies. The following is the energy balance equation in ABAQUS/Explicit:

$$E_I + E_V + E_{KE} + E_{FD} - E_W = constant \qquad \text{(C-4)}$$

where $E_I$ is the internal energy (both elastic and plastic strain energy), $E_V$ is the energy absorbed by viscous dissipation, $E_{KE}$ is the kinetic energy, $E_{FD}$ is the energy absorbed by frictional dissipation, and $E_W$ is the work of external forces.

In a quasi-static analysis, the work applied by the external forces is nearly equal to the internal energy of the system. The viscously dissipated energy is generally small, unless viscoelastic materials, discrete dashpots, or material damping are used. Inertial forces are negligible in a quasi-static analysis because the velocity of the material in the model is very small. These conditions imply that the kinetic energy in the analysis should be very small. The kinetic energy of the deforming material should not exceed a small fraction (typically 5% to 10%) of its internal energy throughout most of the process.

A global energy balance is reported by ABAQUS at the end of the analysis. This includes the kinetic energy of any rigid body with mass. The deformable bodies are of interest when evaluating the results. Hence, the kinetic energy of the rigid bodies should be subtracted from the total energy in the system when evaluating the energy balance.

C.4.19 CONTACT FORMULATION.

Contact constraints are imposed by the penalty method in ABAQUS/Explicit for general contact. This method searches for node-into-face and edge-into-edge penetrations in the current configuration. An automatic value of the penalty stiffness is chosen automatically by ABAQUS/Explicit. This ensures that the effect on the time increment is minimal, yet the penetration is not significant. The user can override this penalty stiffness by specifying a penalty scale factor or a softened contact relationship. A kinematic contact formulation is imposed for the contact pair algorithm. This achieves precise compliance with the contact conditions using a predictor/corrector method. At first, the increment proceeds under the assumption that contact does not occur. At the end of the increment, if ABAQUS detects an overclosure, the acceleration is modified to obtain a corrected configuration. In this configuration, the contact constraints are enforced. The normal penalty contact method can also be enforced for contact pairs. This method can model some types of contact that the kinematic method cannot. When the penalty contact formulation is used, equal and opposite contact forces with magnitudes equal to the penalty stiffness times the penetration distance are applied to the master and slave nodes at the penetration points.

In the pure master-slave approach, one surface is the master surface and the other is the slave surface. As the two bodies come into contact, the penetrations are detected and the contact constraints are applied according to the constraint enforcement method (kinematic or penalty). Regardless of the method, pure master-slave weighting resists only penetrations of slave nodes into master facets. Penetrations of master nodes into the slave surface can go undetected, as shown in figure C-10. This can be avoided by sufficient mesh refinement of the slave surface.

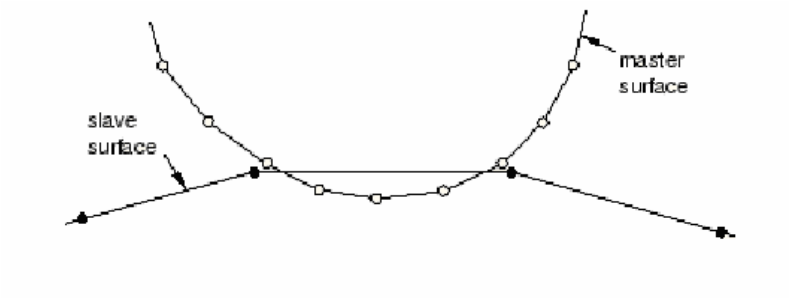


Figure C-10. Penetration of Master Nodes Into Slave Surface With Pure Master-Slave Contact [C-1]

The balanced master-slave contact (figure C-11) approach applies the pure master-slave approach twice. It reverses the surfaces on the second pass. One set of contact constraints is obtained with surface 1 as the slave, and another set of constraints is obtained with surface 2 as the slave. A weighted average of the two computations gives the acceleration corrections or forces.

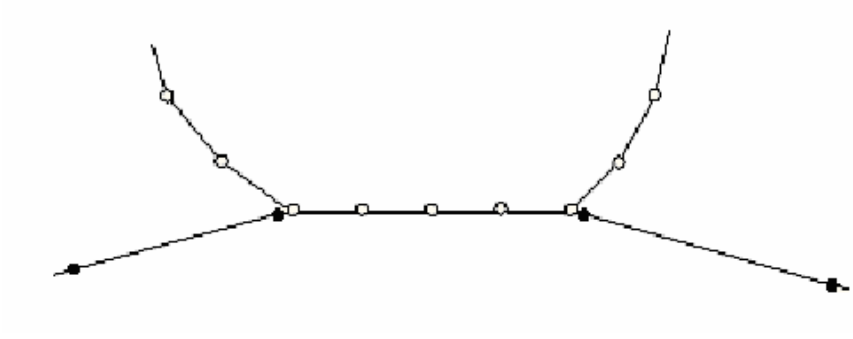

Figure C-11. Balanced Master-Slave Contact Constraint With Kinematic Compliance [C-1]

This balanced approach minimizes the penetration of the contacting bodies, resulting in greater solution accuracy. The user can specify weight of the average for balanced master-slave contact with the contact pair algorithm using the WEIGHT parameter on the *CONTACT PAIR option. The default weight is 0.5. This results in the same weight being used for each acceleration correction. Setting WEIGHT to 1.0 specifies a pure master-slave relationship with the first surface as the master surface. Conversely, a weight of zero indicates that the second surface is the master surface.

The balanced master-slave approach does not require high mesh refinement on the slave surface. Mesh refinement is generally most important with pure master-slave contact between deformable and rigid bodies. Figure C-12 shows an example of the penetration that can occur if the slave surface is meshed poorly in comparison to the dimensions of the features on the master surface.

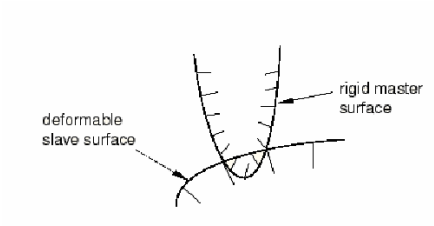


Figure C-12. Example of Inadequate Slave Surface Discretization [C-1]

Any initial overclosures are removed by ABAQUS/Explicit by adjusting the undeformed coordinates of nodes on contact surfaces. The balanced master-slave approach adjusts both surfaces, and the pure master-slave approach adjusts only the slave surface. No initial strain or stress is caused by displacements associated with these adjustments. In case of conflicting constraints, initial overclosures may not be completely resolved by repositioning nodes. Severe mesh distortions can result near the beginning of an analysis when the contact pair algorithm is used.

Subsequently, steps in any nodal adjustments to remove initial overclosures cause strains that can cause severe mesh distortions because the entire nodal adjustments occur in a single, very brief increment, leading to large values of acceleration. Such a large acceleration applied to a single node typically will cause ABAQUS to warn about the deformation speed exceeding the wave speed of the material and warn about severe mesh distortions. It is very important that any additional new contact surfaces that the user defines are not overclosed.

A common case of initial overclosure of two surfaces is shown in figure C-13. All the nodes on the contact surfaces lie exactly on the same arc of a circle. The mesh of the inner surface is finer than the outer surface, and the element edges are linear. Both these reasons cause some nodes on the finer, inner surface to initially penetrate the outer surface.

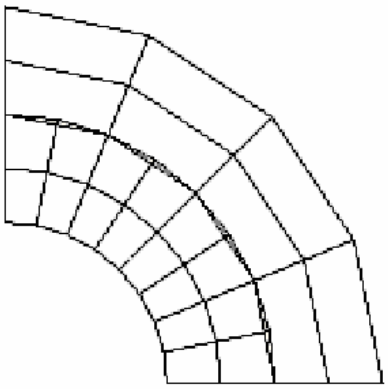

Figure C-13. Original Overclosure of Two Contact Surfaces [C-1]

Figure C-14 shows the initial, strain-free displacements applied to the slave surface nodes by ABAQUS/Explicit for the pure master-slave approach. This geometry is stress-free. The default balanced master-slave approach causes a different initial set of displacements that results in a mesh that is not entirely stress-free.

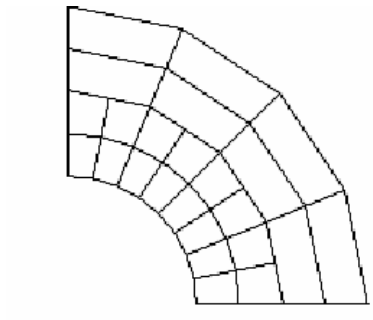

Figure C-14. Corrected Contact Surfaces [C-1]

C.4.20 SPECIAL ANALYSIS TECHNIQUES.

The following sections briefly describe two common and important analysis techniques available in ABAQUS.

C.4.20.1 Transferring Results Between ABAQUS/Standard and ABAQUS/Explicit.

ABAQUS provides the capability to import a deformed mesh and its associated material state from ABAQUS/Standard into ABAQUS/Explicit and vice versa. New model information can be specified during the import analysis. For analysis with several stages, this capability proves to be extremely useful for problems. Contact definitions specified in the original analysis and the contact state are not imported. Contact can be defined again in the import analysis by specifying the surfaces and contact pairs. The user cannot use the exact contact definitions that were used in the original analysis. This is due to the differences in the contact capabilities between ABAQUS/Standard and ABAQUS/Explicit. When the first step in the ABAQUS/Standard import analysis is a *STATIC procedure, the imported stresses are defined at the start of the analysis as the initial stresses in the material. Then an additional set of artificial stresses is defined at each material point. These stresses are equal in magnitude to the imported stresses but are of opposite sign. The sum of the material point stresses and the artificial stresses creates zero internal forces at the beginning of the step. The internal artificial stresses are ramped off linearly in time during the first step. Thus, at the end of the step, the artificial stresses have been removed completely and the remaining stresses in the material will be the residual stress state associated with static equilibrium. Once static equilibrium has been obtained, subsequent steps can be defined using any analysis procedure.

C.4.20.2 Specifying Initial Conditions.

Initial conditions are specified for particular nodes or elements, as appropriate. The user can provide the required data on the data lines of the *INITIAL CONDITIONS option, in an external input file, by a user subroutine or by the results file of a previous ABAQUS analysis. When initial stresses are given, the initial stress state may not be an exact equilibrium state for the finite element model. Therefore, the user should include an initial step to allow ABAQUS to check for equilibrium and iterate, if necessary, to achieve equilibrium. It might happen that the equilibrating step does not converge. This indicates that the initial stress state is far from equilibrium with the applied loads and that significantly large deformations could be generated. In such cases, the user should recheck the specified initial stresses and loads.

## C.4.21 OVERCOMING CONVERGENCE PROBLEMS.

The following sections briefly describe the techniques that can be applied to large-deformation contact simulations exhibiting convergence problems.

### C.4.21.1 Analysis Completed but Gross Penetration of Surfaces.

When a coarsely discretized surface is used as a slave surface, the master surface nodes can grossly penetrate the slave surface. To define contact accurately, use a refined mesh to create the slave surface.

### C.4.21.2 Contact Oscillating in Severe Discontinuity Iterations.

Use *****CONTACT DAMPING to activate viscous damping between contact surfaces. ABAQUS/Standard activates viscous damping in the contact direction at all slave nodes. The viscous damping acts across the clearances of all slave nodes of the contact pair, using a damping coefficient calculated automatically so that a smooth motion is obtained. Roughly, initial contact should be obtained in the first part of the step, and in the second part of the step, damping is reduced continuously to zero while contact continues to be established. As a result, at the end of the step, all viscous forces introduced by this option are removed.

### C.4.21.3 Analysis Aborts Because of Initial Overclosures.

Whenever a node involved in contact is penetrating its master surface, ABAQUS tries to resolve the overclosure in a single increment. If the overclosure occurs during the simulation and is so severe that a converged solution cannot be obtained, ABAQUS will cut back on the increment size in an attempt to reduce the magnitude of the overclosure. However, if the overclosure is present at the start of the analysis, cutting back the increment size will not solve the problem. In this case, use the *****CONTACT INTERFERENCE option to allow ABAQUS to resolve the excessive overclosure gradually during the first step of the analysis.

### C.4.21.4 Avoiding Premature Cutbacks in Difficult Analyses.

Sometimes it is useful to increase both $I_0$ (equilibrium iterations to determine whether residuals are increasing) and $I_R$ (equilibrium iteration at which a logarithmic convergence check begins). These data items can be raised to more appropriate values for severely discontinuous problems by increasing them individually on the *****CONTROLS option.

### C.4.21.5 Improving Solution Efficiency in a Problem That Involves a High Coefficient of Friction.

The solution efficiency can sometimes be improved in an analysis that involves a high coefficient of friction by using both *****CONTROLS, ANALYSIS=DISCONTINUOUS and *STEP, UNSYMM=YES.

C.4.21.6 Severe Discontinuity Iterations.

A severe discontinuity in a model's behavior is caused by a change in contact conditions (a gap or interface opening or closing) and by friction changing from slipping to sticking. In static analysis, a severe discontinuity forces iteration with the contact conditions changed. A limit, $I_S$, is placed on the number of iterations caused by severe discontinuities in an increment. If more than $I_S$ iterations are required for severe discontinuities, the increment is begun again with a time increment size of $D_S$, times the abandoned increment size (for automatic time incrementation). If fixed-time incrementation was chosen, the analysis terminates with an error message. The values of $I_S$ and $D_S$ are defined on the first and second data lines, respectively, of the *CONTROLS, PARAMETERS=TIME INCREMENTATION option.

C.4.21.7 Accuracy of Solution Versus Convergence.

The default control parameters defined in ABAQUS are designed to provide reasonably optimal solutions to complex problems involving combinations of nonlinearities as well as efficient solutions of simpler nonlinear cases. However, the most important consideration in the choice of the control parameters is that any solution accepted as "converged" is a close approximation to the exact solution of the nonlinear equations. The *CONTROLS, PARAMETERS=FIELD option allows many control parameters to be reset. If this option is used to define less strict convergence criteria, the risk that results may be accepted as converged when they are not sufficiently close to the exact solution of the system. Caution should be used when resetting solution control parameters. Lack of convergence is often due to modeling issues, which should be resolved before changing the accuracy controls.

C.4.21.8 Excessive Element Distortion.

Use DISTORTION CONTROL=YES to activate a constraint that acts to prevent negative element volumes or other excessive distortion for crushable materials. The DISTORTION CONTROL parameter is not relevant for linear kinematics and cannot prevent elements from being distorted due to physically unrealistic deformation. This parameter is available only in the ABAQUS/Explicit solver.

C.4.21.9 Negative Eigenvalues.

Negative eigenvalue messages indicate a lack of stability of the model with the tangent stiffness matrix not being positive definite. Typically, these messages mean that a buckling or bifurcation load has been exceeded. In many cases, negative eigenvalues might be because one part of the assembly is not restrained and rigid-body motions exist in the model. The presence of negative eigenvalues does not necessarily mean that the analysis will not converge, though it may lead to convergence difficulties.

C.4.21.10 ABAQUS Version 6.4-1 Versus Version 6.4-4.

Performing large distortion analyses with hyperelastic materials might be a problem in version 6.4-1. The riveting analysis with sealant (discussed in detail earlier) modeled with a hyperelastic material aborted in version 6.4-1. The exact analysis run in version 6.4-4 was successful.

C.4.21.11 Difficulties in Contact Convergence.

If the model has sharp corners on the contact surfaces, smooth the surface. Nodes on the slave surface can be caught in folds in the master surface, causing convergence difficulties when the surrounding elements deform to take this into account. The elements making up the slave surface should be small enough to resolve the geometry. A rough guideline is to use 10 elements around a 90° corner. If the physical problem has a sharp concave fold, two separate surface definitions should be used. Sharp convex folds cannot be modeled with a reasonable finite element mesh. Smooth the fold with a radius larger than the element size on the slave surfaces.

C4.21.12 ABAQUS Version 6.4-4 Versus Version 6.5.

Solving large distortion analyses with hyperelastic materials might be a problem in version 6.5. The riveting analysis with sealant (discussed in detail earlier) modeled with a hyperleastic material, aborted in version 6.5. The same analysis run was successful in version 6.4-4. The simultaneous use of balanced master-slave contact with no separation assumed between the contact surfaces for the hyperelastic material might be causing the model to become unstable in 6.5. Successful completion of the job in 6.4-4, without surface penetration or considering ABAQUS/Explicit "noise," might be attributed to bugv63_4767 in version 6.5.

C.4.21.13 Importing Models in ABAQUS Version 6.4.

ABAQUS 6.4 does not allow for importing analysis results between ABAQUS/Standard and ABAQUS/Explicit if the model is defined as an assembly of part instances. The user needs to implement the command given below to generate an input file independent of part and assembly options to carry out the import.

Command**:** m = mdb.models['Model-1'].setValues(noPartsInputFile=ON)

C.5 REFERENCES.

C-1. Hibbitt, Karlsson and Sorensen, Inc., "ABAQUS/Standard 6.3/6.5 User's Manual," Hibbitt, Karlsson and Sorensen, Inc., Pawtucket, RI, 2003.

APPENDIX D—ARCHIVE OF LAP JOINT FAILURES

The following presents a summary of the damage observed in 16 other tested lap joints. Figures D-1 through D-17 show, at a minimum, the faying surface and the fracture surface of the failed holes.

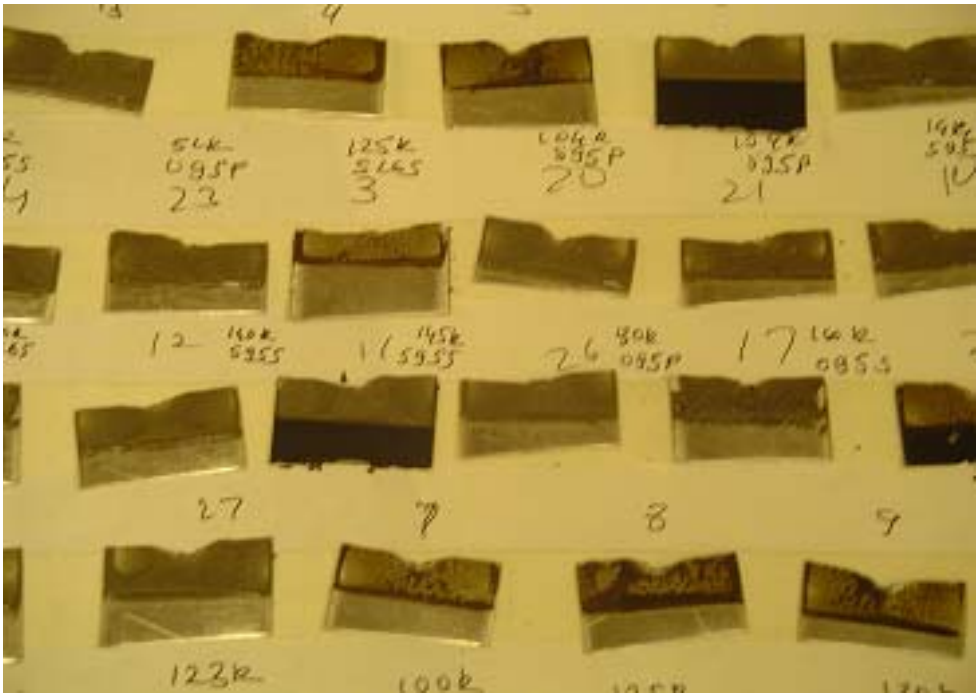

Figure D-1. Specimens Cut for Damage Characterization

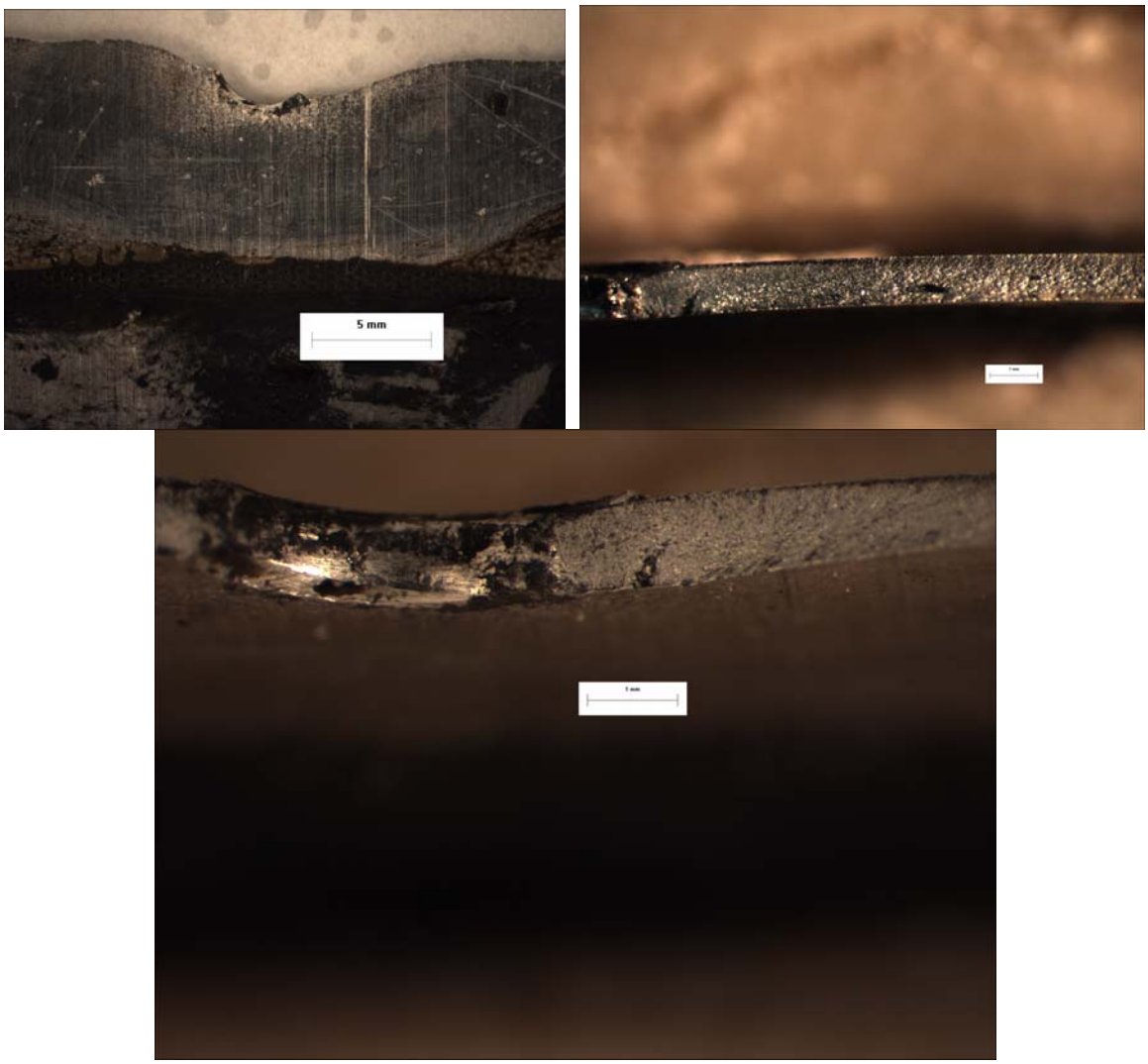


Figure D-2. Damage Characterization of Specimen 02

Lap Joint 02: B26S
Cycles to failure: 125,000
Macroscopic Observations:
Some fretting at hole edge on faying surface.
Faying surface crack origin.
Circumferential groove observed in hole.

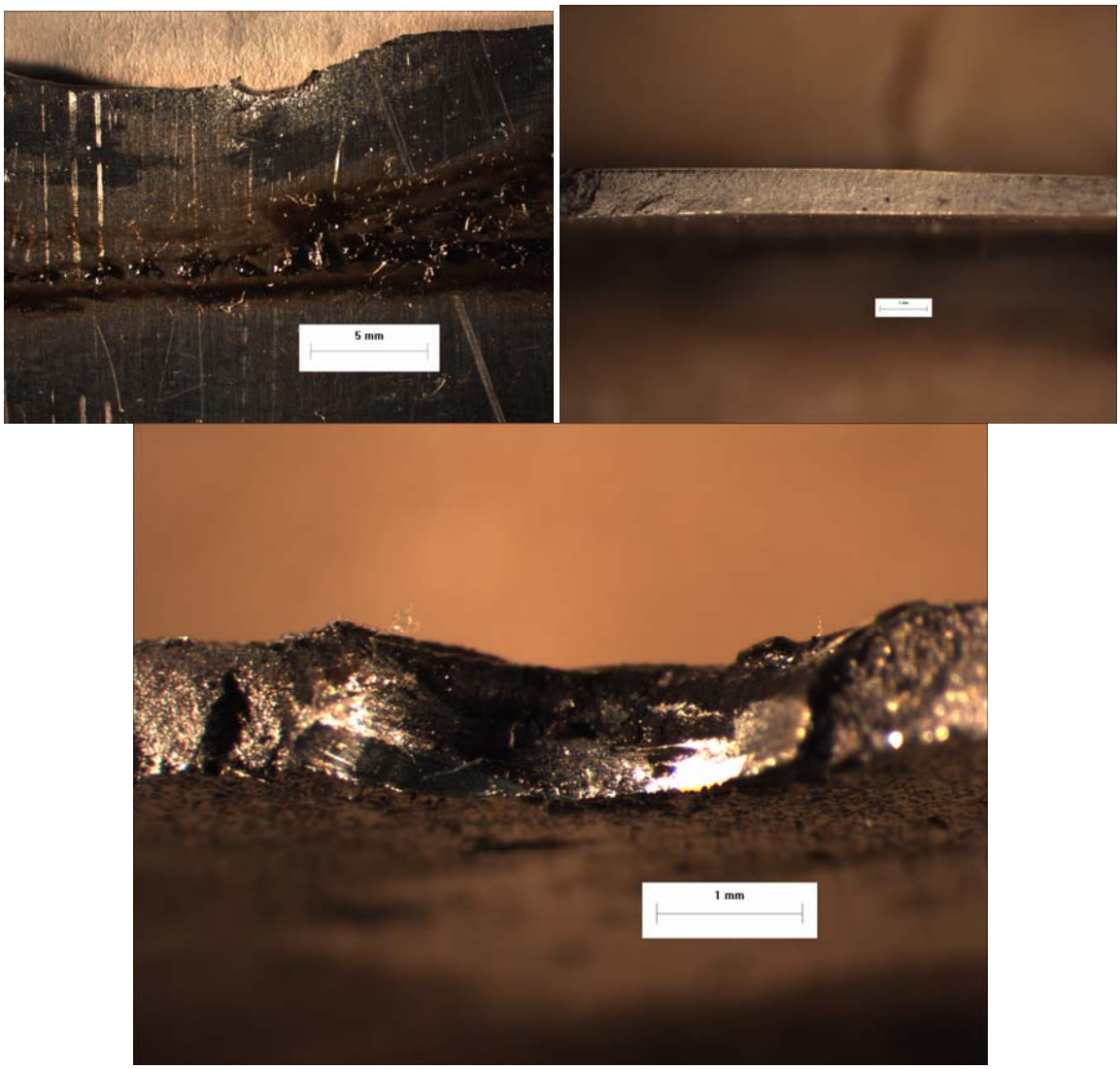


Figure D-3. Damage Characterization of Specimen 04

Lap Joint 04: U26S
Cycles to failure: 80,000
Macroscopic Observations:
No significant fretting at hole edge on faying surface.
Faying surface crack origin, possible hole surface origin.
Circumferential groove observed in hole.

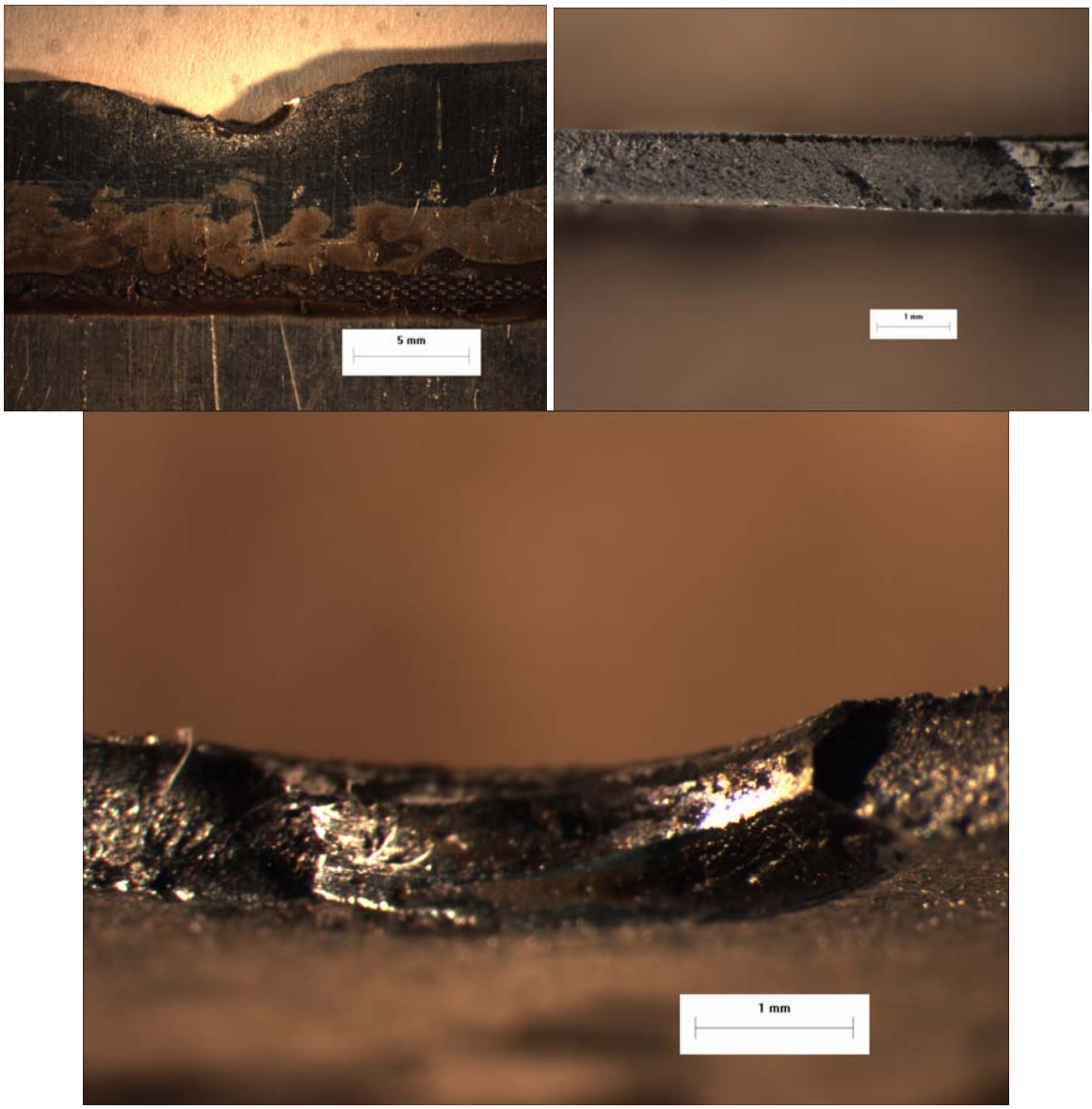


Figure D-4. Damage Characterization of Specimen 07

Lap Joint 07: O26S
Cycles to failure: 100,000
Macroscopic Observations:
Some fretting at hole edge on faying surface.
Faying surface crack origin.
Circumferential groove observed in hole.

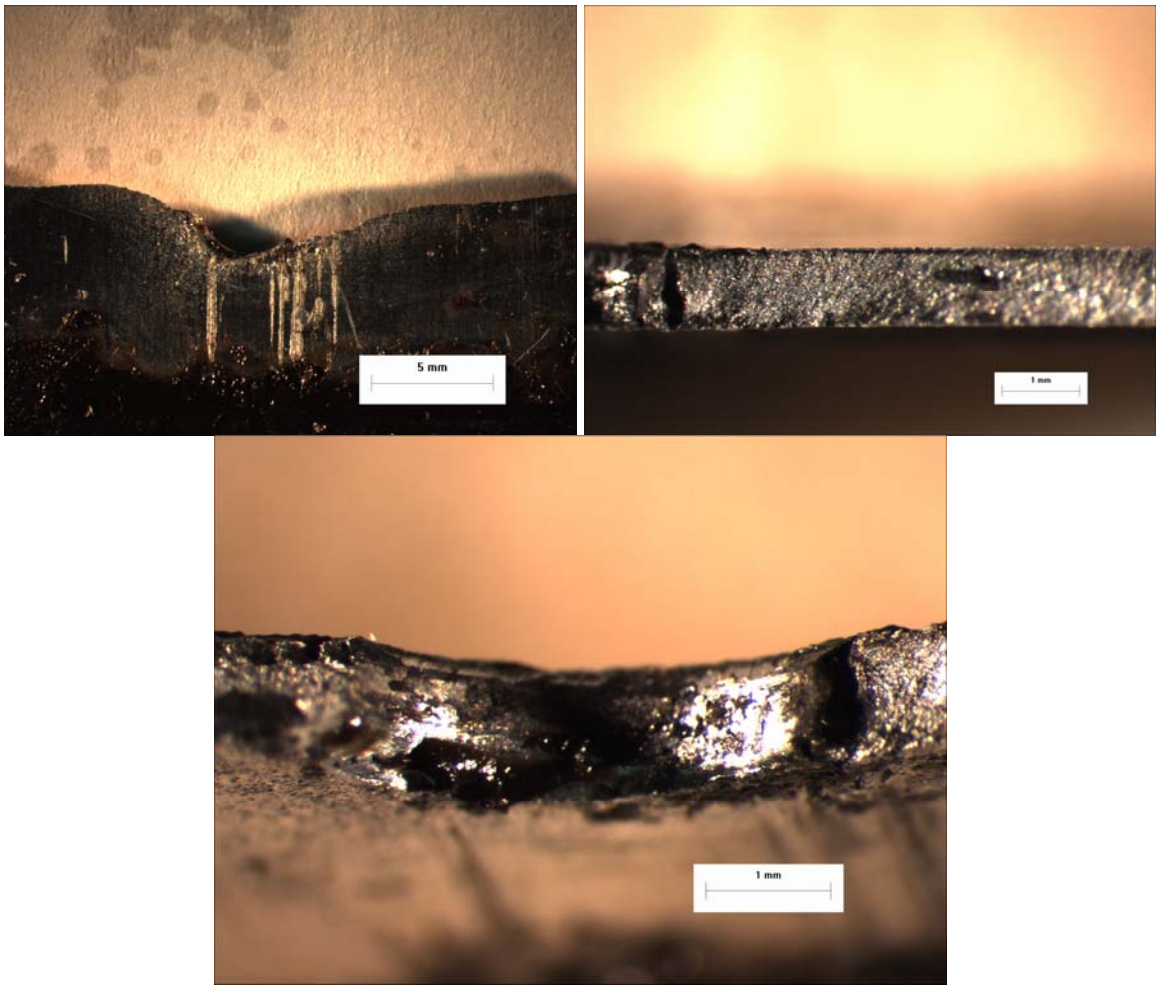


Figure D-5. Damage Characterization of Specimen 08

Lap Joint 08: O26S
Cycles to failure: 125,000
Macroscopic Observations:
Some fretting at hole edge on faying surface. Scratches on specimen due to possible damage.
Faying surface crack origin.
Circumferential groove observed in hole.

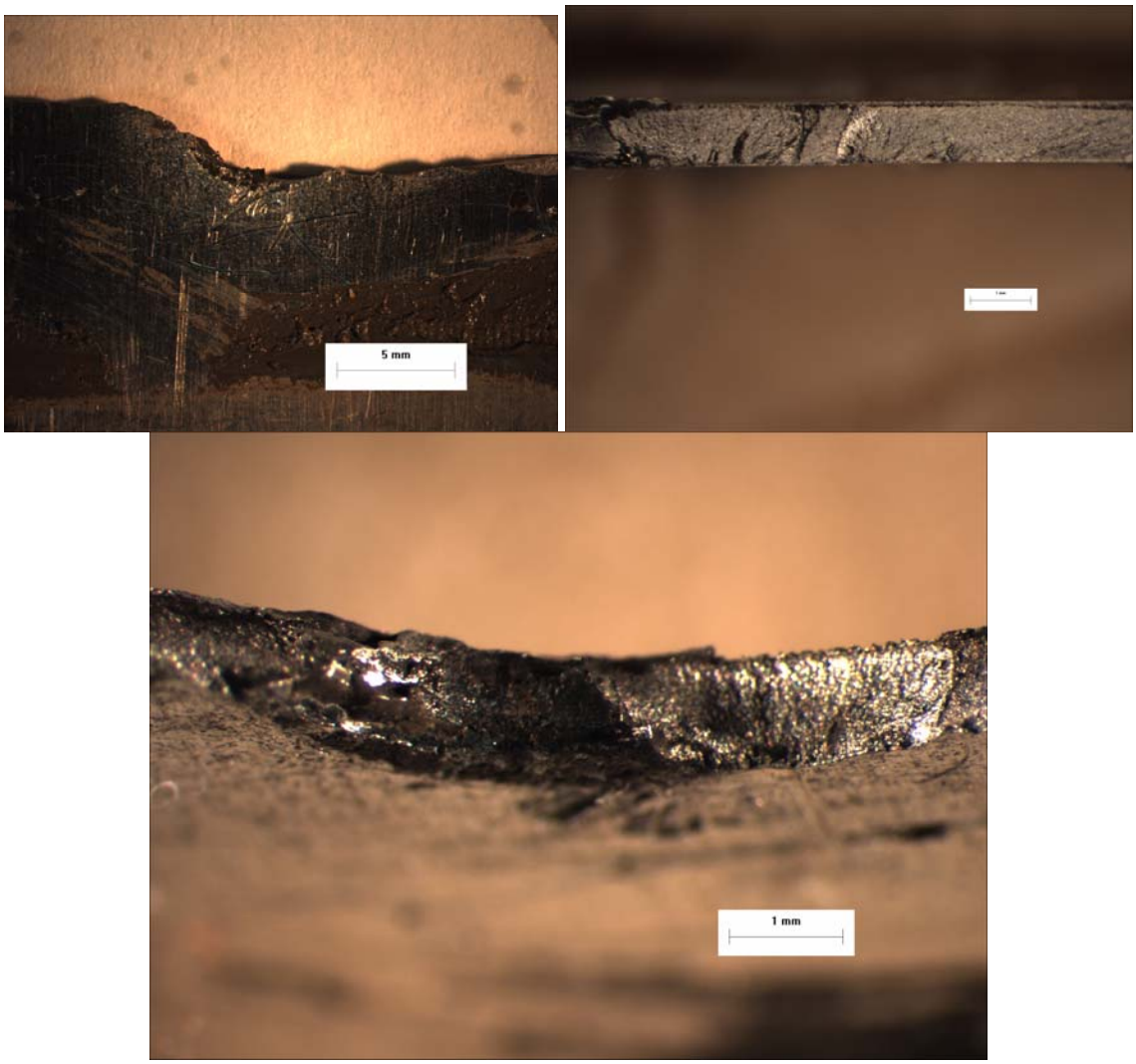


Figure D-6. Damage Characterization of Specimen 10

Lap Joint 10: B95S
Cycles to failure: 144,000
Macroscopic Observations:
Some fretting at hole edge on faying surface. Scratches on faying surface due to possible specimen damage.
Multiple faying surface crack origin, possible hole surface origin.
No circumferential groove observed in hole.

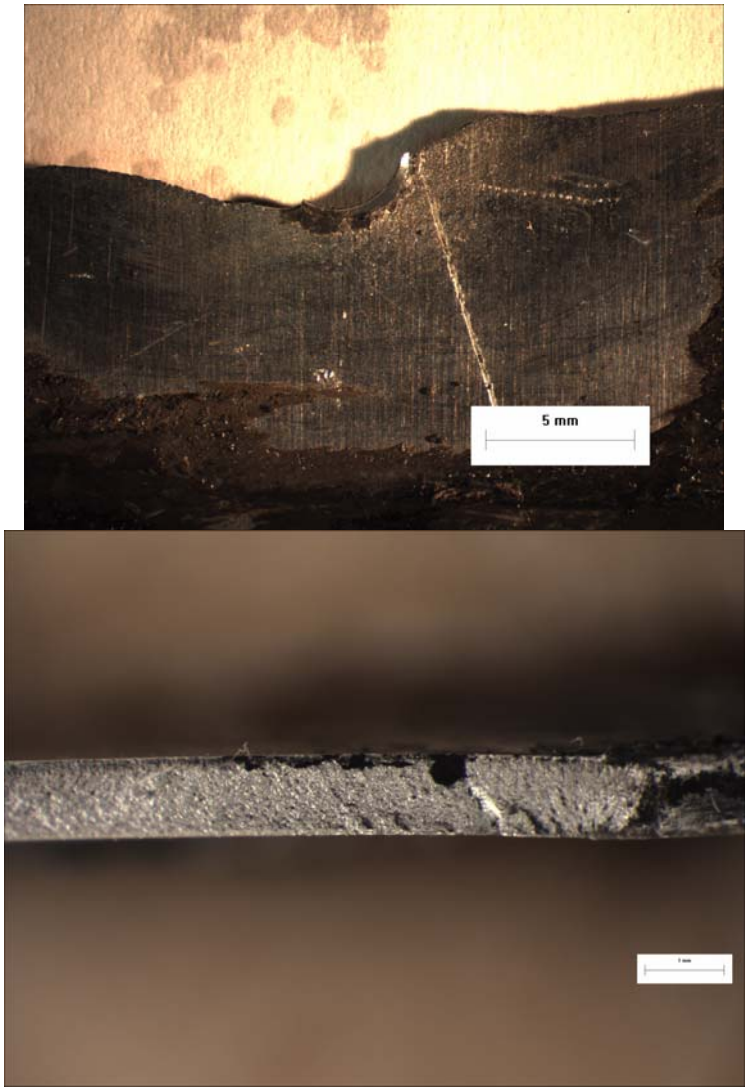


Figure D-7. Damage Characterization of Specimen 11

Lap Joint 11: B95S
Cycles to failure: 145,000
Macroscopic Observations:
Some fretting at hole edge on faying surface.
Faying surface crack origin.
No circumferential groove observed in hole.

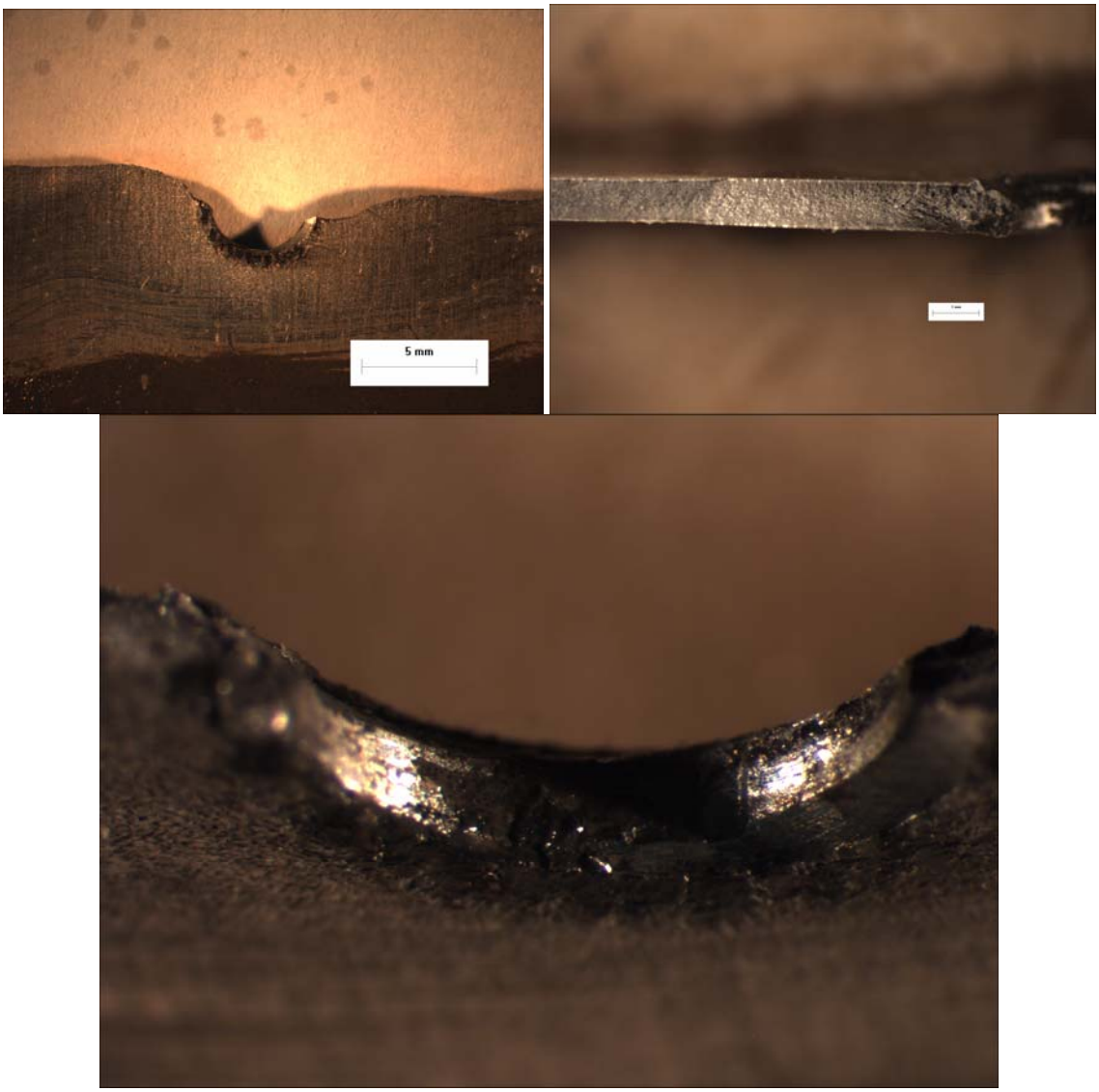


Figure D-8. Damage Characterization of Specimen 13

Lap Joint 13: U95S
Cycles to failure: 60,000
Macroscopic Observations:
Some fretting at hole edge on faying surface.
Faying surface origin and hole surface origin.
No circumferential groove observed in hole.

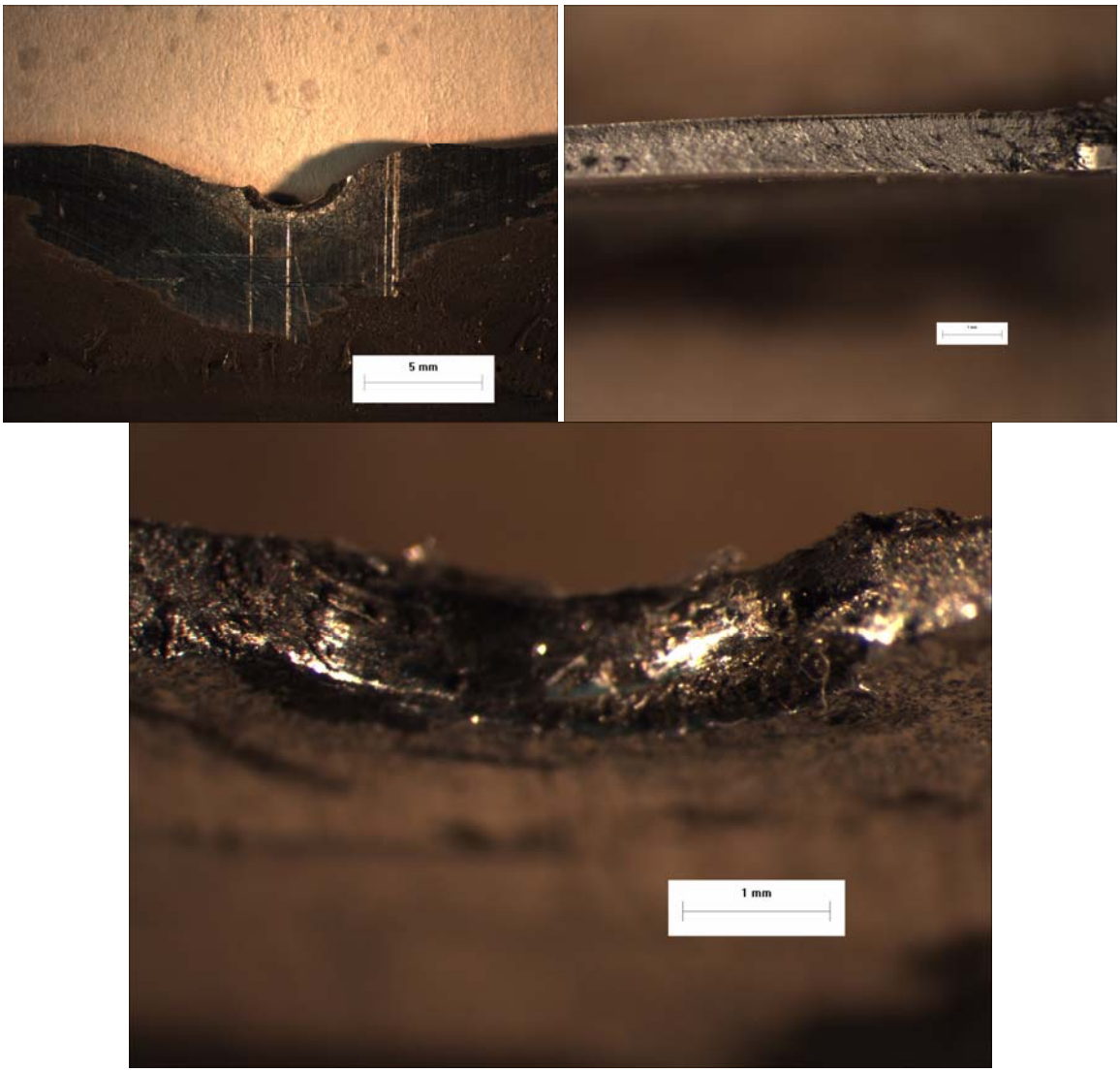


Figure D-9. Damage Characterization of Specimen 14

Lap Joint 14: U95S
Cycles to failure: 81,000
Macroscopic Observations:
Some fretting at hole edge on faying surface.
Faying surface origin and hole surface origin.
No circumferential groove observed in hole.

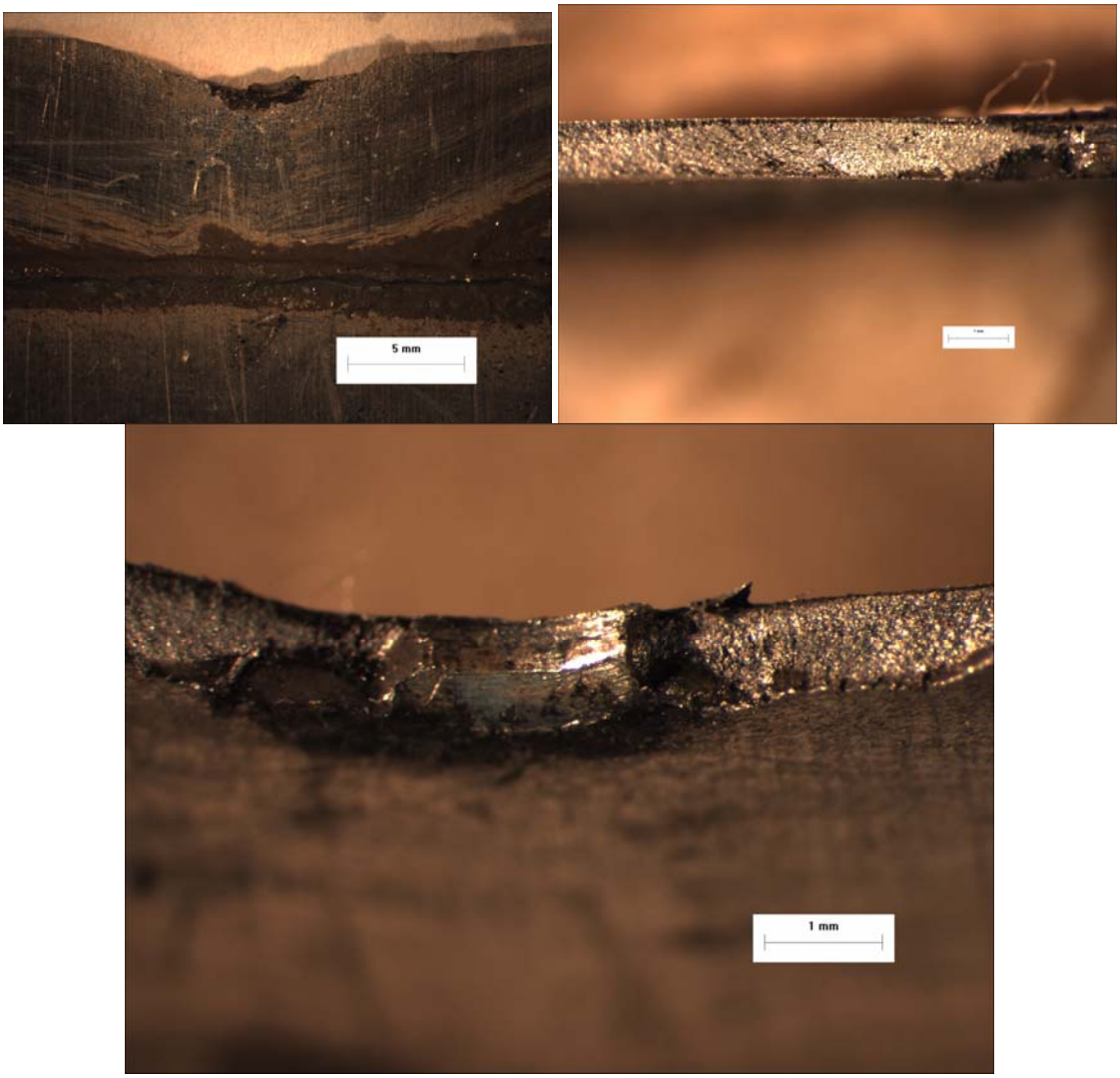


Figure D-10. Damage Characterization of Specimen 16

Lap Joint 16: O95S
Cycles to failure: 140,000
Macroscopic Observations:
Some fretting at hole edge on faying surface.
Faying surface origin.
Circumferential groove observed in hole.

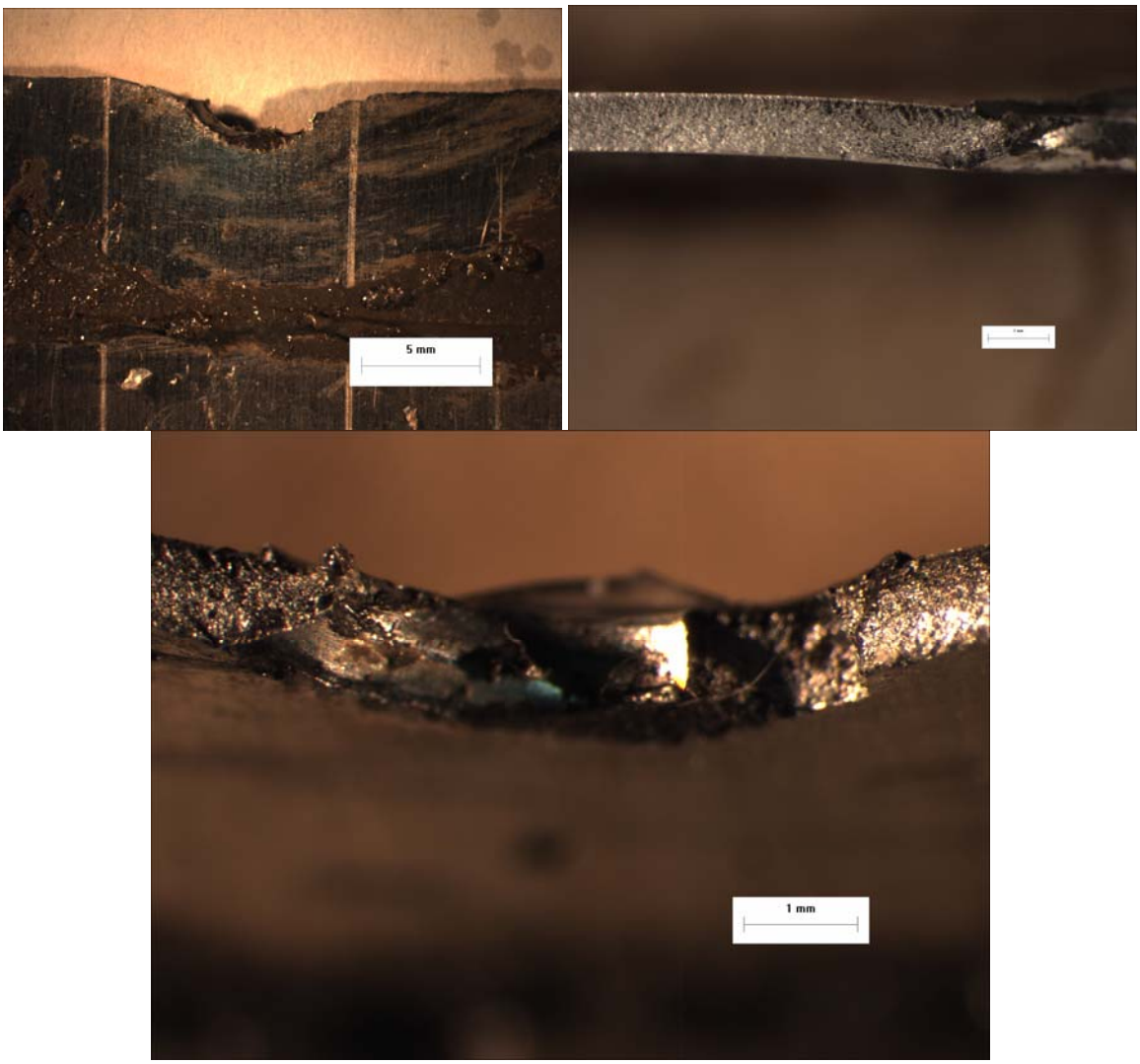


Figure D-11. Damage Characterization of Specimen 17

Lap Joint 17: O95S
Cycles to failure: 160,000
Macroscopic Observations:
Some fretting at hole edge on faying surface.
Exact crack origin difficult to determine. Possible faying surface slightly near hole.
No circumferential groove observed in hole.

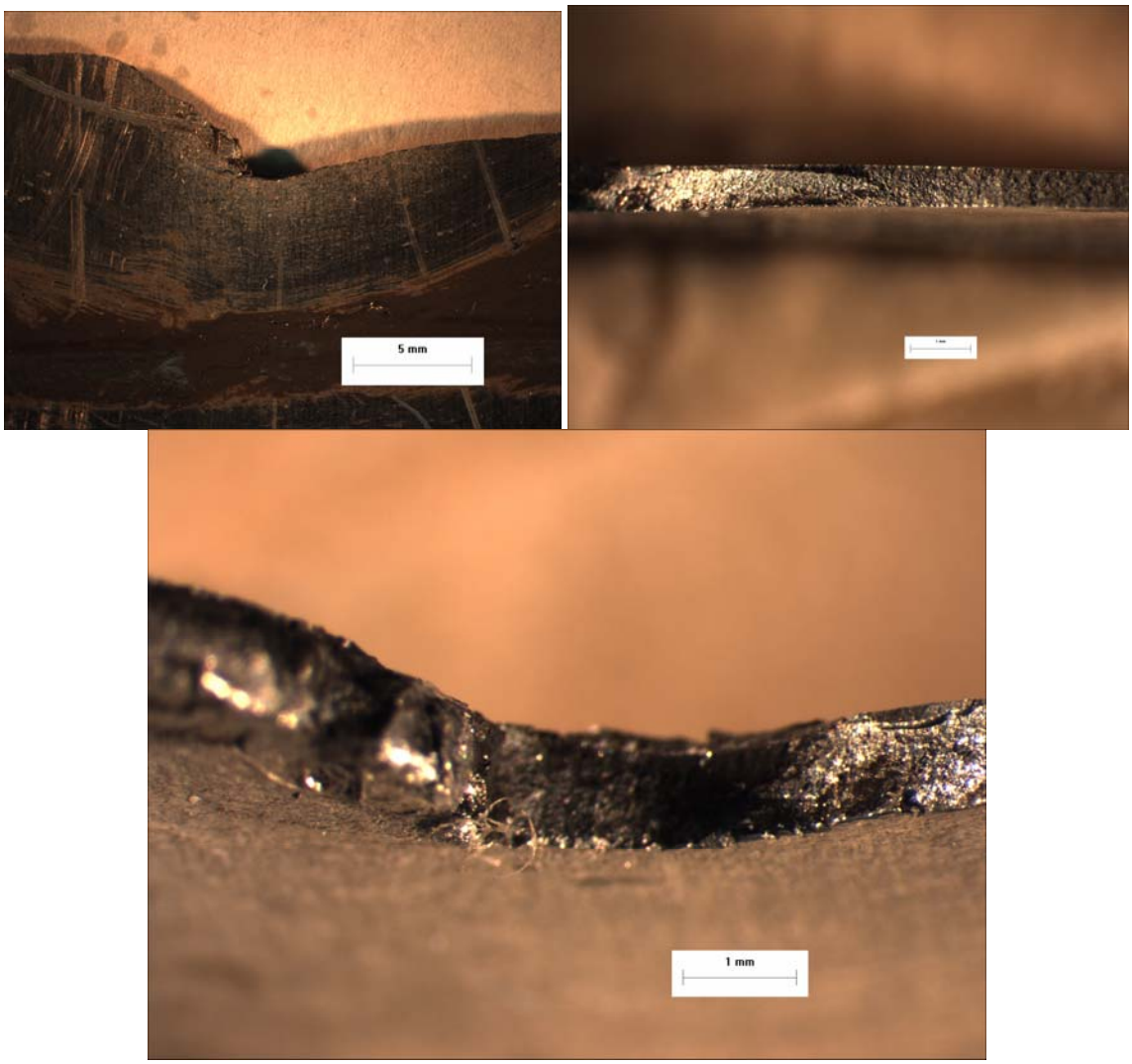


Figure D-12. Damage Characterization of Specimen 19

Lap Joint 19: S95P
Cycles to failure: 150,000
Macroscopic Observations:
Some fretting at hole edge on faying surface.
Faying surface origin and hole surface origin.
No circumferential groove observed in hole.

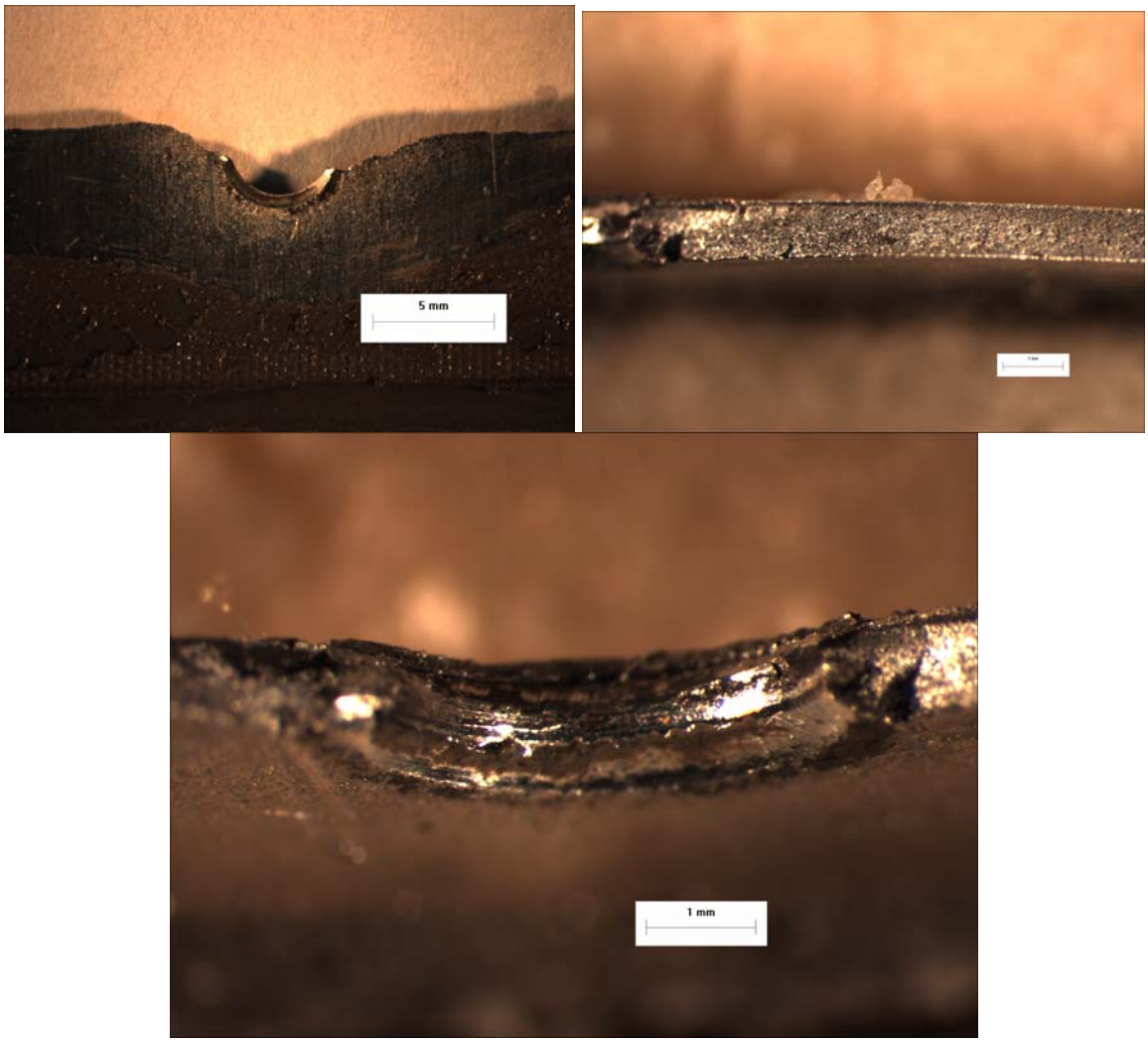


Figure D-13. Damage Characterization of Specimen 20

Lap Joint 20: S95P
Cycles to failure: 104,000
Macroscopic Observations:
No significant fretting at hole edge on faying surface.
Faying surface origin.
Circumferential groove observed in hole.

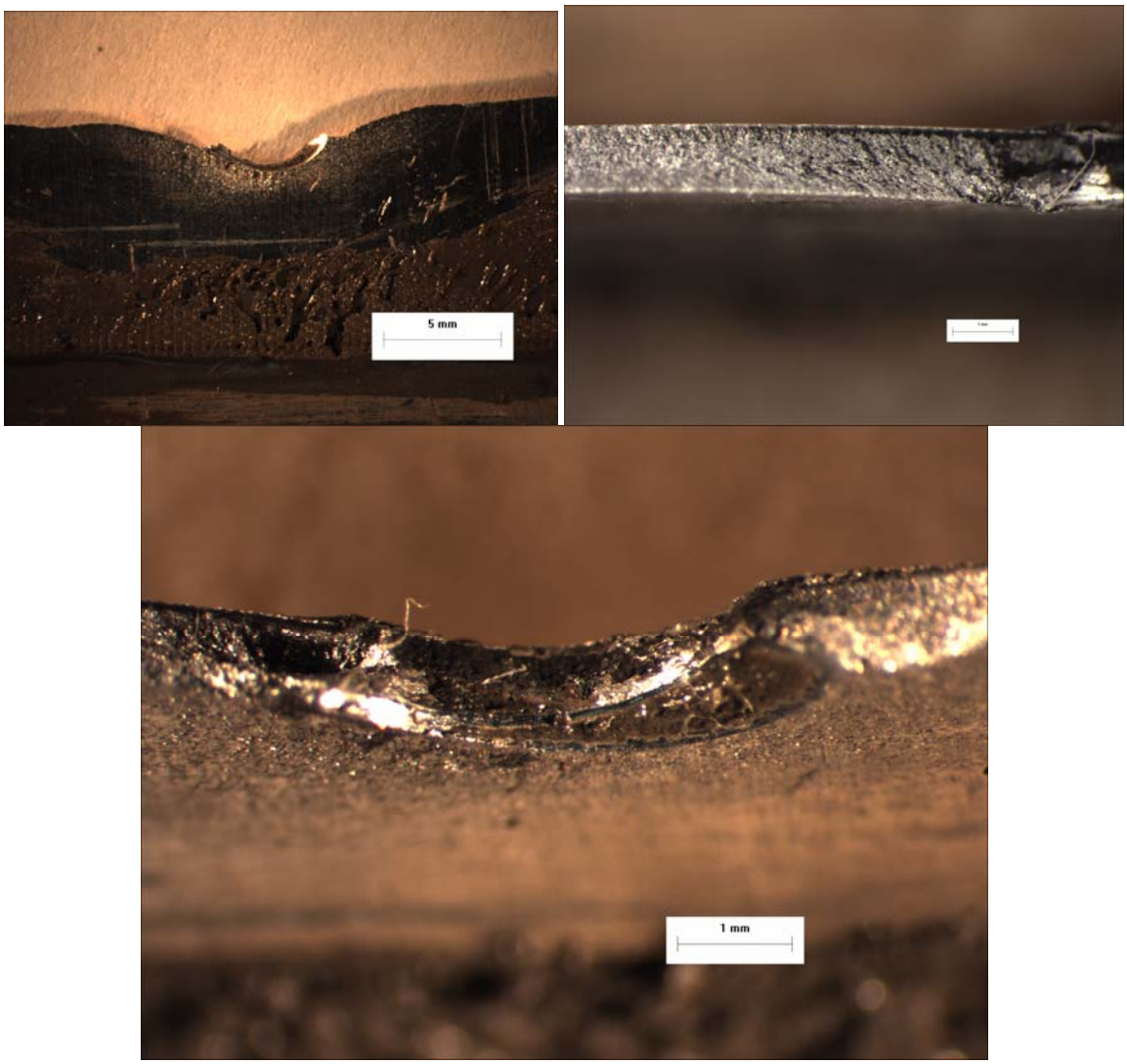


Figure D-14. Damage Characterization of Specimen 22

Lap Joint 22: U95P
Cycles to failure: 42,000
Macroscopic Observations:
Some fretting at hole edge on faying surface.
Hole surface origin.
Circumferential groove observed in hole.

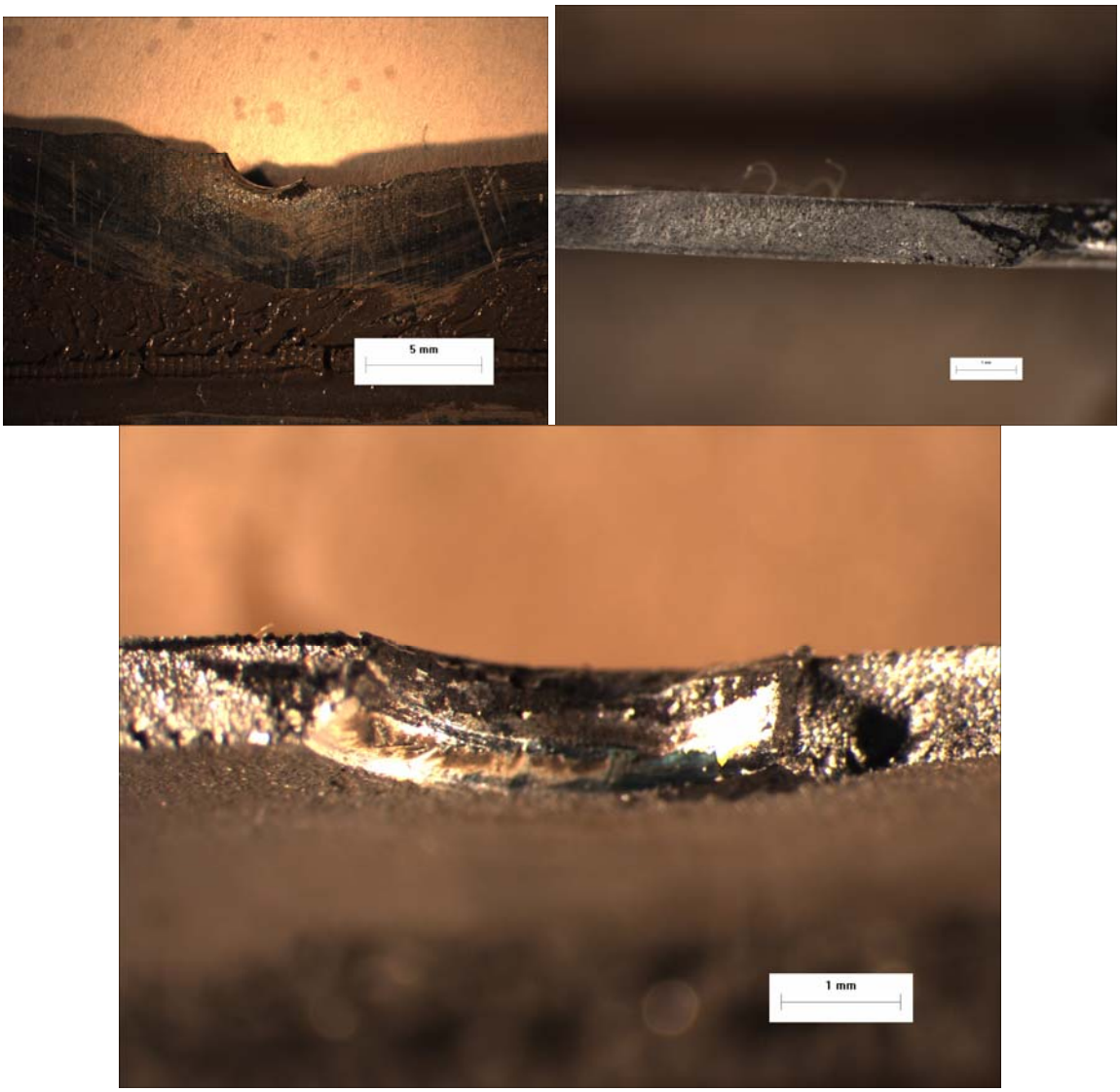


Figure D-15. Damage Characterization of Specimen 23

Lap Joint 23: U95P
Cycles to failure: 52,000
Macroscopic Observations:
Some fretting at hole edge on faying surface.
Hole surface origin.
Circumferential groove observed in hole.

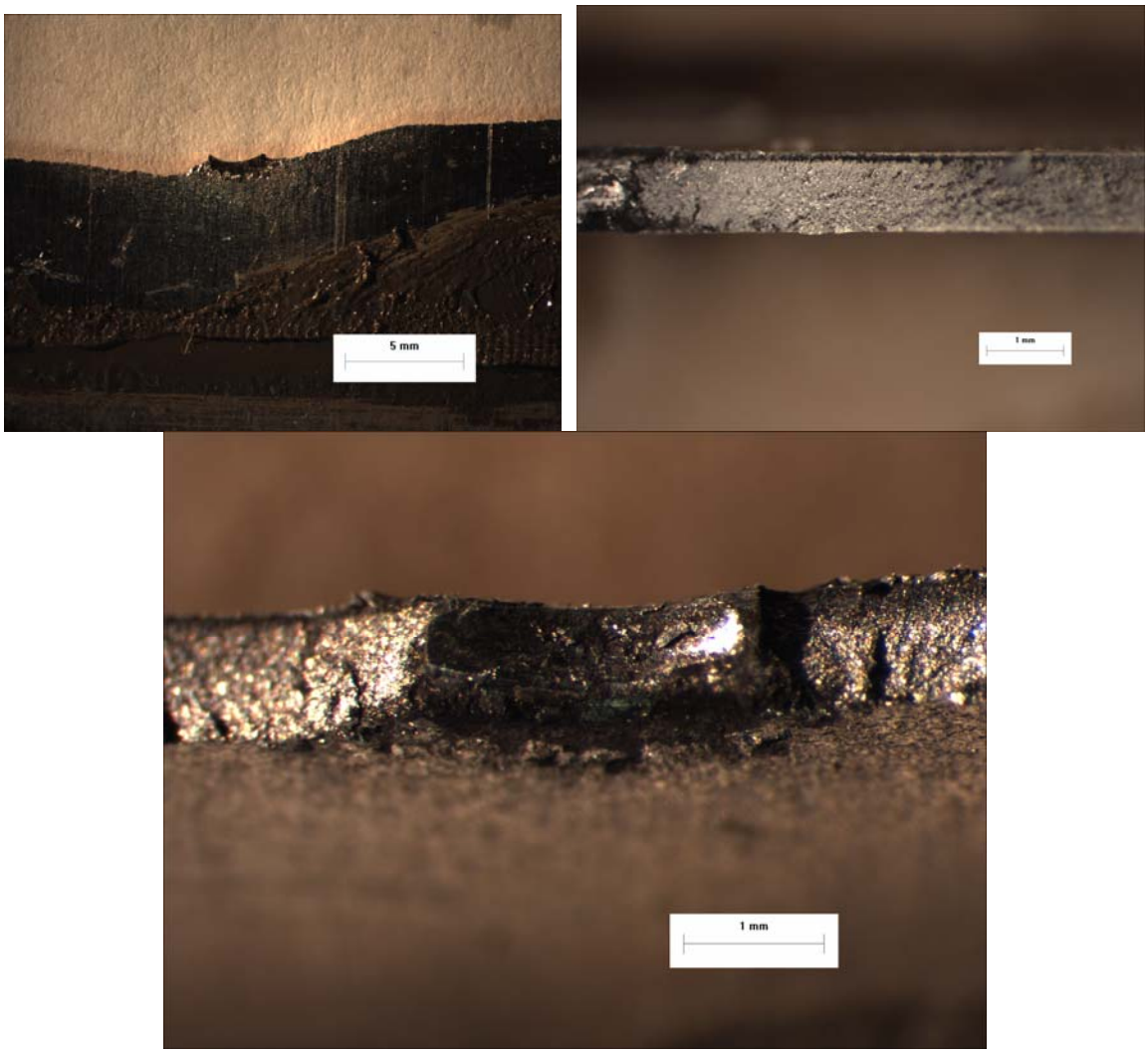


Figure D-16. Damage Characterization of Specimen 26

Lap Joint 26: O95P
Cycles to failure: 130,000
Macroscopic Observations:
Some fretting at hole edge on faying surface.
Faying surface origin.
Circumferential groove observed in hole.

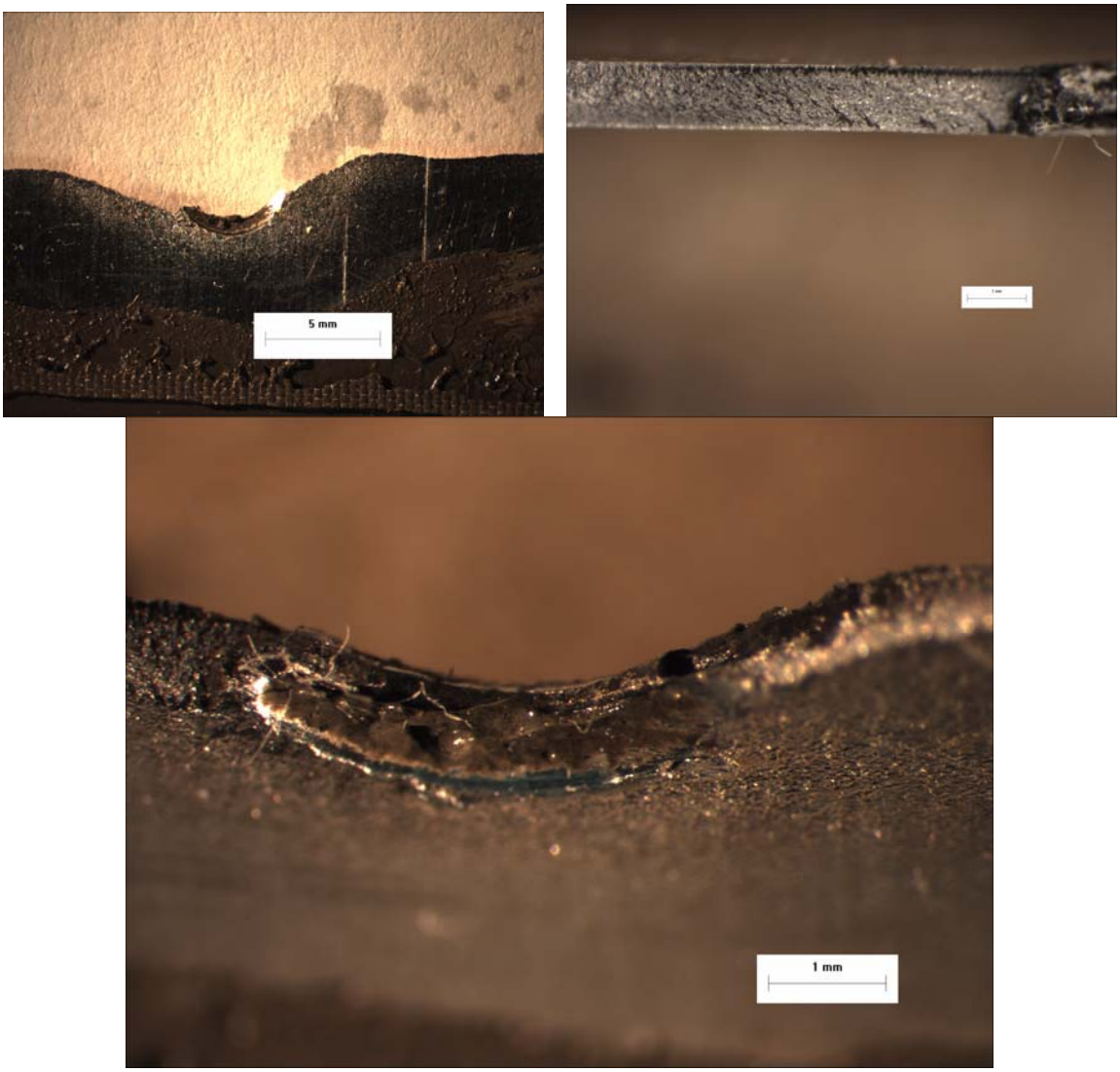


Figure D-17. Damage Characterization of Specimen 27

Lap Joint 27: O95P
Cycles to failure: 123,000
Macroscopic Observations:
No significant fretting at hole edge on faying surface.
Faying surface origin. Possible hole surface origin.
Circumferential groove observed in hole